Aspects of optimisation and qualification in 3D positron emission tomography.

Badawi, Ramsey Derek

Aspects of Optimisation and Quantification in Three-Dimensional Positron Emission Tomography.

A thesis submitted to the University of London
for the Degree of
Doctor of Philosophy

Ramsey D. Badawi
The Clinical PET Centre
Guy's and St. Thomas' Hospital
UMDS, London
March 1998

Abstract

Positron Emission Tomography (PET) is a radio-tracer imaging technique which offers the possibility of quantitative measurements of physiological and biochemical processes *in vivo*, as well as providing a useful clinical diagnostic tool. A key limiting factor in the performance of PET systems is sensitivity, and septa-retracted 3D-mode acquisition (3D) is a technique which has been proposed to improve this. The improved sensitivity in 3D is achieved at the price of increased contamination by scattered photons and random coincidence events, and of increased susceptibility to system dead-time. These effects reduce the effective gain in sensitivity and introduce bias and artefacts into the reconstructed images. This thesis examines some of these issues.

Normalisation of PET detector response is significantly more complex in 3D than in septa-extended 2D mode (2D). In this work an extended normalisation model has been developed and characterised, making use of a range of new algorithms for the calculation of normalisation coefficients.

The optimisation of acquisition parameters for 3D has been addressed, and the factors limiting performance when using 3D in a range of situations have been investigated. An important limiting factor is the noise introduced by random coincidences, and some of the new normalisation algorithms developed in this work are applicable to the problem of variance reduction of random coincidence estimates. These algorithms were tested in this context and the benefits of randoms variance reduction in a range of realistic imaging situations quantified.

Performance in 2D has been compared with 3D, and it has been demonstrated that use of 3D should lead to significant gains in performance in most clinical situations. However, 3D shows only modest gains compared to 2D if the subjects being scanned are very large and may perform less well than 2D when large amounts of activity are present in the camera field of view.

Acknowledgements

A scientific PhD thesis may appear to be the work of one person, but in fact it represents the efforts of a whole team, and there are many key players without whom the thesis could not be produced.

Firstly I would like to thank my primary supervisor Dr. Paul Marsden. His insight and direction have proved the making of this thesis. He took the job of supervising my work very seriously, and I have benefited tremendously from his efforts. Vigorous academic discourse is an enduring (and enjoyable) feature of our work together - nine times out of ten, he is right, and I learn something more. His enthusiasm for science is infectious, and he taught me that the art of scientific thinking is the combination of the creative and the rigorous. When faced with a difficult problem, I now find that asking the question "How would Paul approach this?" usually provides a good place to start. I would also like to thank my second supervisor Dr Mike O'Doherty, who provided encouragement and direction during some of the more difficult phases of this work.

Alongside my supervisors I also thank my wife, without whose continuing support this thesis would not even have been attempted, much less completed. This work is as much hers as mine.

Others provided practical assistance, and I must thank Dale Bailey, Larry Byars, John Ollinger, Steve Meikle and Martin Lodge, who all provided crucial material help in the form of equipment and software. I would also like to thank Charles Watson, Terry Oakes, Dave Gallacher, Tom Lewellen and Steve Kohlmyer, with whom I had useful discussions which contributed in various ways to this work.

From the Clinical PET Centre I thank the radiochemistry team of Julie Sutcliffe, Mark Jacobson and Gerry Brockman, who on many occasions worked out of hours to provide me with tracer, Bernadette Cronin who was particularly helpful in designing and carrying out the clinical studies and Peter Liepins who helped create some of the graphics presented here. I must also thank the entire PET Centre team for providing a

supportive working environment. They made a great deal of difference to both the speed at which I was able to work and the pleasure I experienced while doing it.

Finally I thank Professor Michael Maisey who created the opportunity for me to undertake and complete this work, and remained encouraging and optimistic throughout.

This work has been supported by the Special Trustees of Guy's and St. Thomas' Hospital.

To Ania.

Publications and presentations arising from this work

Journal publications

RD Badawi, MA Lodge and PK Marsden.
Algorithms for calculating detector efficiency normalisation coefficients for true coincidences in 3D PET
Phys. Med. Biol. **43**(1), 189-205, 1998

RD Badawi.
3D-Mode Acquisition in Clinical PET.
Nucl. Med. Comm. **18**(9), 801-804, 1997 (editorial)

RD Badawi, PK Marsden, BF Cronin, JL Sutcliffe and MN Maisey.
Optimization of noise-equivalent count-rates in 3D PET.
Phys. Med. Biol. **41**(9), 1755-1776, 1996

Published Abstracts

RD Badawi and PK Marsden.
An Algorithm for Efficient Detector Normalisation in 3D PET.
Nucl Med. Comm. **18**(4):311, 1997

RD Badawi and PK Marsden.
Optimisation of Acquisition Parameters for 2D and 3D PET.
J. Nucl. Med. **37**(5) Supp.:73P,1996

PK Marsden, **RD Badawi**, JCH Wong and MN Maisey.
Validation of 3D PET for cardiac scanning in young children.
Nucl. Med. Comm. **17**(4):290-291,1996

Proceedings and Conference Records

RD Badawi and PK Marsden.
Algorithms for calculating detector normalisation coefficients in 3D PET.
1997 International Meeting on Fully Three-Dimensional Image Reconstruction in Radiology and Nuclear Medicine, Conference Record. June 1997, Nemacolin Woodlands, Pennsylvannia, USA.

RD Badawi, M Jacobson and PK Marsden.
Noise-Equivalent Count Rates and Image Signal-to-Noise Ratios in 3D PET in the Body.
IEEE Nuclear Science Symposium and Medical Imaging Conference Abstract Book p137 7M12.
October 1995, San Francisco, USA

Table of Contents

1. **BACKGROUND AND INTRODUCTION** **20**

1.1. POSITRON EMISSION TOMOGRAPHY (PET) IN MEDICAL IMAGING. 20

1.2. THE PHYSICAL PRINCIPLES OF PET 22

1.2.1. Introduction *22*

1.2.2. Positron emission and annihilation *22*

1.2.3. Coincidence detection and electronic collimation *24*

1.2.4. Photon interactions in human tissue and correction for gamma-ray attenuation. *25*

1.2.5. Types of coincidence events. *28*

1.3. 2D MODE AND 3D MODE 30

1.3.1. Principles of operation *30*

1.3.2. Sensitivity to true coincidence events *31*

1.3.3. Sensitivity to scattered events. *32*

1.3.4. Sensitivity to random events *33*

1.3.5. Effect of camera geometry. *33*

1.4. IMAGE RECONSTRUCTION 34

1.4.1. Introduction *34*

1.4.2. Notation and mathematical theorems used *34*

1.4.3. Analytic image formation in 2D PET *36*

1.4.4. Filtered Back-Projection in 3D and 3D-RP *38*

1.5. DETECTION SYSTEMS IN PET 40

1.5.1. Introduction *40*

1.5.2. Scintillators and scintillation detectors *40*

1.5.3. Pulse processing. *43*

1.5.4. Coincidence processing. *44*

1.5.5. Dead-time *45*

1.5.6. Block detectors *46*

1.5.7. Camera configurations in PET *47*

1.6. CORRECTIONS FOR QUANTITATIVE PET IN 2D AND 3D MODE 48

1.6.1. Introduction *48*

1.6.2. Attenuation correction *48*

1.6.3. Correction for random coincidences *49*

1.6.4. Scatter correction *49*

1.6.5. Detector normalisation *51*

1.6.6. Dead time correction *52*

1.7. OBJECTIVES OF THIS WORK. 53

1.8. REFERENCES 54

2. FEATURES AND BASIC PERFORMANCE PARAMETERS OF THE ECAT 951R SCANNER AND RECONSTRUCTION ALGORITHMS USED 58

2.1. INTRODUCTION 58
2.2. DESIGN FEATURES OF THE ECAT 951R 58
2.2.1. Scanner geometry 58
2.2.2. Block detectors and coincidence circuitry 59
2.2.3. Singles measurements and dead-time correction 60
2.2.4. Transaxial sampling 60
2.2.5. Acquisition modes 61
2.2.6. Transmission scanning and sources 61
2.3. RECONSTRUCTION ENGINES USED 62
2.4. VARIATIONS IN RESOLUTION AND IMAGE SIGNAL-TO-NOISE RATIOS IN 2D AND 3D MODE 63
2.5. PERFORMANCE OF 3D-RP WITH SIMULATED DATA 64
2.6. REFERENCES 65

3. VARIANCE REDUCTION ALGORITHMS FOR DETECTOR NORMALISATION IN 3D MODE 66

3.1. INTRODUCTION 66
3.2. THEORY 68
3.2.1. Normalisation model 68
3.2.2. Algorithms for calculation of intrinsic efficiencies 68
3.2.2.1. The single-plane fan-sum method 69
3.2.2.2. The single-plane method due to Casey 71
3.2.2.3. Extended version of the single-plane method due to Defrise 73
3.2.2.4. The Fully-3D methods 75
3.3. COMPARATIVE ASSESSMENT METHODS 77
3.3.1. Normalisation scheme, reconstruction and assessment methods 77
3.3.2. Crystal efficiency simulation 79
3.3.3. Acquisition of normalisation data 80
3.3.3.1. Scanning line-source data 80
3.3.3.2. Rotating line-source data 81
3.3.3.3. 20 cm cylinder data 81
3.3.4. Optimisation of group size for extended Defrise algorithms. 82
3.3.5. Assessment of the effect of gantry set-up and of the accuracy of the algorithms with noise-free data 82
3.3.6. Assessment of the effectiveness of the algorithms in terms of variance reduction 83
3.3.7. Assessment of the effects of using different sources for the calculation of crystal efficiencies 84
3.4. RESULTS 85
3.4.1. Optimum group sizes for extended Defrise algorithm 85
3.4.2. The effect of gantry set-up and the accuracy of the algorithms with noise-free data 86
3.4.3. Performance as a function of noise in the efficiency dataset 86
3.4.4. The effects of using different sources for the calculation of crystal efficiencies 89

3.5. DISCUSSION 93
3.6. REFERENCES 95

4. COMPONENT-BASED NORMALISATION IN 3D PET 96

4.1. INTRODUCTION 96
4.1.1. A synthesised model for component-based normalisation 96
4.1.2. Critique of the synthesised normalisation model 99
4.1.2.1. Scatter correction 99
4.1.2.2 Time-window alignment 99
4.1.2.3. NCs for scattered coincidences 100
4.1.2.4. Dead-time correction 101
4.1.2.5. Variations in sensitivity within an LOR 102
4.1.3. Summary of chapter 4 102
4.2. THE GAUSSIAN FIT SCATTER CORRECTION METHOD FOR NORMALISATION 103
4.2.1. Implementation 103
4.2.2. Validation of the Gaussian fit algorithm for use in normalisation 103
4.3. METHODS FOR CALCULATING NORMALISATION COMPONENTS 109
4.3.1. Count-rate dependent, variable and fixed components 109
4.3.2. Algorithms for calculating correction factors 109
4.3.2.1. Block-profile factors, $b_{u\,\mathrm{mod}D}$ 110
4.3.2.2. Intrinsic crystal efficiency factors, ε_{ui} 110
4.3.2.3. Plane efficiencies, f_{uv} 110
4.3.2.4. Radial geometric factors, $g_{u\,r}$ 112
4.3.2.5. Crystal interference factors, d_{uvrk} 112
4.3.2.6. Time-window alignment factors, $h_{\mathrm{int}\,1+u\,D\,\bullet\,\mathrm{int}\,D\quad\mathrm{int}\,1+v\,D\,\bullet\,\mathrm{int}(j\,D}$ 113
4.4. COMPUTATIONAL AND ACQUISITION PROTOCOLS 114
4.4.1. Calculation of fixed components d_{uvrk}, g_{uvr} and $h_{(\mathrm{int}(1+u/D)\bullet\,\mathrm{int}(v/D))\,(\mathrm{int}\,1+v\,D)\bullet\,\mathrm{int}(j\,D))}$ 114
4.4.2. Calculation of variable components 116
4.4.3. Calculation of rate-dependent components 116
4.5. CHARACTERISATION OF NORMALISATION COMPONENTS 120
4.5.1. Radial geometric profile 120
4.5.2. Transaxial Block-profile 128
4.5.3. Axial Block-profile and Plane Efficiency 129
4.5.4. Detector efficiency 133
4.5.5. Crystal interference 134
4.5.6. Time-window alignment 134
4.6. SIGNIFICANCE OF NORMALISATION COMPONENTS IN REALISTIC IMAGING SITUATIONS 136
4.7. DISCUSSION 138
4.8. REFERENCES 140

5. COMPARISON OF PERFORMANCE IN 2D AND 3D PET 141

5.1. INTRODUCTION 141

5.2. MATERIALS AND METHODS 143
5.2.1. Scanner and Phantoms *143*
5.2.2. Scatter Measurements *143*
5.2.3. Count-Rate Measurements *145*
5.3. RESULTS 147
5.3.1. Scatter Fractions *147*
5.3.2. Count Rates *147*
5.3.3. NEC Rates *149*
5.3.4. Comparison of 3D and 2D NEC rates *152*
5.4. DISCUSSION 154
5.4.1. Factors limiting NEC rates *154*
5.4.2. Optimisation of NEC rates *155*
5.4.3. The effect of scanner geometry on NEC rates *156*
5.5. CONCLUSIONS 158
5.6. REFERENCES 159

6. VARIANCE REDUCTION TECHNIQUES FOR RANDOM COINCIDENCES IN 3D PET 161

6.1. INTRODUCTION 161
6.2. MATERIALS AND METHODS 164
6.2.1. Applicability and implementation of normalisation algorithms *164*
6.2.2. The effect of randoms variance reduction and reduction in randoms fraction on NEC rates. *165*
6.2.3. Accuracy of the variance reduction algorithms *166*
6.2.4. Measurement of the effect of randoms variance reduction on image SNRs in phantom studies *166*
6.2.5. The effect of randoms variance reduction in human studies. *167*
6.3. RESULTS 168
6.3.1. The effect of randoms variance reduction on noise-equivalent count-rates. *168*
6.3.2. Comparison of accuracy of randoms variance reduction methods *169*
6.3.3. Measurement of the effect of randoms variance reduction on image SNRs in phantom studies *171*
6.3.4. The effect of randoms variance reduction in human studies. *172*
6.4. DISCUSSION AND CONCLUSIONS 174
6.5. REFERENCES 175

7. HUMAN STUDIES IN 2D AND 3D MODE 176

7.1. INTRODUCTION 176
7.2. METHODS 176
7.3. RESULTS 177
7.3.1. Adult brain, ^{11}C-flumazenil *178*
7.3.2. Adult brain, ^{18}F- FDG *179*
7.3.3. Adult head and neck, ^{18}F- FDG *180*
7.3.4. Adult axillae, ^{18}F- FDG. *181*
7.3.5. Adult heart, ^{18}F- FDG. *182*

7.3.6. Adult pelvis, ^{18}F- FDG. *183*
7 3.7. Adult pelvis, ^{18}F- F^{-} *184*
7.4. DISCUSSION 185
7.5. CONCLUSIONS 187
7.6. REFERENCES 187
8. SUMMARY, CONCLUSIONS AND FUTURE WORK. 188
8.1. SUMMARY 188
8.2. KEY CONCLUSIONS 190
8.3. FUTURE WORK 191
8.4. REFERENCES 193

List of Figures

Chapter 1

Figure 1.1. Positron emission and annihilation. 23
Figure 1.2. Coincidence detection in a PET camera....24
Figure 1.3. Variation of point source response function (psrf) with position *P* in SPECT and in PET. 25
Figure 1.4. Coincidence detection in an attenuating object....27
Figure 1.5. Types of coincidences in PET....28
Figure 1.6. Axial cut-away view of a multi-ring PET camera (not to scale) operating in 2D mode, showing direct and cross-plane rebinning. 30
Figure 1.7. Axial cut-away view of a PET camera in 2D and 3D mode showing how the number of possible LORs can increase when the septa are removed....31
Figure 1.8. Predicted sensitivity from the number of LORs used in 2D and 3D mode. 32
Figure 1.9. Effect of septa removal on sensitivity to scattered coincidences 32
Figure 1.10. Effect of septa removal on sensitivity to single events 33
Figure 1.11. 3D co-ordinate system for a full-ring PET camera 35
Figure 1.12. Projections generated from a single central point source (3 projections shown). 36
Figure 1.13. Back-projections of a point source....37
Figure 1.14. The Ramp and Hanning filters 38
Figure 1.15. Parallel projections in 2D (left) and 3D (right). 38
Figure 1.16. Axial cut-away diagram of a PET camera operating in 3D mode, showing the extent of the projection sets as a function of angle φ. 39
Figure 1.17. Features of a typical energy distribution for electrons involved in interactions with 511 keV photons. 41
Figure 1.18. Features of a typical energy distribution measured by a scintillation detector system exposed to 511 keV photons....42
Figure 1.19. Schematic diagram showing coincidence processing in a PET camera. 45
Figure 1.20. A block detector....46

Chapter 2

Figure 2.1. Detector configuration for the ECAT 951R camera. 58
Figure 2.2. Singles rates as a function of distance from the edge of the FOV in 3D mode....59
Figure 2.3. Transaxial sampling on the ECAT 951....60
Figure 2.4. Events arising from retracted rod-sources during a 3D emission scan. 62
Figure 2.5. Number of events arising from retracted rod-sources during a 3D emission scan....62
Figure 2.6. Reconstructed image FWHM for a central line source as a function of axial position. 63
Figure 2.7. SNR quantified as % std. dev. of reconstructed image elements as a function of image plane. 64
Figure 2.8. Mean count density in reconstructed simulated 3D data as a function of axial position. 65
Figure 2.9. Radial profiles through image planes 1 (left) and 3 (right) from the reconstructed simulated 3D data. 65

Chapter 3

Figure 3.1. Elements of the single-plane fan-sum method. 69
Figure 3.2. The single-plane Casey method in 3D. 71
Figure 3.3. Elements of the single-plane Defrise method 74
Figure 3.4. LORs in a 3D fan-sum. 75
Figure 3.5. Normalisation scheme. 78
Figure 3.6. Generation of simulated data. 79
Figure 3.7. Formation of a composite sinogram from a series of line-source acquisitions. 80
Figure 3.8. Performance of original and extended Defrise algorithms 85
Figure 3.9. Noise performance of SP and 3D algorithms. 87
Figure 3.10. Noise performance of best performing algorithms. 87
Figure 3.11. Sinogram data acquired using a 20 cm cylinder - effectiveness of SP and 3D normalisation. 88
Figure 3.12. Uniformity of normalised images. 89
Figure 3.13. Images (summed over all reconstructed planes) of 19,200 second 20cm cylinder acquisition 89
Figure 3.14. Axially summed images of a 20 cm cylinder self normalised using different algorithms. 91
Figure 3.15. Summed images reconstructed from 20 cm cylinder data normalised using different sources 92

Chapter 4

Figure 4.1. LORs at the same radial position θ. 98
Figure 4.2. Position of ROIs for calculation of scatter fraction on image of off-centre cylinder with cold insert. 105
Figure 4.3. Residual scatter fractions for each image plane for off-centre cylinder with cold insert. 105
Figure 4.4. Summed images of and vertical profiles through central uniform cylinder. 106
Figure 4.5. Summed images of and vertical profiles through off-centre cylinder with cold insert. 108
Figure 4.6. LORs crossing a uniform attenuating source 111
Figure 4.7. Protocol for calculating fixed normalisation components from low-scatter data 114
Figure 4.8. Protocol for calculation of variable normalisation components from a scan of a central uniform cylinder. 115
Figure 4.9. Summed images of off-centre 17cm-diameter slot phantom. 117
Figure 4.10. Summed normalised and scatter-corrected sinograms from an ^{18}F-FDG adult brain study. 118
Figure 4.11. Plane 19 from images reconstructed from the normalised and scatter-corrected sinograms from the ^{18}F-FDG brain study shown in figure 4.10 118
Figure 4.12. Summed normalised and scatter-corrected sinograms from an ^{18}F-FDG paediatric brain study. 119
Figure 4.13. Plane 18 from images reconstructed from the normalised and scatter-corrected sinograms from the paediatric ^{18}F-FDG brain study shown in figure 4.12. 119
Figure 4.14. Image planes 1, 3, 5, ... , 31 from a uniform 20 cm cylinder acquisition reconstructed and normalised for all components except radial geometric profile 120
Figure 4.15. Mean radial geometric profiles obtained from the scanning and rotating line source acquisitions. 121
Figure 4.16. Reconstructions of a uniform 20 cm cylinder with different radial geometric corrections 123

Figure 4.17. Summed images and vertical profiles through uniform central cylinder normalised using different radial geometric corrections. 124
Figure 4.18. Summed images and vertical profile through off-centre cylinder with cold insert, normalised using different radial geometric corrections....125
Figure 4.19. Summed images and profiles through high and low activity cylinders. 126
Figure 4.20. Scatter in a scanning line-source acquisition. 127
Figure 4.21. Block profiles for different crystal rings obtained from a 20 cm cylindrical source (50 MBq in the FOV)....128
Figure 4.22. Summed sinograms from high and low activity 20 cm cylinder acquisitions....128
Figure 4.23. Summed images from high and low activity 20 cm cylinder acquisitions....129
Figure 4.24. Features of the axial block-profile normalisation component....130
Figure 4.25. Axial uniformity plots for a reconstructed scan of 20 cm cylinder with 50 MBq in the FOV with different corrections for axial block-profile. 130
Figure 4.26. Mean plane efficiencies as a function of ring difference. 131
Figure 4.27. Axial uniformity plots for a reconstructed scan of 20 cm cylinder with 50 MBq in the FOV with and without corrections for plane efficiency. 132
Figure 4.28. Image axial uniformity as a function of counts in the normalisation data. 133
Figure 4.29. Histogram of crystal efficiencies. 133
Figure 4.30. Crystal interference factors (a) and time-window alignment factors (b) calculated from a rotating line-source acquisition. 134
Figure 4.31. Summed sinograms from low-variance 20 cm cylinder acquisition. 135
Figure 4.32. Summed images from low-variance 20 cm cylinder acquisition, 50 MBq in FOV. 135
Figure 4.33. Reconstructed images derived from an ^{18}F-FDG adult human brain scan. 137

Chapter 5

Figure 5.1. Phantoms used in the NEC rate measurements. 145
Figure 5.2. Scatter fractions. 147
Figure 5.3. 3D mode count-rates as a function of activity in the FOV....148
Figure 5.4. 2D mode count-rates as a function of activity in the FOV....148
Figure 5.5. Calculated fractional dead-times in 3D mode for all phantoms as a function of activity in the FOV. 149
Figure 5.6. 3D NEC as a function of activity in the FOV and of LLD for the 13 cm cylinder. 149
Figure 5.7. 3D NEC as a function of activity in the FOV and of LLD for the 37x48 cm chest phantom. 150
Figure 5.8. 2D NEC as a function of activity in the FOV and of LLD for the 13 cm cylinder. 151
Figure 5.9. 2D NEC as a function of activity in the FOV and of LLD for the 37x48 cm chest phantom. 151
Figure 5.10. 3D NEC rates as a function of activity in the FOV for all phantoms. The curves are plotted at the LLDs given in table 5.5. 152
Figure 5.11. 2D and 3D mode NEC ratios. 153

Chapter 6

Figure 6.1. Improvement in NEC due to randoms variance reduction as a function of activity in the FOV.... 168
Figure 6.2. Effect of randoms reduction on NEC.... 169
Figure 6.3. Raw randoms sinogram summed over all axial planes.... 170
Figure 6.4. Effect of randoms variance reduction on sinogram uniformity.... 170
Figure 6.5. Visual effect of randoms variance reduction on an ^{18}F- FDG cardiac study.... 172
Figure 6.6. Visual effect of randoms variance reduction on an ^{18}F- FDG head and neck study.... 172
Figure 6.7. Visual effect of randoms variance reduction on an ^{18}F- FDG pelvic study.... 173

Chapter 7

Figure 7.1. Selected image planes from adult ^{11}C-flumazenil brain study.... 178
Figure 7.2. Selected image planes from adult ^{18}F- FDG brain study.... 179
Figure 7.3. Selected image planes from adult ^{18}F- FDG head and neck study.... 180
Figure 7.4. Selected image planes from adult ^{18}F- FDG axillae study.... 181
Figure 7.5. Selected image planes from adult ^{18}F- FDG heart study.... 182
Figure 7.6. Selected image planes from adult ^{18}F- FDG pelvis study.... 183
Figure 7.7. Selected image planes from adult ^{18}F- F^- pelvis study.... 184
Figure 7.8. Heavily smoothed selected image planes from adult ^{18}F- F- pelvis study.... 186

List of Tables

Chapter 1

Table 1.1. Examples of radiotracers and their applications. 20

Table 1.2. Properties of commonly used positron emitting radio-isotopes 22

Table 1.3. Notation for spatial and Fourier quantities. 35

Table 1.4. Examples of scintillators and their properties 43

Chapter 3

Table 3.1. The six normalisation algorithms and their properties. 76

Table 3.2. Optimum parameters for extended Defrise algorithm for various normalisation source configurations. 85

Table 3.3. Percentage SDs of normalised sinogram elements, averaged over 50 different gantry set-ups. 86

Table 3.4. Percentage SDs of normalised sinogram elements using different normalisation sources. 90

Table 3.5. Percentage SDs of normalised sinogram elements using simulated data. 90

Table 3.6. Uniformity of reconstructed images normalised by different methods. 91

Table 3.7. Uniformity of reconstructed images normalised using different sources. 92

Chapter 4

Table 4.1. Percentage errors in the total counts in individual image planes due to variations in corrections for axial block-profile. 130

Chapter 5

Table 5.1. Physical properties of the phantoms. 143

Table 5.2. Rod source positions and annulus outer boundaries for scatter measurements. 145

Table 5.3. Optimum 3D-mode LLDs in keV at different activities for all phantoms. 150

Table 5.4. Optimum 2D-mode LLDs in keV at different activities for all phantoms. 151

Table 5.5. Optimum LLDs for typical clinical studies (20 MBq in the FOV) 152

Chapter 6

Table 6.1. Uniformity of ratio of variance reduced to raw randoms sinograms using different algorithms 170

Table 6.2. SNR gain due to randoms variance reduction (phantom studies) 171

Chapter 7

Table 7.1. Protocol details and count-rates for adult ^{11}C-flumazenil brain study. 178

Table 7.2. Protocol details and count-rates for adult ^{18}F- FDG brain study. 179

Table 7.3. Protocol details and count-rates for adult ^{18}F- FDG head and neck study. 180

Table 7.4. Protocol details and count-rates for adult ^{18}F- FDG axillae study. 181

Table 7.5. Protocol details and count-rates for adult ^{18}F- FDG heart study 182

Table 7.6. Protocol details and count-rates for adult ^{18}F- FDG pelvis study. 183

Table 7.7. Protocol details and count-rates for adult ^{18}F- F pelvis study. 184

It is common to include a literary quotation at the start of a thesis to help put the work in perspective. I have been unable to find an appropriate quote from a traditional source, and so have included one from a colleague which left a particularly deep impression:

I can see that writing this thesis is causing you a great deal of stress.
Do not worry.
No-one will ever read it.

Dr M. Koutroumanidis,
January 1998

1. Background and Introduction.

1.1. Positron Emission Tomography (PET) in Medical Imaging.

Positron Emission Tomography (PET) is a radiotracer imaging technique, in which tracer compounds labelled with positron-emitting radionuclides are injected into the subject of the study. These tracer compounds can then be used to track biochemical and physiological processes *in vivo*. One of the prime reasons for the importance of PET in medical research and practice is the existence of positron-emitting isotopes of elements such as carbon, nitrogen, oxygen and fluorine which may be processed to create a range of tracer compounds which are similar to naturally occurring substances in the body. Some examples of these radio-tracers are shown in table 1.1, together with some typical clinical and research applications.

Isotope	Tracer compound	Physiological process or function	Typical application	Example reference
^{11}C	methionine	protein synthesis	oncology	Hellman *et al* (1994)
	flumazenil	benzodiazepine receptor antagonist	epilepsy	Burdette *et al* (1995)
	raclopride	D2 receptor agonist	movement disorders	Antonini *et al* (1997)
^{13}N	ammonia	blood perfusion	myocardial perfusion	Kuhle *et al* (1992)
^{15}O	carbon dioxide	blood perfusion	brain activation studies	Kanno *et al* (1984)
	water	blood perfusion	brain activation studies	Huang *et al* (1983)
^{18}F	Fluoro-deoxy-glucose	glucose metabolism	oncology, neurology, cardiology	Brock *et al*, 1997 (review)
	Fluoride ion	bone metabolism	oncology	Hawkins *et al*(1992)
	Fluoro-mizonidazole	hypoxia	oncology - response to radiotherapy	Koh *et al* (1995)

Table 1.1. Examples of radiotracers and their applications.

While PET was originally used primarily as a research tool, in recent years it has come to have an increasingly important clinical role. The largest area of clinical use of PET is in oncology. The most widely used tracer in oncology is ^{18}F-fluoro-deoxy-glucose (^{18}F-FDG). ^{18}F-FDG is relatively easy to synthesise with a high radiochemical yield (Hamacher *et al* 1986). It also follows a similar metabolic pathway to glucose *in vivo*, except that it is not metabolised to CO_2 and water, but remains trapped within tissue. This makes it well suited to use as a glucose uptake tracer. This is of interest in oncology because proliferating cancer

cells have a higher than average rate of glucose metabolism (Warburg 1931). ^{11}C-methionine is also used in oncology, where it acts as a marker for protein synthesis.

PET has applications in cardiology, where ^{13}N-NH_3 is used as a tracer for myocardial perfusion. When ^{13}N-NH_3 and ^{18}F-FDG scans of the same patient are interpreted together, PET can be used to distinguish between viable and non-viable tissue in poorly perfused areas of the heart (Marshall *et al* 1982). Such information can be extremely valuable in identifying candidates for coronary by-pass surgery.

In neurology, PET has been used in a range of conditions, and in particular in severe focal epilepsy, where it may be used to compliment Magnetic Resonance Imaging.

Another reason for the importance of PET lies in the fact that, unlike earlier radiotracer techniques it offers the possibility of quantitative measurements of biochemical and physiological processes *in vivo*. This is important in both research and in clinical applications. For example, it has been shown that semi-quantitative measurements of FDG uptake in tumours can be useful in the grading of disease (Strauss and Conti 1991). By modelling the kinetics of tracers *in vivo* it is also possible to obtain quantitative values of physiological parameters such as myocardial blood-flow in ml/min/g or FDG uptake in mmol/min/g providing the acquired data is an accurate measure of tracer concentration. Absolute values of myocardial blood flow can by useful in, for example, the identification of triple-vessel coronary artery disease and absolute values of FDG uptake can be useful in studies of cerebral metabolism.

1.2. The physical principles of PET.

1.2.1. Introduction

After injection of a tracer compound labelled with a positron emitting radionuclide the subject of a PET study is placed with in the field of view (FOV) of a number of detectors capable of registering incident gamma rays. The radionuclide in the radiotracer decays and the resulting positrons subsequently annihilate on contact with electrons after travelling a short distance (~ 1 mm) within the body. Each annihilation produces two 511 keV photons travelling in opposite directions and these photons may be detected by the detectors surrounding the subject. The detector electronics are linked so that two detection events unambiguously occurring within a certain time window may be called coincident and thus be determined to have come from the same annihilation. These "coincidence events" can be stored in arrays corresponding to projections through the patient and reconstructed using standard tomographic techniques. The resulting images show the tracer distribution throughout the body of the subject. This section describes the physical principles underlying PET and will discuss some of the intrinsic advantages that PET exhibits over Single Photon Emission Computed Tomography (SPECT) techniques.

1.2.2. Positron emission and annihilation

Proton-rich isotopes may decay via positron emission, in which a proton in the nucleus decays to a neutron, a positron and a neutrino. The daughter isotope has an atomic number one less than the parent. Examples of isotopes which undergo decay via positron emission are shown in table 1.2.

Isotope	half-life (min)	Maximum positron energy (MeV)	Positron range in water (FWHM in mm)	Production method
^{11}C	20.3	0.96	1.1	cyclotron
^{13}N	9.97	1.19	1.4	cyclotron
^{15}O	2.03	1.70	1.5	cyclotron
^{18}F	109.8	0.64	1.0	cyclotron
^{68}Ga	67.8	1.89	1.7	generator
^{82}Rb	1.26	3.15	1.7	generator

Table 1.2. Properties of commonly used positron emittmg radio-isotopes (Raylman *et al* 1992, Bailey 1996)

As positrons travel through human tissue they give up their kinetic energy principally by Coulomb interactions with electrons. As the rest mass of the positron is the same as that of the electron, the positrons may undergo large deviations in direction with each Coulomb interaction, and they follow a tortuous path through the tissue as they give up their kinetic energy (figure 1.1).

When the positrons reach thermal energies, they start to interact with electrons either by annihilation, which produces two 511 keV photons which are anti-parallel in the positron's frame, or by the formation of a hydrogen-like orbiting couple called positronium. In its ground-state, positronium has two forms - ortho-positronium, where the spins of the electron and positron are parallel, and para-positronium, where the spins are anti-parallel. Para-positronium again decays by self-annihilation, generating two anti-parallel 511 keV photons. Ortho-positronium self-annihilates by the emission of three photons (Evans, 1955). Both forms are susceptible to the "pick-off" process, where the positron annihilates with another electron. Free annihilation and the pick-off process are responsible for over 80% of the decay events. Variations in the momentum of the interacting particles involved in free annihilation and pick-off result in an angular uncertainty in the direction of the 511 keV photons of around 4 mrad in the observer's frame (Rickey *et al* 1992). In a PET camera of diameter 1m and active transaxial FOV of 0.6m this results in a positional inaccuracy of 2-3 mm.

The finite positron range and the non-collinearity of the annihilation photons give rise to an inherent positional inaccuracy not present in conventional single photon emission techniques. However, other characteristics of PET which are discussed below more than offset this disadvantage.

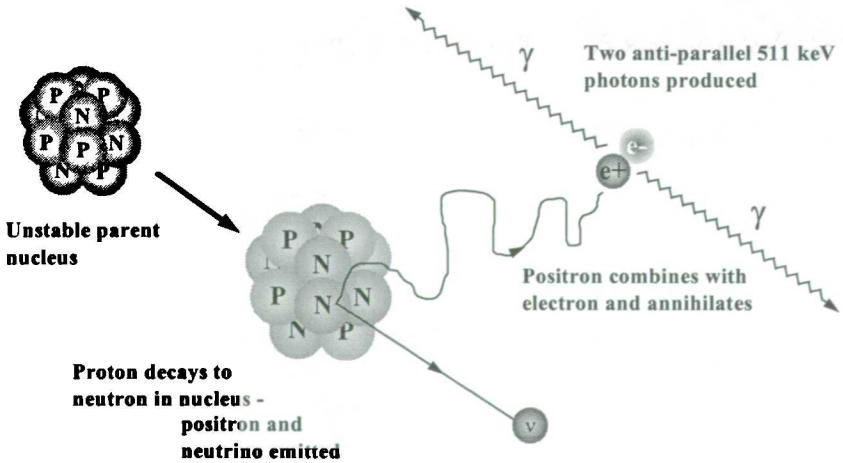

Figure 1.1. Positron emission and annihilation.

1.2.3. Coincidence detection and electronic collimation.

In a PET camera, each detector generates a timed pulse when it registers an incident photon. These pulses are then combined in coincidence circuitry, and if the pulses fall within a short time-window, they are deemed to be coincident. A conceptualised diagram of this process is shown in figure 1.2.

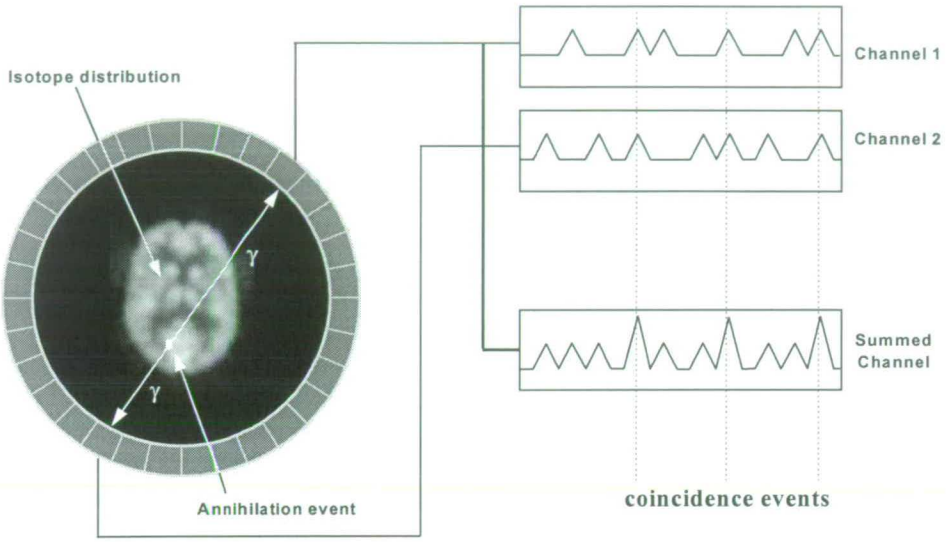

Figure 1.2. Coincidence detection in a PET camera.

A coincidence event is assigned to a line of response (LOR) joining the two relevant detectors. In this way, positional information is gained from the detected radiation without the need for a physical collimator. This is known as *electronic collimation.* Electronic collimation has two major advantages over physical collimation. These are improved sensitivity and improved uniformity of the point source response function (psrf).

When a physical collimator is used, directional information is gained by preventing photons which are not normal or nearly normal to the collimator face from falling on the detector. In electronic collimation, these photons may be detected and used as signal. This results in a significant gain in sensitivity (typically a factor of 10 for 2D mode PET compared with SPECT). This increase in sensitivity means that typical realisable image resolution in PET is around 5-10 mm, whereas in SPECT it is around 15-20 mm.

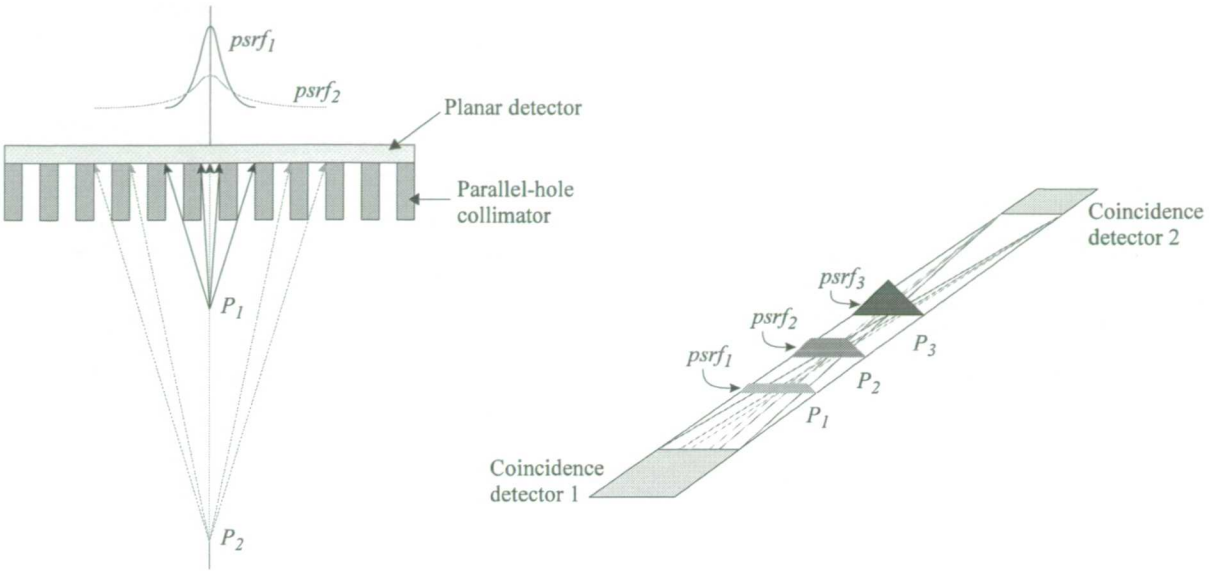

Figure 1.3. Variation of point source response function (psrf) with position *P* in SPECT and in PET.
In SPECT (a) the FWHM of the psrf increases with increasing distance from the collimator. In PET (b), the FWHM of the psrf varies from one detector width at the edge of the FOV to approximately 1/2 detector width at the centre of the FOV.

In SPECT, the full-width at half-maximum (FWHM) of the psrf increases with increasing distance of the source from the collimator (figure 1.3 (a)). This results in variable resolution in the reconstructed images. In PET, a coincidence event may be detected if the direction of the annihilation photons is constrained to lie along a line-of-sight joining both detector faces. If the annihilation photons are strictly anti-parallel, this results in a psrf which varies in a similar way to that shown in figure 1.3(b). This constraint is relaxed somewhat because of the small uncertainty in the direction of the annihilation photons, and in practice the psrf changes only very slightly in the central third of the FOV (Phelps *et al* 1986). As a result, the resolution of reconstructed PET images is more uniform than is the case for SPECT images.

1.2.4. Photon interactions in human tissue and correction for gamma-ray attenuation.

The most important interactions which photons resulting from the positron annihilation undergo in human tissue are Compton scatter and photoelectric absorption.

In Compton scatter a photon interacts with an electron in the absorber material. In the process the kinetic energy of the electron is increased, and the direction of the photon is changed. The energy of the photon after interaction is given by (Evans 1955):

$$E' = \frac{E}{1 + \left(E/m\,c^2\right)\left(1 - \cos\theta\right)} \tag{1.1}$$

where E is the energy of the incident photon, E' is the energy of the scattered photon, m_0c^2 is the rest mass of the electron and θ is the scattering angle. Equation 1.1 implies that quite large deflections can occur with quite small energy loss - for example, for 511 keV photons, a Compton scattering event in which 10% of the photon energy is lost will result in a deflection of just over 25 degrees.

In photoelectric absorption a photon is absorbed by an atom and in the process an electron is ejected from one of its bound shells. The probability of photoelectric absorption increases rapidly with increasing atomic number of the absorber atom, and decreases rapidly with increasing photon energy (Evans, 1955). In water, the probability of photoelectric absorption decreases with roughly the 3rd power of the photon energy and is negligible at 511 keV (Johns and Cunningham 1983).

The total probability that a photon of a particular energy will undergo some kind of interaction with matter in when travelling unit distance through a particular substance is called the linear attenuation coefficient (μ) of that substance. If I_0 is the initial intensity of a parallel beam of monoenergetic photons, then the intensity $I(x)$ at a distance x through some attenuating object will be given by:

$$I(x) = I_0 e^{-\int_0^x \mu(x)dx} \tag{1.2}$$

provided scattered photons are removed from the beam. This relation has important consequences for PET. Consider a small volume v in an attenuating object, located at a distance x' along an LOR joining two detectors in the FOV of a PET camera (figure 1.4). Let the volume v contain some positron emitting substance, so that there is a flux of 511 keV photons along the line of response joining detector 1 and detector 2. If the linear attenuation coefficient at a point x along the LOR is $\mu(x)$, and a is the distance between detectors 1 and 2, we can state the following:

Probability of a photon reaching detector 1 from v is $P_1 = e^{-\int_0^{} \mu(x)dx}$

Probability of a photon reaching detector 2 from v is $P_2 = e^{-\int_{x'}^{a} \mu(x)dx}$

The probabilities are independent of each other, and both photons must reach the detectors for a coincidence to be recorded. The probability of a coincidence P_c, is the product of P_1 and P_2 :

$$P_C = P_1 P_2 = e^{-\int_{0}^{a} \mu(x)dx} \tag{1.3}$$

So the quantity (1 -P_c), which is the attenuation factor of the photons travelling along the LOR from *v*, is the same for any position along the line of response. By measuring the coincidence signal as a positron-emitting source is moved around the object within the FOV, it is possible to obtain attenuation factors for each LOR. In principle, this enables quantitative measurements of isotope distribution to be made. In SPECT techniques, where the attenuation factors increase with increasing distance from the detectors, there is no simple way to correct for photon attenuation.

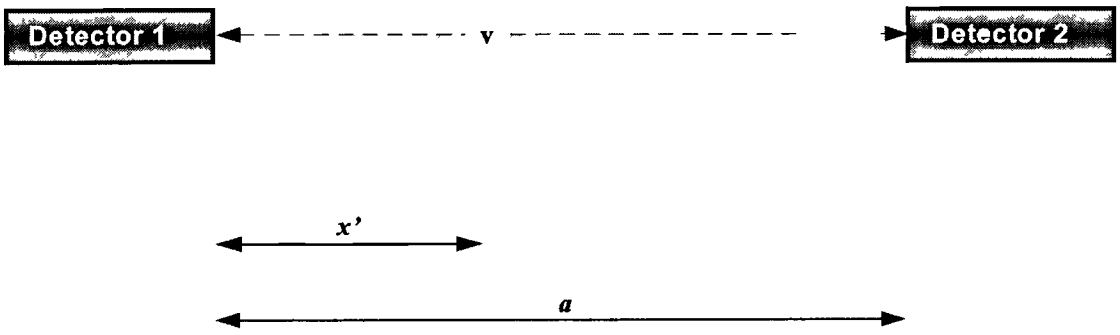

Figure 1.4. Coincidence detection in an attenuating object

For 511 keV photons, in human tissue the half-value layer (the distance a beam of photons must travel before 50% have interacted) is around 7 cm. Attenuation factors in human studies can rise to around 50 for LORs crossing large dense areas, for example those crossing the shoulders perpendicularly to the sagittal plane.

1.2.5. Types of coincidence events.

Coincidence events in PET fall into 4 categories: true, scattered, random and multiple. The first three of these are illustrated in figure 1.5.

True coincidences occur when both photons from an annihilation event are detected by detectors in coincidence, neither photon undergoes any form of interaction prior to detection, and no other event is detected within the coincidence time-window.

A scattered coincidence is one in which at least one of the detected photons has undergone at least one Compton scattering event prior to detection. Since the direction of the photon is changed during the Compton scattering process, it is highly likely that the resulting coincidence event will be assigned to the wrong LOR. Scattered coincidences add a background to the true coincidence distribution which changes slowly with position, decreasing contrast and causing the isotope concentrations to be overestimated. They also add statistical noise to the signal. The number of scattered events detected depends on the volume and attenuation characteristics of the object being imaged, and on the geometry of the camera.

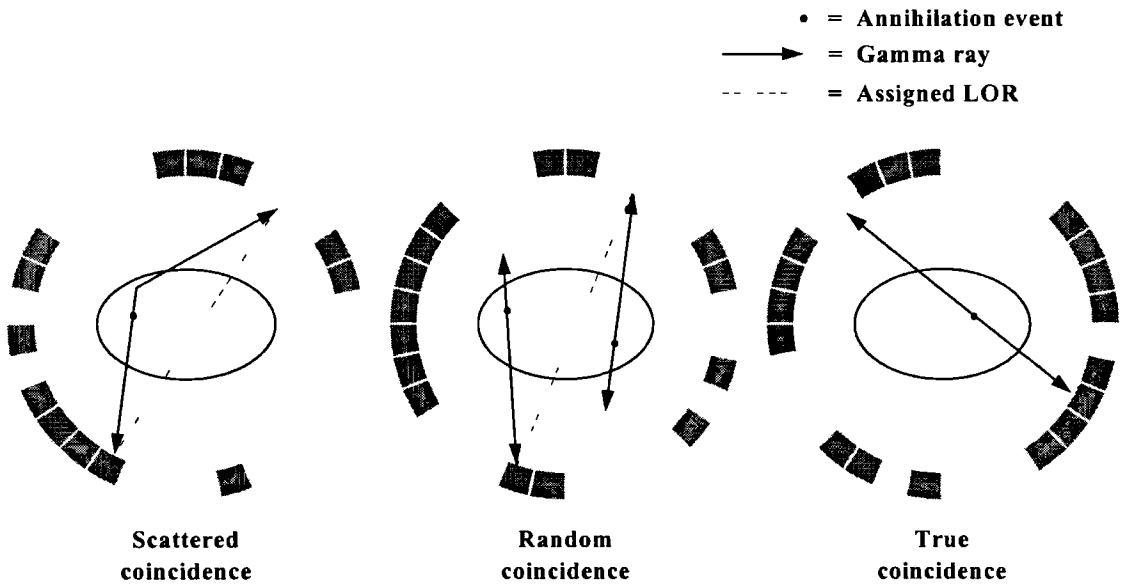

Figure 1.5. Types of coincidences in PET.

Random coincidences occur when two photons not arising from the same annihilation event are incident on the detectors within the coincidence time window of the system. The number of random coincidences in a given LOR is closely linked to the rate of single events measured by the detectors joined by that LOR and the rate of random coincidences increase

roughly with the square of the activity in the FOV. As with scattered events, the number of random coincidences detected also depends on the volume and attenuation characteristics of the object being imaged, and on the geometry of the camera. The distribution of random coincidences is fairly uniform across the FOV, and will cause isotope concentrations to be overestimated if not corrected for. Random coincidences also add statistical noise to the data.

A simple expression relating the number of random coincidences assigned to an LOR to the number of single events incident upon the relevant detectors can be derived as follows:

Define τ, the coincidence resolving time of the system, such that any events detected with a time difference of less than 2τ are considered to be coincident (see section 1.5.4). Let r_1 be the single event rate (singles rate) on detector channel 1. Then in one second, the total time-window during which coincidences will be recorded is $2\tau\ r_1$. If the singles rate on detector channel 2 is r_2, we can say that the number of random coincidences R_{12} assigned to the LOR joining detectors 1 and 2 is given by

$$R_{12} = 2\tau\ r_1\ r_2 \tag{1.4}$$

This relation is true provided that the singles rate is much larger than the rate of coincidence events, and that the singles rates are small compared to the reciprocal of the coincidence resolving time τ, so that dead-time effects can be ignored.

Multiple coincidences occur when more than two photons are detected in different detectors within the coincidence resolving time. In this situation, it is not possible to determine the LOR to which the event should be assigned, and the event is rejected. Multiple coincidences can also cause event mis-positioning (see section 1.5.6).

1.3. 2D mode and 3D mode

1.3.1. Principles of operation

Most cameras employing block-detector technology (section 1.5) may be operated either in "2D" mode or "3D" mode. In 2D mode thin septa of lead or tungsten separate each crystal ring and coincidences are only recorded between detectors within the same ring or lying in closely neighbouring rings. Coincidences between detectors in closely neighbouring rings are summed (figure 1.6) or rebinned to produce a dataset consisting of $2P+1$ co-planar sets of LORs normal to the axis of the camera, where P is the number of detector rings. Such a dataset may be reconstructed into images using standard tomographic techniques (section 1.4).

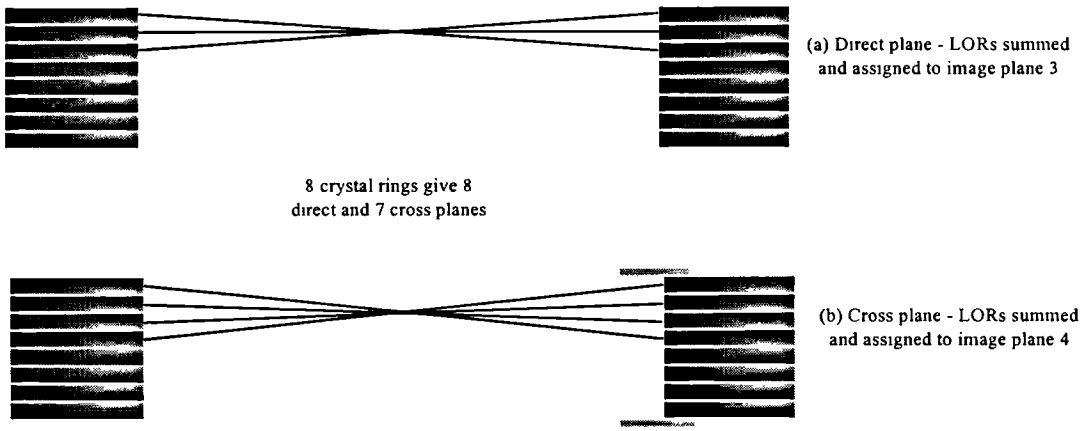

Figure 1.6. Axial cut-away view of a multi-ring PET camera (not to scale) operating in 2D mode, showing direct and cross-plane rebinning.
In direct-plane rebinning (top), data in corresponding LORs with ring difference 0 and +/-2 are summed, whereas in cross-plane rebinning (bottom) corresponding LORs with ring difference +/-1 and +/-3 are summed. More or less LORs may be summed depending on the camera geometry and the imaging requirements.

In 3D mode, the septa are removed, and coincidences are recorded between detectors lying in any ring combination (figure 1.7). The rebinning technique described above may be directly applied to this 3D dataset (Daube-Witherspoon and Muehllehner 1987), but this results in significant image distortion which increases towards the edge of the FOV. Usually more computationally intensive fully-3D image reconstruction techniques are employed. The computational burden increases with the number of crystal rings used, and for cameras with a large number of rings some degree of rebinning between closely neighbouring LORs may be applied to reduce the dataset to more manageable proportions (e.g. Brix *et al* 1997) - this process is known as "mashing".

1.3.2. Sensitivity to true coincidence events.

Removal of the septa allows the use of a much larger number of measured LORs (see figure 1.7). This results in a significant increase in sensitivity to true coincidence events (Cherry *et al*, 1991). The increase in the number of LORs depends on the number of crystal rings and the degree of rebinning used in 2D mode. Rebinning in 2D mode results in a variation in sensitivity along the axial FOV. In 3D mode there is a much stronger variation in sensitivity (see figure 1.8), which peaks in the centre of the axial FOV.

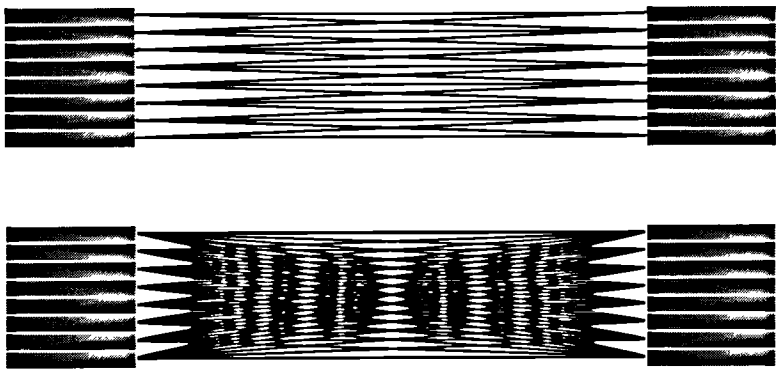

Figure 1.7. Axial cut-away view of a PET camera in 2D and 3D mode showing how the number of possible LORs can increase when the septa are removed.
For a 16-ring camera where the maximum permissible ring difference in 2D mode is +/-3, just over 2.5 times as many LORs are used in 3D mode than in 2D mode.

The septa themselves subtend an appreciable solid angle in the camera FOV, and as a result they have a significant shadowing effect on the detectors. The magnitude of the septa shadowing effect can be as high as 50%, and this is another reason why 3D mode is more sensitive than 2D mode. The increase in sensitivity to true coincidences is the prime motivation for the removal of septa, although the increased cost of manufacturing cameras with septa is also a factor.

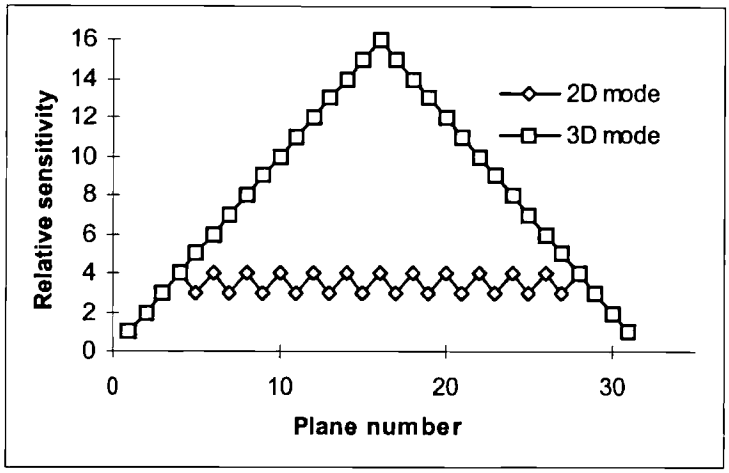

Figure 1.8. Predicted sensitivity from the number of LORs used in 2D and 3D mode. The sensitivity is plotted as a function of image plane number for a 16-ring camera where the maximum ring difference in 2D mode is +/-3. At the edge of the axial FOV 2D mode and 3D mode have the same predicted sensitivity but in the centre of the FOV the sensitivity in 3D mode is significantly greater.

1.3.3. Sensitivity to scattered events.

In the presence of septa, only those photons scattered in the plane of each detector ring have a reasonable probability of being detected. When the septa are removed, it is possible to detect photons with a much greater range of scattering angles (figure 1.9). As a result, the sensitivity to scattered events in 3D mode increases significantly (Cherry *et al*, 1991).

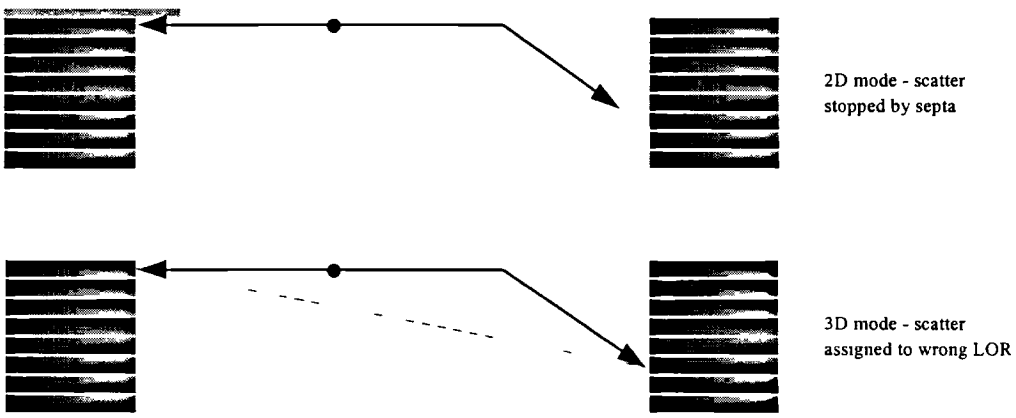

Figure 1.9. Effect of septa removal on sensitivity to scattered coincidences

1.3.4. Sensitivity to random events.

When the septa are removed, the FOV for single events is increased (figure 1.10). This can result in a significant increase in the number of random coincidences detected, particularly when imaging near organs which may contain significant amounts of activity, such as the brain, heart or bladder.

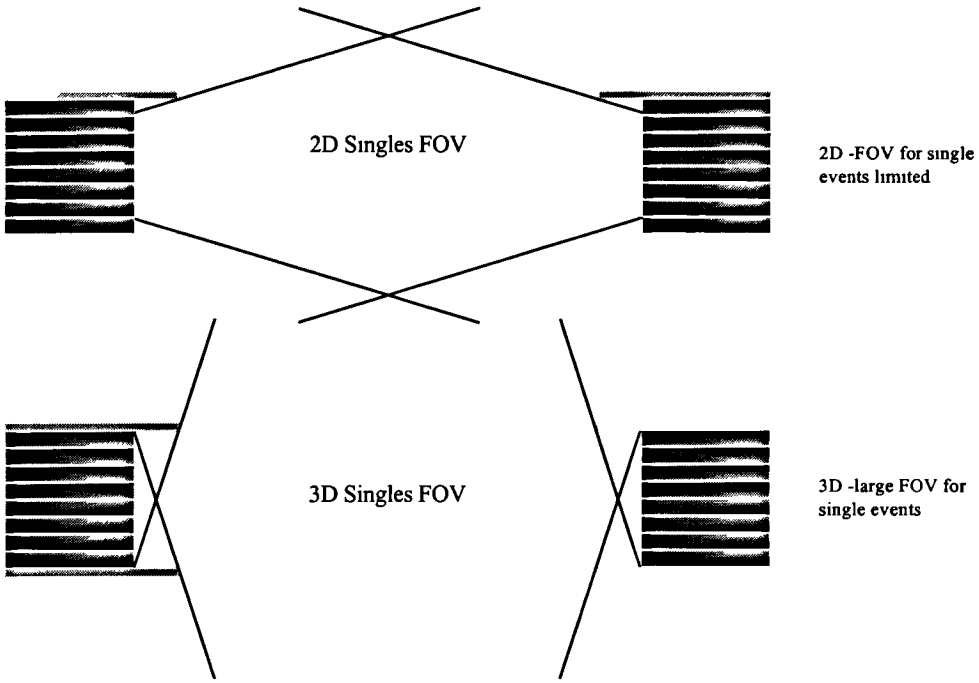

Figure 1.10. Effect of septa removal on sensitivity to single events

1.3.5. Effect of camera geometry.

The geometry of the camera also has a significant effect on performance, particularly in 3D mode, where increasing the axial FOV or the camera acceptance angle not only increases the sensitivity to true coincidences, but also increases the sensitivity to randoms and scatter. While the sensitivity to randoms can be reduced by increasing the radial extent of the end-shields (Spinks *et al* 1998), it remains a serious problem in whole-body imaging and for cameras using large-area planar detectors (which tend to have open geometries and can only operate in 3D mode).

1.4. Image reconstruction

1.4.1. Introduction

After all corrections (e.g. for scatter, randoms and the effects of attenuation) have been applied to data acquired in a PET camera, the number of counts assigned to an LOR joining a pair of crystals is proportional to a line integral of the activity along that LOR. Parallel sets of such line integrals are known as projections. Reconstruction of images from projections is a problem to which much attention has been paid over the last 30 years, and many analytical and iterative reconstruction schema exist. For 2D reconstruction, the most commonly used algorithm is the analytical method called Filtered Back-projection (FBP). FBP is straight-forward to implement but does have the property of amplifying noise in the signal (see section 1.4.3 below). Recently, considerable interest has been shown in iterative reconstruction schema, such as the Ordered Subsets - Expectation Maximisation (OSEM) algorithm (Hudson and Larkin 1994), which possess different noise properties to FBP. For 3D reconstruction, the Reprojection and Filtered Back-projection (3D-RP) method of Kinahan and Rogers (1990) has been the most popular, in part because of the significant computational burden of newer 3D iterative reconstruction methods. 3D-RP itself is computationally expensive, and this has led to the development of approximate 3D reconstruction algorithms. Of these, Fourier Rebinning (Defrise *et al* 1997), which reduces the 3D problem to a series of 2D problems without significantly distorting the image and results in a significant reduction in the computational burden, is stimulating particular interest.

In this section FBP in 2 and 3 dimensions will be briefly summarised and the basic elements of 3D-RP will be described.

1.4.2. Notation and mathematical theorems used

In this work the following notation will be adopted:

	Spatial variables			Fourier variables		
	vector	Cartesian components	polar components	vector	Cartesian components	polar components
1D	-	x	-	-	k	-
2D	$\underline{\mathbf{x}}$	$x\,y$	r,θ	$\underline{\mathbf{k}}$	$k_x k$	$r_k \theta_k$
3D	$\underline{\mathbf{x}}$	$x\,y,z$	$r\,\theta\,\varphi$	$\mathbf{k}$	k_x, k, k	$r_k\ \theta_k\ \varphi_k$

Table 1.3. Notation for spatial and Fourier quantities.

$\Im(\ )$	Fourier transform	$\Im^{-1}(\ )$	inverse Fourier transform
$b(\ )$	Back-projection	$*$	Convolution operator

The spatial co-ordinates for a full-ring PET camera are shown in figure 1.11.

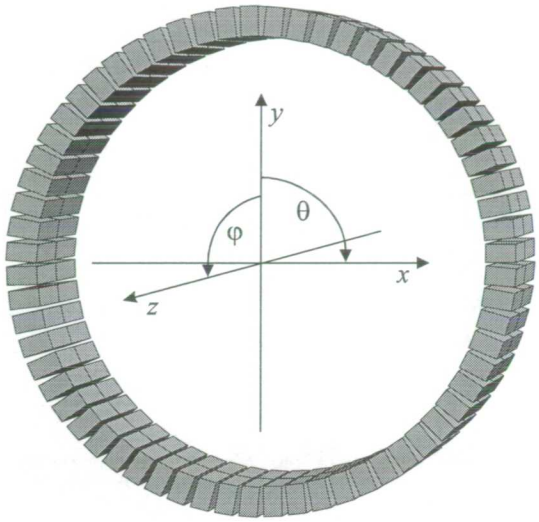

Figure 1.11. 3D co-ordinate system for a full-ring PET camera

Several mathematical theorems will be used without proof. These include the following:

Fourier's theorem:

$$f(x) = \Im^{-1}\left(\Im(f(x))\right) \tag{1.5}$$

Fourier addition theorem:

$$\Im\left(f(x) + g(x)\right) = F(k) + G(k) \tag{1.6}$$

where $\Im(f(x)) = F(k)$ and $\Im(g(x)) = G(k)$

Convolution theorem:

$$\Im\left(f(x) * g(x)\right) = F(k) \cdot G(k) \tag{1.7a}$$

and

$$\Im\left(f(x) \cdot g(x)\right) = F(k) * G(k) \tag{1.7b}$$

Shannon's sampling theorem:

If a function is sampled with a sampling distance d then it may be fully recovered from its samples (apart from harmonic components which are zero-valued at the sample points) if its Fourier transform has no non-zero components at frequencies beyond a particular value k_c where $k_c = (1/2d)$.

The critical frequency $k_c = (1/2d)$ is known as the Nyquist frequency. A more detailed treatment of this material may be found in, for example, Bracewell (1986).

1.4.3. Analytic image formation in 2D PET

In 2D PET, data from LORs are arranged into sets of parallel projections. For a point source distribution, this gives rise to a series of intensity profiles as shown in figure 1.12.

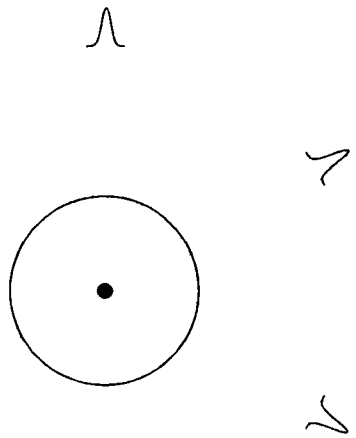

Figure 1.12. Projections generated from a single central point source (3 projections shown).

An estimate of the original source distribution may be obtained by a process known as back-projection. In this process, the magnitude of each value in a projection is added to every point in image space corresponding to the relevant line of integration in object space. Back-projections for a single point-source are shown in figure 1.13. When a small number of projections are used, the resultant image contains star-shaped artefacts. In the limit of an infinite number of projection angles, this process is the equivalent of convolving the original source distribution with the function $f(r,\theta) = |r|^{-1}$.

An extended source distribution can be considered as being made up of a series of points of varying intensity, each of which, after back-projection, is convolved with $|r|^{-1}$. Since convolution is distributive over addition, the relationship between the density function and the back projection $b(r,\theta)$ may be written:

$$b(r,\theta) = \rho(r,\theta) * r|^{-1} \qquad (1.8)$$

where $\rho(r,\theta)$ is the extended source distribution. Application of the convolution theorem gives:

$$\Im(b(r,\theta)) = \Im(\rho(r,\theta)) \cdot \Im\left(|r|^{-1}\right) \tag{1.9}$$

Now the Fourier transform of $|r|^{-1}$ is just $|r_k|^{-1}$, so that

$$\rho(r,\theta) = \Im^{-1}\left(\Im(b(r,\theta)) \cdot |r_k|\right) \tag{1.10}$$

and we have recovered the extended source distribution function. In practice the source distribution is sampled with a finite sample-width, so to enable application of the Sampling theorem it is necessary cut off the Fourier transform of the back-projection at the Nyquist frequency. This is achieved by multiplying it with a gate function of the appropriate width. In real space this is equivalent to convolution with the sinc function. This can result in "undershoot" artefacts in the image (where image values are underestimated or even negative), particularly in regions close to sharp edges in the source distribution.

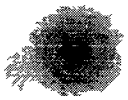

(a) 3 projections (b) 6 projections (c) Many projections

Figure 1.13. Back-projections of a point source.
With finite numbers of back-projection angles, "star" artefacts are seen.

Filtered Back-projection is a mathematically equivalent process to that described above. Fourier transforms of the projections are first calculated and multiplied by the cut-off 1D version of $|r_k|$ (the ramp filter). The inverse Fourier transform of the result is then calculated and back-projected to create the image.

Use of the ramp filter amplifies high-frequency components in the back-projection. Unfortunately statistical noise in the data manifests in Fourier space as high-frequency components. So the process of FBP amplifies noise in the image. In order to reduce this effect, a range of modifications to the ramp filter can be used. Perhaps the most commonly used of these is the Hanning filter (figure 1.14). Such filters are equivalent to some form of smoothing in image space.

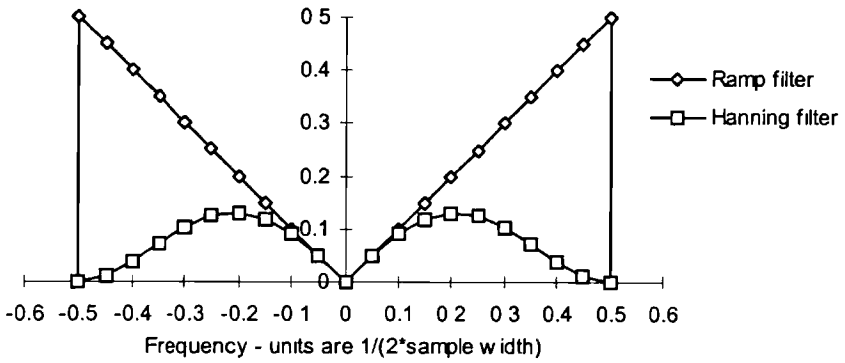

Figure 1.14. The Ramp and Hanning filters

1.4.4. Filtered Back-Projection in 3D and 3D-RP

In three dimensions, the data from the LORs may be arranged into 2D sets of parallel projections (figure 1.15). FBP generalises to 3D directly if the projections can be obtained over all φ as well as θ. Unfortunately in real cameras projections cannot easily be obtained over the full range of φ, and a different filter must be found for the de-convolution step (Colsher 1980).

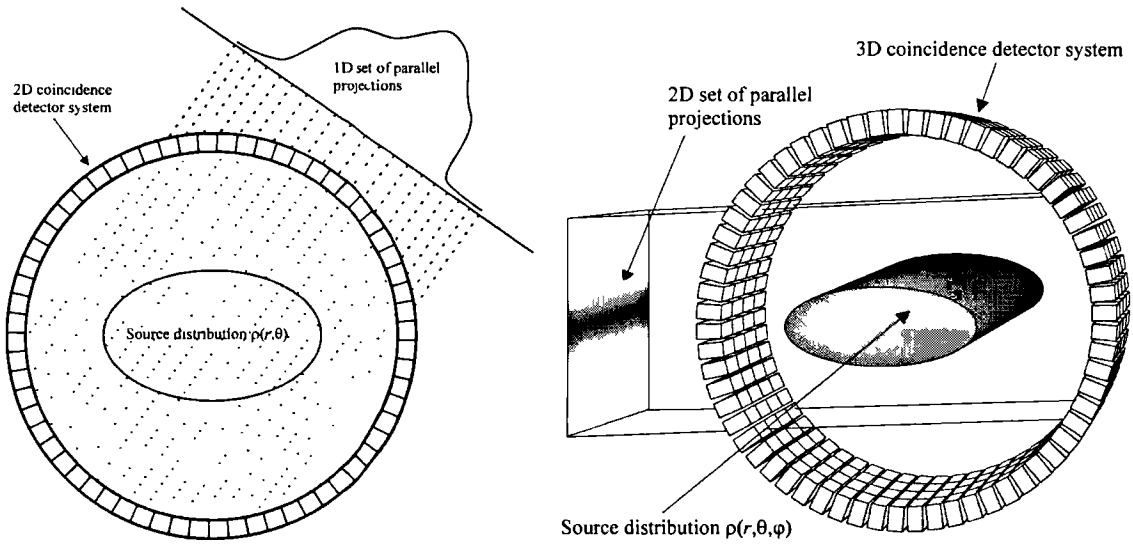

Figure 1.15. Parallel projections in 2D (left) and 3D (right).
Note that the LORs become closer together towards the edge of the FOV. To correct for this, the data must be re-sampled (*arc corrected*) prior to reconstruction.

Another problem is the fact that the limited axial extent of the camera causes some of the 2D projections to be truncated, and the degree of truncation depends on position (figure 1.16). As a result there is no single filter which is appropriate for every projection set. The 3D-RP

algorithm circumvents this problem by performing a 2D reconstruction on a subset of the 3D projections first. The resulting image volume is then reprojected in order to obtain estimates of the truncated projections and a 3D FBP is then performed on the combined real and synthesised data.

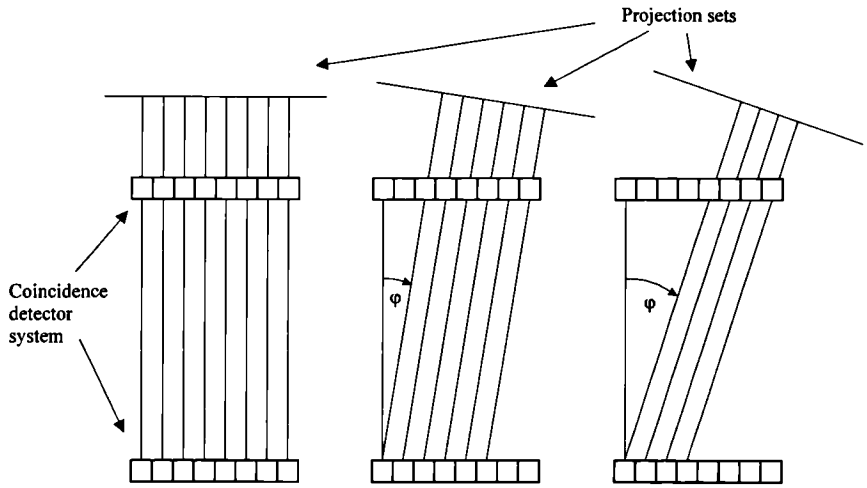

Figure 1.16. Axial cut-away diagram of a PET camera operating in 3D mode, showing the extent of the projection sets as a function of angle φ.
As φ increases, the measurable extent of the projection set decreases, requiring the reconstruction filter to change with position. To avoid this, an initial 2D reconstruction is performed on the φ = 0 projection set, and estimates of the missing parts of the truncated projections obtained by reprojecting through the image volume.

1.5. Detection systems in PET

1.5.1. Introduction

Detection systems are a key component of any imaging system, and an understanding of their properties is important for establishing appropriate operating criteria or designing schemes for obtaining quantitative information. In this section scintillation detection systems, which are used in the majority of PET tomographs, are discussed.

1.5.2. Scintillators and scintillation detectors

The scintillation process involves the conversion of high-energy photons into visible light via interaction with a scintillating material, and consists of the following steps:

1) a photon incident on the scintillator creates an energetic electron, either by Compton scatter or by photoelectric absorption.
2) as the electron passes through the scintillator, it loses energy and excites other electrons in the process.
3) these excited electrons decay back to their ground state, giving off light as they do so.

In a scintillation detector, the scintillator is optically coupled to a photomultiplier tube (PMT) which then generates an electrical signal in response to light incident upon its face. There are several variations on this theme which are used in PET - for example, a 2D array of crystals may be coupled to 4 PMTs (the block-detector, Casey and Nutt, 1986), an array of PMTs may be coupled to a single planar crystal (the Anger camera, Anger, 1958), or an array of crystals may be coupled to a multi-channel PMT (Cherry *et al* 1997).

Compton scatter and photo-electric absorption generate electrons of differing energy distributions. In photo-electric absorption, all the photon energy is transferred to the electron, and the energy distribution of the photo-electrons is sharply peaked close to the energy of the incident photon. In Compton scatter, the recoil electrons have a range of energies, depending on the scattering angle. From equation 1.1 we can say that the energy of the recoil electron will be

$$E_\beta = E - E' = E\left(\frac{\left(E/m_e c^2\right)(1-\cos\theta)}{1+\left(E/m_e c^2\right)(1-\cos\theta)}\right) \tag{1.11}$$

where θ is the photon scattering angle, E_β is the energy of the electron, E is the energy of the incident photon and E' is the energy of the scattered photon. E_β reaches a maximum when θ = π. For 511 keV photons, this value is 261.5 keV. A typical energy distribution for electrons involved in interactions with 511 keV photons is shown in figure 1.17. When real scintillation detectors are exposed to mono-energetic photons, the energy measured is not that of the electron generated by the initial interaction, but rather the total energy deposited by the photon in the detector. This distinction is important because photons initially interacting by Compton scatter may subsequently be involved in further interactions within the detector. In a sufficiently large detector, most Compton-scattered photons will eventually deposit all their energy, and most events will register in the photon energy peak. Under these circumstances, this feature of the energy distribution is better described by the term "full-energy peak" rather than "photo-peak".

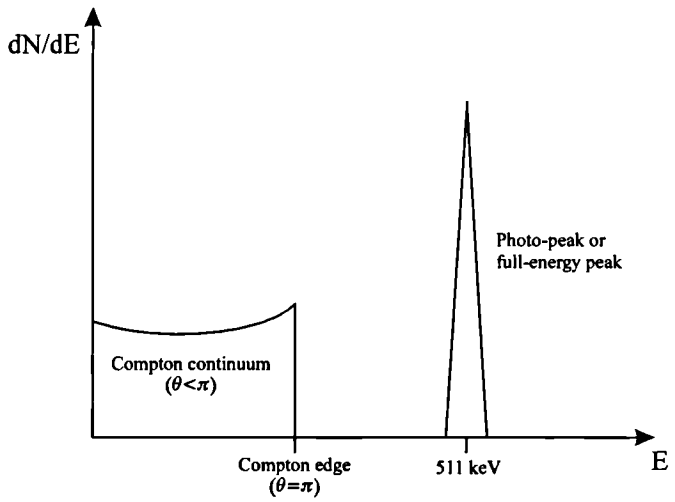

Figure 1.17. Features of a typical energy distribution for electrons involved in interactions with 511 keV photons.

In small detectors, photons may escape after depositing only part of their energy in the crystal, and the measured energy distribution is closer to that shown in figure 1.18. In practice, the energy distribution is also blurred by the finite energy resolution of the detector system, and by the fact that the incident radiation is not mono-energetic, as a proportion of the photons will have undergone Compton scatter prior to detection. There will also be some events with energy greater than the full-energy peak, where photon interactions with the

detector occur sufficiently close together in time that they cannot be resolved as separate events. The energy resolution of the system is defined as the ratio of the full-width at half-maximum (FWHM) of the full energy peak and the energy value at the full energy peak maximum.

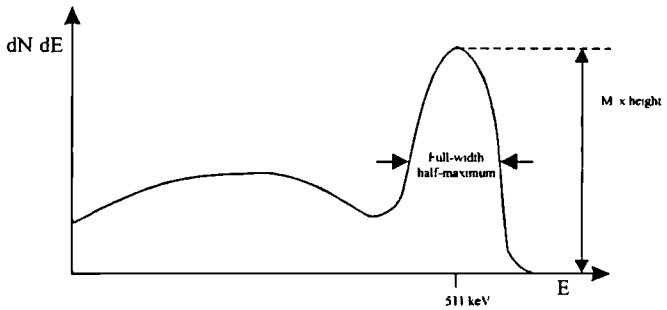

Figure 1.18. Features of a typical energy distribution measured by a scintillation detector system exposed to 511 keV photons.

If a large proportion of the incident photons register in the full-energy peak and the energy resolution of the detector system is good, then it is possible to discriminate against events arising from photons scattered within the object by rejecting those with a low measured energy. As discussed above, the proportion of events in the full-energy peak increases with increasing detector size. However, large detectors reduce the spatial resolution of the system. The number of events in the full-energy peak can also be increased by increasing the proportion of photons which interact by photo-electric absorption. This may be achieved by choosing scintillators with a large value of effective atomic number (effective Z). The linear attenuation coefficient also increases with increasing effective Z, so choosing scintillators with high effective Z also increases sensitivity. The energy resolution of the system may be improved by improving the statistical quality of the signal from the PMT - this may be achieved by increasing the number of scintillation photons incident upon its face. In summary, the following qualities are desirable in a scintillator:

- the scintillator should have a large value of effective Z
- an incident gamma ray should generate a large number of scintillation photons
- the scintillator should have a low self-absorption factor for the scintillation light
- the scintillator should have an index of refraction close to that of glass, to improve the optical coupling between the scintillator and the PMT

PET detectors have to work at high count-rates, so it is important that the decay time of the scintillator should be short. Shorter decay times also allow faster timing signals for coincidence detection. An undesirable characteristic in a scintillator is the existence of secondary scintillation components with long decay times, as in high count-rate operation these can cause a build-up of back-ground light.

The final considerations are that the scintillator should ideally be robust and easy to manufacture.

The properties of some important scintillators are shown in table 1.4. Some of these, e.g. NaI and LSO, require doping with an activator substance in order to obtain optimum scintillation properties. NaI has been used extensively in SPECT and to a lesser extent in PET, although it is both hygroscopic and fragile. However the scintillator of choice for PET cameras using block-detectors has been Bismuth germanate (BGO), which has a high effective Z, is not hygroscopic and does not have long-lived secondary scintillation components. Cerium-doped lutetium oxy-orthosilicate or LSO (Daghighian, *et al* 1993) is a scintillator which shows considerable promise for the future, and has already been used with some success (Cherry *et al* 1997). However, it is currently significantly more difficult to manufacture than BGO.

	NaI	BaF_2	BGO	LSO	GSO
Effective atomic no. (Z)	51	54	74	66	59
Lin. atten. coef. (cm^{-1})	0.34	0.44	0.92	0.87	0.62
Index of refraction	1.85		2.15	1.82	1.85
Light yield [%NaI:Tl]	100	5	15	75	41
Peak Wavelength (nm)	410	220	480	420	430
Decay const. (nS)	230	0.8	300	40	56
Fragile	Yes	Slight	No	No	No
Hygroscopic	Yes	No	No	No	No

Table 1.4. Examples of scintillators and their properties.
Compiled from Dahlbom *et al* (1997), Ficke *et al* (1996), Knoll (1989), Phelps *et al* (1986) and Bailey (1996).

1.5.3. Pulse processing.

When a scintillation detector detects a photon, the electrical pulse generated by the PMT or PMT array is used to generate a timing signal. This is done by passing the pulse through a constant fraction discriminator (CFD), which generates a digital pulse when the signal reaches a constant fraction of the peak pulse height. This pulse is then used in the coincidence circuitry.

The pulses from the PMTs are also passed through a differential discriminator to sort them according to pulse height. Usually there is a lower energy-level discriminator (LLD), and an upper energy-level discriminator (ULD) which may be used to reject pulses below or above particular values. The LLD can be used to discriminate against scatter, as scattered annihilation photons have lower energy than those which are unscattered. Not all scatter can be removed this way, as many scattered photons have an energy quite close to 511 keV and the energy resolution of typical detector systems is insufficient to distinguish them from unscattered photons. Also, as discussed in section 1.5.2 a significant proportion of unscattered photons interact with the scintillator by the Compton process, and many of these will not deposit all their energy in the crystal. Therefore a high value for the LLD will cause the rejection of a significant number of true events and there is a trade-off between scatter fraction and sensitivity to true coincidences. Optimisation of LLD value is discussed in detail in chapter 5. The ULD may be used to reject some events where more than one photon is incident on the block-detector at the same time. LLDs and ULDs have also been used to divide the acquired data into different energy-windows for analysis (e.g. Shao *et al* 1994, Grootoonk *et al* 1996).

1.5.4. Coincidence processing.

Once timing signals have been generated from each pulse, they are passed to coincidence circuitry for processing. Figure 1.19 shows a schematic diagram of a coincidence circuit. There will usually be some time difference between two timing pulses arising from a coincidence event due to the finite time resolution of the detector and CFD system. In order to deal with this, the timing pulses are passed to a gate generator, which creates an electronic pulse of duration τ. τ is known as the *coincidence resolving time* of the system. These fixed-width pulses are then passed to a logic unit, which generates a pulse if there is a signal on both of its inputs at the same time. So if a timing pulse is generated on one channel at time t, a coincidence will be recorded if there is a timing pulse on the other channel between $t - \tau$ and $t + \tau$. The value of τ must be carefully chosen. If it is too small compared to the time resolution of the detection system, true coincidences will be missed. If it is too large, more random coincidences will be counted without significant increase in the number of true

coincidences. For a typical BGO block-detector system τ is about 12 nS - considerably shorter than the decay time for BGO, which is about 300 nS.

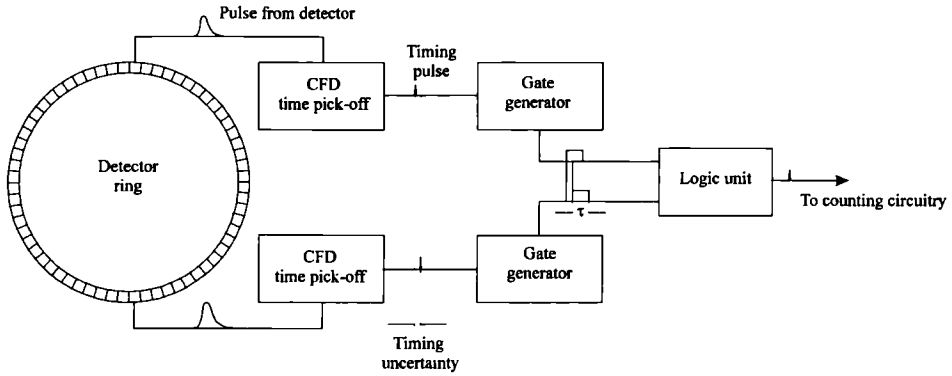

Figure 1.19. Schematic diagram showing coincidence processing in a PET camera.

If τ is sufficiently small, then time-of-flight effects may become important. These effects occur when the time taken for one photon from an annihilation event takes significantly longer to reach the detectors than the other. For a camera with a ring diameter of 1m and an active FOV of 60 cm, the maximum time difference for photons to reach the detectors is about 2.7 nS. Some attempts have been made to build PET imaging systems which make use of time-of-flight information to improve spatial resolution and signal-to-noise ratio (Ter Pogossian *et al* 1981). These require extremely fast scintillators such as BaF_2, which has a fast-component decay constant of 0.8 nS.

1.5.5. Dead-time

All detection systems have limits to the rate at which events may be processed. For example, if light pulses from separate photon interactions overlap to a significant extent, only one pulse will be measured by the PMTs. This is known as pulse pile-up. The electronics will also have a finite maximum rate at which they can process data, with typical maximum rates for pulse-processing electronics being around 1 MHz. These facts mean that some events will be missed. Since nuclear decay is a random process, there will always be a finite probability that some events will occur too close together to be distinguished even at very low average count-rates. At high count-rates such losses can become very significant. These losses are known as dead-time losses.

1.5.6. Block detectors

In a block detector, a 2D array of crystals are attached to 4 PMTs (see figure 1.20) via a light guide. Usually the array will be cut from a single crystal and the cuts filled with light-reflecting material. When a photon is incident on one of the crystals, the resultant light is shared by all 4 PMTs. Information on the position of the detecting crystal may be obtained from the PMT outputs by calculating the following ratios and comparing them to pre-set values:

$$R_x = \frac{A+B}{A+B+C+D} \tag{1.12}$$

$$R_y = \frac{A+C}{A+B+C+D} \tag{1.13}$$

where A, B, C and D are the fractional amounts of light detected by each PMT (Casey 1992). The positioning algorithm is subject to statistical error, the magnitude of which depends on the number of scintillation photons detected by the PMTs.

At high count-rates, light-pulses from two or more photon interactions may overlap as described in section 1.5.6. If the photons are incident on different crystals, the resultant pulse may then be incorrectly assigned to a crystal lying between them. Event mis-positioning can also occur when photons incident in one crystal penetrate another prior to interaction, or when photons are scattered in one crystal and subsequently interact with another. The latter two categories of mis-positioning are common to many types of detection systems.

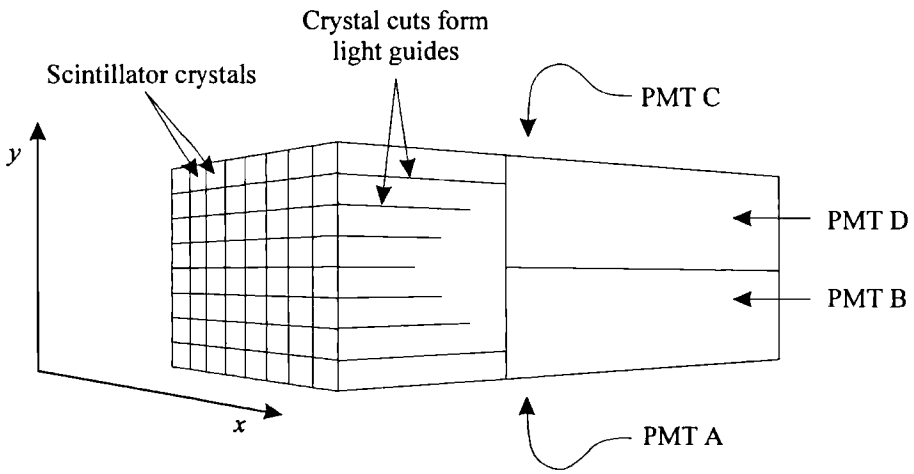

Figure 1.20. A block detector

1.5.7. Camera configurations in PET

A pre-requisite for high-resolution images in PET is accurate localisation of detected annihilation photons. This may be achieved by using small detectors. Early PET cameras used small individual scintillating crystals attached to single PMT tubes arranged in a ring. The main limiting factor on scintillation detector size is the PMT, and using this configuration it is extremely difficult to construct cameras with an axial extent greater than one or two rings of detectors. This constraint led to the development of the block detector described above. Cameras with up to 48 adjacent rings of crystal detector elements and an axial FOV of ~24 cm have been constructed using block-detector technology (Jones *et al* 1996). Cheaper versions of full ring cameras have been built which consist of a partial ring of block detectors which rotate around the FOV (Bailey *et al* 1997). A recent solution to the problem of detector packing has been to use small crystals with a high light output (made from LSO) coupled to optical fibres, which guide the light to a multi-channel PMT some distance away. Another approach is to use pairs of large-area planar detectors. To achieve acceptable spatial resolution with large-area planar detectors a high scintillation light output is required, and NaI is the scintillator of choice in such systems. These systems are considerably cheaper to manufacture than full-ring PET cameras, although they do suffer from several intrinsic performance problems (Jarritt and Acton 1996). A more effective variation on this theme is to use 6 planar detectors arranged in a hexagon (Muehllehner and Karp, 1986).

1.6. Corrections for quantitative PET in 2D and 3D mode

1.6.1. Introduction

PET offers the possibility of quantitative measurements of tracer concentration *in vivo*. However, there are several issues which must be addressed in order to realise this potential. These issues are discussed in this section, and some of the complicating factors associated with operation in 3D mode are introduced.

1.6.2. Attenuation correction

In 2D PET, attenuation correction factors are usually measured by illuminating the FOV with circular or rotating rod sources with the subject in the field of view. Sources containing quite large amounts of activity can be used to speed up the process, and scatter can be minimised by a technique called "rod windowing", whereby only LORs passing through the rod source are used for the transmission measurement (Thompson *et al* 1986). In certain cases it may be possible dispense with the measurement by using a calculated attenuation correction (Siegel and Dahlbom 1992), or to improve it by reconstructing the attenuation data and segmenting it into regions with similar linear attenuation factors. This segmented image may then be reprojected to obtain the attenuation correction factors for each LOR (e.g. Xu *et al* 1996).

With the septa retracted, the problem becomes more complex. If highly active transmission sources are used without septa, the detectors near the source will experience unacceptably large levels of dead-time. The amount of scatter also rises significantly, affecting the quantitative values of the attenuation factors. For cameras with septa, the septa may be extended into the FOV prior to the attenuation measurements being made. For septaless cameras, this is not an option. Work is still proceeding on the issue of 3D mode attenuation measurements. Promising avenues include the method of "singles attenuation correction", where a collimated source of photons of energy similar to annihilation photons is used in a manner analogous to the acquisition of an X-ray CT scan (Karp *et al* 1995). Segmentation may be used to reduce the errors due to scatter and the variation of linear attenuation with photon energy.

1.6.3. Correction for random coincidences

To obtain quantitative data in PET it is necessary to estimate and subtract the random coincidences from the measured data in each LOR to yield the sum of the true and scattered coincidences. As shown in section 1.2.5 above the rate of random coincidences on a particular LOR is given by

$$R_{12} = 2\tau\, r_1\, r_2 \qquad (1.14)$$

where R_{12} is the random coincidence rate on the LOR defined by channels 1 and 2, r_1 is the singles rate on channel 1, r_2 is the singles rate on channel 2 and τ is the coincidence resolving time. Therefore if r_1 and r_2 can be measured and τ is known, R_{12} can be calculated for each line of response. This method has the advantage that in a particular acquisition the singles rates are generally much higher than the coincidence rates, so that the statistical quality of the estimate of R_{12} tends to be good. A more commonly implemented method for estimating the randoms rate in a particular LOR is the delayed coincidence channel method. Here timing signals from one detector are delayed by a time significantly greater that the coincidence resolving time of the circuitry. There will therefore be no true coincidences in the delayed coincidence channel (although it is possible for an event from one true coincidence to be split from its partner and paired with an event from another), and the number of coincidences found is a good estimate of the number of random coincidences in the prompt signal. The estimate from the delayed channel may be subtracted from the prompt signal on-line, or stored as a separate sinogram for later processing. The advantage of this method is that the delayed channel has identical dead-time properties to the prompt channel. The disadvantage is that the statistical quality of the randoms estimate is poorer, as R_{12} is a much smaller quantity than r_1 and r_2. A method for improving the noise characteristics of random coincidence estimates obtained in this way was described by Casey and Hoffman (1986) - this subject is covered in detail in chapter 6.

1.6.4. Scatter correction

As stated in section 1.3.3, the sensitivity to scattered coincidences is greater in 3D mode than in 2D mode. In 2D mode, many workers ignore scatter altogether. However, as will be shown in chapter 5, in 3D mode the amount of scatter in the signal can become extremely large, and

accurate scatter correction methods are required. Many schemes have been proposed for scatter correction in 3D mode. These include convolution-subtraction techniques (e.g. Bailey and Meikle 1994, Bentourkia *et al* 1995), Monte-Carlo modelling techniques (e.g. Levin *et al* 1995), direct measurement techniques (Cherry *et al*, 1993) and multiple energy window methods (e.g. Shao *et al* 1994, Grootoonk *et al* 1996). The methods in widest use to date are the "Gaussian fit" technique (e.g. Stearns, 1995), and model-based scatter correction algorithms (Ollinger 1996, Watson *et al* 1996).

The Gaussian fit method consists of fitting a Gaussian profile to the scatter tails found at the edge of each projection. This works well in brain scanning, where the activity and the scattering medium is fairly uniformly distributed and concentrated in the centre of the field of view, resulting in a simple slowly changing scatter distribution. It fails in the body, as the scatter tails available for fitting are very much shorter (because the body occupies a large portion of the field of view) and the scatter distribution contains more structure.

The model-based scatter correction algorithms use the attenuation map obtained from a transmission scan together with the emission data and a model of the scanner geometry and detector systems to calculate the percentage of photons falling on each detector, using the Klein-Nishina formula. The Klein-Nishina formula gives the differential scattering cross-section $d\sigma/d\Omega$ as a function of scattering angle θ as follows:

$$\frac{d\sigma}{d\Omega} = \frac{Zr^2}{2}\left(1+\left(E/m\,c^2\right)(1-\cos\theta)\right)^{-2}\left(1+\cos^2\theta\right)\left(1+\frac{\left(E/m_0c^2\right)^2(1-\cos\theta)^2}{(1+\cos^2\theta)(1+\left(E/m_0c^2\right)(1-\cos\theta))}\right) \quad (1.15)$$

where E is the energy of the incident photon, $m\,c^2$ is the rest mass of the electron, r_0 is the classical electron radius and Z is the atomic number of the scattering atom. Since the original emission data contains scatter, the correction method must be applied iteratively. In the case where all the activity is contained within the field of view, these methods are highly accurate. However, where there is activity outside the field of view these methods start to fail. In whole-body scanning, it may sometimes be possible to obtain emission and attenuation data for most of the regions contributing to scatter, thus improving the accuracy of the scatter estimate, but in general this is not a practical option.

Because of the limitations described, scatter correction in 3D PET remains an area of active research.

1.6.5. Detector normalisation

Fourier-based reconstruction techniques assume that all LORs have the same sensitivity. Unfortunately this is not the case for experimentally acquired data. For example, the sensitivity of a particular LOR is strongly affected by the angle that the LOR makes with the two detector faces at each end. This means that the sensitivity of the LOR relative to the mean is affected both by the geometry of the camera and the LOR position. Apart from such geometric effects, the block detectors themselves vary in efficiency, as the PMT gains are not all exactly the same (and may change with time), and the scintillation crystals are not all identical. The process of correcting for these effects is referred to as normalisation, and the individual correction factors for each LOR are referred to as normalisation coefficients (NCs).

The most straightforward way of obtaining a full set of NCs is to perform a scan where every possible LOR is illuminated by the same coincidence source. NCs are then proportional to the inverse of the counts recorded in any given LOR. This approach, known as *direct normalisation*, unfortunately has a number of disadvantages. As will be discussed in chapters 3 and 4, scattered coincidences require a different normalisation to trues (Ollinger 1995), and direct normalisation does not yield these different factors. In 3D mode, small amounts of activity must be used to reduce dead-time effects FOV (Liow and Strother 1995), and this means that the amount of time required to obtain sufficient counts for reasonable statistical accuracy in each LOR quite large (tens of hours). Since NCs can change with time and should be measured as part of routine quality control, this poses a significant practical problem.

Both these problems can be overcome in conventional PET cameras by using a component-based variance reduction method (e.g. Hoffman *et al* 1989). NCs are modelled as the product of intrinsic crystal efficiencies and a small number of geometric factors that account, for example, for the variation in crystal efficiency with photon incidence angle. The NCs are not all independent, as any given crystal efficiency is a factor for many NCs, and, if the

geometric factors are accurately known, the number of unknowns is reduced from the number of LORs to the number of crystals. There is a trade-off between systematic errors and statistical accuracy that depends on the complexity of the model - however, for an ECAT 951R operating in 3D mode there are about 1.25 million LORs and just 8192 detectors, so the potential for variance reduction is very large.

While component-based normalisation is a promising technique, it remains a developing field of study in 3D PET, and several authors have reported the presence of residual artefacts in images reconstructed from normalised acquisitions of uniform cylindrical phantoms (e.g. Bailey *et al* 1996, Oakes *et al* 1998).

1.6.6. Dead-time correction

In both 2D and 3D mode, there will be losses due to detector and system dead-time. To obtain quantitative results, acquired data should be corrected for these losses. This is usually done by modelling the dead-time losses as a combination of paralyzable and non-paralyzable components and obtaining parameters for the model by means of experiment involving repeated measurements of a decaying source (e.g. Casey *et al* 1995).

As discussed in section 1.5.6, a feature of block-detector systems is event mis-positioning at high count-rates due to pulse pile-up. In 2D mode, mis-positioning due to pulse pile-up has been shown to be unimportant except at very high activities (Germano and Hoffman, 1990). However, little work has been published on this effect in 3D mode. Casey *et al* (1995) suggest a possible correction scheme, but it has not been implemented on any commercially available system to date. This problem is discussed further in chapter 4.

1.7. Objectives of this work.

If the potential benefits of PET imaging in 3D mode are to be realised in clinical situations, the following questions need to be answered:

1. How may 3D PET data be accurately corrected for scattered coincidences?
2. How may attenuation correction factors be obtained in the absence of septa?
3. How may 3D PET data be accurately normalised?
4. How may 3D PET data be accurately corrected for pulse pile-up effects?
5. What are the optimum acquisition parameters for 3D PET?
6. Under what circumstances does the increase in sensitivity to true coincidences obtained in 3D mode outweigh the effect of increased sensitivity to scatter and random coincidences?

To find adequate answers to all of these questions is a very large task, to which many workers have applied themselves over the last decade. In this work only a subset of these questions have been addressed. In chapter 3 new variance reduction algorithms for detector efficiency normalisation have been developed and compared with existing methods. In chapter 4 wider issues in component-based normalisation have been examined and a new model for normalisation developed which addresses the problem of event mis-positioning due to pulse pile-up. In chapter 5 scanning parameters for 2D and 3D mode acquisition have been optimised and the performance of 2D and 3D mode compared for a wide range of situations reflecting those which might be encountered in clinical practice. In chapter 6 three of the variance reduction methods derived in chapter 3 for normalisation have been used to enable low-noise subtraction of random coincidences from emission data, and the resulting performance improvement quantified. Finally in chapter 7 a simple performance comparison of 2D and 3D mode acquisition has been performed *in vivo*.

1.8. References

HO Anger 1958 "Scintillation camera" *Rev. Sci. Instr.* **29**(1) 27-33

A Antonini, J Schwarz, WH Oertel, O Pogarell and KL Leenders 1997 "Long-term changes of striatal dopamine D-2 receptors in patients with Parkinson's disease: A study with positron emission tomography and [C-11]Raclopride" *Movement Disorders* **12**(1), 33-38

DL Bailey, and SR Meikle 1994 "A Convolution-Subtraction scatter correction method for 3D PET" *Phys. Med. Biol* **39**, 411-424

DL Bailey 1996 Quantification in 3D Positron Emission Tomography PhD Thesis, University of Surrey, United Kingdom

DL Bailey, DW Townsend, PE Kinahan, S Grootoonk and T Jones 1996 "An investigation of factors affecting detector and geometric correction in normalisation of 3-D PET data." *IEEE Trans. Nucl. Sci.* **43**(6), 3300-3307

DL Bailey, H Young, PM Bloomfield, SR Meikle, D Glass, MJ Myers, TJ Spinks, CC Watson, P Luk, AM Peters and Terry Jones 1997 "ECAT ART - a continuously rotating PET camera: performance characteristics, initial clinical studies, and installation considerations in a nuclear medicine department" *Eur. J. Nucl. Med* **24** (1) 6-15

M Bentourkia, P Msaki, J Cadorette and R Lecompte 1995 "Assessment of Scatter Components in High-Resolution PET: Correction by Nonstationary Convolution Subtraction" *J Nucl Med* **36**: 121-130

RN Bracewell 1986 The Fourier Transform and its Application (2nd Edition, revised) McGraw-Hill International Editions, Singapore. ISBN 0-07-066454-4

G Brix, J Zaers, L-E Adam, ME Beleman, H Ostertag, H Trojan, U Haberkorn 1997 "Performance Evaluation of a Whole-Body PET Scanner Using the NEMA Protocol" *J Nucl Med* **38**(10): 1614-1623

CS Brock, SR Meikle, P Price 1997 "Does fluorine-18 fluorodeoxyglucose metabolic imaging of tumours benefit oncology?" *Eur J Nucl Med* **24**:691-705

DE Burdette, SY Sakurai, TR Henry, DA Ross, PB Penell, KA Frey, JC Sackellares and RL Albin 1995 "Temporal lobe central benzodiazepine binding in unilateral mesial temporal lobe epilepsy" *Neurology* **45**(5) 934-941

ME Casey and R Nutt 1986 "A Multicrystal Two Dimensional BGO Detector System For Positron Emission Tomography" *IEEE Trans. Nucl. Sci.* **33**(1),460-463

ME Casey 1992 An Analysis of Counting Losses in Positron Emission Tomography PhD Thesis, University of Tennessee, Knoxville, USA.

ME Casey, H Gadagkar and D Newport 1995 "A component based method for normalisation in volume PET" Proceedings of the 3rd International Meeting on Fully Three-Dimensional Image Reconstruction in Radiology and Nuclear Medicine, Aix-les-Bains, France.

SR Cherry, M Dahlbom and E J Hoffman 1991 "3D PET using a conventional multislice tomograph without septa" *J. Comput. Assist. Tomogr.* **15** 655-68

SR Cherry, SR Meikle and EJ Hoffman 1993 "Correction and Characterisation of Scattered Events in Three-Dimensional PET Using Scanners with Retractable Septa" *J Nucl Med* **34**:671-678

SR Cherry, Y Shao, RW Silverman, K Meadors, S Siegel, A. Chatziioannou, JW Young, WF Jones, JC Moyers, D Newport, A Boiutefnouchet, TH Farquhar, M Andreaco, MJ Paulus, DM Binkley, R Nutt and ME Phelps, 1997 "MicroPET: A High Resolution PET Scanner for Imaging Small Animals" *IEEE Trans. Nucl. Sci.*, **44**(3), 1161-1166F

JG Colsher 1980 "Fully three-dimensional positron emission tomography" *Phys. Med. Biol.* **25**(1) 103-115

F Daghighian, P Shenderov, KS Pentlow, MC Graham, B Eshaghian, CL Melcher and JS Schweitzer 1993 "Evaluation of Cerium Doped Lutetium Oxyorthosilicate (LSO) Scintillation Crystal for PET." *IEEE Trans Nucl Sci.* **40**(4):1045-1047

M Dahlbom, LR MacDonald, L Ericsson, M Paulus, M Andreaco, ME Casey and C Moyers, 1997 "Performance of a YSO/LSO Phoswich Detector for use in a PET SPECT System" *IEEE Trans. Nucl. Sci.*, **44**(3), 1114-1119

ME Daube-Witherspoon and G Muehllehner, 1987 "Treatment of axial data in three-dimensional PET" *J. Nucl Med.* **28**, 1717-1724

M Defrise, PE Kinahan, DW Townsend, C Michel, M Sibomana and DF Newport, 1997 "Exact and approximate rebinning algorithms for 3D-PET data" *IEEE Trans. Med. Imag.* **16**(2) 145-158

RD Evans 1955 The Atomic Nucleus McGraw-Hill, New York, 1955 LCCCN 55-7275

DC Ficke, JT Hood and MM Ter-Pogossian (1996) "A Spheroidal Positron Emission Tomograph for Brain Imaging: A Feasibility Study" *J. Nucl. Med.* **37**(7) 1219-1225

G Germano and EJ Hoffman 1990 "A study of data loss and mispositioning due to pileup in 2-D detectors in PET" IEEE trans. Nucl. Sci. 37(2), 671-675

S Grootoonk, TJ Spinks, D Sashin, NM Spryou and T Jones 1996 "Correction for scatter in 3D brain PET using a dual energy window method" *Phys. Med. Biol.* **41**, 2757-2774

K Hamacher, HH Coenen and G Stocklin 1986 "Efficient stereospecific synthesis of no-carrier-added 2-[^{18}F]fluoro-2-deoxy-D-glucose using aminopolyether supported nucleophilic substitution" *J Nucl Med* **27**(2), 235-238

RA Hawkins, Y Choi, S-C Huang, CK Hoh, M Dahlbom, C Schiepers, N Satyamurthy, JR Barrio and ME Phelps 1992 "Evaluation of the Skeletal Kinetics of Fluorine-18-Fluoride Ion with PET" *J Nucl Med* **33**(5), 633-642

P Hellman, H Ahlström, M Bergström, A Sundin, B Långström, Göran Weterberg and C Julin 1994 "Positron emission tomography with ^{11}C-methionine in hyperparathyroidism" *Surgery*, **116**(6), 974-981

EJ Hoffman, TM Guerrero, G Germano, WM Digby and M Dahlbom 1989 "PET system calibrations and corrections for quantitative and spatially accurate images" *IEEE Trans. Nuc. Sci.* **36**(1), 1108-1112

S-C Huang, RE Carson, EJ Hoffman, J Carson, N MacDonald, JR Barrio and ME Phelps 1983 "Quantitative measurement of local cerebral blood flow in humans by positron emission tomography and ^{15}O-water" *J. Cereb. Blood Flow Metabol.* **3**(2), 141-153

HM Hudson and RS Larkin 1994 "Accelerated Image Reconstruction using Ordered Subsets of Projection Data" *IEEE Trans. Med. Imag.* **13**, 601-609

PH Jarritt and PD Acton 1996 "PET imaging using gamma camera systems: A review" *Nucl. Med. Comm.* **17** 758-766

HE Johns and JR Cunningham 1983 The Physics of Radiology (fourth edition) Charles C Thomas, Ill. USA, ISBN 0-398-04669-7

T Jones, DL Bailey, PM Bloomfield, TJ Spinks, W Jones, K Vaigneur, J Reed, J Young, D Newport, C Moyers, ME Casey, and R Nutt 1996 "Performance characteristics and novel design aspects of the most sensitive PET camera for high temporal and spatial resolution" *J. Nucl. Med.* **37** 85P

I Kanno, AA Lammertsma, JD Heather, JM Gibbs, CG Rhodes, JC Clark and T Jones 1984 "Measurements of cerebral blood flow using bolus inhalation of $C^{15}O_2$ and positron emission tomography: description of the

method and comparison with $C^{15}O_2$ continuous inhalation method" *J. Cereb. Blood Flow Metabol.* **4**(2), 224-234

JS Karp, G Muehllehner, H Qu and XH Yan 1995 "Singles Transmission in Volume-Imaging PET with a Cs-137 Source" *Phys. Med. Biol.* **40** (5) 929-944

PE Kinahan and JG Rogers 1990 "Analytic 3D Image Reconstruction Using All Detected Events" *IEEE Trans. Nucl Sci.* **36**(1), 964-968

GF Knoll, 1989 Radiation detection and measurement (2nd Edition) John Wiley and Sons 88-26142

WJ Koh, KS Bergman, JS Rasey, LM Peterson, ML Evans, MM Graham, JR Grierson, KL Lindsley, TK Lewellen, KA Krohn and TW Griffin 1995 "Evaluation of oxygenation status during fractionated radiotherapy in human non-small cell cancers using ^{18}F-Fluoromisonidazole positron emission tomography" Int. J. Rad. Onc. Biol. Phys **33**(2) 391-398

WG Kuhle, G Porenta, S-C Huang, D Buxton, SS Gambhir, H Hansen, ME Phelps and HR Schelbert 1992 "Quantification of regional myocardial blood flow using ^{13}N ammonia and reoriented dynamic positron emission tomographic imaging" *Circulation* **86**(3), 1004-1017

CS Levin, M Dahlbom and EJ Hoffman 1995 "A Monte-Carlo Correction for the Effect of Compton Scattering in 3-D PET Brain Imaging" *IEEE Trans. Nucl. Sci.* **42**(4) 1181-1185

J-S Liow and SC Strother 1995 "Normalisation using rotating rods for 3D PET" Proceedings of the 3rd International Meeting on Fully Three-Dimensional Image Reconstruction in Radiology and Nuclear Medicine, Aix-les-Bains, France.

RC Marshall, JH Tillisch, ME Phelps, S-C Huang, R Carson, E Henze and HR Schelbert 1983 "Identification and differentiation of resting myocardial ischemia and infarction in man with positron computed tomography, ^{18}F-labelled fluorodeoxyglucose and N-13 ammonia. *Circulation* **67**(4), 766-778

G Muehllehner and JS Karp 1986 "A Positron Camera Using Position-Sensitive Detectors: PENN-PET" *J. Nucl. Med.* **27** 90-98

T R Oakes, V Sossi and T J Ruth 1998 "Normalization for 3D PET with a low-scatter planar source and measured geometric factors" *Phys. Med. Biol.* **43**(4) *To appear.*

JM Ollinger 1995 "Detector efficiency and Compton scatter in fully 3D PET" *IEEE Trans. Nucl. Sci.* **42**(4) 1168-1173

JM Ollinger 1996 "Model-based scatter correction for fully 3D PET" *Phys. Med. Biol.* **41** 153-176

ME Phelps, JC Mazziotta and HR Schelbert (editors) 1986 Positron emission tomography and autoradiography - principles and applications for the brain and heart Raven Press, ISBN 0-88167-118-5

R A Raylman, BE Hammer and NL Christensen 1992 "Combined MRI-PET scanner: a Monte-Carlo evaluation of improvements in PET resolution due to the effects of a static homogeneous magnetic field" *IEEE Trans. Nuc. Sci.* **43**(4) 2406-2412

DW Rickey, R Gordon and W Huda 1992 "On lifting the inherent limitations of positron emission tomography by using magnetic fields (MagPET)" *Automedica*, **14** 355-369

L Shao, R Freifelder and J S Karp 1994 "Triple Energy Window Scatter Correction Technique in PET" *IEEE Trans. Med Imag* **13** (4) 641-648

S Siegel and M Dahlbom 1992 "Implementation and evaluation of a calculated attenuation correction for PET" *IEEE Trans. Nucl. Sci* **39** (4) 1117-1121

TJ Spinks, MP Miller, DL Bailey, PM Bloomfield, L Livieratos and T Jones 1998 "The effect of activity outside the direct field of view in a 3D only whole body positron tomograph" *Phys. Med. Biol.* **43**(4) *to appear.*

CW Stearns 1995 "Scatter correction method for 3D PET using 2D fitted Gaussian functions" *J. Nucl. Med.* **36** 105

LG Strauss and PS Conti 1991 "The Application of PET in Clinical Oncology" *J Nucl Med* **32**(4):623-648

MM Ter Pogossian, NA Mullani and DC Ficke 1981 "Photon time-of-flight assisted positron emission tomography" *J Comput Assist Tomogr* **5** 227-239

CJ Thompson, A Dagher, DN Lunney, SC Strother and AC Evans 1986 "A technique to reject scattered radiation in PET transmission scans", in *Int. Wkshp. Phys. Eng. Computerised Multidimensional Imag. Processing*, PROC SPIE, **671** 244-253

O Warburg 1931 "The metabolism of tumors" New York: Richard Smith;129-161

CC Watson, D Newport and ME Casey 1996 "A single-scatter simulation technique for scatter correction in 3D PET" Fully Three-Dimensional Image Reconstruction in Radiology and Nuclear Medicine, Eds P Grangeat and JL Amans, Kluwer Academic Publishers, ISBN 0 7923 4129 5

M Xu, PD Cutler, WK Luk 1996 "Adaptive, Segmented Attenuation Correction for Whole-Body PET Imaging" *IEEE Trans. Nucl. Sci.*, **43** (1) 331-336

2. Features and basic performance parameters of the ECAT 951R Scanner and reconstruction algorithms used.

2.1. Introduction

In this chapter the key operating features of the ECAT 951R (Siemens/CTI, Knoxville, TN, USA) scanner used in this work are reviewed. Measurements of some basic performance parameters of the scanner and reconstruction engines used are also presented.

2.2. Design features of the ECAT 951R

2.2.1. Scanner geometry

The ECAT 951R scanner is a whole-body block-detector design consisting of 128 BGO block detectors, each containing 8x8 crystal detector elements. The block detectors are arranged in a double ring as shown in figure 2.1. The ring diameter is 102.0 cm and the total axial FOV is 10.8 cm giving maximum acceptance angle of 12.1 degrees for 3D acquisition.

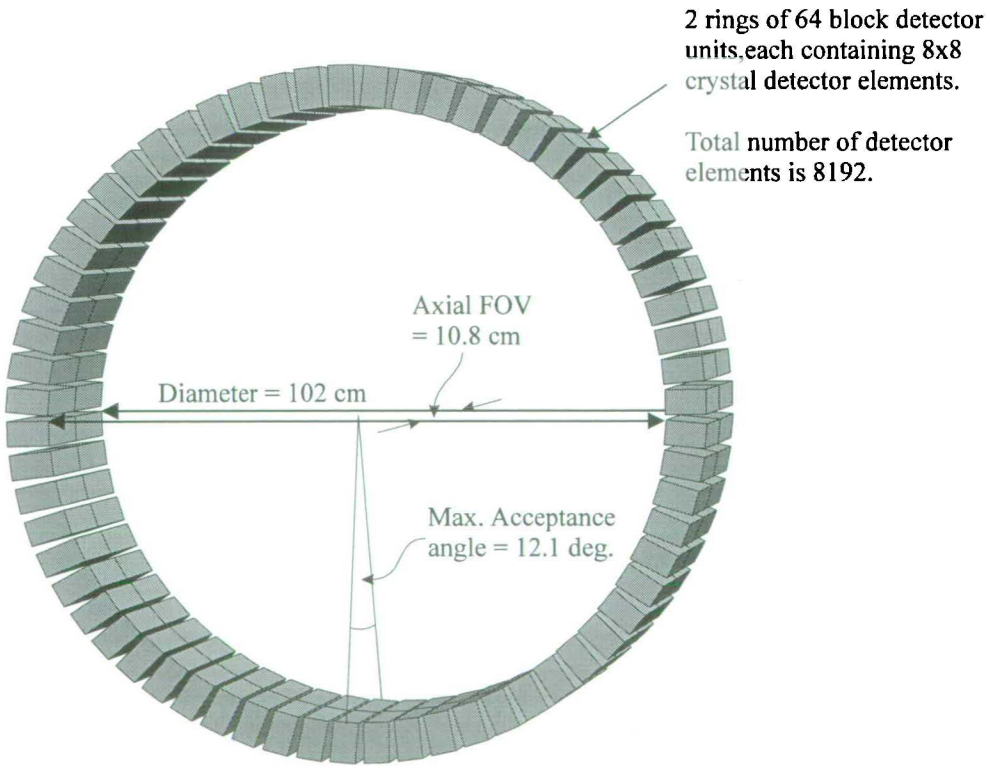

Figure 2.1. Detector configuration for the ECAT 951R camera.

Data are acquired over a transaxial FOV of diameter 60 cm. Parallel-sided annular tungsten septa of width 1 mm and radial depth 77 mm separate each detector element in the axial direction. These may be retracted to allow fully-3D (3D mode) operation. In 3D mode the axial FOV for single events is considerably larger than the axial FOV for true coincidence events. The extent of the axial FOV for single events in 3D mode was measured by placing a small vial containing a solution of ^{18}F in water just outside the FOV and monitoring the single event rate measured by the camera as the source was moved along the axial centre-line of the camera. The results are shown in figure 2.2. It can be seen that the sensitivity to activity decreases in a near linear fashion to a distance of about 10 cm. Beyond about 15 cm the sensitivity to single events becomes quite small.

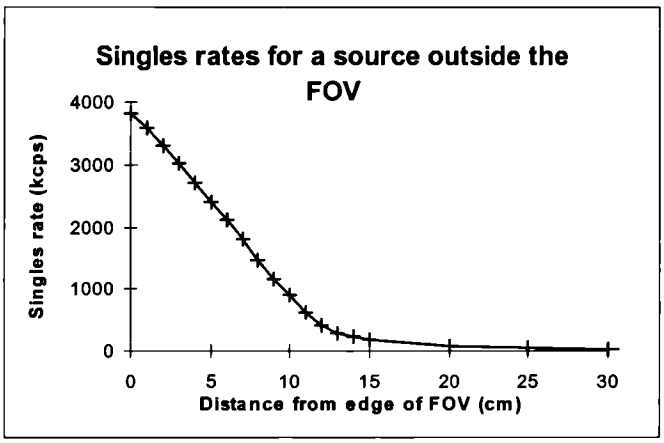

Figure 2.2. Singles rates as a function of distance from the edge of the FOV in 3D mode.
Measurements were made as a small vial of activity was moved along the centre line of the scanner away from the edge of the FOV. The back-ground count-rate (about 620 kcps) has been subtracted. The amount of activity in the vial was approximately 30 MBq at the start of the measurements and the maximum dead-time was approximately 7%.

2.2.2. Block detectors and coincidence circuitry

The BGO block detectors consist of arrays of 8x8 crystal elements attached to 4 PMTs. The crystal elements have dimensions 5.62 mm (transaxially) by 6.11 mm (axially) except for the edge crystals which are 0.1 mm smaller. The crystal depth is 30 mm. The blocks are arranged in "buckets" of 4 blocks each. The energy resolution of the detectors is 23% at 511 keV (Spinks *et al* 1992). The ULD and LLD values are set for each bucket (and are modified for each crystal element) and are alterable by the operator at acquisition time. The resolving time of the coincidence circuitry is 12 ns, and is not alterable by the operator.

2.2.3. Singles measurements and dead-time correction

Singles rates are stored for each bucket during normal acquisition. There is a dead-time correction scheme for 2D mode based solely on bucket singles rates. There is no dead-time correction method implemented for 3D mode, although the individual bucket singles-rate correction factors are stored in the 3D sinogram headers. There is also no correction scheme for mispositioned events caused by pulse pile-up effects within the block detectors themselves.

2.2.4. Transaxial sampling

If projections are constructed of parallel LORs and all possible angular projections are obtained, the data is sampled transaxially every detector width, which by application of the sampling theorem leads to a maximum resolution of twice one detector width. This may be improved by interleaving LORs from one projection with LORs from its nearest angular neighbour to construct a new set of composite projections (see figure 2.3). At the centre of the FOV, the data is now sampled every half detector width. This procedure halves the angular sampling, but this is acceptable because at the centre of the FOV the data is over-sampled in θ_p.

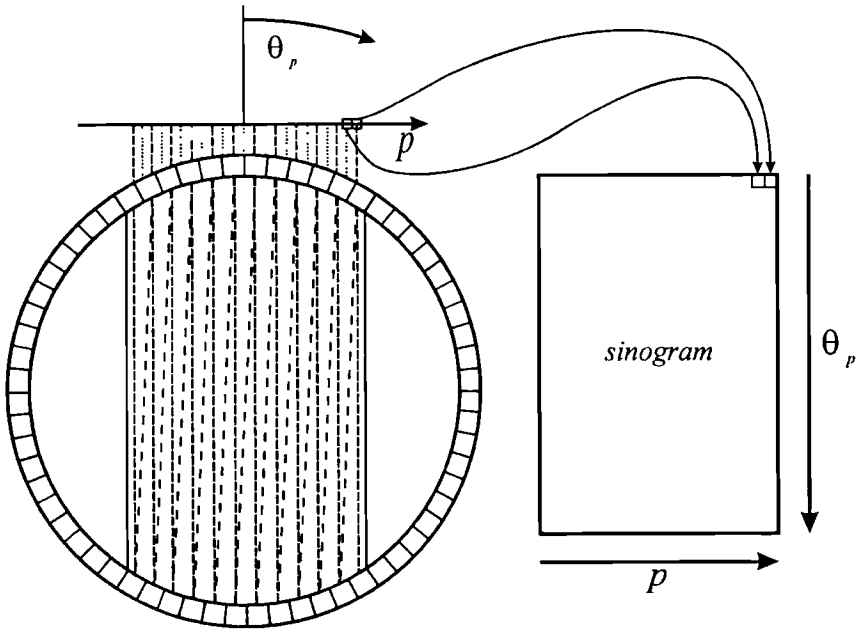

Figure 2.3. Transaxial sampling on the ECAT 951.
Projections at adjacent angular positions are interleaved in the sinogram to achieve greater sampling in the *p*-direction.

2.2.5. Acquisition modes

In 2D mode datasets consist of 31 sinograms, made up from 16 direct and 15 cross-planes. For direct planes, coincidences are acquired within a ring and between rings that are 2 rings apart (ring difference of 2). For cross planes, coincidences are acquired for ring differences of 1 and 3. In 3D mode, all ring-differences are allowed are allowed. 3D datasets consist of 16 sinograms corresponding to direct planes and 240 pseudo-sinograms (where the LORs are not co-planar) corresponding to cross-planes. The number of adjacent detectors used in a given angular projection is 96 and the method of transaxial sampling discussed above results in sinograms containing 192 by 256 elements.

Sinogram data is stored in 2-byte integer format. 2D acquired datasets are approximately 3 Mbytes in size, and 3D datasets approximately 25 Mbytes.

Data may be acquired with on-line randoms correction (with coincidences from the delayed channel subtracted from each LOR) or as a double-size dataset with delayed and prompt coincidences stored separately.

2.2.6. Transmission scanning and sources

Transmission scanning in 2D mode is performed using 3 rotating rod sources which are housed in lead wells (with steel end-caps) outside of the FOV when not in use. Data can be acquired in rod-windowed mode as described in section 1.5.2. The transmission rod sources each contain between 30 and 110 MBq of ^{68}Ge, and are 11 cm long by 3 mm wide. There is no implemented technique for processing transmission data acquired with the septa retracted.

The steel end-caps do not offer complete shielding of the retracted transmission sources during 3D-mode emission scanning. To characterise the effects of spill-over from the retracted rod sources during normal acquisition, a uniform 20 cm cylinder containing water and no activity was placed in the centre of the FOV, and a 14-hour acquisition performed with the septa retracted. A total of 2.9×10^7 counts were acquired. The distribution of the spill-over coincidence events is not uniform across the FOV. Figure 2.4 shows the acquired data summed over all planes, together with a profile averaged over all angles. The events are concentrated at the edges of the FOV. Figure 2.5 shows the counts in each direct (ring difference = 0) plane. When retracted, the rod sources lie closest to ring 1. It can be seen that

the number of counts increases with distance from the rods. Although this effect appears to be small it can have a significant effect on scatter correction algorithms which fit profiles to the scatter tails at the edges of the FOV (see section 4.2).

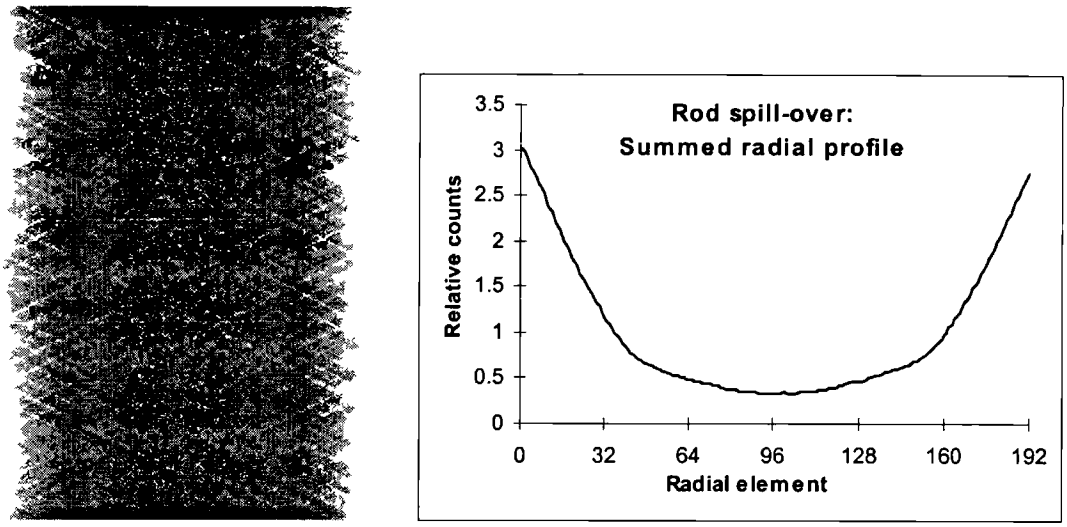

Figure 2.4. Events arising from retracted rod-sources during a 3D emission scan.
Left: sinogram summed over all planes; right: profile summed over all angles.

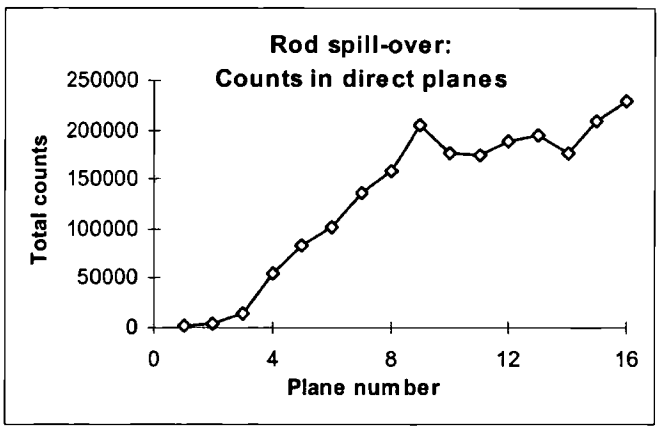

Figure 2.5. Number of events arising from retracted rod-sources during a 3D emission scan.
Counts are plotted as a function of direct plane number. Plane 1 is nearest the rod-source wells.

2.3. Reconstruction engines used

Throughout this work FBP (as implemented by the manufacturer) has been used for reconstruction in 2D mode, and the Byars Consulting (Knoxville, TN, USA) implementation of 3D-RP used for 3D mode (Kinahan and Rogers, 1990). In this implementation, only LORs

with ring difference of <= 11 are used, and attenuation correction is performed by projecting measured or calculated 2D attenuation factors into a 3D volume prior to application.

2.4. Variations in resolution and image signal-to-noise ratios in 2D and 3D mode

To measure the variation in transaxial resolution with axial position, a thin (diameter = 3mm) line-source containing ^{68}Ge was placed in the centre of the FOV and scanned in 2D and 3D mode. The resultant datasets were reconstructed and in each plane two mutually perpendicular transaxial profiles were drawn passing through the image maximum. The mean value of the full-width at half-maximum (FWHM) for both profiles is plotted as a function of image plane in figure 2.6. The resolution for both modes is very similar in the central third of the axial FOV. However, the resolution in the 3D image volume degrades as the edges of the axial FOV are approached. This effect is not seen in 2D mode.

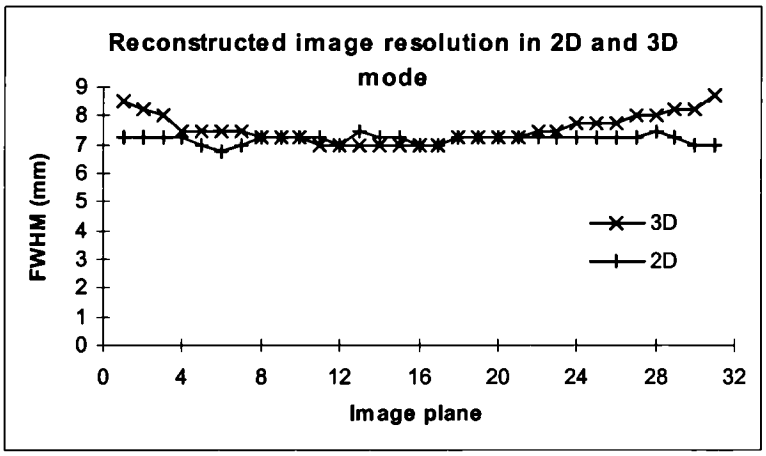

Figure 2.6. Reconstructed image FWHM for a central line source as a function of axial position.

Variations in image signal-to-noise ratio (SNR) with axial position were measured by comparing the % standard deviation of a large central circular region of interest (ROI) drawn on a reconstructed image of a 20 cm cylindrical phantom uniformly filled with activity acquired in both 2D and 3D mode. The 2D data was normalised and attenuation corrected using the manufacturer's protocols and no scatter correction was applied. The 3D data was normalised and scatter corrected using the methods described in chapter 4, and attenuation correction performed by projecting the attenuation factors measured in 2D mode into the 3D volume. Reconstructions were performed using a ramp filter with a cut-off at the Nyquist

frequency (with a generalised Colsher filter for the 3D reconstruction). The results are plotted in figure 2.7. In both 2D and 3D mode there is a similar degradation of SNR at the edges of the FOV. In the central portion of the FOV, a "saw-tooth" pattern is evident in the 2D image, whereas the SNR in the 3D image is quite uniform. The variation in SNR in the 2D case simply reflects the axial variation in sensitivity described in section 1.3.2. However, in 3D mode, the improvement in sensitivity as the centre of the axial FOV is approached manifests not as improved SNR but as improved spatial resolution. This is a feature of the 3D-RP algorithm used.

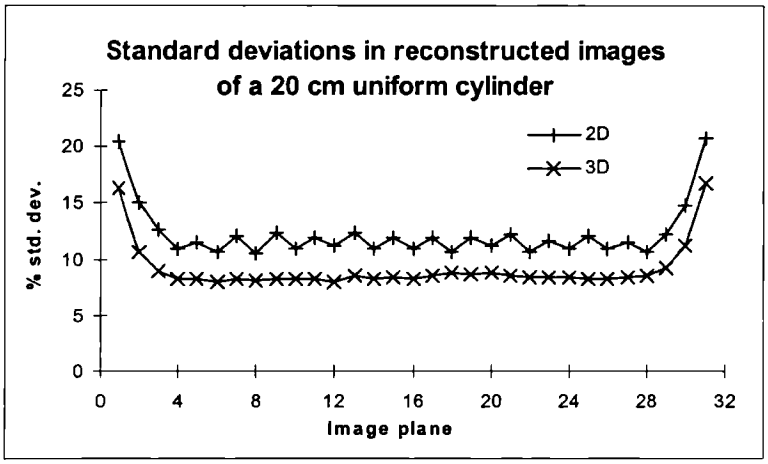

Figure 2.7. SNR quantified as % std. dev. of reconstructed image elements as a function of image plane.
The relative performance in 2D and 3D mode shown here is arbitrary.

2.5. Performance of 3D-RP with simulated data

To measure the uniformity of reconstructed images generated from 3D data by the 3D-RP algorithm, a noise-free simulated data set equivalent to an acquisition of a uniform 20 cm cylinder of activity was generated (simulation courtesy of Martin Lodge, the Clinical PET Centre, UMDS, London). This data was reconstructed using 3D-RP and the axial and transaxial uniformity examined. The outermost 2 planes at each end show significantly reduced count-density compared to the others, whereas image planes 3 and 29 showed increased count-density (figure 2.8). Axial profiles though the two outermost planes at either end of the image volume show a distinct peak at the centre of the image, but profiles through image planes 3-29 are qu'te uniform (figure 2.9).

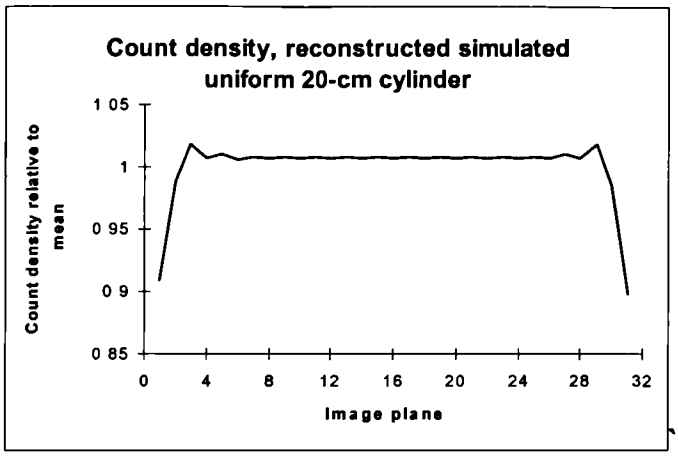

Figure 2.8. Mean count density in reconstructed simulated 3D data as a function of axial position.

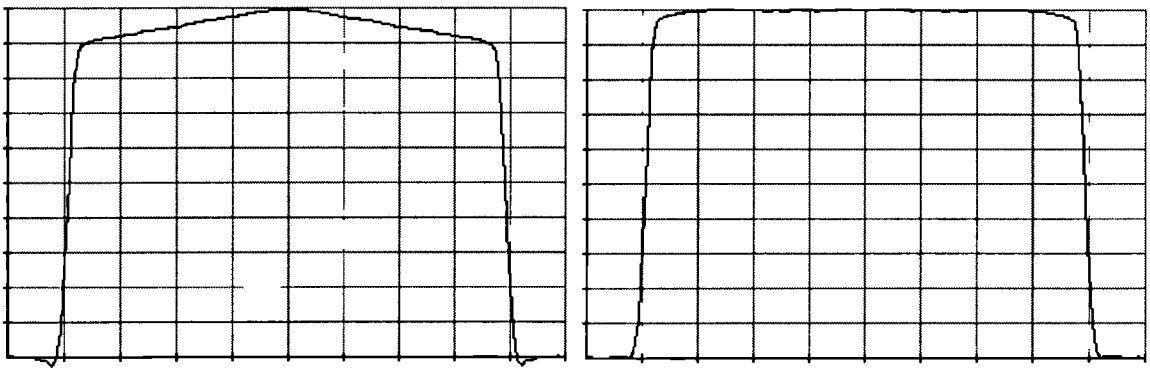

Figure 2.9. Radial profiles through image planes 1 (left) and 3 (right) from the reconstructed simulated 3D data.

2.6. References

PE Kinahan and JG Rogers 1990 "Analytic 3D Image Reconstruction Using All Detected Events" *IEEE Trans. Nucl. Sci.* **36**(1), 964-968

TJ Spinks, T Jones, DL Bailey, DW Townsend, S Grootoonk, PM Bloomfield, M-C Gilardi, ME Casey, B Sipe and J Reed 1992 "Physical performance of a positron tomograph for brain imaging with retractable septa" *Phys. Med. Biol.* **37**(8), 1637-1655

3. Variance reduction algorithms for detector normalisation in 3D mode.

3.1. Introduction

As stated in section 1.6.5, most reconstruction algorithms require that all LORs have the same sensitivity. Deviations from uniform sensitivity arise because of random variations in individual crystal efficiencies, variations in the PMT gains, systematic variations in crystal efficiencies due to intrinsic non-uniformities in the block-detector response, and variations due to geometric effects. Failure to correct for these deviations leads to both high and low-frequency artefacts in reconstructed images.

Correction factors for these effects are called normalisation coefficients (NCs). Direct measurement of NCs by inverting the elements of a scan of a source which uniformly illuminates the FOV is problematic, firstly because of difficulties in obtaining sufficient counts in each LOR for adequate statistical accuracy, and secondly because of the difference in NCs for true and scattered coincidences. The practical difficulty in acquiring sufficient counts for reasonable statistical accuracy in the NC estimates can be overcome by means of a variance reduction method as first suggested by Casey and Hoffman (1986). Variance reduction methods make use of the fact that the performance of any given crystal affects many NCs, thus considerably reducing the number of unknowns in the problem. This technique was refined by Hoffman *et al* (1989) who suggested incorporating a component-based approach into the normalisation process. In component-based methods, NCs are modelled as the product of intrinsic crystal efficiencies and a small number of other factors that account for the variation in crystal efficiency with photon incidence angle and other systematic effects. Ollinger (1995) developed the concept further, introducing new geometric components and reporting the fact that scattered and true coincidences have different NCs. Ollinger addressed the latter issue by applying correction factors for efficiency effects to both scattered and true coincidences, but correction factors for geometric effects to trues only.

In this chapter methods for obtaining estimates of the intrinsic crystal efficiency factors will be examined. Crystal efficiencies vary over time as PMT gains drift or block-detectors are replaced, so normalisation data for these components is usually acquired as part of routine

quality assurance. Several methods for the calculation of intrinsic efficiencies have been described in the literature. The method proposed by Casey and Hoffman (1986) gives the efficiency for each LOR directly and individual crystal efficiencies are not calculated explicitly. The method provides an unbiased result with noise-free normalisation data, but is only valid for LORs illuminated by the normalisation source. Hoffman's approximate fan-sum method (Hoffman *et al* 1989), originally developed in order to normalise LORs not illuminated by the normalisation source, does provide values for individual crystal efficiencies but can introduce bias, even with noise-free normalisation data. Defrise *et al* (1991) developed a method for calculating individual crystal efficiencies based on the fan-sum technique which is actually exact when used with noise-free normalisation data. In all of these methods, efficiencies for a given crystal or LOR are calculated using data from a single direct-plane sinogram.

In section 3.2 below the algorithms for crystal efficiency calculation described above are reviewed, and it is shown how the Casey method may be implemented for normalisation in 3D mode. The Defrise method is also generalised to make more efficient use of the normalisation data. The three single-plane algorithms are then extended so that LORs from all rings are utilised in the calculation of any given crystal or LOR efficiency. A similar, fully-3D, implementation of the fan-sum algorithm has previously been reported by Stazyk et al (1994). In sections 3.3 and 3.4 the various algorithms are assessed in terms of their performance as a function of noise in the normalisation data and their systematic accuracy with a range of normalisation sources.

3.2. Theory

3.2.1. Normalisation model

In component based normalisation, NCs for each LOR are modelled as the product of intrinsic crystal efficiencies and other systematic factors. If the systematic factors are combined, this may be written as follows (ignoring statistical noise and provided the normalisation model is correct):

$$n_{uivj} = G_{uivj}\varepsilon_{ui}\varepsilon_{vj} \tag{3.1}$$

where n_{uivj} is the NC for the LOR joining detector i in ring u and detector j in ring v, G_{uivj} is the combined systematic factor for the LOR and ε_{ui} and ε_{vj} are the intrinsic efficiencies of detectors i in ring u and j in ring v respectively. If data is acquired with all LORs uniformly illuminated by the source, the counts in each element of the resulting sinogram E_{uivj} may be written as:

$$E_{uivj} = An_{uivj} = AG_{uivj}\varepsilon_{ui}\varepsilon_{vj} \tag{3.2}$$

where A is a constant reflecting the source strength and acquisition time. If the systematic correction factors are applied and the data scaled so that the mean value of all LORs is unity, the sinogram elements are equal to the product of the detector efficiency coefficients:

$$\eta_{uivj} = \varepsilon_{ui}\varepsilon_{vj} \tag{3.3}$$

The purpose of variance reduction algorithms is to obtain estimates of the η_{uvij} from the scaled data in such a way that the contribution of statistical noise to each NC is minimised.

3.2.2. Algorithms for calculation of intrinsic efficiencies

Consider a camera consisting of P detector rings. In a given ring there are N detectors indexed by i where i lies between 0 and N-1. Any detector i is in coincidence with a group of other detectors, of which R in any particular ring are uniformly illuminated by the normalisation source. It will be assumed that i is replaced by $i \bmod N$ where appropriate.

3.2.2.1. The single-plane fan-sum method

Given a detector i in a particular ring u, define a group A of M ($<= R$) consecutive detectors in the same ring, indexed by j such that

$$i + N/2 - M/2 <= j < i + N/2 + M/2$$

i.e. A is a block of detectors diametrically opposed to i (see figure 3.1), and all the LORs joining i and the detectors j in A intersect the source. Then the efficiency ε_{ui} of each detector i is given by:

$$\varepsilon_{ui} = \frac{\left(\varepsilon_{ui} \sum_{j \in A} \varepsilon_{uj}\right)}{\sum_{j \in A} \varepsilon_{uj}} \tag{3.4}$$

If M is sufficiently large, it may be possible to assume the following:

$$\sum_{j \in A} \varepsilon_{uj} \approx M \tag{3.5}$$

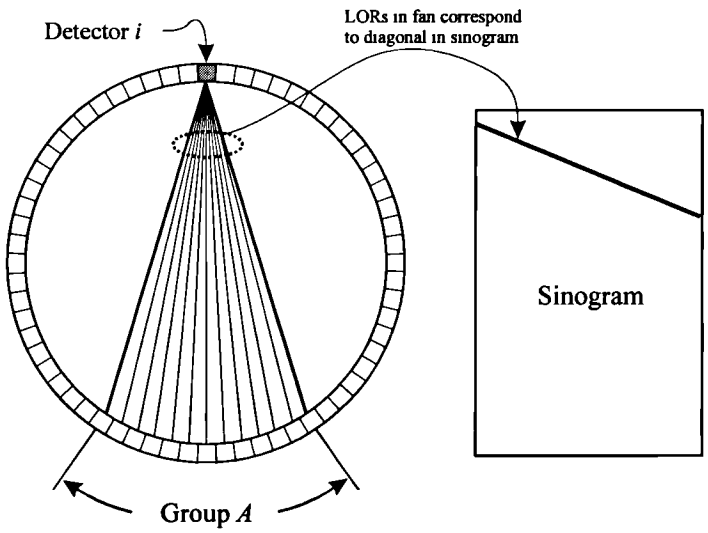

Figure 3.1. Elements of the single-plane fan-sum method.
A fan of LORs with a particular detector at its apex corresponds to a diagonal line of elements in the sinogram. Note that the angle of the diagonal is π 8 rather than π 4 - this is due to the interleaving of adjacent projections described in section 2.2.5

Equation 3.5 is the fan-sum approximation. If there are systematic variations in the efficiencies ε_{ui} over a similar number of detectors to M then it may be invalid. For example, if a scanner uses block detectors with 8 crystals per side, then one would require that $M >>$

8. The numerator of equation 3.4 is readily obtainable from experimentally acquired data (see figure 3.1), so having made the fan-sum approximation, we can calculate fan-sums around the detector ring and obtain estimates for all ε_{ui}. The process is repeated for all rings, and the efficiency for any LOR is then given by equation 3.3, even if detectors i and j lie in different rings.

If there are C counts per LOR then σ_{direct}, the average fractional standard deviation for direct estimates of η_{utvj}, is given by

$$\sigma_{direct}^{2} = \frac{1}{C} \tag{3.6}$$

provided we can ignore the effect of variations in the efficiencies themselves. If the fan-sum approximation is also good, the fractional standard deviation for the fan-sum estimate would be given by the fractional standard deviation of the product of 2 fan-sums:

$$\sigma_{fan-sum}^{2} = \frac{1}{MC} + \frac{1}{MC} \tag{3.7}$$

The improvement in the standard deviation $I_{fan-sum}$ is the ratio of these:

$$I_{fan-sum}^{2} = \frac{\sigma_{direct}^{2}}{\sigma_{fan-sum}^{2}} = \frac{M}{2} \tag{3.8}$$

So roughly speaking the improvement increases with the square root of the number of elements in the fan-sum, and there is a net gain if 3 or more elements are used.

As shown by Hoffman *et al* (1989), the right hand side of equation 3.5 does not have to be approximately equal to M. It merely has to be approximately equal to a constant, which is the case for any circularly symmetric normalisation source (e.g. a uniform cylinder) centred on the axis of the scanner. The effect of using an off-axis cylinder for fan-sum normalisation has been investigated by Chatziioannou (1996). Chesler and Stearns (1990) describe a simple geometric correction for off-centre cylinder data, together with an iterative deconvolution approach for reducing any bias due to the fan-sum approximation.

3.2.2.2.The single-plane method due to Casey

Define a group A of M detectors i in ring u, which are all in coincidence with all M detectors j in a second group B lying in ring v (see figure 3.2). If the positions of A and B are constrained such that all LORs between all their constituent detectors intersect the source, then M takes its largest value $R/2$ if A and B are diametrically opposed to each other.

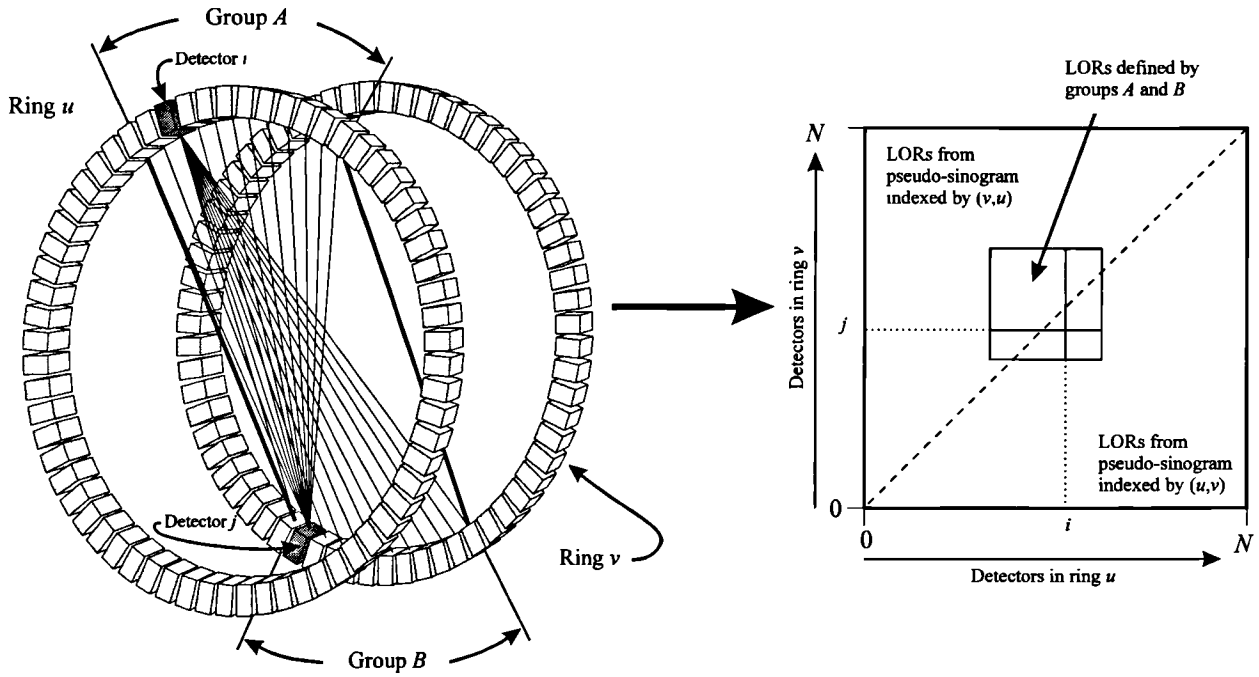

Figure 3.2. The single-plane Casey method in 3D.
To obtain a variance-reduced estimate of the efficiency of the LOR joining detectors i and j, the product of the mean values of the LORs in each of the two LOR fans shown is calculated, and divided by the mean value of all possible LORs between detectors in groups A and B. For ease of implementation, the data from each pair of complimentary pseudo-sinograms are rebinned into a separate histogram where data elements are plotted as a function of detector j in ring v and detector i in ring u (as opposed to sinogram space, where they are plotted as a function of projection angle and radial position). In histogram space, fan-sums may be calculated as sums of elements lying on lines parallel to one of the axes, and the LORs joining all detectors in a pair of groups of equal size are defined by a square.

The following argument closely follows that given by Defrise *et al* (1991), although they did not explicitly consider the possibility of using Casey's method to obtain efficiencies for cross-plane LORs:

Summing equation (3.3) over j in B and dividing by M gives:

$$\varepsilon_{ui}\frac{1}{M}\sum_{j\in B}\varepsilon_{vj}=\frac{1}{M}\sum_{j\in B}\eta_{uivj} \tag{3.9}$$

Define a mean detector efficiency $<\varepsilon>_B$ for group B and a mean "fan LOR sensitivity" $<\eta>_{uiB}$ as follows:

$$<\varepsilon>_B=\frac{1}{M}\sum_{j\in B}\varepsilon_{vj} \quad , \quad <\eta>_{uiB}=\frac{1}{M}\sum_{j\in B}\eta_{uivj} \tag{3.10}$$

Defining $<\varepsilon>_A$ and $<\eta>_{vjA}$ in a similar way gives rise to the following:

$$\varepsilon_{ui}=\frac{<\eta>_{uiB}}{<\varepsilon>_B} \text{ for all } i\in A, \text{ and } \varepsilon_{vj}=\frac{<\eta>_{vjA}}{<\varepsilon>_A} \text{ for all } j\in B \tag{3.11}$$

If a mean "block LOR sensitivity" $<\eta>_{AB}$ is defined as follows:

$$<\eta>_{AB}=\frac{1}{M}\sum_{i\in A}<\eta>_{uiB} \tag{3.12}$$

and it is noted that $<\eta>_{AB}=<\varepsilon>_A<\varepsilon>_B$ then:

$$\eta_{uivj}=\varepsilon_{ui}\varepsilon_{vj}=\frac{(<\eta>_{uiB})}{<\varepsilon>_B}\cdot\frac{(<\eta>_{vjA})}{<\varepsilon>_A}=\frac{(<\eta>_{uiB})(<\eta>_{vjA})}{(<\eta>_{AB})} \tag{3.13}$$

where the quantities in parentheses are easily obtainable from experimentally acquired data. A and B only define a portion of the LORs between rings u and v - the others may be obtained by rotating A and B around the scanner axis.

This method is exact, in that its accuracy is not sensitive to changes in the detector efficiencies. However, it does not yield the detector efficiencies themselves, and so cannot be used outside of the illuminated FOV. It should also be noted that the source must illuminate all LORs uniformly or the terms defined by equations 3.10, 3.11 and 3.12 will not be interpretable as mean efficiencies or sensitivities. However, if the source illumination varies in a known systematic way (as a uniform cylinder does, for example), it may be possible to

modify each projection appropriately to simulate a uniform source prior to calculation. LORs not illuminated by the normalisation source may then be normalised using the fan-sum approach.

3.2.2.3. Extended version of the single-plane method due to Defrise

Defrise *et al* take equation 3.11 and calculate an exact expression for $<\varepsilon>_A$. Having done this, it is then possible to calculate ε_{ui} for each detector and, as in the fan-sum method, generate LOR efficiencies from the products of the detector efficiencies. The argument proceeds as follows:

The detector ring is divided into an even number G of groups containing M detectors each. Each detector is in coincidence with $2K$ +1 other detectors and all of the corresponding LORs must be uniformly illuminated. The group A (where $A = 0, \ldots, G\text{-}1$) denotes detectors with indices i such that $AM <= i < AM + M$. Let the group size M be such that a group A is in coincidence with 3 opposing groups, which will be the case if $2M <= K$. Since $<\eta>_{AB} = <\varepsilon>_A <\varepsilon>_B$ it can be shown that:

$$<\varepsilon>_A = \left(<\eta>_{A,A+G/2} \prod_{k=0}^{G/2-1} \frac{<\eta>_{A+k,A+k+G/2}}{<\eta>_{A+k+1,A+k+G/2}} \right)^{1/2} \tag{3.14}$$

and the ε_{ui} can be obtained from equation 3.11:

$$\varepsilon_{ui} = \frac{1}{3} \sum_{q=-1}^{1} \frac{<\eta>_{ui,(A+G/2+q)}}{<\varepsilon>_{A+G/2+q}} \tag{3.15}$$

This is the original Defrise method. For an ECAT 951R, $N = 512$ and there are 192 detectors in coincidence with any given detector, so $K<96$. Since M must be a factor of N, then for the original Defrise method the maximum value for M corresponds to just 32 detectors, and much of the acquired data is not used in the estimate of $<\varepsilon>_A$. It is possible to extend this method to use more of the acquired data. The expression $<\eta>_{AB}$ represents the mean value of LORs residing in a diamond in sinogram space. The series $<\eta>_{A+k,A+k+G/2}$ represents mean LORs in a centrally placed column of diamonds in sinogram space and the product term in

equation 3.14 represents the ratio of the product of this series with those of one of its neighbours (see figure 3.3).

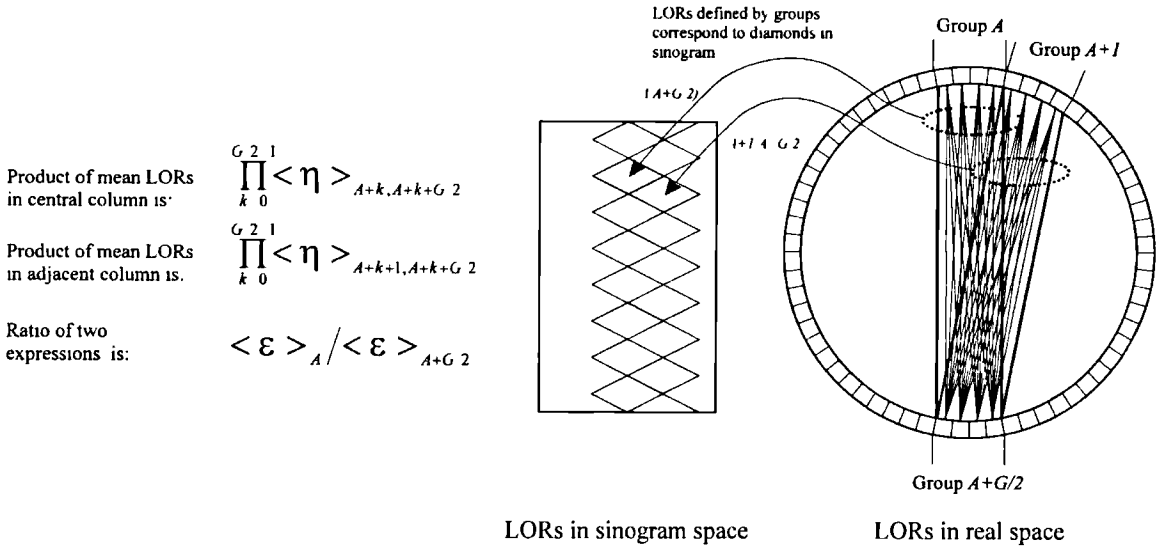

Figure 3.3. Elements of the single-plane Defrise method.

A second estimate for $<\varepsilon>_A$ may therefore be obtained by considering the product of the mean LORs from the central column with those from its other neighbour. This increases the amount of data used in the estimate of $<\varepsilon>_A$ by 50%. Reducing the group size M enables us to use even more of the data to obtain further estimates of $<\varepsilon>_A$. These two extensions to the Defrise method can result in significant improvements in performance with respect to noise in the normalisation data (see section 3.4.1 below).

The extended version of the Defrise method developed here may formally be written as follows:

The group size M is defined such that a group A is in coincidence with T opposing groups, where T is odd. This is true if $((T+1)/2)M <= K$. We then obtain a new version of equation 3.14:

$$<\varepsilon>_A = \frac{1}{T-1}\sum_{p=S}^{S-1}\left(<\eta>_{A,A+G/2}\prod_{k=0}^{G/2-1}\frac{<\eta>_{A+k,A+k+G/2-p}}{<\eta>_{A+k+1,A+k+G/2-p}}\right)^{1/2} \qquad (3.16)$$

where $S = (T-1)/2$.

Also,

$$\varepsilon_{ui} = \frac{1}{T}\sum_{q=-S}^{S}\frac{\langle \eta \rangle_{ui,(A+G\ 2+q)}}{\langle \varepsilon \rangle_{A+G\ 2+q}} \tag{3.17}$$

In fact, it is possible to average over U fan-sums where $U <= (2K+1)/M$.

3.2.2.4. The Fully-3D methods

Extension of the methods above to include cross-plane data is straightforward. The detector groups are defined in an identical manner to the single-plane versions, except that they are allowed to include detectors from all rings. For example, the fan-sum method can be extended as follows:

Given a detector i in ring u, define a group A consisting of adjacent rows of $M <= R$ consecutive detectors from all P rings, indexed by v and j such that

$0 < v <= P$, and

$i + N/2 - M/2 <= j < i + N/2 + M/2$ (see figure 3.4)

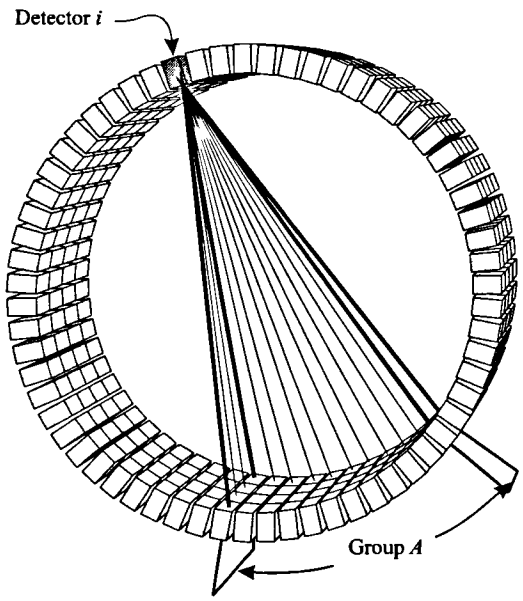

Figure 3.4. LORs in a 3D fan-sum.
The bold lines represent the extent of the fan.

Equation 3.4 then becomes

$$\varepsilon_{ut} = \frac{\left(\varepsilon_{ut}\sum_{v\in A}\sum_{j\in A}\varepsilon_{vj}\right)}{\sum_{v\in A}\sum_{j\in A}\varepsilon_{vj}} \tag{3.18}$$

and the argument proceeds as for the single-plane algorithm. The improvement in fractional standard deviation using this method compared to the single-plane fan-sum method can be derived from equation 3.8:

$$\frac{I_{SP-fansum}^{\ 2}}{I_{3D-fansum}^{\ 2}} = P \tag{3.19}$$

Analogous extensions can be made to the Casey and extended Defrise methods, and the six algorithms and their properties are summarised in Table 3.1.

Name	Abbreviation	References	LOR or detector efficiencies	Accuracy with noise-free data	Region of validity
Single-plane fan-sum	SP-FS	2D - Hoffman *et al* (1989), 3D - Casey *et al* (1995)	Detector	Approx.	Entire FOV
Single-plane extended Defrise	SP-ED	Defrise *et al* (1991), Badawi *et al* (1998)	Detector	Exact	Entire FOV
Single-plane Casey	SP-C	2D - Casey and Hoffman (1986), 3D - Badawi *et al* (1998)	LORs	Exact	Illuminated FOV only
Fully-3D fan-sum	3D-FS	Stazyk *et al* (1994)	Detector	Approx.	Entire FOV
Fully-3D extended Defrise	3D-ED	Badawi *et al* (1998)	Detector	Exact	Entire FOV
Fully-3D Casey	3D-C	Badawi *et al* (1998)	LORs	Exact	Illuminated FOV only

Table 3.1. The six normalisation algorithms and their properties.

3.3. Comparative assessment methods

In this section experiments will be described which are intended to answer the following questions:

- How do the various algorithms perform with noise-free normalisation data, and in particular, what is the effect of the fan-sum approximation on normalisation accuracy?
- Does the performance of the algorithms depend on the distribution of crystal efficiencies (i.e. the "gantry set-up")?
- How do the algorithms perform with noisy normalisation data? Do the 3D methods out-perform the SP methods in practice?
- How do the algorithms compare when different normalisation sources are used?
- What is the effect of using different normalisation sources on reconstructed image uniformity?

3.3.1. Normalisation scheme, reconstruction and assessment methods

Data was normalised according to the scheme shown in figure 3.5, for which the following terms are defined :

- S_{Tg}, the dataset to be normalised (the "target dataset");
- S_e, the dataset from which the detector efficiencies are calculated, and
- S_N, the fully normalised dataset.

Corrections for all normalisation components apart from crystal efficiency and, where appropriate, for scatter, were performed using the methods described in chapter 4.

If S_e and S_{Tg} are the same, then all the elements of the normalised sinogram, S_N , will be equal to unity apart from the effects of statistical noise and inaccuracies in the normalisation procedure. The performance of the normalisation algorithms was assessed by examining the standard deviation (SD) of the elements of S_N. Low-frequency features in the S_N were assessed by calculating the SD of the sinogram elements after an 8x8 element running mean smooth.

The 20 cm cylinder data (normalised in various ways described below) were reconstructed using the Byars Consulting implementation of the 3D-RP algorithm with a filter cut-off at the Nyquist frequency for the initial 2D reconstruction and a generalised Colsher filter for the 3D reconstruction. The reconstructed voxel dimensions were 2 mm x 2 mm transaxially, and 3.5 mm axially.

The reconstructed images were assessed by placing a large (radius 8 cm) circular region of interest (ROI) on the centre of the cylinder and calculating the SD of the elements before and after the application of spatial smoothing. The smoothing was performed using a Gaussian kernel with a full-width half-maximum (FWHM) of 12 mm. In these assessments, only the central 27 out of a possible 31 image planes were included, as the reconstructed image SNR is approximately uniform everywhere except in the end-planes, where it is significantly reduced.

While the uniformity measures used here are not particularly sensitive to the radial artefacts reported by other workers (e.g. Bailey *et al* 1996), it will be shown in the following chapter that such artefacts are usually introduced by poor corrections for other normalisation components, rather than random crystal efficiency variations.

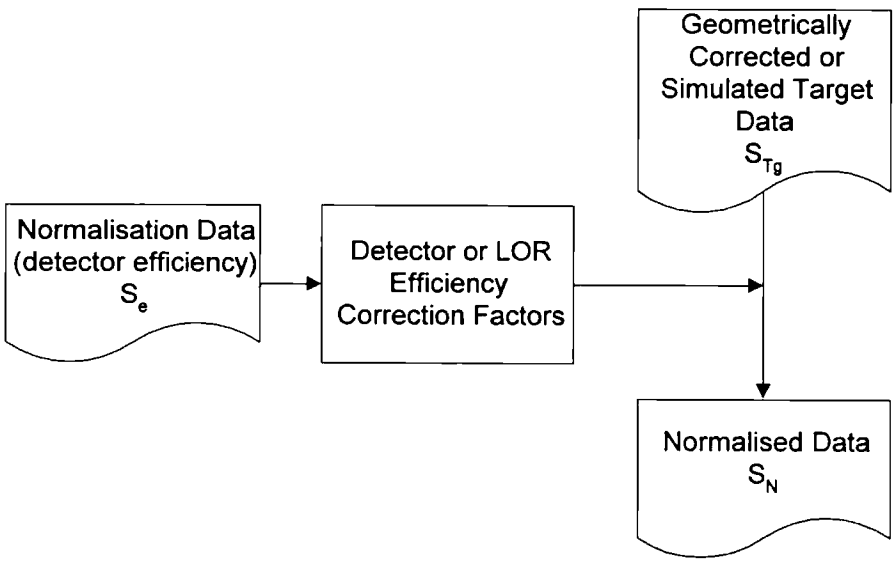

Figure 3.5. Normalisation scheme.

3.3.2. Crystal efficiency simulation

The following expression was used to generate realistic sets of crystal efficiencies ε_{ui}:

$$\varepsilon_{ui} = (1 + BF_{\text{int}(1+(u\ D)\bullet\text{int}(i\ D))})(1 + CG_{Nu+i}) \qquad (3.18)$$

where F and G are Gaussian deviates with unit variance and a mean of zero (indexed such that there is a unique sample for each block and crystal respectively). B accounts for the magnitude of the variation in the block efficiency, C accounts for the magnitude of the variation in the crystal efficiency, D is the number of crystals along one side of a block detector, N is the number of crystals per ring, u is the crystal ring index (ranging from 0 to P-1, P being the number of crystal rings) and i is the detector index (ranging from 0 to N-1). Unlike the simulation used by Defrise *et al* (1991), there is no term describing the variation of crystal efficiency across a block, because this is computed separately (see section 4.3.2.1). The magnitudes of B and C were set to 0.04 and 0.09 respectively after examination of data obtained using a scanning line source as described below. Both simulated crystal efficiency datasets, S_e, and simulated target datasets, S_{Tg}, were generated from the simulated scanner crystal efficiencies by the addition of Poisson noise according the scheme shown in figure 3.6. The simulated data does not contain scatter, and does not incorporate any geometric effects.

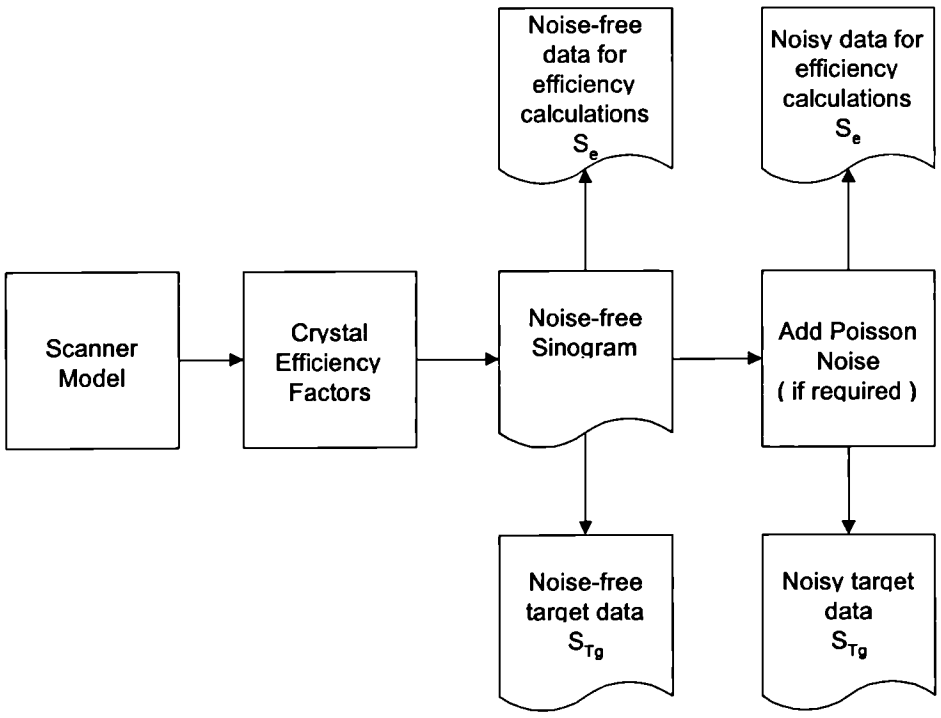

Figure 3.6. Generation of simulated data.

3.3.3. Acquisition of normalisation data

3.3.3.1.Scanning line-source data

The scanning line-source used in this work is the one described by Bailey *et al* (1996). It consists of a line-source holder which is attached to an aluminium rail. The holder has a tapped screw-thread which is coupled to a piece of steel studding which runs the length of the apparatus. In operation the studding is rotated by a 12V DC motor, and this drives the source holder along at a rate of 5mm/min. At each end of the rail there are limit switches which when depressed reverse the direction of operation of the DC motor. These limit switches are positioned so that they can be activated by the approaching source-holder to allow continuous back-and-forth operation. The entire gantry may be rotated about a central support, which has a fitting compatible with the head-holding device located at the end of the patient bed. The holder is designed to contain line-sources of the same dimensions as those used for transmission scanning in the CTI ECAT 95x series of scanners. In this work a spent transmission source from a 951R scanner was used.

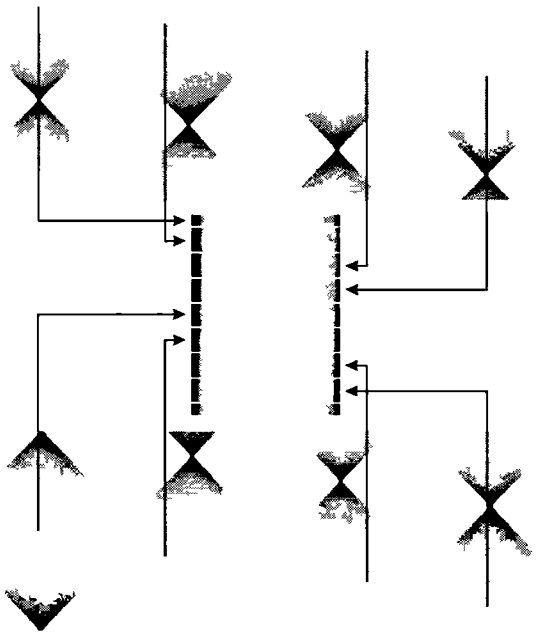

Figure 3.7. Formation of a composite sinogram from a series of line-source acquisitions.

A series of 8 scanning line-source acquisitions at evenly spaced angular positions was performed. Each acquisition at each position lasted approximately 13 hours and consisted of four passes of the line source, which contained 3.5 MBq of activity. A composite sinogram

was then created by extracting the 12.5% of LORs most nearly normal to the plane of motion of the scanning line-source from each acquired dataset, and combining them into one sinogram, as illustrated in figure 3.7. The data was corrected for the sinusoidal variation in the path-length of the line-source across the LORs as a function of projection angle within each angular line-source position. The central 162 (out of a possible 192) elements in each projection of the resultant composite sinogram were uniformly illuminated. Each of these elements contained approximately 275 counts.

3.3.3.2.Rotating line-source data

Rotating line-source data was acquired using the mechanism used for transmission scanning. This consists of three source holders equally spaced on a circle of radius 35 cm aligned with the centre of the scanner gantry. When not in use the sources reside just outside the FOV. When activated they are driven into the FOV where they rotate at a speed of approximately 10 rpm. For the normalisation acquisition the three transmission sources were replaced with spent sources each containing 1.5 MBq of ^{68}Ge. A fully 3D blank scan was then acquired over a 22 hour period. A total of 2.9 x 10^9 counts were acquired, giving a mean of 159 counts per LOR at the centre of the FOV and 228 counts per LOR across the entire FOV.

The prime cause of the variation in the number of counts per LOR with radial position in this type of acquisition is the fact that the rotating rods spend more time traversing LORs at the edge of the FOV than they do LORs in the centre. This phenomenon has been described as "rod-dwell" and has been addressed by several workers in the context of simultaneous emission-transmission scanning (e.g. Luk *et al* 1995) as well as normalisation (Casey *et al* 1995). The data was corrected for rod-dwell exactly as described by Casey *et al* (1995), with the exception that correction for radial changes in LOR thickness was not applied (see section 4.1.1). Visual inspection of the resultant sinograms showed that the sources do not rotate about the exact centre of the FOV, resulting in an asymmetry in illumination which was minimal in the centre but quite marked at the extreme edges of the FOV.

3.3.3.3. 20 cm cylinder data

A very low-variance acquisition of a uniform 20 cm cylinder was obtained by repeatedly filling the phantom with an aqueous solution of ^{18}F and scanning it after accurately placing it

in the centre of the FOV. A total of 9.4 x 10^9 counts were acquired in 16 separate acquisitions with a total acquisition time of approximately 24 hours. Attenuation correction factors were obtained from a 4-hour 2D mode "post-injection" transmission scan (Hooper *et al* 1996), and contamination arising from the retracted transmission rod sources was corrected for by subtracting an appropriately scaled low-variance 3D emission acquisition of the cold phantom with the rod sources and septa in the retracted position.

3.3.4. Optimisation of group size for extended Defrise algorithms.

The group size *M* for the extended Defrise algorithm was optimised for situations similar to rotating line-source normalisation, scanning line-source normalisation and 20 cm cylinder normalisation, by means of a simulation and by examining acquired data. In the simulation a single noise-free target dataset S_{Tg} was created, and a series of simulated efficiency datasets S_e were derived from it by adding Poisson noise such that the noise varied from the equivalent of 1 count per LOR to the equivalent of 256 counts per LOR. Efficiency factors were then calculated from the noisy S_e varying both the group size M and the number of illuminated elements in each projection. The resulting efficiencies where then used to normalise the noise-free S_{Tg}. The SDs of the elements in the resultant normalised S_N were calculated and compared. The optimum values for M obtained in this way were then tested using real data and some changes made. Results for the extended method with the optimum choice of M were compared with the results for the original Defrise method.

3.3.5. Assessment of the effect of gantry set-up and of the accuracy of the algorithms with noise-free data

If the accuracy of the algorithms are significantly affected by the distribution of scanner crystal efficiencies ('gantry set-up'), the results of an assessment using relatively few acquisitions on just one camera would be of limited value. In order to investigate the effect of gantry set-up on the accuracy of the algorithms, and to investigate the performance of the approximate algorithms with noise-free data, 50 noise-free target datasets S_{Tg} , and 50 noise-free efficiency datasets S_e, corresponding to 50 different gantry set-ups were simulated. These were used as input to the normalisation scheme shown in figure 3.5, using all six algorithms. The effective number of "illuminated LORs" in the S_e was set to 192, 162 and 66. The SDs of the elements in the resulting normalised S_N were then calculated. SDs were

evaluated over the whole dataset, except for SP-C and 3D-C where the evaluation was confined to the accurately normalised region. The mean of these SD values gives an indication of the systematic accuracy of the normalisation algorithms, and the variation of the values over the 50 simulated datasets gives an indication of the effect of gantry set-up.

3.3.6. Assessment of the effectiveness of the algorithms in terms of variance reduction

The effectiveness of the algorithms in terms of variance reduction can be measured by quantifying their accuracy as a function of number of counts acquired for the S_e. To achieve this, the following experiment was performed:

A 20 cm cylinder uniformly filled with ^{68}Ge such that there were 4.4 MBq of activity in the FOV was placed in the centre of the scanner gantry. A series of 3D scans of the cylinder was acquired, with acquisition times varying from 150 seconds (4.6 x10^6 total counts, 1.1 counts per illuminated LOR) to 4800 seconds (147 x10^6 total counts, 35.1 counts per illuminated LOR). A series of S_e containing decreasing levels of statistical noise were generated by correcting these acquisitions for all normalisation components except crystal efficiency using the methods described in chapter 4. A 19200 second cylinder scan was also acquired (approx. 140 counts per illuminated LOR) and corrected to create a low-noise S_{Tg}. Finally attenuation correction factors were obtained by means of a 2D-mode post-injection transmission scan.

Crystal efficiencies were calculated from the noisy S_e and applied to the low-noise S_{Tg}. The exact algorithms require that the LORs in the S_e be uniformly illuminated within the source boundary, so a radial profile correction (generated by means of the algorithm described in section 4.3.2.4) was applied to flatten the profile of each projection prior to the intrinsic efficiency calculation. This same correction was also applied to the normalised scans prior to sinogram uniformity assessment.

In order to examine the effect of noise in the S_e on reconstructed images, a series of scans generated as above (but without the final profile flattening) were normalised using SP-C and 3D-FS. The scans were reconstructed and the resultant images assessed for uniformity. The 19200 second scan was also reconstructed without crystal efficiency normalisation and the image uniformity assessed.

3.3.7. Assessment of the effects of using different sources for the calculation of crystal efficiencies.

The purpose of this experiment was to examine the systematic accuracy of the normalisation algorithms when using a range of normalisation sources, and to determine if the use of different normalisation sources affects reconstructed image uniformity.

Three target datasets S_{Tg} were derived from the datasets described in section 3.3.3 by correcting them for all normalisation components except crystal efficiency, and in the case of the 20 cm cylinder data, for scatter, using the methods described in chapter 4.

The normalisation scheme shown in figure 3.5 was applied, with S_e set to S_{Tg} , using all six algorithms, and sinogram uniformity assessments performed as described in section 3.3.2. To avoid edge effects at the radial extremes of the illuminated regions, the rotating line-source data was assessed over the central 176 elements, the scanning line-source data was assessed over the central 160 elements and the cylinder data was assessed over the central 56 elements.

Since with real data the target datasets S_{Tg} are not noise-free a simulation was performed to ascertain the effect of noise in the S_{Tg} on the assessment of sinogram uniformity. Ten datasets were generated with Poisson noise equivalent to that obtained in the scanning line source acquisition (effectively 275 counts per LOR). These datasets were processed and analysed in the same way as the real data.

Additionally, the 20 cm cylinder data was reconstructed after self-normalisation with each of the algorithms and the uniformity of the 6 resultant images assessed. The data was also reconstructed using efficiencies derived from the scanning and rotating line-sources. This final comparison was limited by the fact that while the cylinder and rotating line-source data were acquired approximately contemporaneously, the scanning line-source data was acquired some 15 months previously.

3.4. Results

3.4.1. Optimum group sizes for extended Defrise algorithm

Table 3.2 shows the optimum values of M, T and U as defined in section 3.2.3.3 above for the various normalisation sources. It was found that the extended Defrise algorithm is particularly sensitive to the non-uniformities in LOR illumination found at the edges of the cylinder and rotating line-source data. This necessitated a reduction in the number of elements used.

Source	group size M	number of opposing groups T	number of fan-sums U
20 cm cylinder (48 elements)	4	11	12
scanning line-source (162 elements)	16	9	10
rotating line-sources (176 elements)	16	9	11

Table 3.2. Optimum parameters for extended Defrise algorithm for various normalisation source configurations.

Figure 3.8 shows a plot of the % SD of the normalised sinogram elements obtained by using the optimal single-plane extended method compared to the original method as a function of counts per LOR when 192 elements are illuminated. The fractional improvement is a roughly constant 50%. For situations equivalent to normalisation using 20 cm cylinder data, the gain is reduced to around 30%.

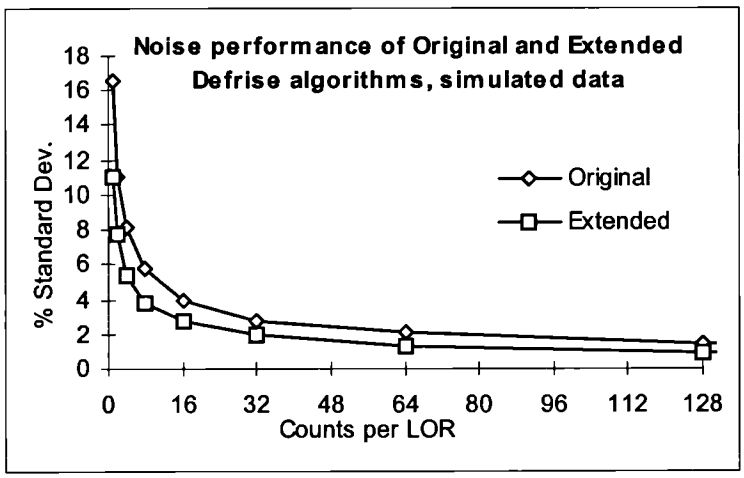

Figure 3.8. Performance of original and extended Defrise algorithms. Standard deviation of sinogram elements as a function of counts/LOR for simulated data normalised by the single-plane original and extended Defrise methods. 192 elements were used in the calculations.

3.4.2. The effect of gantry set-up and the accuracy of the algorithms with noise-free data

For the exact algorithms (SP-C, SP-ED, 3D-C and 3D-ED), the elements of the S_N datasets are all equal to unity to within 0.003% for all gantry set-ups (table 3.3). This error is attributable to the 2-byte storage format used. This result confirms that the algorithms have been implemented correctly. The SDs for the approximate algorithms (SP-FS and 3D-FS) are much larger. The magnitude of the mean SDs are a measure of the bias introduced by the fan-sum approximation (equation 3.5).

The accuracy of the fan-sum method improves with increasing fan size. This is because the fan-sum approximation improves with increasing numbers of elements, and by using data from all rings instead of just one, the mean SD using noise-free data is halved. The mean SDs range from roughly 0.5 to 2%, and the standard deviation of measurements lie between roughly 10% and 20% of these values. So whilst the accuracy of the normalisation does depend to some extent on the particular gantry set-up, the small magnitude of the non-uniformities found indicate that the results obtained elsewhere in this study using real data are valid without having to be repeated for many different gantry set-ups.

Algorithm	% standard dev., 192 elements	% standard dev., 162 elements	% standard dev., 66 elements
SP-FS	1.01 +/- 0.15	1.14 +/- 0.16	2.15 +/- 0.22
SP-ED	<0.003	<0.003	<0.003
SP-C	<0.003	<0.003	<0.003
3D-FS	0.46 +/- 0.10	0.50 +/- 0.11	1.12 +/- 0.23
3D-ED	<0.003	<0.003	<0.003
3D-C	<0.003	<0.003	<0.003

Table 3.3. Percentage SDs of normalised sinogram elements, averaged over 50 different gantry set-ups.
Simulated data was used. Quoted errors are +/- 1 standard deviation from the mean values.

3.4.3. Performance as a function of noise in the efficiency dataset

Figure 3.9 shows the percentage SD of normalised sinogram elements from the 20 cm cylinder data as a function of counts per crystal in the normalisation data. 10,000 counts per crystal is equivalent to about 19 counts per illuminated LOR or an acquisition total of approximately 8×10^7 counts.

The best-performing SP and 3D algorithms in the region of 500 to 10,000 counts per crystal are SP-FS and 3D-ED. Curves for these two algorithms are plotted in figure 3.10. It can be seen that the 3D method is consistently more accurate over the entire range, and the SP method is significantly less accurate at low count levels.

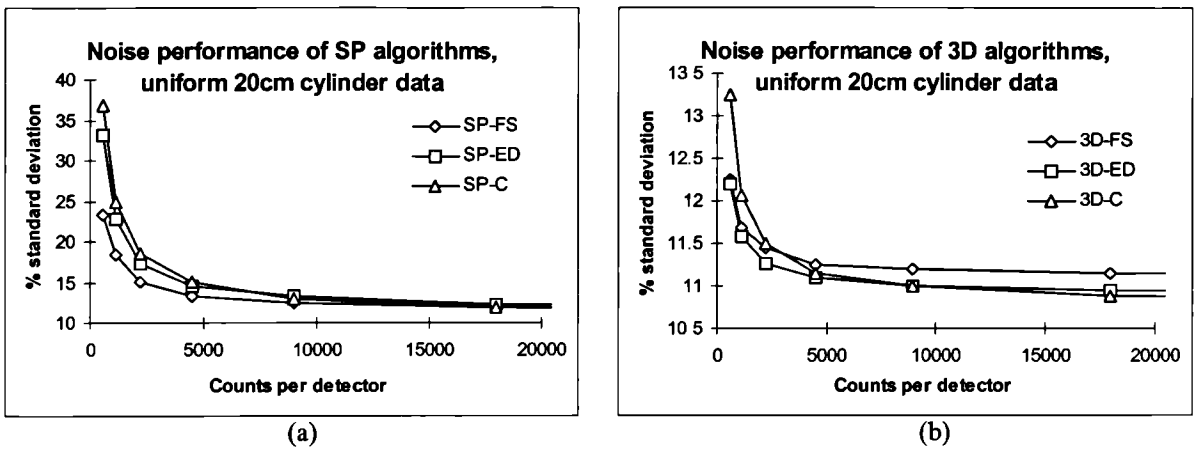

(a) (b)

Figure 3.9. Noise performance of SP and 3D algorithms.
Percentage SDs of normalised sinogram elements as a function of counts per LOR in the crystal efficiency dataset. Results obtained using real data. a) Single-plane algorithms. b) 3D algorithms. Note the 3-fold reduction in scale for the 3D case.

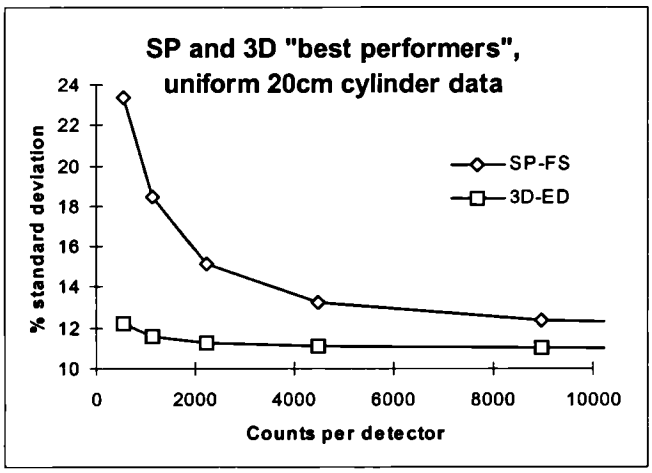

Figure 3.10. Noise performance of best performing algorithms.
Percentage SDs of normalised sinogram elements as a function of counts per LOR in the crystal efficiency dataset. Results for the best performing SP and 3D algorithms. Similar results are obtained with 500 counts per crystal and 10,000 counts per crystal for the 3D and SP algorithms respectively.

Figure 3.11 illustrates the quality of normalisation achievable with an acquisition time of 5 minutes (about 1,250 counts per crystal or 2-3 counts per LOR in the S_e). The data normalised by the SP algorithm shows clear discontinuities, whereas the 3D algorithm produces a much more uniform normalisation.

Figure 3.12 shows the mean %SDs of reconstructed images generated from the series of scans normalised using 3D-FS and SP-C, together with the value obtained for the image reconstructed from the 19,200 second scan without crystal efficiency normalisation. The 3D method gives a good normalisation with as few as 5 million total counts (about 600 counts per crystal or 1.2 counts per illuminated LOR), whereas similar uniformity is only obtained using SP-C when around 80 million counts are acquired. If more than 250 million counts are acquired, the extra accuracy afforded by the exact nature of the SP-C algorithm becomes evident. It is interesting to note that the change in uniformity between the well-normalised and un-normalised images is quite small. The effect of normalisation in realistic imaging situations is examined in more detail in chapter 4.

The effectiveness of the normalisation with 3D-FS and 5 million counts in total can be seen in figure 3.13, which shows reconstructed images of the low-noise 19,200 second acquisition summed over all axial planes. There is little to choose between the image normalised with data containing 5 million count and the image normalised with data containing 590 million counts (~140 counts per illuminated LOR).

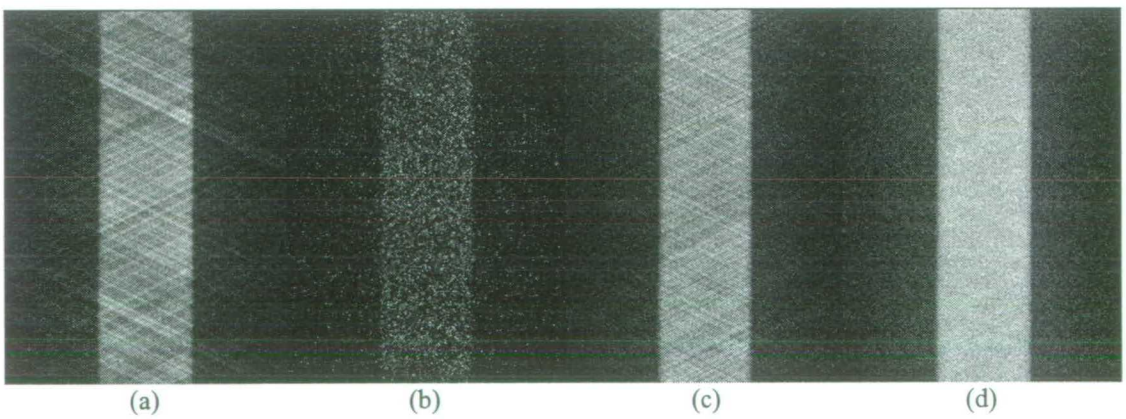

Figure 3.11. Sinogram data acquired using a 20 cm cylinder - effectiveness of SP and 3D normalisation.
(a) 20 cm cylinder, unprocessed, scan time 19200 sec. ~140 counts per illuminated LOR .
(b) 20 cm cylinder, unprocessed, scan time 300 sec. ~2-3 counts per illuminated LOR.
(c) Scan "a" normalised with efficiency data derived from scan "b" and single-plane fan sum algorithm
(d) Scan "a" normalised with efficiency data derived from scan "b" and 3D fan sum algorithm

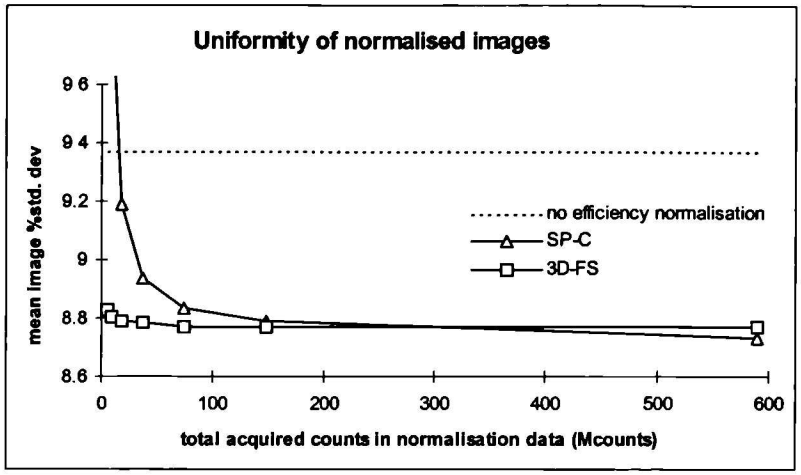

Figure 3.12. Uniformity of normalised images.
Mean %SDs of reconstructed images normalised using cylinder data with total acquired counts shown. The emission data contained 5.9 x10^8 counts prior to scatter correction.

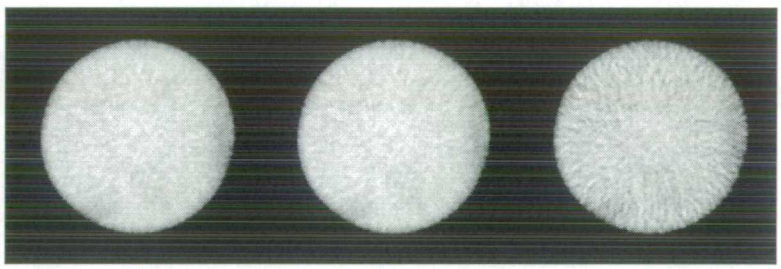

(a) (b) (c)

Figure 3.13. Images (summed over all reconstructed planes) of 19,200 second 20cm cylinder acquisition.
There are ~ 140 counts per illuminated LOR. The zero-point of the grey-scale has been set to 50% of the image maximum.
(a) Self-normalised with 3D-FS
(b) Normalised with 3D-FS, 5 million total counts (~ 1.2 counts per illuminated LOR) in normalisation data
(c) No crystal efficiency normalisation

3.4.4. The effects of using different sources for the calculation of crystal efficiencies.

Sinogram uniformities for the various sources are shown in table 3.4. Corresponding results for the simulated data are shown in table 3.5. The simulation results indicate that SD measurements themselves are not subject to significant error due to statistical noise.

Since the statistical noise properties of each acquisition are very different, direct comparison of the results between sources is difficult. However, the relative performance of the different algorithms can be examined. For the cylinder data, the exact algorithms show significantly improved performance compared to the approximate methods. For the sources which cover a

large part of the FOV, the difference between the exact and approximate algorithms is reduced. In part this is because the fan-sum approximation becomes more accurate as more elements are included in the fan. However, the performance of the Defrise algorithm appears particularly degraded in the two line-source acquisitions, where it performs no better than the fan-sum method. The reason for this is not clear.

algorithm	%SD, cylinder source. 56 elements used	%SD after smoothing, cylinder source. 56 elements used.	%SD, scanning line-source 160 elements used	%SD after smoothing, scanning line-source. 160 elements used	% SD, rotating line-source. 176 elements used	%SD after smoothing, rotating line-source. 176 elements used
SP-FS	5.53	3.81	7.33	2.80	7.69	2.30
SP-ED	4.24	1.35	7.36	2.86	7.69	2.29
SP-C	3.95	0.55	6.68	1.38	7.23	1.05
3D-FS	4.77	2.67	6.99	2.03	7.43	1.46
3D-ED	4.00	0.62	6.98	2.02	7.42	1.43
3D-C	3.97	0.58	6.93	1.96	7.35	1.34

Table 3.4. Percentage SDs of normalised sinogram elements using different normalisation sources.
The smoothing kernel was an 8x8 element box-car. Caution should be exercised when comparing the results for different sources as the number of counts per LOR are different. 20 cm cylinder data: ~1400 counts per illuminated LOR, ranging from ~1330 in centre of FOV to ~1430 at edge of cylinder.
Scanning line-source data: ~275 counts per illuminated LOR.
Rotating line-source data: ~228 counts per illuminated LOR, ranging from ~160 in centre of FOV to ~390 at edge.

algorithm	%SD,162 elements used	%SD after smoothing,162 elements used
SP-FS	6.365 +/- 0.002	2.058 +/- 0.004
SP-ED	6.077 +/- 0.001	0.798 +/- 0.002
SP-C	5.967 +/- 0.002	0.702 +/- 0.002
3D-FS	6.263 +/- 0.002	1.099 +/- 0.001
3D-ED	6.039 +/- 0.002	0.760 +/- 0.001
3D-C	6.037 +/- 0.001	0.758 +/- 0.001

Table 3.5. Percentage SDs of normalised sinogram elements using simulated data.
Data has the same statistical quality as the scanning line source data in table 3.4.
Results are an average and SD of 10 runs.

In these favourable signal-to-noise environments, SP-C remains the best performer overall, while SP-FS with cylinder data, which is the configuration most closely resembling common current practice, is the least accurate method.

Reconstructed images of the 20 cm cylinder data self-normalised with the different algorithms and summed over all axial planes are shown in figure 3.14. The image uniformities are shown in table 3.6. The variations in uniformity between the data processed with the different algorithms is less than for the sinogram data, and SP-ED rather than SP-FS appears to be the least accurate. The fact that after smoothing, the fan-sum methods and SP-

ED produce images which are less uniform than those reconstructed from the un-normalised data suggests that some of the low-frequency bias noted in the sinogram data may be propagating into the reconstructed images.

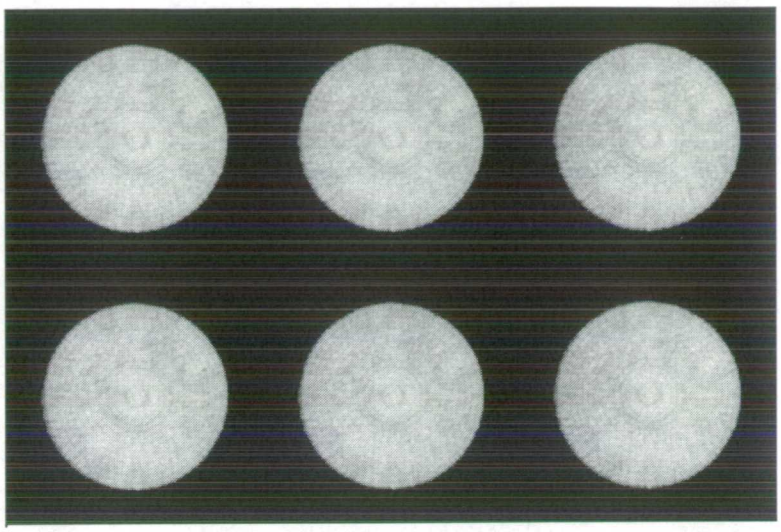

Figure 3.14. Axially summed images of a 20 cm cylinder self normalised using different algorithms.
Total of 9.4 x 10^9 counts acquired. Measured attenuation correction, zero-point of grey-scale at 80% of image maximum.
Top row: SP-C, SP-ED, SP-FS
Bottom row: 3D-C, 3D-ED, 3D-FS
A low-intensity high-frequency concentric ring artefact is visible in all the images, the origin of which is unknown.

algorithm	image %standard dev., ROI radius = 8cm	image %standard dev., ROI radius = 8cm (smoothed)
SP-FS	3.23	1.65
SP-ED	3.51	2.08
SP-C	3.10	1.40
3D-FS	3.23	1.65
3D-ED	3.09	1.44
3D-C	3.11	1.40
No efficiency correction	4.28	1.39

Table 3.6. Uniformity of reconstructed images normalised by different methods. Uniformity was calculated before and after spatial smoothing with a Gaussian kernel of 12 mm FWHM.

Figure 3.15 shows summed images derived from cylinder data normalised by the different sources, together with an image of the data without normalisation for crystal efficiency. Table 3.7 shows the calculated image uniformities. It can be seen that there is increase noise in the image normalised using the scanning line-source data, but this can be attributed to the fact that the cylinder and scanning line-source data are not contemporaneous. In fact, given

the fact that there was a time delay of 15 months separating the two acquisitions (during which time 3 block detectors were replaced), it is perhaps surprising that the non-uniformities are so small. The similar uniformities seen after smoothing suggest that none of the sources are introducing significant low-frequency bias.

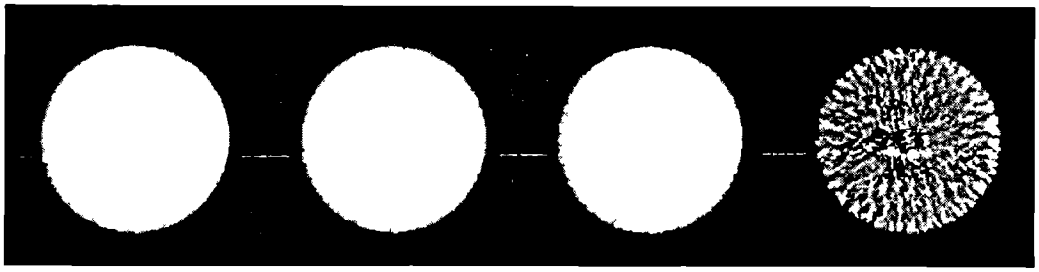

(a) (b) (c) (d)

Figure 3.15. Summed images reconstructed from 20 cm cylinder data normalised using different sources
The zero-point of the grey-scale has been set to 80% of the image maximum.
(a) Self-normalised
(b) Crystal efficiency factors calculated from rotating line-source data
(c) Crystal efficiency factors calculated from non-contemporaneous scanning line-source data
(d) No crystal efficiency normalisation.
It should be noted that the grey-scale windowing of the images has been chosen to greatly exaggerate the non-uniformities, which are actually quite difficult to visualise if the grey-scale is allowed to cover the entire dynamic range (see figure 4.32).

source	image %SD, ROI radius = 8cm	image %SD after smoothing, ROI radius = 8cm
20 cm cylinder	3.10	1.40
rotating line sources	3.12	1.44
scanning line source	3.29	1.47
No efficiency correction	4.28	1.39

Table 3.7. Uniformity of reconstructed images normalised using different sources. Uniformity was calculated before and after spatial smoothing with a Gaussian kernel of 12 mm FWHM. The normalisation algorithm was SP-C.

3.5. Discussion

A clear result from this work is that the amount of data required for accurate calculation of crystal efficiencies can be significantly reduced by using 3D rather than SP methods. In fact, good normalisations can be achieved from datasets containing as few as 5 million counts (600 counts per crystal). Such datasets can easily be acquired in a few minutes. Of all the algorithms, the single-plane Casey algorithm is the most accurate, provided the normalisation data is of sufficiently high statistical quality.

Another result of this assessment is that the improvements in image uniformity from normalisation of random variations in crystal efficiency are actually quite small (just 1% decrease in %SD for the 9.4 x 10^9 count uniform cylinder image), and while the efficiencies do vary with time, the effect of this drift on reconstructed images is also quite small. This suggests that on an ECAT 951R scanner routine normalisations need not be carried out very frequently.

It is also interesting to note that there is very little difference in the accuracy of the results obtained from any of the normalisation sources examined. Other observers (e.g. Kinahan *et al* 1996, Bailey *et al* 1996, Oakes *et al* 1998) have consistently noted the presence of circular "saw-tooth" artefacts in normalised images of uniform cylinders, which are not seen in this work. This is due to the fact that the component-based model used here splits the intrinsic detector efficiencies themselves into random and systematic components, and a new method for correcting for the systematic component has been implemented. This technique is discussed in detail in the following chapter, and is the main reason why the accuracy of the crystal efficiency normalisations shown here are effectively independent of the normalisation source used.

A factor governing the practicability of any technique is its ease of implementation and use. The 3D Casey method is significantly more CPU-intensive than 3D-FS or 3D-ED, taking approximately 1 hour on a SUN Sparc-20 clone driven by a 125 MHz HyperSparc processor (Axil Computer Inc., Santa Clara, CA, USA). 3D-ED is in fact not much more demanding than 3D-FS, and both algorithms complete in a few minutes. 3D-FS is significantly easier to implement than either 3D-ED or 3D-C. All algorithms may be used with a cylindrical

normalisation source, if where necessary the profiles are modified to provide uniform illumination.

3.6. References

DL Bailey, DW Townsend, PE Kinahan, S Grootoonk and T Jones 1996 "An investigation of factors affecting detector and geometric correction in normalisation of 3-D PET data." *IEEE Trans. Nucl. Sci.* **43**(6), 3300-3307

ME Casey and R Nutt 1986 "A Multicrystal Two Dimensional BGO Detector System For Positron Emission Tomography" *IEEE Trans. Nucl. Sci.* **33**(1),460-463

ME Casey and EJ Hoffman 1986 "Quantitation in Positron Emission Computed Tomography: 7. A technique to reduce noise in accidental coincidence measurements and coincidence efficiency calibration" *J. Comput Assist. Tomogr.* **10**,845-850

ME Casey, H Gadagkar and D Newport 1995 "A component based method for normalisation in volume PET" Proceedings of the 3rd International Meeting on Fully Three-Dimensional Image Reconstruction in Radiology and Nuclear Medicine, Aix-les-Bains, France.

SR Cherry, M Dahlbom and E J Hoffman 1991 "3D PET using a conventional multislice tomograph without septa" *J. Comput. Assist. Tomogr.* **15** 655-68

A-X F Chatziioannou 1996, "Measurements and Calculations Towards Quantitative Whole Body PET Imaging", PhD Thesis, UCLA.

DA Chesler and CW Stearns 1990, "Calibration of Detector Sensitivity in Positron Cameras" *IEEE Trans. Nuc. Sci.* **37**(2), 768-772

M Dahlbom and EJ Hoffman 1988 "An evaluation of a two-dimensional array detector for high-resolution PET" *IEEE Trans. Med. Imag.* **7**(4), 264-272

M Defrise, DW Townsend, D Bailey, A Geissbuhler, C Michel and T Jones 1991 "A normalisation technique for 3D PET data", *Phys. Med. Biol.* **36**, 939-952

EJ Hoffman, TM Guerrero, G Germano, WM Digby and M Dahlbom 1989 "PET system calibrations and corrections for quantitative and spatially accurate images" *IEEE Trans. Nuc. Sci.* **36**(1), 1108-1112

PK Hooper, SR Meikle, S Eberl and MJ Fulham 1996 "Validation of Postinjection Transmission Measurements for Attenuation Correction in Neurological FDG-PET Studies" *J. Nucl. Med.* **37**(1) 128-136

J-S Liow and SC Strother 1995 "Normalisation using rotating rods for 3D PET" Proceedings of the 3rd International Meeting on Fully Three-Dimensional Image Reconstruction in Radiology and Nuclear Medicine, Aix-les-Bains, France.

PE Kinahan, DW Townsend, DL Bailey, D Sashin, F Jadali and MA Mintun 1995 "Efficiency Normalisation Techniques for 3D PET Data" *IEEE Nuclear Science symposium and Medical Imaging Conference Record* **2**, 1021-1025 IEEE cat. 95CH35898

WK Luk, WD Digby WF Jones and ME Casey 1995 "An Analysis of Correction Methods for Emission Contamination in PET Postinjection Transmission Measurement" *IEEE Trans. Nuc. Sci.* **42**(6), 2303-2308

T R Oakes, V Sossi and T J Ruth 1998 "Normalization for 3D PET with a low-scatter planar source and measured geometric factors" *Phys. Med. Biol.* **43**(4) *To appear.*

JM Ollinger 1995 "Detector efficiency and Compton scatter in fully 3D PET" *IEEE Trans. Nuc. Sci.* **42**(4) 1168-1173

MW Stazyk, V Sossi, KR Buckley and TJ Ruth 1994 "Normalisation measurement in septa-less PET cameras" *J. Nucl. Med.* **35**(5) 41P

CW Stearns 1995 "Scatter correction method for 3D PET using 2D fitted Gaussian functions" *J. Nucl. Med.* **36**(5) 105P

4. Component-based Normalisation in 3D PET

4.1. Introduction

4.1.1. A synthesised model for component-based normalisation

In the previous chapter the requirement for normalisation in PET was explained, and the concept of a component-based normalisation technique introduced. The process of dividing normalisation coefficients into "geometric" and "efficiency" components was first implemented by Hoffman *et al* (1989), and was further refined by Casey *et al* (1995) and Ollinger (1995). A synthesis of models used in these papers yields the following expression for the activity within an LOR in a PET study:

$$A_{uivj} \propto \left(\left[C(prompt)_{uivj} - C(random)_{uivj} \right] NC(true)_{uivj} - \left[C(scatter)_{uivj} \right] NC(scatter)_{uivj} \right) \cdot att_{uivj} \cdot dt_{uivj} \qquad (4.1)$$

where A_{uivj} is the activity concentration within the volume defined by the LOR joining the detectors i in ring u and j in ring v, $C(prompt)_{uivj}$, $C(randoms)_{uivj}$ and $C(scatter)_{uivj}$ are the prompt, random and scattered coincidence count-rates respectively, $NC(true)_{uivj}$ and $NC(scatter)_{uivj}$ are the normalisation coefficients for true and scattered coincidences, att_{uivj} is the attenuation correction factor and dt_{uivj} is the dead-time correction factor. $C(prompt)_{uivj}$, $C(randoms)_{uivj}$ and att_{uivj} are assumed to be accurately measurable for each acquisition. If quantitative images are desired, then accurate estimates of the scatter distribution, the NCs for true and scattered coincidences and the dead-time correction factors have to be obtained and applied to the data.

As discussed in section 1.6.4, there are many algorithms for estimating the scatter component in a 3D acquisition. Ollinger (1995) uses a model-based scatter correction algorithm. In this method, the number of single-scatter events in an LOR are estimated from the emission and attenuation data by applying the Klein-Nishina formula. Multiple scatters are then modelled by convolving the single-scatter distribution with a suitable multiple-scatter kernel. Since the emission data contains scatter the correction must be applied iteratively. A similar algorithm, due to Watson (1996) has been implemented on many commercially available cameras. This

algorithm ignores events arising from photons which have undergone more than one scatter prior to detection.

In the synthesised model the NCs are broken down into 4 components which may be written:

$$NC_{uivj} = \varepsilon_{ui}\varepsilon_{vj}d_{uvrk}f_{uv}g_{uvr} \tag{4.2}$$

where the ε_{ui} are the "intrinsic crystal efficiencies", the g_{uvr} are the "radial geometric profile" factors, the f_{uv} are the "plane-efficiency" factors and the d_{uvrk} are the "crystal interference" factors. r is the radial position of a given LOR and k is an index describing the relative position of the crystals in an LOR with respect to their block detectors.

The intrinsic crystal efficiencies relate to the average sensitivity of each crystal relative to the others - as discussed in chapter 3 they are dependent on, for example, the gains on the relevant detector PMTs, the quality of each scintillation crystal and in particular, the relative position of the crystals within each block detector. The radial geometric profile describes the systematic variation in LOR efficiency with radial position in a particular projection. This effect is due to, for example, changes in the effective crystal depth due to the changing mean angle of incidence of photons on the crystal face. Some authors also include the change in LOR width as the radius increases in the geometric profile - however, this is a matter of implementation as other workers account for this effect during reconstruction. The radial geometric profile is modulated by the relative position of the crystals in the block detectors. If there are D crystals on each side of a block detector, then there are D possible combinations of detector block-postion for each radial position. These modulating factors have become known as the "crystal interference" factors. This is illustrated in figure 4.1, where a possible mechanism for crystal interference is described. It is important to note that the crystal interference effect is separate to the systematic variation in intrinsic crystal efficiency with position within the block detector.

Finally, the "plane-efficiency" factors describe the relative mean efficiency of the LORs in each sinogram compared to the others. These factors account for any changes of LOR efficiency with mean photon incidence angle in the axial direction, and also the mean

changes in crystal efficiency due to the axial position of the crystals within their block detectors.

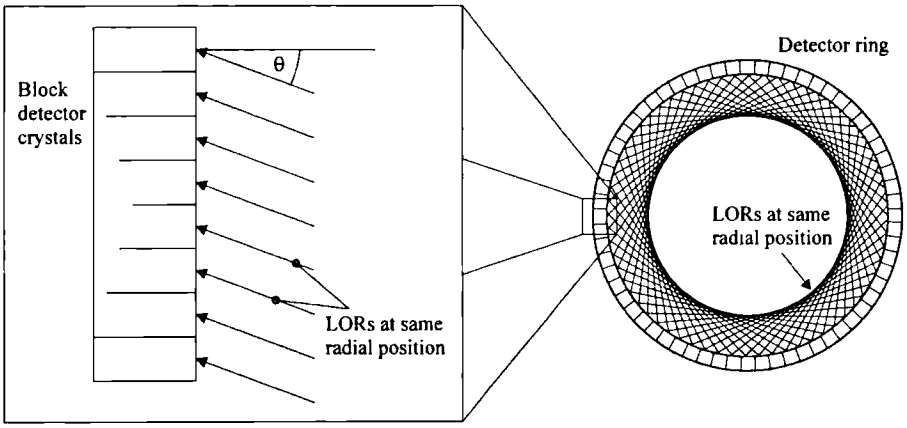

Figure 4.1. LORs at the same radial position θ.
The degree of inter-crystal penetration may vary systematically with both θ and the position of the crystal in the block detector, giving rise to a "crystal interference" effect.

This model for NCs can equally be applied to both true and scattered coincidences. However, in practice there are significant difficulties in obtaining appropriate correction factors for scatter, and the following assumptions are made:

$$\varepsilon^{s}_{ui} = \varepsilon^{t}_{ui} \tag{4.3}$$

$$d^{s}_{ui} = g^{s}_{ui} = 1 \tag{4.4}$$

where the superscripts *s* and *t* refer to scattered and true coincidences respectively. In other words, the assumptions are made that:

1) there is no difference between efficiency factors for scatter and true coincidences, and

2) there are no geometric effects for scatter.

f^{s}_{uv} is only obtainable if a model-based scatter correction technique is used. In this case it is a scaling factor describing the difference between the predicted and measured scatter in the region outside of the object in each sinogram. However, Ollinger (1995) reports that f^{s}_{uv} and f^{t}_{uv} are the same to within 2%, so if an alternative scatter correction method is used, they may be set equal without introducing significant error.

Finally, a conventional dead-time model may be applied by measuring the singles rates for each block-detector, and applying a correction for losses in each crystal based on fitted values for the paralysing and non-paralysing components of dead-time. The fitted values for each crystal may be calculated from a series of ε_{ui} obtained by filling a uniform 20 cm cylinder with ^{18}F or ^{11}C and repeatedly scanning it as the activity decays.

4.1.2. Critique of the synthesised normalisation model

4.1.2.1.Scatter correction

The model-based scatter correction algorithms of Ollinger and Watson have been implemented widely since their publication. The main difficulty which currently exists with these algorithms relates to scatter arising from events occurring outside of the FOV, which cannot be estimated from the emission data, which necessarily lies within the FOV. Model-based scatter corrections are also extremely computationally intensive. For simple objects which do not occupy a large portion of the FOV, good results can also be obtained using a Gaussian fit scatter-correction method (e.g. Stearns *et al* 1995), where Gaussian curves are fitted to the scatter tails in each projection and used to estimate the proportion of scattered events within the distribution of true coincidences. While such methods can give rise to problems in larger and more complex objects, in the context of an investigation into normalisation they have the advantage of being computationally cheap and simple to integrate with a normalisation protocol.

4.1.2.2.Time-window alignment

A further normalisation component which can be accounted for is "time-window alignment". As described in section 1.5.4, absorption events occurring in different detectors must occur within a period of twice the coincidence resolving time in order to be counted as coincidence events. For this process to work effectively, timing signals between the detectors must be accurately synchronised. On the ECAT 951R, there are measurable variations in synchronicity between timing signals for different block detectors (Watson, 1997). Time-window misalignment results in a reduction in the effective coincidence resolving time for true and scattered (but not random) coincidences for a given LOR, and a corresponding

reduction in efficiency. In this work a new component is therefore suggested for the normalisation model, which becomes

$$NC_{uivj} = \varepsilon_{ui}\varepsilon_{vj} d_{uvrk} f_{uv} g_{uvr} h_{(\mathrm{int}(1+u\ D))(\mathrm{int}(i\ D))(\mathrm{int}(1+v\ D))(\mathrm{int}(J\ D))} \qquad (4.5)$$

where h is the time-window alignment factor and D are the number of crystals along the side of a block detector. There is one factor for each possible combination of block detectors.

4.1.2.3.NCs for scattered coincidences

Since the energy spectrum for scattered photons is different to that of unscattered photons, we would not necessarily expect the intrinsic crystal efficiencies to be the same for both scattered and true coincidences. However, since there is no validated method for measuring the ε^{s}_{ui} , the assumption that they do not differ significantly from the values for true coincidences is difficult to avoid.

In the synthesised model, the assumption that there are no geometric effects for scatter is justified by arguing that scattered photons are incident on the detector faces with a wide range of angles, unlike trues, whose incidence angles are constrained by the position and width of the relevant LOR. Any geometric factors for scatter are therefore averaged over a large range of angles and can effectively be ignored. However, if the assumption is made that most scattered coincidences arise from scatter events which occur within the object being imaged (rather than for example, the camera gantry), then it follows that there are object-dependent constraints on the possible and likely angles of incidence for scattered photons on the detector faces. This points to a weakness in the assumption that the geometric and crystal interference factors for scattered coincidences may be set to unity, and may help to explain the difficulties which many workers have encountered when attempting to normalise non-radially symmetric distributions of activity, such as off-centre uniform cylinders (Bailey, 1997). In the future, the angle of incidence for scatter in a particular LOR arising from a particular source and scattering medium distribution could be calculated using a model-based scatter estimation algorithm, and appropriate correction factors applied to accurately account for the radial geometric profile and crystal interference effect for scattered coincidences. Unfortunately such a scheme has not been implemented here.

In this work it has been assumed that time-window alignment factors are the same for both trues and scatter. However, it is possible that time-of-flight effects may cause some small differences between the effect of time-window misalignment on true and scattered coincidences.

4.1.2.4.Dead-time correction

The use of a conventional dead-time model to correct for the mean reduction in efficiency of the crystals in a block-detector as the incident singles rate increases has a sound basis in physical reality, and is easily implementable on the ECAT 951R, since correction factors for each bucket are stored with the acquired data. However, the extension of such a scheme for correction for variations in the efficiencies of individual crystals within a block detector is somewhat problematic. Conventional dead-time correction models predict losses in counted events due to pulse pile-up. However, in a block-detector, there is also a mechanism for gain of events due to pulse pile-up. If two photons interact with a block detector at the same time, and the total energy deposited falls below the ULD, the two events will be counted as one (representing a loss for the crystals in which the photons where incident), which is highly likely to be mispositioned (representing a gain for a third crystal). This phenomenon has been examined in detail in 2D mode by Germano and Hoffman, 1990 and 1991. Ideally, all such events should be rejected, and in this case a conventional dead-time model operating on each crystal would be appropriate.

Simple corrections for the systematic variations of crystal efficiency within a block detector with count-rate may be obtained by treating them as a normalisation component rather than as a separate dead-time problem. The normalisation model now becomes:

$$NC_{uivj} - \varepsilon_{ui}\varepsilon_{vj}d_{uvrk}f_{uv}g_{uvr}h_{(\mathrm{int}(1+u\ D)\ (\mathrm{int}(i\ D))(\mathrm{int}(1+v\ D)\cdot(\mathrm{int}(j\ D))}b_{ui \bmod D}b_{vj \bmod D} \qquad (4.6)$$

where b_{uimodD} is a function describing the variation in crystal efficiency within a block detector as a function of count-rate. It incorporates count-rate dependent components from both the ε_{ui} and the f_{uv}. In this work b_{uimodD} will be referred to as the block-profile.

4.1.2.5.Variations in sensitivity within an LOR

An intrinsic assumption of the synthesised model is that the sensitivity of an LOR does not vary with the position along that LOR. This assumption has not been investigated in any rigorous way in this work. However, the sensitivity to true events along an LOR is constrained by the solid angle subtended by the most distant detector, which certainly changes with position. The solid angle subtended by the detector also affects sensitivity to scattered coincidences, although in this case the relevant angle is that subtended by the more distant detector at the point of scatter rather than at the point of annihilation.

4.1.3. Summary of chapter 4

In this chapter a brief validation of a Gaussian fit scatter correction algorithm for situations relevant to this study will be presented, and means for deriving the various normalisation components from a combination of low-scatter and scattering sources will be described. The normalisation components for an ECAT 951R scanner will then be characterised, and the importance of the various components in realistic imaging situations discussed.

4.2. The Gaussian fit scatter correction method for normalisation

4.2.1. Implementation

In PET, scattered coincidences are distributed across the entire FOV. In regions of the FOV which do not contain activity, there will be no true coincidences, and after randoms subtraction, only scatter will be measured. In the Gaussian fit scatter correction method, structural information gained from the regions which do not contain true events is used to estimate the scatter distribution in the regions which do. The key assumption which is made is that the scatter distribution in any single projection may be well modelled by a Gaussian curve. There is no physical justification for this assumption. However, the method appears to work reasonably well provided that:

1) The regions in each projection which contain only scatter are sufficiently large and contain data of sufficiently high statistical quality that the Gaussian fitting algorithm is reasonably stable

2) The activity distribution and attenuation characteristics of the object are such that the scatter distribution is only slowly changing.

Stearns (1995) fits a 2D Gaussian using data from the entire axial FOV. In this work, a 1D Gaussian is fitted to each projection. Prior to fitting, the projection data is smoothed in r, θ and φ. If the distribution of activity and attenuating medium is circularly symmetric about the axis of the scanner, the data may be averaged over all θ . In order to reduce the effects of discontinuities due to normalisation effects, corrections for detector efficiency and for variations in the plane efficiencies in the scatter regions are applied first. After smoothing, a scatter estimate is obtained by fitting Gaussian curves to each projection using the downhill simplex method as implemented by Press *et al* (1992). The normalisation corrections are then reversed prior to subtraction of the scatter estimate from the original data. This method fortuitously avoids assumption that the plane-efficiencies are the same for both true and scattered events, although the assumptions in equations 4.3 and 4.4 are still applied.

4.2.2. Validation of the Gaussian fit algorithm for use in normalisation

For normalisation purposes, an accurate scatter correction is required for a centrally placed uniform cylinder of activity only. This greatly simplifies the task of validating the accuracy

of the scatter correction method used, as complex source distributions need not be examined. However a complicating factor in the assessment is the existence of a hot-spot in the centre of the FOV which has been repeatedly found in reconstructions of uniform cylinders.

In order to examine the transaxial accuracy of the scatter correction, the very low-variance 20 cm cylinder acqusition described in section 3.3.3.3 (containing total of 9.4×10^9 counts) was used. In order to examine the axial accuracy of the scatter correction, a cylinder containing a central cylindrical insert of perspex and an aqueous solution of ^{18}F was placed in the FOV and scanned. Approximately 9×10^8 counts were acquired. To separate the problems of scatter correction accuracy and the central hot-spot, the cylinder was positioned so that its centre was 3.5 cm below the centre of the camera FOV. In both cases attenuation correction factors were obtained from a low-variance 2D mode simultaneous emission-transmission scan, and spill-over from the transmission rod sources was corrected for by subtracting an appropriately scaled low-variance 3D emission acquisition of the cold phantom with the rod sources and septa in the retracted position.

For each acquisition three reconstructions were performed as follows:
1) No scatter correction, full normalisation as described below.
2) Gaussian fit scatter correction, full normalisation as described below.
3) Model-based scatter correction as described by Ollinger (1995), full normalisation as described below.

In all cases geometric factors were obtained from the scanning line-source acquisition described in section 3.3.3.1. Reconstruction was performed using 3D-RP with a ramp filter cut-off at the Nyquist frequency for the initial 2D reconstruction and a generalised Colsher filter for the 3D reconstruction.

The reconstructed images of the uniform central cylinder were summed and radial profiles through the images plotted. For the off-centre phantom acquisitions, regions of interest (ROIs) were drawn in the cold and active parts of the reconstructed images as shown in figure 4.2. The centre of the FOV was avoided. The scatter fraction (the ratio of scattered counts to [true + scattered] counts) as a function of image plane was then obtained by

calculating ratios of the mean values within the ROIs in the cold and active parts of the phantom. The results are plotted in figure 4.3.

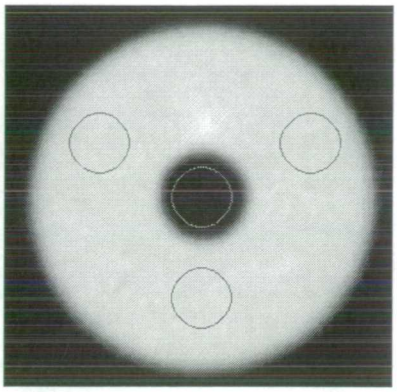

Figure 4.2. Position of ROIs for calculation of scatter fraction on image of off-centre cylinder with cold insert.
The hot-spot seen above the cold insert is located at the exact centre of the FOV. The ROIs have been deliberately positioned to avoid this hot-spot.

The reconstructed images of the uniform central cylinder (summed over all planes) are shown in figure 4.4, together with corresponding radial profiles. The central hot-spot is clearly visible, but apart from that the radial profiles of both scatter-corrected images are reasonably uniform. The non-scatter-corrected image shows a curved profile peaking in the centre.

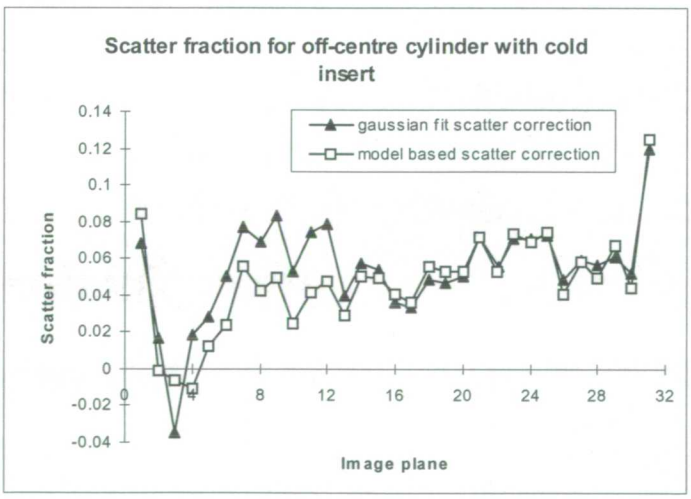

Figure 4.3. Residual scatter fractions for each image plane for off-centre cylinder with cold insert.
Scatter fractions obtained by calculating ratios of the mean values in the central cold region and the peripheral hot region of the phantom for data corrected using the model-based scatter correction and the Gaussian fit algorithm.

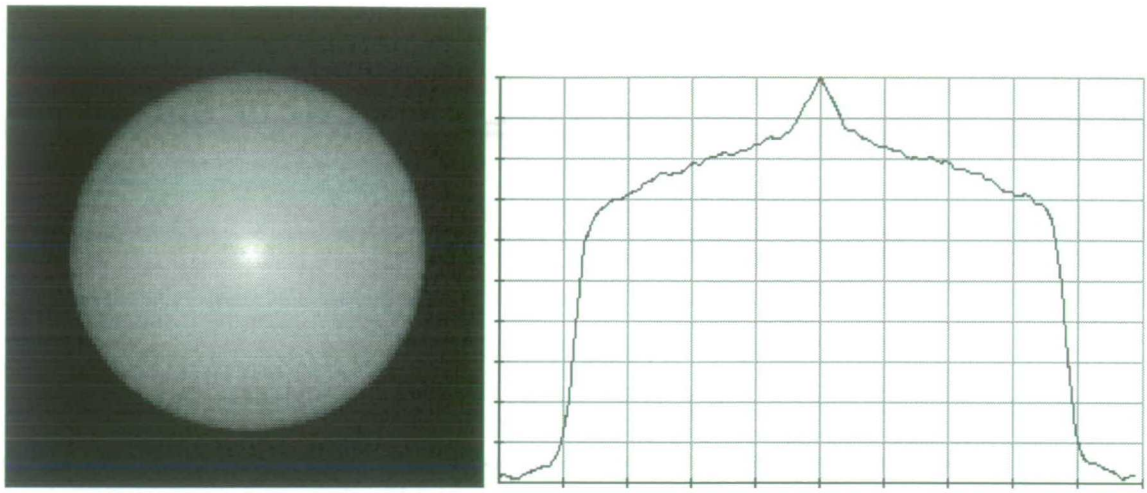

(a) Fully normalised as described below, but no scatter correction applied.

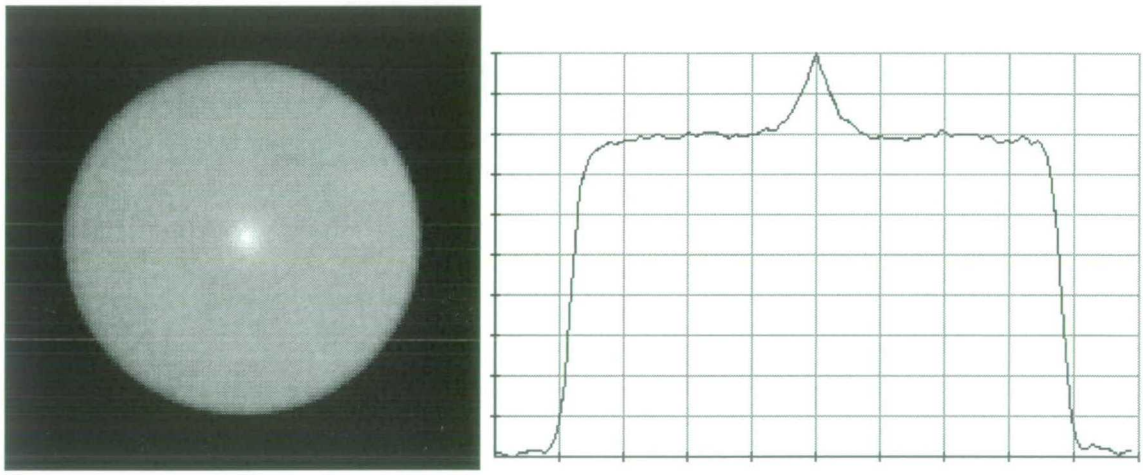

(b) Fully normalised as described below, with Gaussian fit scatter correction applied.

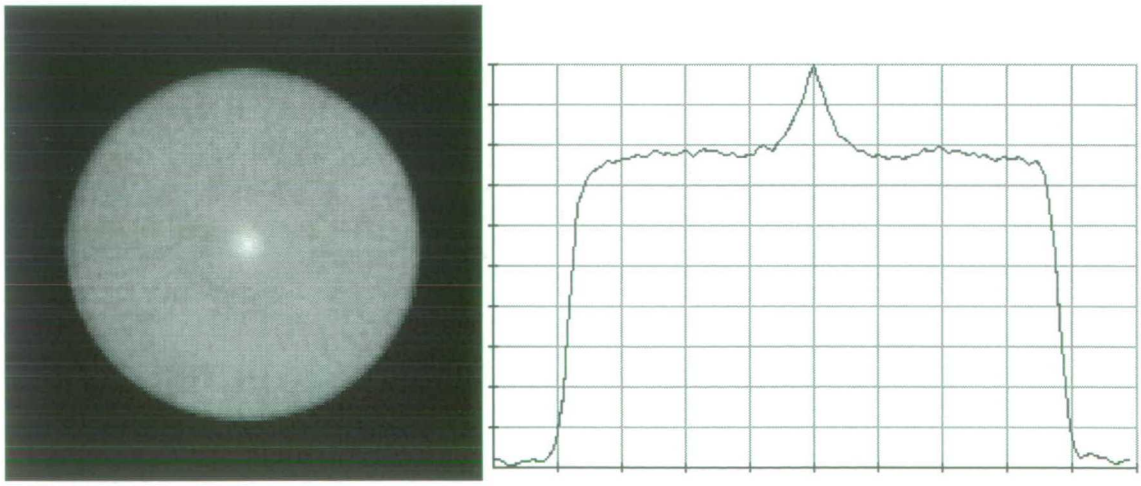

(c) Fully normalised as described below, model-based scatter correction (Ollinger's implementation) applied.

Figure 4.4. Summed images of and vertical profiles through central uniform cylinder.
Reconstructed with (a) no scatter correction, (b) Gaussian fit scatter correction and (c) model-based scatter correction. Zero-point of colour-scale set to 50% of image maximum. Apart from the central spike, the cylinder images are reasonably uniform in the radial direction. Interestingly, the central spike is less pronounced in the image which has not been scatter corrected.

For the non-scatter-corrected image of the off-centre phantom, the mean scatter fraction was 35%, whereas for the image corrected with the Gaussian fit algorithm, the mean scatter fraction was 5.7%. For the image corrected with the model-based algorithm, the ratio was 4.8%. As can be seen from figure 4.3, the results for the Gaussian fit algorithm are quite similar to those for the model-based algorithm, particularly for image planes 16-31. For both methods, the error increases significantly in the end planes. Summed images and axial profiles through the images of the off-centre phantom are shown in figure 4.5. The images have been reconstructed with a spatial offset, but the hot-spots seen are located at the centre of the scanner FOV.

These experiments show that for these simple objects, the Gaussian fit algorithm is not significantly less effective than a model-based scheme. The axial accuracy of both the scatter correction methods examined here is quite variable and this will have an impact on the accuracy of any plane-efficiency values derived from normalisation schemes which incorporate these methods.

Some preliminary conclusions may also be drawn regarding the cause of the central hot spot. In particular, if the central hot-spot were to be caused solely by inaccurate scatter correction, we would expect it to

(a) vary in nature depending on the scatter correction algorithm, and

(b) track the centre of the phantom, rather than the centre of the scanner FOV.

Since the hot-spot is not significantly affected by the choice of scatter-correction algorithm, and remains fixed in the centre of the FOV, other causes need to be examined. This matter is discussed further in section 4.5 below, where a hot-spot correction scheme is presented.

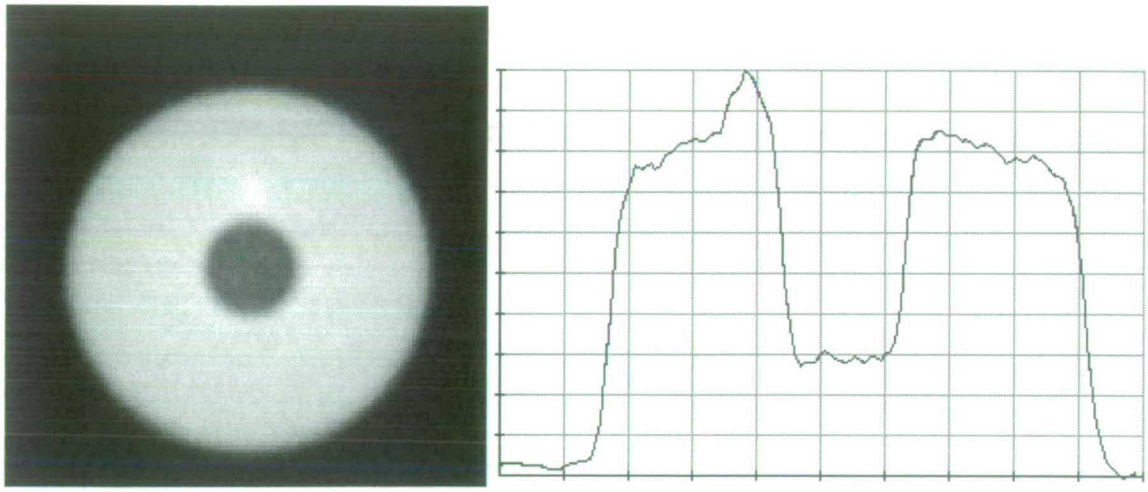

(a) Fully normalised as described below, but no scatter correction applied.

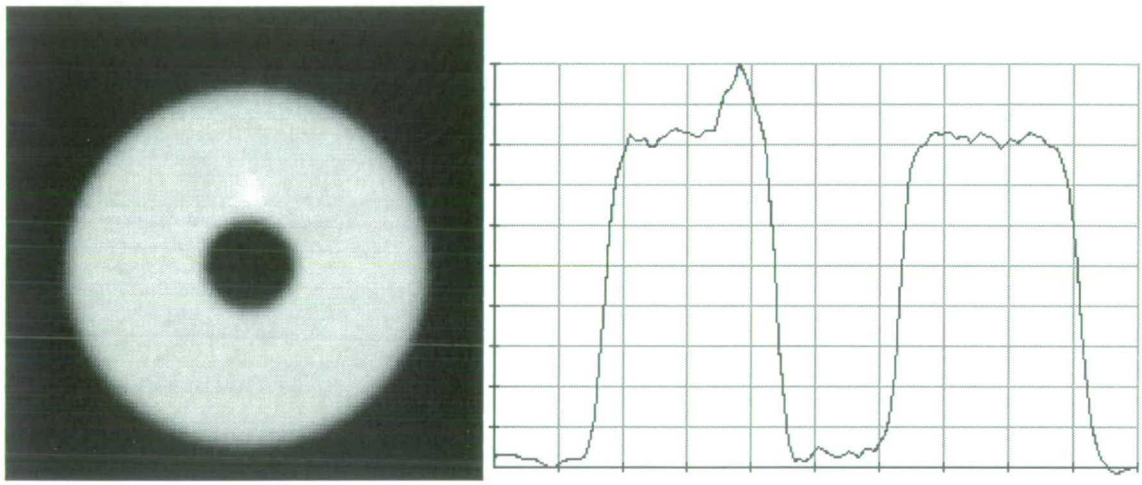

(b) Fully normalised as described below with Gaussian fit scatter correction applied.

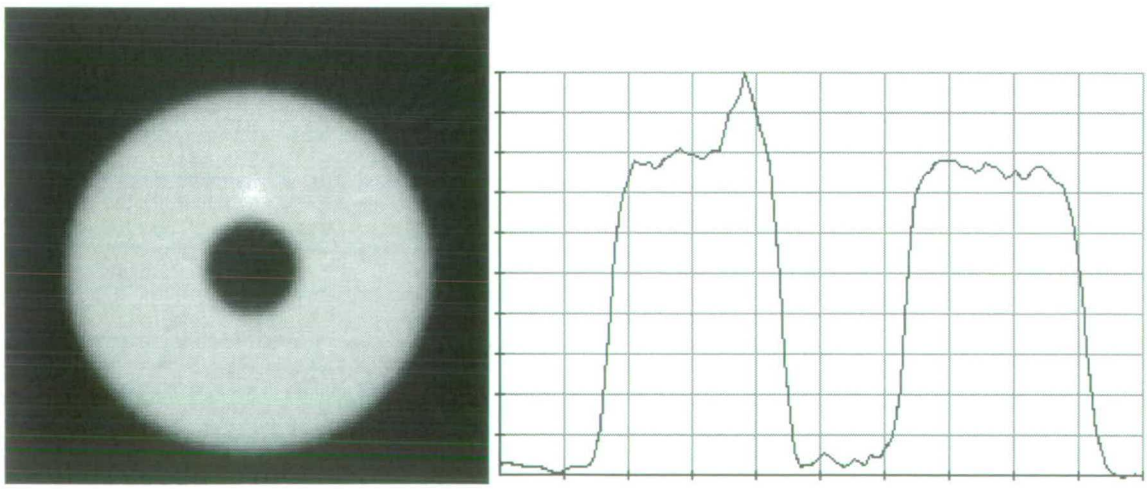

(c) Fully normalised as described below, model-based scatter correction (Ollinger's implementation) applied.

Figure 4.5. Summed images of and vertical profiles through off-centre cylinder with cold insert.
Reconstructed with (a) no scatter correction, (b) Gaussian fit scatter correction and (c) model-based scatter correction. Colour scale covers entire dynamic range. The hot-spot seen is located in the exact centre of the camera FOV. Both scatter correction methods are quite effective in reducing the apparent level of activity in the region of the cold insert. In the hot regions of the scatter-corrected images, the radial non-uniformity appears to be more marked than for the central cylinder data.

4.3. Methods for calculating normalisation components

As stated in equation 4.6, the normalisation model used in this work may be written:

$$NC_{uivj} = \varepsilon_{ui}\varepsilon_{vj}d_{uvrk}f_{uv}g_{uvr}h_{(\mathrm{int}(1+u\ D)\cdot(\mathrm{int}(i\ D))(\mathrm{int}(1+v\ D)\ (\mathrm{int}(j\ D))}b_{ui\bmod D}b_{vj\bmod D}$$

4.3.1. Count-rate dependent, variable and fixed components

Each component may be categorised as count-rate dependent, variable, or fixed. Count-rate dependent parameters must be calculated and applied to each acquisition together with a dead-time correction. Variable components change with time, as PMT gains drift, or block-detectors are changed, and should be measured as part of routine quality control. Fixed components are governed by the intrinsic geometry of the camera and need be measured only once after installation.

In the literature the intrinsic crystal efficiencies ε_{ui} and the plane efficiencies f_{uv} are considered to be variable, and the crystal interference factors d_{uvrk} and the radial geometric factors g_{uvr} are considered to be fixed. No data has been obtained to categorise the new timing component, $h_{(\mathrm{int}(1+u/D)\bullet(\mathrm{int}(i/D))\ (\mathrm{int}(1\ v/D)\bullet(\mathrm{int}(j\ D))}$ as variable or fixed. Given that the timing alignment is a function of the block circuitry, and block detectors are replaceable items, it is likely that the timing component should be considered as variable. However, a practical scheme for routinely obtaining time-alignment factors has not been developed in this work, so for simplicity they have been treated as fixed. The block-profile factors $b_{ui\mathrm{mod}D}$ are count-rate dependent.

4.3.2. Algorithms for calculating correction factors

Given an appropriate set of fully-3D normalisation sinograms, the various components discussed above may be calculated as follows:

4.3.2.1.Block-profile factors, $b_{ui \bmod D}$

The block-profile factors each contain a transaxial and an axial component. The transaxial components may be calculated from individual detector efficiency factors obtained from either a fan-sum or Defrise-type algorithm. They are given by :

$$b(trans)_{ui \bmod D} = \frac{\sum_{n\ 0}^{\frac{N}{D}\ 1} \varepsilon_{u,nD+i \bmod D}}{N/D} \qquad (4.7)$$

where N is the number of crystals in a ring and the ε_{ui} are the estimates of the detector efficiency factors. In practice, the transaxial components of the block-profile factors may be calculated from an initial estimate of the ε_{ui} calculated using an approximate method such as 3D-FS. Since the factors are calculated by averaging efficiencies from all around the ring, they are not significantly affected by the low-frequency errors associated with the fan-sum method. There is a different transaxial block-profile for each axial position in the block-detector (see section 4.5.2)

The axial components may be calculated by summing all the elements in each direct-plane (ring-difference = 0) sinogram and taking the ratio of each sum to the mean of all sums. The square-root of this ratio is the axial component of the block-profile for that particular axial detector position.

4.3.2.2.Intrinsic crystal efficiency factors, ε_{ui}

These may be calculated using any of the algorithms described in chapter 3. It should be noted, however, that the exact methods (i.e. the Casey or Defrise-type algorithms) should only be used after corrections for geometry and crystal interference have been applied, or biases may be introduced.

4.3.2.3.Plane efficiencies, f_{uv}

Estimates of the plane efficiencies f_{uv} are obtained by summing all the elements in each sinogram and taking the ratio of each sum to the mean of all sums. If the acceptance angle of

the scanner is large, it may be necessary to apply an analytical correction for the fact that cross-planes will see a thicker normalisation source than direct planes. The magnitude of these corrections for an ECAT 951 camera may be calculated as follows:

Consider a uniform source with constant linear attenuation coefficient μ, activity per unit volume ρ and diameter d (figure 4.6).

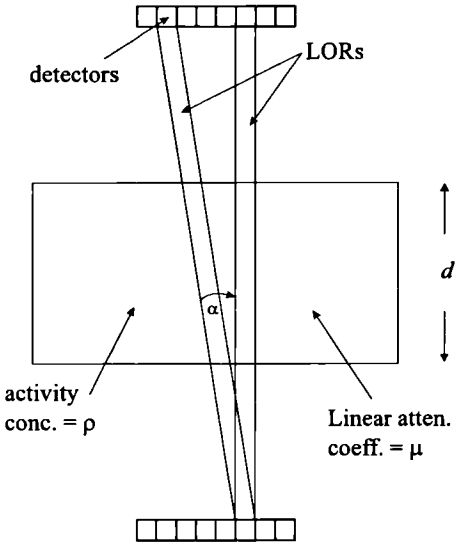

Figure 4.6. LORs crossing a uniform attenuating source

The activity a within an LOR of unit thickness normal to the source and in the transaxial centre of the scanner is just ρd. The attenuation b along the LOR is given by

$$b = e^{-\int_0^d \mu(x)dx} = e^{-\mu d} \tag{4.8}$$

and the flux f along the LOR becomes:

$$f = ae^{-\mu d} \tag{4.9}$$

Now consider an LOR at an angle α to the normal. The active volume within the LOR is constant, since while it becomes longer in proportion to $(\cos\alpha)^{-1}$, it becomes thinner in proportion to $\cos\alpha$. However, if the LOR width is corrected for during reconstruction the effective active volume may be written

$$a(\alpha) = a(\cos\alpha)^{-1} \tag{4.10}$$

and the attenuation factor becomes

$$b(\alpha) = e^{-\mu d(\cos\alpha)^{-1}} \tag{4.11}$$

which gives rise to a flux of

$$f(\alpha) = a(\cos\alpha)^{-1} e^{-\mu d(\cos\alpha)^{-1}} \tag{4.12}$$

The correction factor C(α) is just the ratio of the two fluxes:

$$C(\alpha) = e^{\mu d(1/\cos\alpha - 1)} \cos\alpha \tag{4.13}$$

For a central LOR of ring difference 15, with a 20cm uniform water-filled cylinder, we have:

$\mu = 0.095$ cm^{-1},
$d = 20$ cm,
$\alpha = 6.04$ degrees

This gives rise to a correction factor of 1.005. In practice, LORs of ring-difference greater than 11 are not used in the reconstruction, so that α becomes 4.54 degrees, and the correction factor 1.003.

LORs at the edge of the FOV in a cross-plane sinogram lie at a greater angle to the normal than those in the centre. For a 951 with ring difference 15, the maximum angle is 7.24 degrees, and for ring difference 11 it is just 5.44 degrees. In practice, therefore, these corrections are all less than 0.5% and can be ignored.

4.3.2.4.Radial geometric factors, g_{uvr}

The radial geometric factors g_{uvr} are estimated for each sinogram by summing the LORs at a given radial distance from the centre and calculating the ratio of each sum to the mean for that sinogram (Hoffman *et al* 1989).

4.3.2.5.Crystal interference factors, d_{uvrk}

The crystal interference pattern is accounted for by selectively sampling the sinogram columns used in the radial profile calculation (Casey *et al* 1995). If there are D crystals along the side of a block, then D profiles are generated, by summing LORs in every Dth projection. If exact methods (i.e. the Casey and Defrise-type algorithms) are to be used for the calculation of the crystal efficiency factors, the correction for the crystal interference effect

should be applied prior to their calculation. However in this situation, selective sampling will have the added effect of including the transaxial components of the block-profile (at the count-rate obtained from the normalisation source). This is undesirable because in this scheme the block-profile factors are applicable to scatter and the crystal interference factors are not. To avoid this, the block-profile factors should be calculated and corrected for prior to calculation of the crystal interference factors.

4.3.2.6.Time-window alignment factors, $h_{(\mathrm{int}(1+w/D)\bullet(\mathrm{int}(i/D))\,(\mathrm{int}(1+w/D)\bullet(\mathrm{int}(j/D))}$

Time-window alignment factors may be estimated by summing all the elements associated with each possible combination of block-detectors, and taking the ratio of each sum to the mean of all sums. If this process is carried out prior to correction for the intrinsic crystal efficiencies, then the time-window alignment factors will include the average efficiencies of each block-detector. This is unimportant for routine normalisation, but should be avoided when characterising the factors themselves. In this work provisional estimates of the intrinsic efficiencies were calculated and estimates of the mean block-detector efficiencies calculated from them. Mean block-detector efficiency correction factors were then applied prior to calculation of the time-alignment factors.

4.4. Computational and acquisition protocols

4.4.1. Calculation of fixed components d_{uvrk}, g_{uvr} and $h_{(\text{int}(1+u/D)\bullet(\text{int}(i/D))\ (\text{int}(1+v/D)\bullet(\text{int}(j/D))}$.

The fixed components must be calculated from an acquisition involving uniform illumination of a large portion of the FOV. In addition, the radial geometric and crystal interference factors should ideally be calculated from scatter-free data. Acquisitions using rotating transmission sources or scanning line-sources, which cover all or most of the FOV and produce only small amounts of scatter should therefore be appropriate for calculation of these factors. The protocol shown in figure 4.7 may be used to calculate the fixed components from such an acquisition.

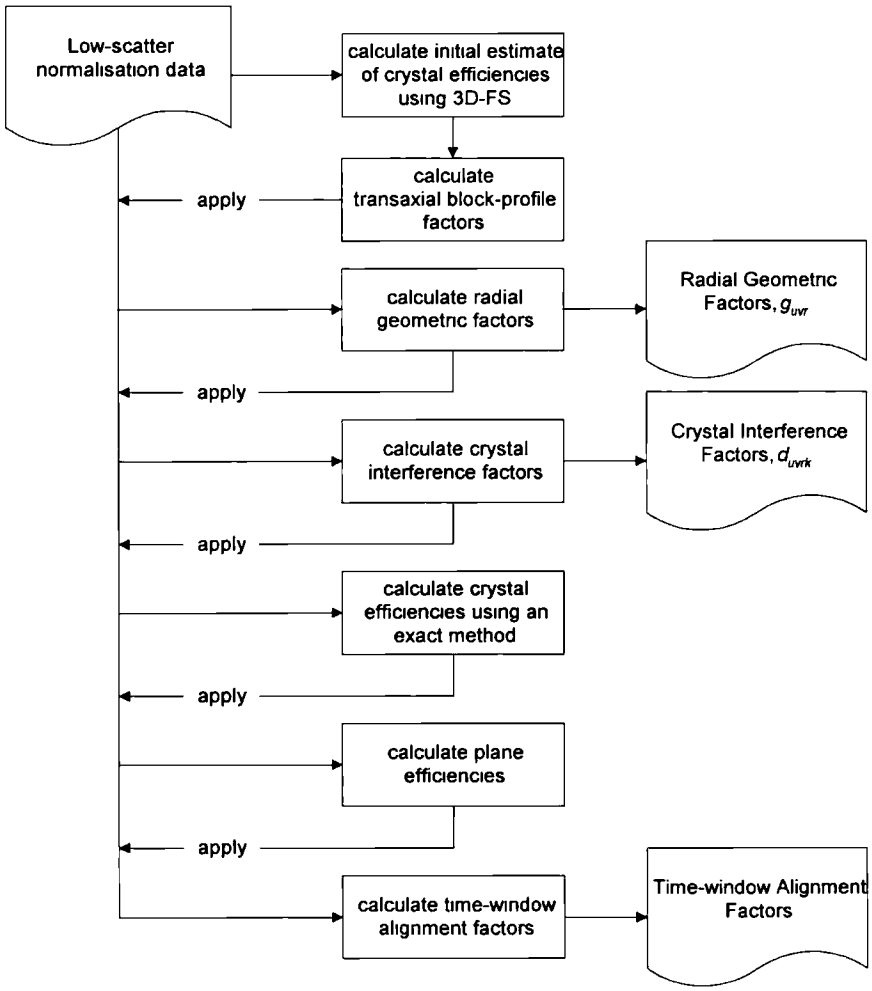

Figure 4.7. Protocol for calculating fixed normalisation components from low-scatter data

If desired, the variable components can also be calculated from such an acquisition. However, the accuracy of the plane-efficiency factors will be dependent on the linear uniformity of the line-sources used. It should also be noted that transmission sources used in 2D mode will be too active for use as 3D normalisation sources, and must be replaced with low-activity sources for the acquisition. Low-activity rod sources must also be used when using a scanning line-source, or variations in dead-time effects during the acquisition may introduce bias. If a scanning line-source is used, it may be necessary to correct for spill-over from the retracted transmission rod-sources.

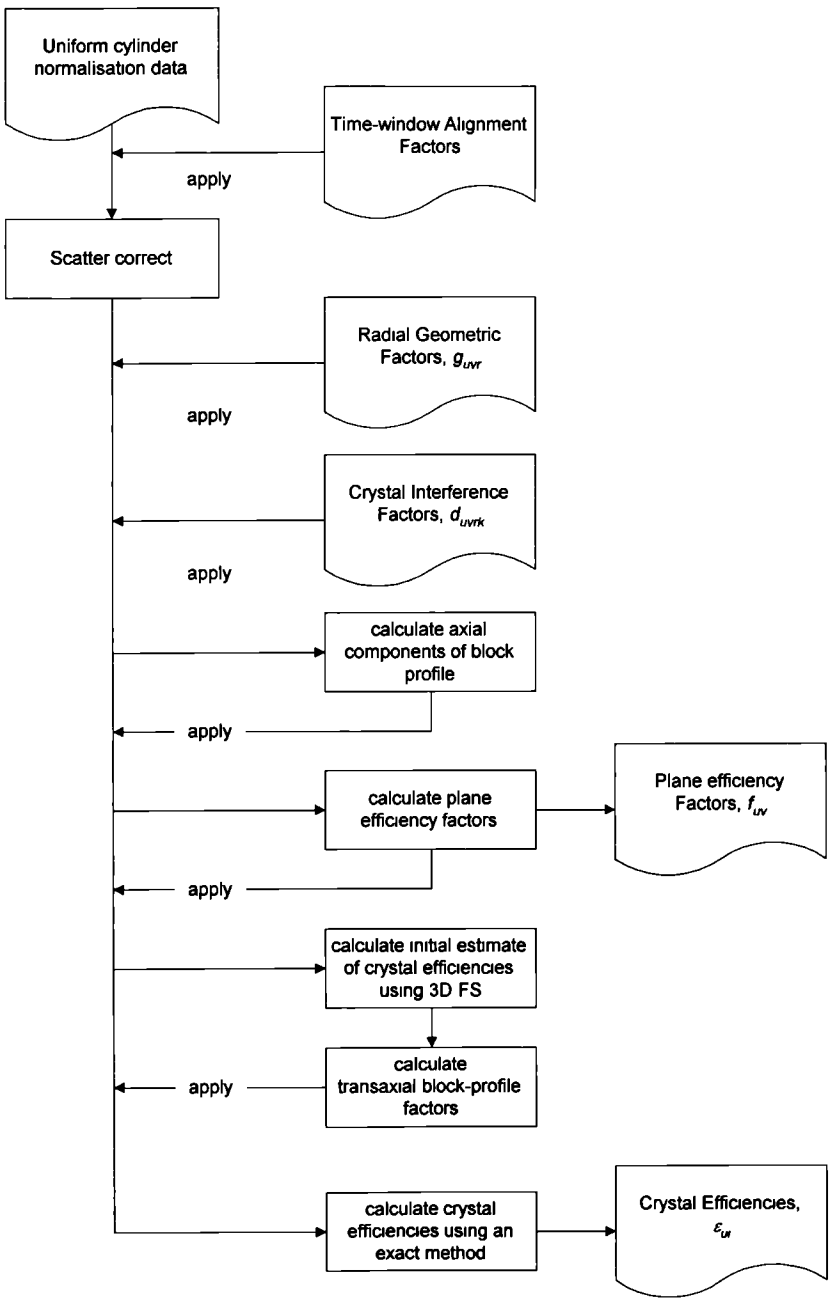

Figure 4.8. Protocol for calculation of variable normalisation components from a scan of a central uniform cylinder.

4.4.2. Calculation of variable components.

The variable components may be calculated from an acquisition of a central uniform 20cm cylinder phantom using the protocol shown in figure 4.8 above. The resulting ε_{ui} and f_{uv} should contain no rate-dependent components.

4.4.3. Calculation of rate-dependent components

A uniform 20cm cylinder phantom is filled with ^{18}F or ^{11}C in aqueous solution such that there is more activity in the FOV than would be encountered in normal 3D-mode operation. A series of short acquisitions are then made as the activity decays. The block-profiles are then calculated for each acquisition using the protocol described in 4.4.2 above. The mean block-detector singles rate is noted for each acquisition and a look-up table of block-profile factors and singles rates is created. For any particular acquisition, appropriate block-profile factors can now be applied to each individual block depending on its singles rate. Intermediate values may be obtained from the look-up table by linear interpolation.

In practice, a good estimate of the average transaxial block-profile components can by obtained from the emission data itself, simply by applying the 3D-FS algorithm to the data and computing the block-profile from the resultant "pseudo-efficiencies". The assumption is made that in a detector ring containing J block detectors, the total number of counts in a group of J evenly spaced fan-sums is equal to that in any other, except for the effects of block-profile. Clearly there are source distributions for which this may not be valid, for example a point-source located close to the edge of the FOV. However, for the source distributions which are likely to be encountered in human studies the assumption should be reasonable.

Such a technique has the advantage that the block-profile correction is derived from data which has been appropriately integrated over all count-rates in the study, whereas corrections obtained from look-up tables must be derived from the mean count-rate for each block-detector during the study (at least on systems with no on-line dead-time correction facility). The disadvantage of this scheme lies in the fact that different block-detectors in the camera will experience different singles rates and therefore should ideally be corrected with different block-profile factors. Incorrect block-profile factors manifest as radial "saw-tooth" artefacts and are clearly visible as diamond-patterns in sinogram data (see section 4.5.2). It can be

seen from figures 4.9 to 4.13 that the self-normalisation method proposed here can significantly reduce such non-uniformities, even for non-uniform and non-central distributions.

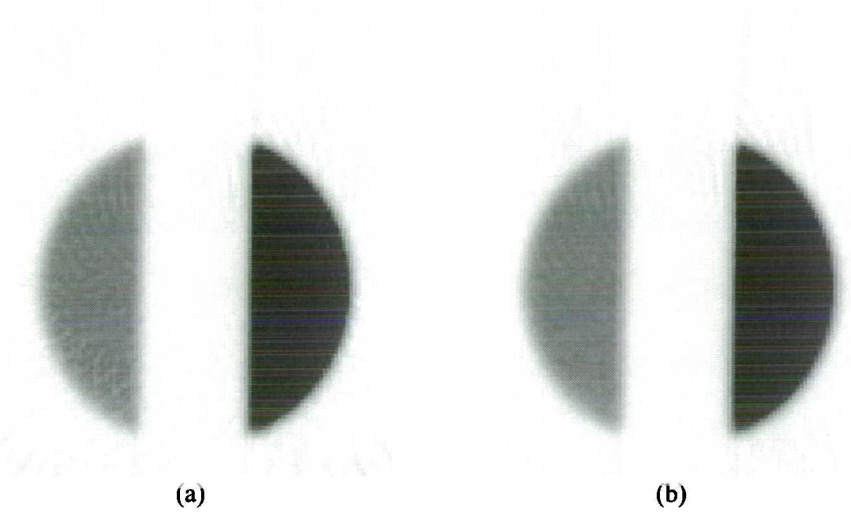

Figure 4.9. Summed images of off-centre 17cm-diameter slot phantom.
The inverse grey-scale saturates at 65% of the image maximum. Approximately $9x10^8$ counts were acquired in total and the ratio of activity in the three compartments was 1.00:0.00:2.13. The average dead-time correction factor was 1.042, and ranged from 1.030 to 1.052.
(a) no block-profile correction
(b) self-normalised for block-profile
In both images high frequency circular artefacts centred on the centre of the FOV are visible. Circular "saw-tooth" artefacts also centred on the centre of the FOV can be seen on the image not corrected for block-profile, but are absent from the self-normalised image.

(a) (b)

Figure 4.10. Summed normalised and scatter-corrected sinograms from an ^{18}F-FDG adult brain study.
The grey-scale covers the entire dynamic range. Approximately $2x10^8$ counts were acquired in total. The average dead-time correction factor was 1.076, and ranged from 1.059 to 1.092.
(a) normalised using conventional method, where both the crystal efficiencies and block-profile factors are derived from a scan of a central 20 cm cylinder (average dead-time correction factor of 1.040)
(b) crystal efficiencies from a scan of a central 20 cm cylinder, but self-normalised for block-profile
A diamond pattern can clearly be seen in the data normalised using the conventional method. This pattern is not seen in the data which has been self-normalised for block-profile.

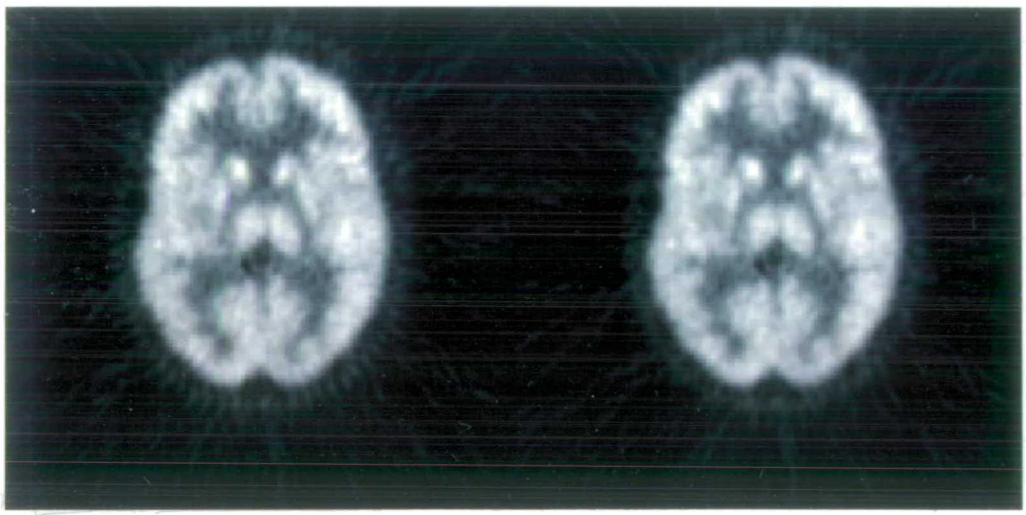

(a) (b)

Figure 4.11. Plane 19 from images reconstructed from the normalised and scatter-corrected sinograms from the ^{18}F-FDG brain study shown in figure 4.10.
The grey-scale covers the entire dynamic range.
(a) normalised using conventional method, where the crystal efficiencies and block-profile factors are derived from a scan of a central 20 cm cylinder
(b) crystal efficiencies from a scan of a central 20 cm cylinder, but self-normalised for block-profile.
Circular "saw-tooth" artefacts are visible in the conventionally normalised image, but not in the image self-normalised for block profile.

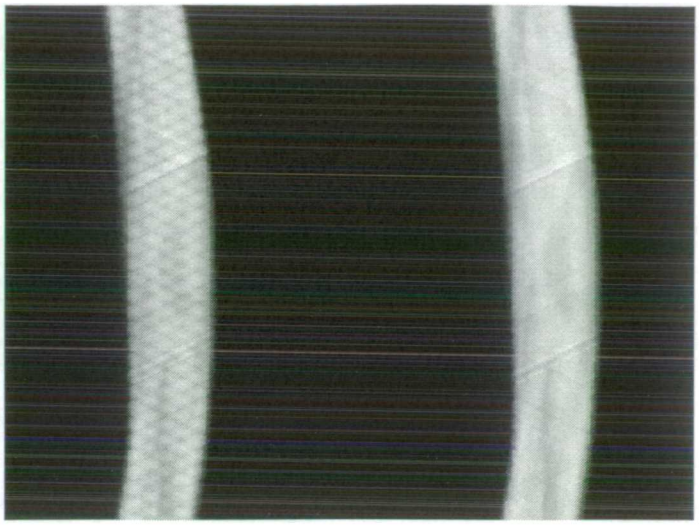

(a) (b)

Figure 4.12. Summed normalised and scatter-corrected sinograms from an ^{18}F-FDG paediatric brain study. The grey-scale covers the entire dynamic range. Approximately 10^8 counts were acquired in total. The average dead-time correction factor was 1.027, and ranged from 1.021 to 1.034.
(a) Normalised for all components except for block-profile
(b) As (a), but self-normalised for block profile.
Self-normalisation removes the diamond pattern from the sinogram without the use of a separate normalisation acquisition.

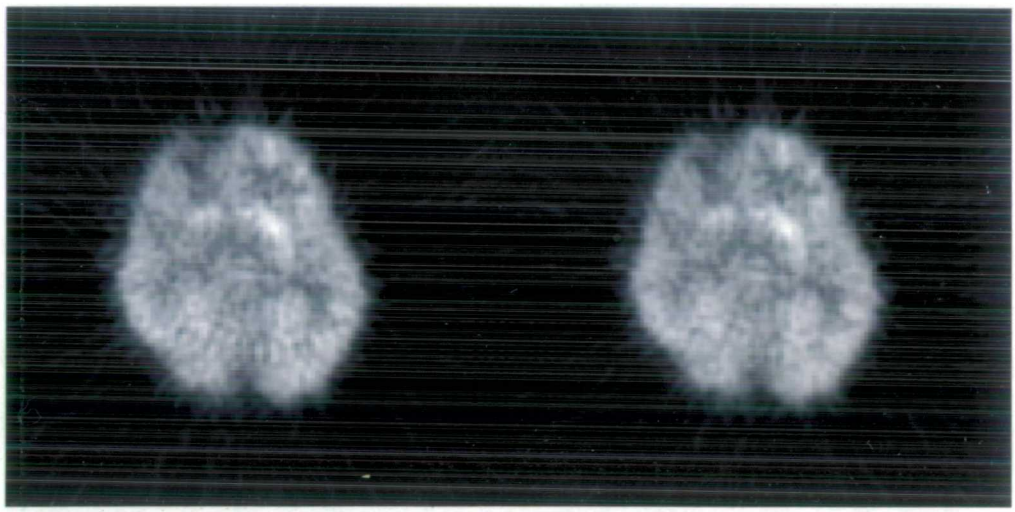

(a) (b)

Figure 4.13. Plane 18 from images reconstructed from the normalised and scatter-corrected sinograms from the paediatric ^{18}F-FDG brain study shown in figure 4.12.
Contrast is significantly reduced compared to the adult study shown above because the patient was scanned while under general anaesthetic. The grey-scale covers the entire dynamic range.
(a) Normalised for all components except for block-profile
(b) As (a), but self-normalised for block profile.
Again, self-normalisation for block-profile removes circular "saw-tooth" artefacts from the image.

4.5. Characterisation of normalisation components

4.5.1. Radial geometric profile

The radial geometric profile is a very significant component in normalisation. Figure 4.14 shows the effect of not applying radial geometric corrections to an acquisition of a uniform cylinder. There is a pronounced dip in the middle of the image, and a central hot-spot is superimposed on this in the end-planes of the image volume.

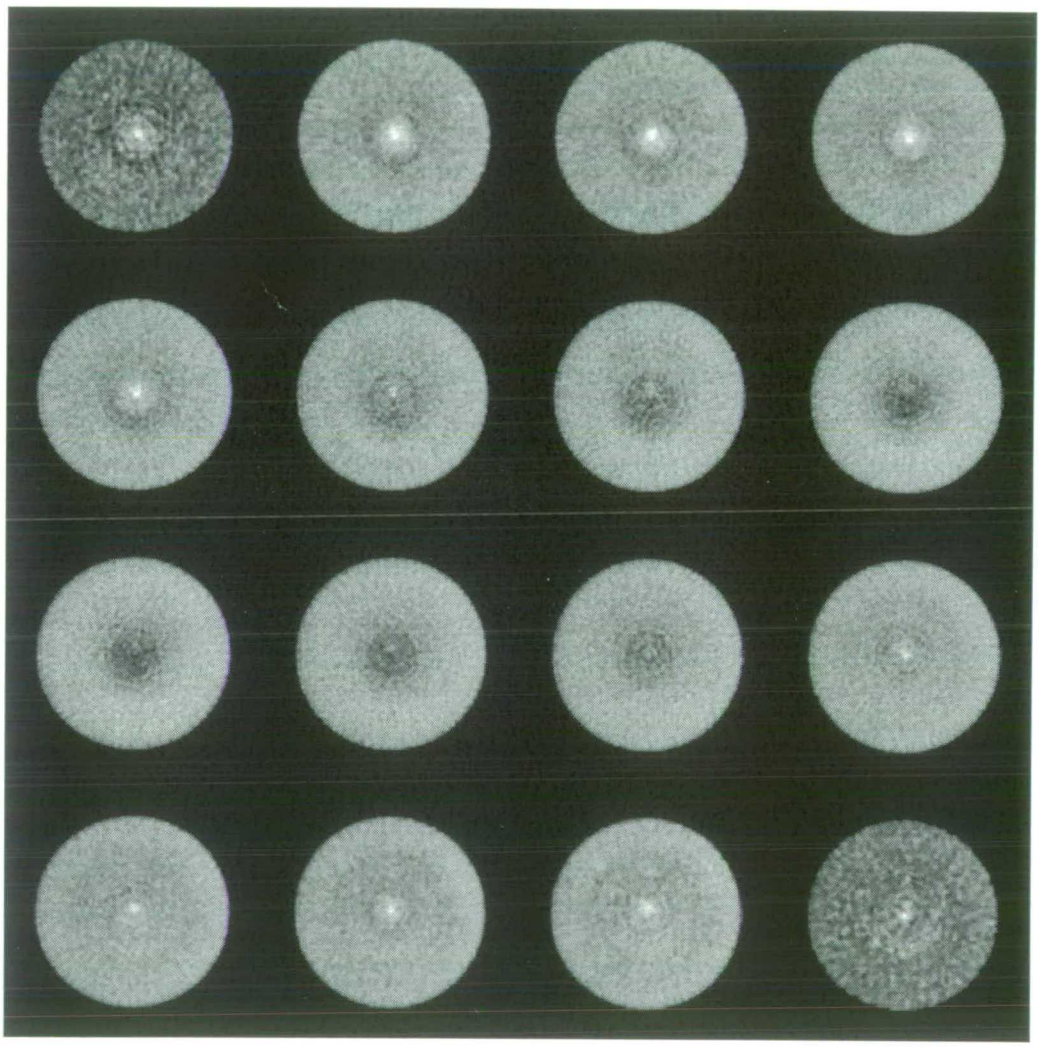

Figure 4.14. Image planes 1, 3, 5, ... , 31 from a uniform 20 cm cylinder acquisition reconstructed and normalised for all components except radial geometric profile.
The zero-point of grey-scale is set to 50% of image maximum. Marked non-uniformities are visible. Values in the centre vary by +/-25% of the mean value within the cylinder boundary.

Radial geometric correction factors were obtained from the rotating and scanning line-source acquisitions described in section 3.3.3. The correction factors averaged over all planes are plotted in figure 4.15. It is interesting to note that the two methods give different profiles, particularly in the centre of the FOV.

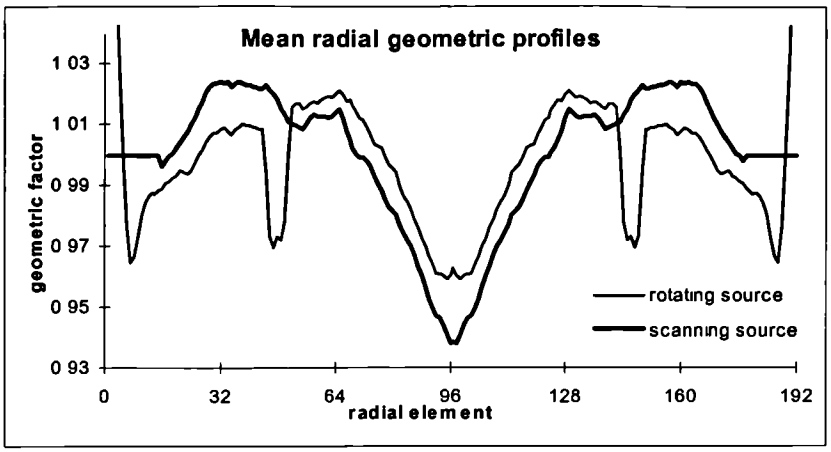

Figure 4.15. Mean radial geometric profiles obtained from the scanning and rotating line source acquisitions.
The dips in the profile for the rotating sources near elements 48 and 144 are due to mutual attenuation of the sources. There is a particularly significant difference between the two profiles close to the centre of the FOV (radial element 96).

An ad-hoc correction for the central hot-spot can be obtained directly from low-variance 20 cm cylinder data as follows:

1. Sinograms are multiplied by appropriate attenuation factors
2. Sinograms are then multiplied by factors reflecting the amount of activity in each LOR
3. Radial geometric profile factors are calculated for the central 12 elements in each projection using the algorithm described in section 4.3.

In the absence of artefacts, the resultant profile factors would be equal. However, in this case, the profile factors will reflect the shape of the central hot-spot in sinogram space and can be used to correct for it. This process was performed on the low-variance 20 cm cylinder data described in section 3.3.3.3. The radial geometric factors used in the initial normalisation were generated from the scanning line-source data. A composite set of radial geometric factors was obtained by combining the scanning line-source correction factors and the hot-spot correction factors derived from the 20 cm cylinder scan. This was then used to self-normalise the 20 cm cylinder data. When the data was reconstructed, some high-frequency "spikes" in the exact centre of the FOV were noted, together with ring-artefacts in the region of the central hot-spot correction. These artefacts were reduced after application of a light smooth of the hot-spot correction factors in r and φ.

The scanning line-source, rotating line-source and composite geometric factors were used to normalise the low-variance 20 cm cylinder acquisition data. Selected planes from the resultant reconstructions can be seen in figure 4.16, and summed planes and profiles in figure 4.17. The composite geometric factors give the best results, followed by those from the rotating line-source acquisition. However, all reconstructions contain some high-frequency spikes in the exact centre of the FOV.

The three sets of radial geometric factors were also used to normalise the off-centre cylinder data described in section 4.2. The results are shown in figure 4.18. The composite factors again give the best results, indicating that they are not solely applicable to the data from which they were derived.

Apart from the central hot-spot, another feature which can be seen from the reconstructed images are a series of high-frequency concentric ring artefacts centred on the centre of the FOV. The cause of these artefacts is not known.

Possible causes of the central hot-spot include the following:
a) inadequate scatter correction
b) an interaction between residual scatter and the radial profile correction factors
c) failure to account for geometric factors for scatter
d) count-rate dependence of the radial profile corrections
e) inaccurate measurement of the radial profiles due to, for example, scatter
f) inadequate normalisation model - that is, there is no such thing as a unique radial geometric profile as currently defined for all source distributions.

It may well be that the central hot-spot is caused by a combination of some or all of these effects. However, it is possible to draw some conclusions as to the significance of each. In particular, the hot-spot is unlikely to be caused by gross inaccuracies in the scatter correction, for the reasons discussed in section 4.2 above.

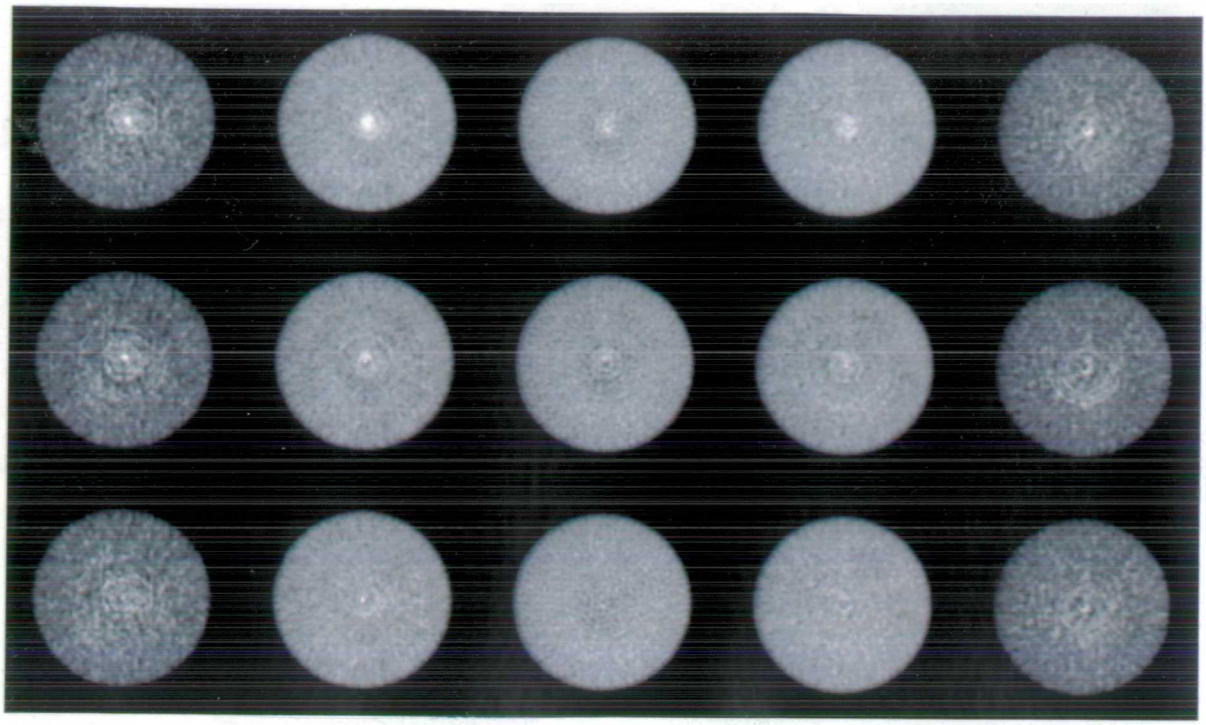

Figure 4.16. Reconstructions of a uniform 20 cm cylinder with different radial geometric corrections. Zero-point of grey-scale is set to 50% of image maximum. From left to right: planes 1, 5, 16, 27 and 31.
Top: geometric correction from a scanning line-source acquisition
Middle: geometric correction from a rotating line-source acquisition
Bottom: composite geometric correction from the scanning line-source and low-variance cylinder data.
The composite geometric correction delivers the most uniform images, although even in this case high-frequency spikes in the exact centre of the FOV are sometimes found.

Figure 4.4(a) above (in section 4.2) shows a reconstruction of non-scatter corrected but fully normalised data from the high statistics 20 cm cylinder acquisition. If anything, the hot-spot is less pronounced than in the scatter corrected images. If an interaction between residual scatter and the geometric correction were responsible for the problem, we would expect the hot spot to get worse under these conditions. In any case, the average residual scatter at the centre of a reconstructed image of a 20 cm cylinder is only around 5-6%, and would seem to be too small an effect to be significant in this context, even if magnified by an inappropriate geometric correction.

Failure of the assumption that the geometric factors for scatter are negligible cannot be ruled out as a contributor to the problem. However, if it were the principle factor we would not expect to see such significant changes in the nature of the hot-spot when the radial geometric profiles are measured with different sources.

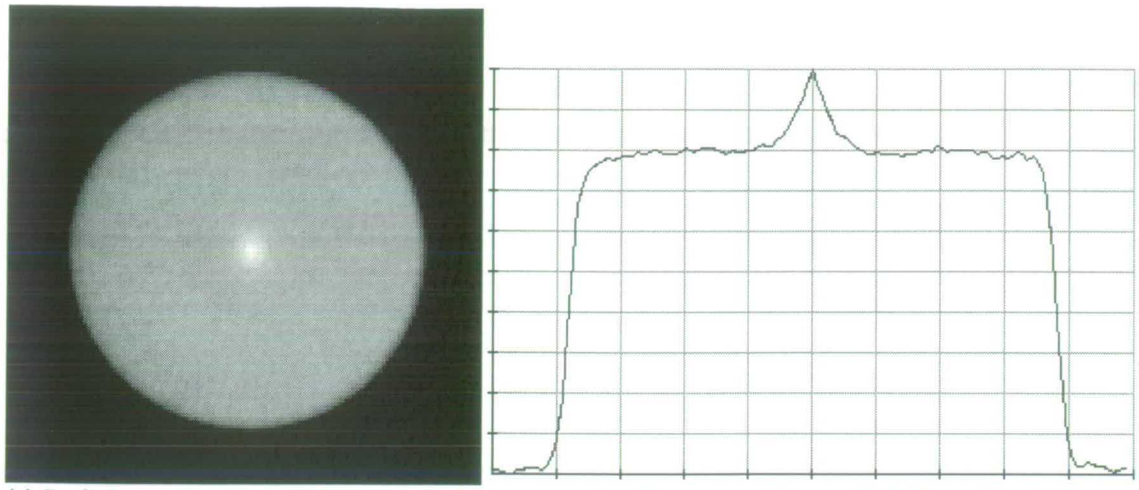

(a) Radial geometric correction generated from scanning line-source data applied. The value at the centre of the FOV is about 25% greater than that in the main body of the phantom.

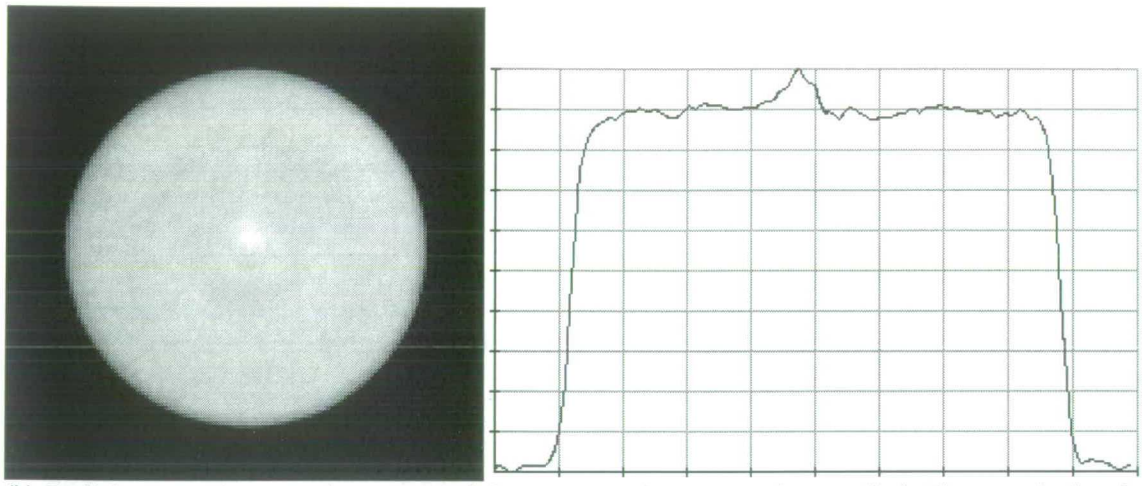

(b) Radial geometric correction generated from rotating line-source data applied. The magnitude of the central hot-spot is about half that obtained with the scanning line source correction.

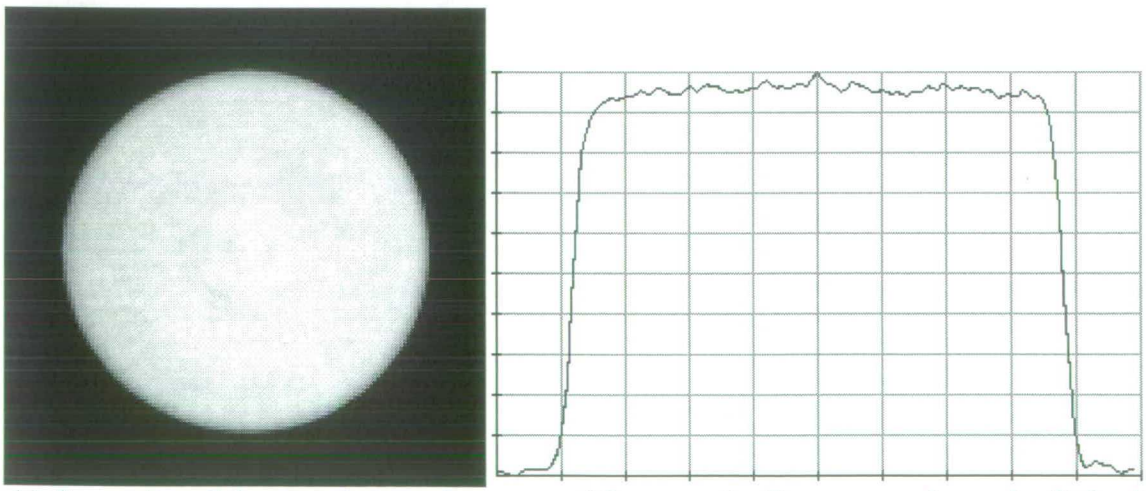

(c) Composite radial geometric correction generated from scanning line-source and central cylinder data applied. There is a small residual hot-spot due to smoothing of the composite profile in the centre of the FOV.

Figure 4.17. Summed images and vertical profiles through uniform central cylinder normalised using different radial geometric corrections.
Zero-point of grey-scale set to 50% of maximum value.

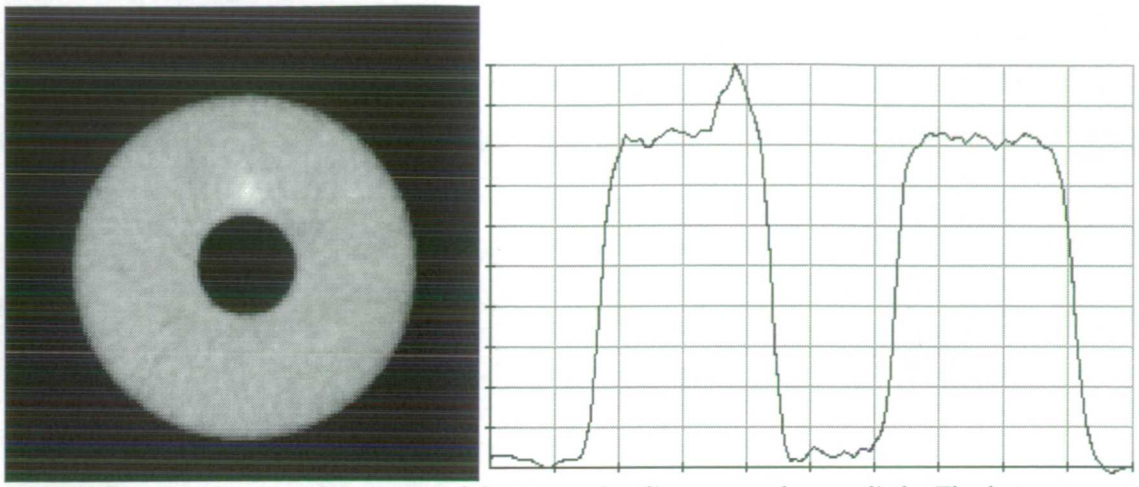

(a) Radial geometric correction generated from scanning line-source data applied. The hot-spot seen is located at the exact centre of the FOV.

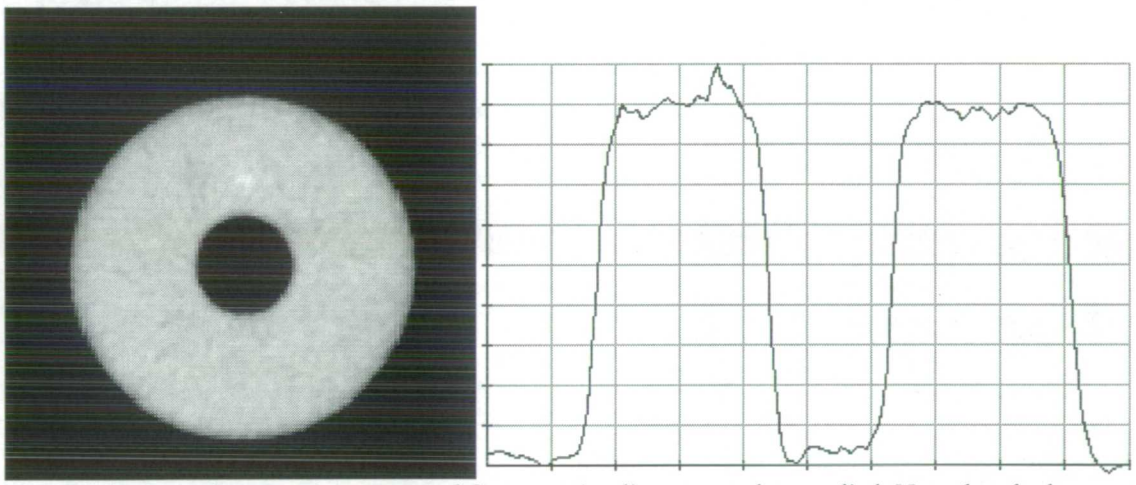

(b) Radial geometric correction generated from rotating line-source data applied. Note that the hot-spot is smaller than that seen in 4.18(a).

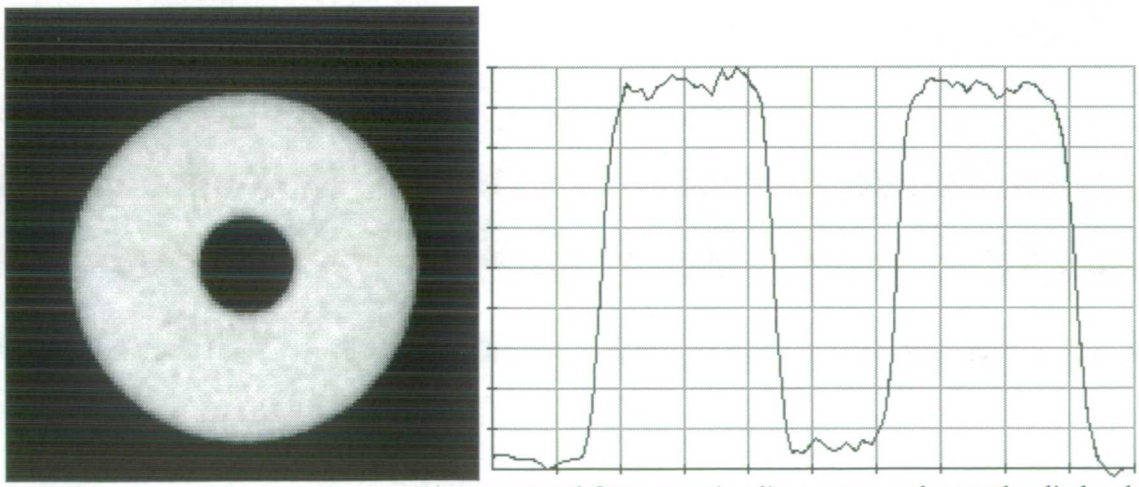

(c) Composite radial geometric correction generated from scanning line-source and central cylinder data applied. The central hot-spot is considerably reduced compared to both 4.18(a) and 4.18(b)

Figure 4.18. Summed images and vertical profile through off-centre cylinder with cold insert, normalised using different radial geometric corrections.
Zero-point of grey-scale set to 50% of maximum value.

In order to ascertain if count-rate effects could be involved in the problem, two acquisitions of central uniform 20 cm cylinders were performed, one with an average of 4.4 MBq in the FOV, and the other with an average of 50 MBq in the FOV. Both acquisitions contained approximately $4x10^8$ counts. Summed images reconstructed from these acquisitions together with radial profiles are shown in figure 4.19. The hot-spot appears to be more intense and more sharply defined in the high activity image. This suggests that count-rate effects may play some role in the phenomenon.

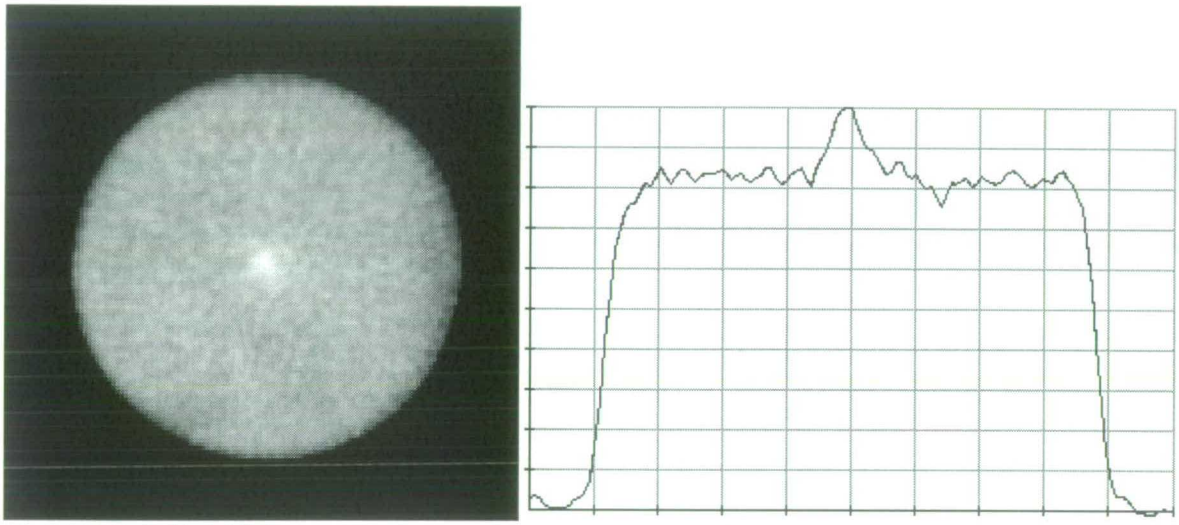

(a) 4.4.MBq in the FOV

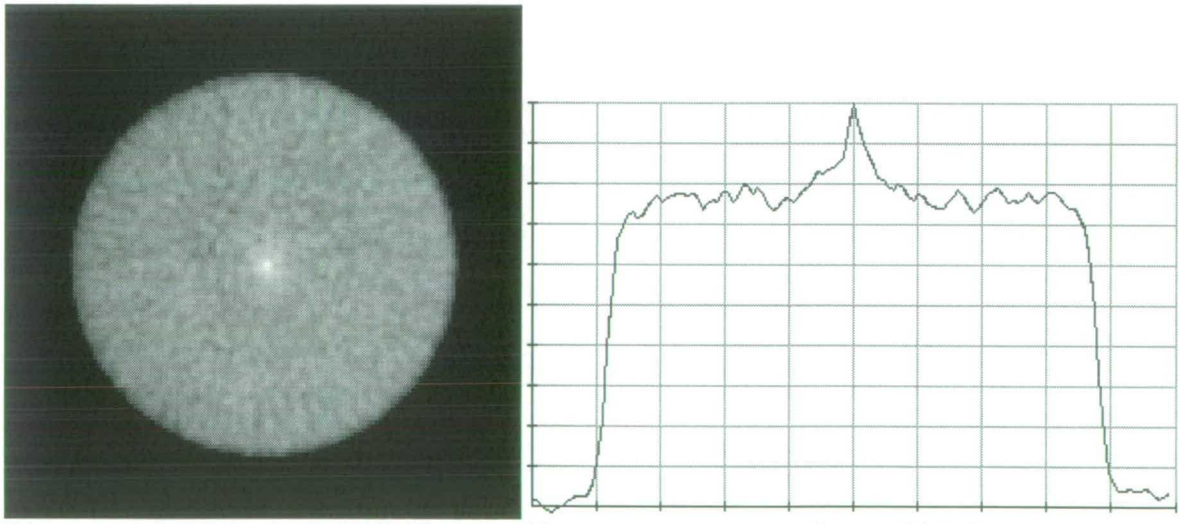

(b) average of 50 MBq in the FOV. The central hot-spot appears to contain more high-frequency components than in the image obtained from the 4.4 MBq source.

Figure 4.19. Summed images and profiles through high and low activity cylinders.
Radial geometric factors obtained from the scanning line-source acquisition. Zero-point of colour scale set to 50% of image maximum.

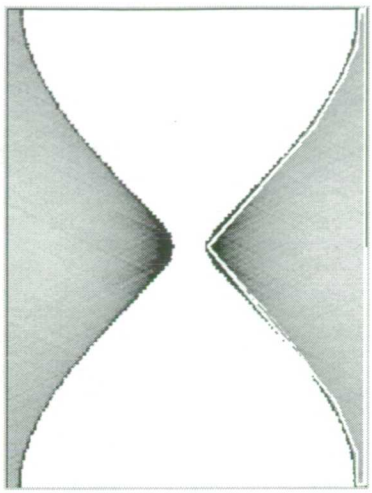

Figure 4.20. Scatter in a scanning line-source acquisition.
The region sampled by the source has been set to zero. The mean value within the polygonal region of interest corresponds to approximately 16 counts per LOR, or about 6% of the mean value in the composite sinogram.

Neither inadequacies in the normalisation model nor inaccuracies in the measurement of the radial geometric factors can be eliminated as a cause of the central hot-spot on the basis of the work done here. Clearly the sources for the rotating and scanning line acquisitions occupy very different positions in the FOV, and this may well contribute to the differences in the factors generated from the two acquisitions. On the other hand, it does appear that the rotating line-source data gives better results when normalising central source distributions than the scanning- line-source data does (at least in terms of the magnitude of the hot-spot), in spite of the fact that the rotating sources are at all times further from the centre of the FOV. A simple estimate indicates that the mean amount of scatter in the composite sinogram generated from the scanning line-source acquisitions is around 6% (figure 4.20). However, the distribution of this scatter is unknown and may not be uniform. The amount of scatter in the rotating line-source acquisition was estimated by acquiring a blank 2D simultaneous emission-transmission scan with the septa in the retracted position, and comparing the number of counts in the emission component (which should contain only scatter) with that in the transmission component (which should contain only true events). The amount of scatter was approximately 5% of the total signal, and the distribution appeared to be fairly uniform across the FOV. A full implementation of rod-windowing in 3D mode would help to clarify this point. If the central hot-spot is indeed caused by errors in the measurement of the radial profiles, a correction calculated from the 20 cm cylinder data should give generally applicable results. However it would be unwise to apply such a correction to data acquired from source distributions which are significantly different without further validation.

4.5.2. Transaxial Block-profile

The transaxial block-profiles calculated from a 20 cm cylinder acquisition with 50 MBq in the FOV are shown in figure 4.21. Summed sinograms and reconstructed images of data not corrected for block-profile variations are shown in figure 4.22 and 4.23. If the block-profile is not corrected for, characteristic circular "saw-tooth" artefacts appear in the images. While these artefacts are small at low count-rates, they become increasingly important as the count-rate increases.

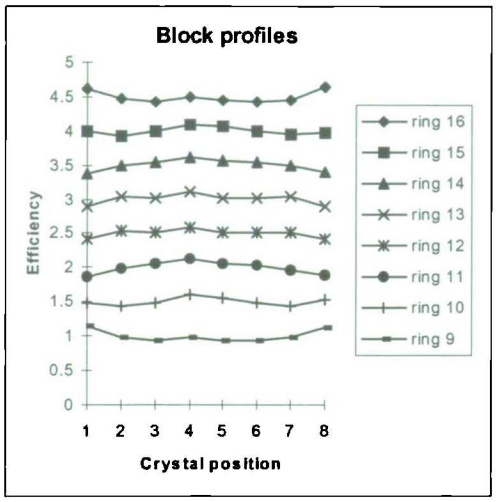

Figure 4.21. Block profiles for different crystal rings obtained from a 20 cm cylindrical source (50 MBq in the FOV).
For ease of display, the profiles have been incremented by 0.5 for each ring number.

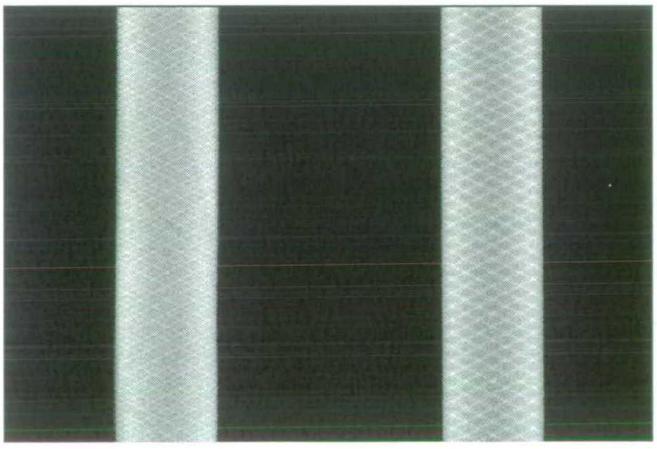

(a) (b)

Figure 4.22. Summed sinograms from high and low activity 20 cm cylinder acquisitions.
Zero-point of grey-scale is set to 50% of maximum value.
(a) 4.4 MBq in FOV, no block-profile correction
(b) 50 MBq in FOV, no block-profile correction

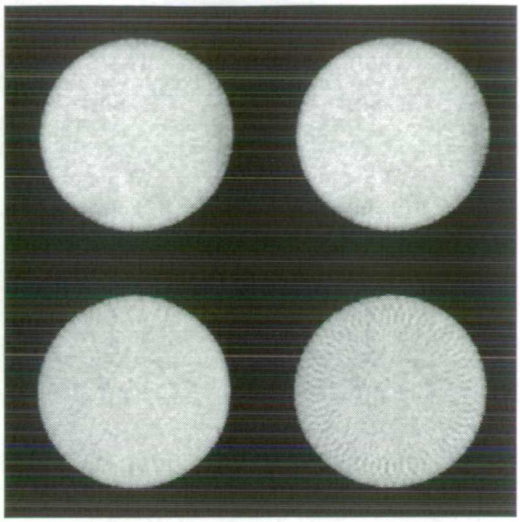

Figure 4.23. Summed images from high and low activity 20 cm cylinder acquisitions. Zero-point of grey-scale is set to 50% of maximum value. In all cases a composite radial geometric correction has been applied. The cause of the dark blotches on the limb of the low-activity cylinder is not known.
Top left: 4.4 MBq in FOV, fully normalised
Top right: 4.4 MBq in FOV, no block-profile correction
Bottom left: 50 MBq in FOV, fully normalised
Bottom Right: 50 MBq in FOV, no block-profile correction

Failure to separate crystal efficiencies into rate-dependent and rate-independent components (i.e. into intrinsic crystal efficiency and block-profile components) may cause particular problems when rotating or scanning line-sources are used for normalisation, as the block singles rates in such acquisitions are quite different to those encountered in normal operation.

4.5.3. Axial Block-profile and Plane Efficiency

The axial components of the block-profile with 50 MBq in the FOV are plotted in figure 4.24(a). It can be seen that the efficiency of crystal ring 1 is significantly lower than those of the other rings. Subsequent inspection of the camera gantry revealed that the cause of this was incomplete retraction of the septa, resulting in partial occlusion of the first crystal ring. Ratios of the block-profiles with 50 MBq and 4.4 MBq in the FOV are plotted in figure 4.25(b). The factors increase in the rings corresponding to crystals in central positions in the block detectors as the activity in the FOV increases. This is the result of event mispositioning due to pulse pile-up.

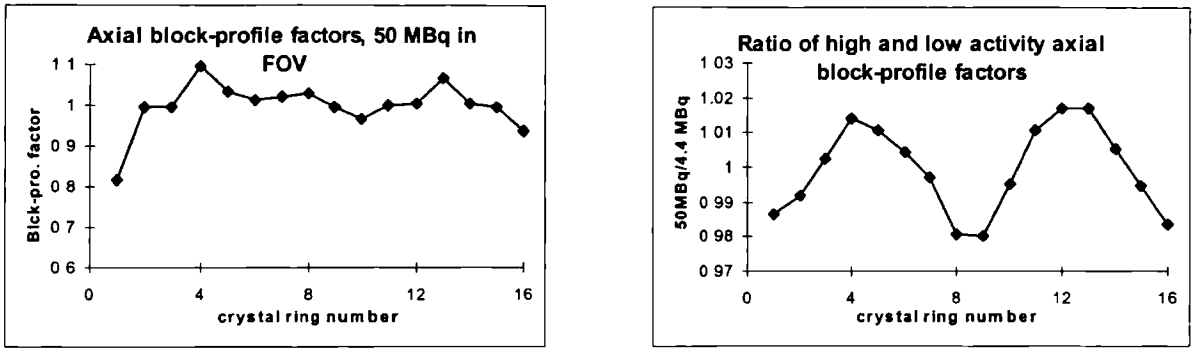

Figure 4.24. Features of the axial block-profile normalisation component.
(a) Axial block-profile factors calculated from a 20 cm cylinder acquisition with 50 MBq in the FOV.
(b) Ratios of axial block-profile factors calculated from a 20 cm cylinder acquisition with 50 MBq in the FOV and one with 4.4 MBq in the FOV.

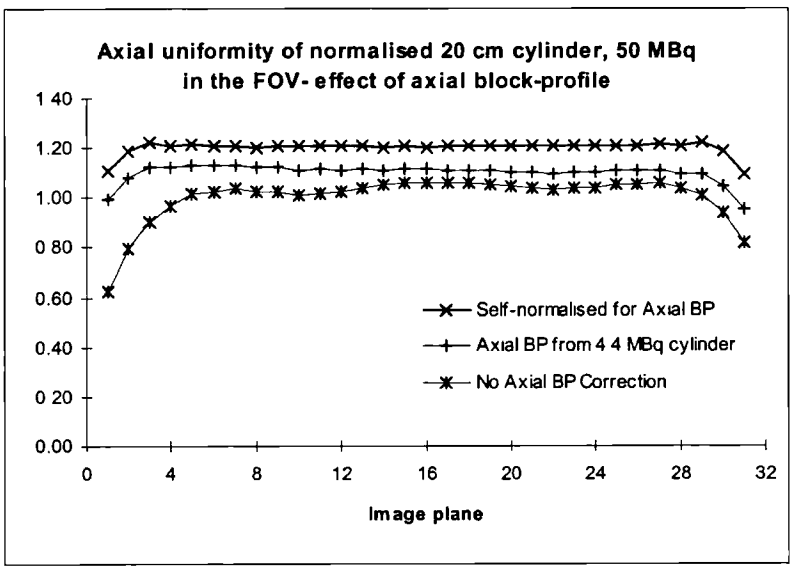

Figure 4.25. Axial uniformity plots for a reconstructed scan of 20 cm cylinder with 50 MBq in the FOV with different corrections for axial block-profile.
The plots are derived by computing the ratio of the total counts in each image plane to the mean for that image. The points in the upper curve has been incremented by 0.2 and the points in the middle curve by 0.1 to assist visualisation. The difference between the uncorrected image and the image corrected with data from the low-activity source is much greater than the difference between the image corrected with the low-activity source and the self-normalised image.

	Correction from low activity source, all planes	Correction from low activity source, central 27 planes	No correction, all planes	No correction, central 27 planes
Mean error	1.2	0.9	5.7	3.5
Max. error	5.0	2.7	44.5	13.4

Table 4.1. Percentage errors in the total counts in individual image planes due to variations in corrections for axial block-profile.
The errors are calculated with respect to a self-normalised image. The largest errors are found in the 2 outermost image planes at each end of the reconstructed volume.

The axial component of the block-profile has a very significant effect on the axial uniformity of reconstructed images. Figure 4.25 shows the axial uniformity of the 50 MBq cylinder data reconstructed with full normalisation, with no axial block-profile correction and with a correction derived from the 4.4 MBq cylinder scan. The plot shows the ratio of total counts in each reconstructed image plane compared to the mean. The curves have been incrementally offset by 0.1 to assist visualisation. Average and maximum fractional differences between the lower curves and the curve for the fully normalised image are shown in table 4.1. It can be seen that the axial block-profile as calculated here contains an important component which is not in fact count-rate dependent, since the mean difference seen in the image corrected with factors derived from the 4.4 MBq scan compared to the self-normalised image is just 1.2%, with a maximum deviation of 5%, whereas for the uncorrected data the figures are 5.7% and 44%. The largest errors are found in the end-planes.

Figure 4.26 shows the mean plane efficiency derived from a 20 cm cylinder scan as a function of ring difference. Data from ring 1 has been excluded. There is an increasing trend in plane-efficiency with ring-difference when the ring difference is greater than 8.

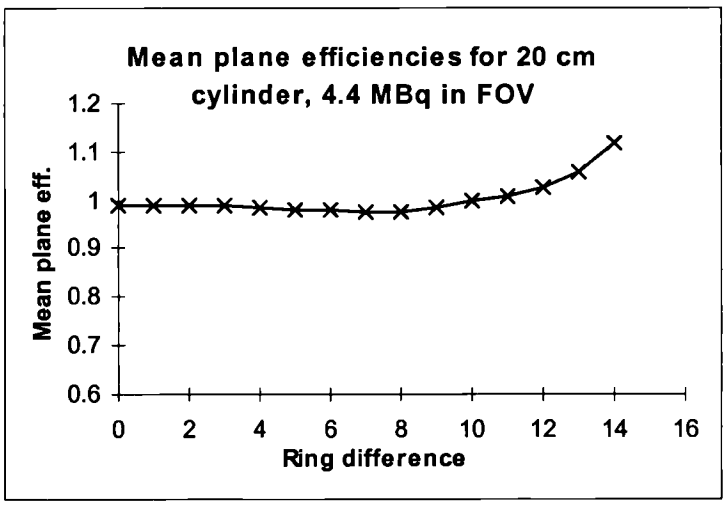

Figure 4.26. Mean plane efficiencies as a function of ring difference. Data from ring 1 has been excluded.

The effect of plane efficiency on axial uniformity is shown in figure 4.28. Without a plane-efficiency correction, the axial profile dips in the centre of the reconstructed volume. Comparison of figure 4.27 and figure 4.25 shows that plane efficiency is a less important normalisation component than axial block-profile. The mean difference seen in the image

without plane-efficiency correction compared to the fully normalised image is 1.3%, with a maximum deviation of 3.0%.

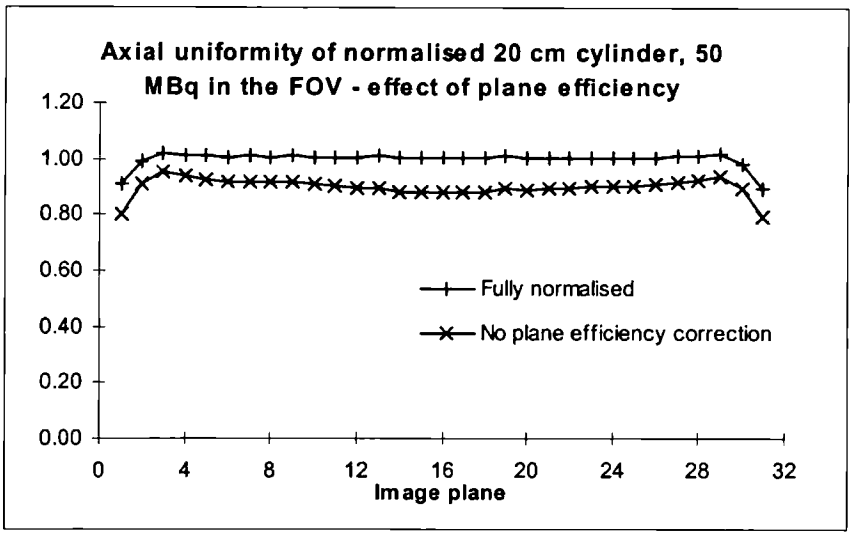

Figure 4.27. Axial uniformity plots for a reconstructed scan of 20 cm cylinder with 50 MBq in the FOV with and without corrections for plane efficiency.
The plots are derived by computing the ratio of the total counts in each image plane to the mean for that image. The points in the lower curve have been decremented by 0.1 to assist visualisation. Absence of plane-efficiency correction results in a dip in the centre of the axial uniformity profile.

The accuracy of the plane-efficiency and axial block-profile estimates are dependent on the statistical quality of the normalisation data used. In order to examine this relationship, the cylinder data acquired for testing the accuracy of the algorithms for calculating the ε_{ui} described in section 3.3.6 was re-processed. This data consisted of a series of 3D scans of a central 20 cm diameter cylinder uniformly filled with ^{68}Ge such that there were 4.4 MBq of activity within the FOV. The acquisition times varied from 150 seconds (4.6 x10^6 total counts) to 4800 seconds (1.5 x10^7 total counts). A single low-variance 19200 second cylinder scan (5.9 x10^8 total counts) was also acquired.

Each acquisition was corrected for transmission rod-spill. Subsequently plane efficiencies and axial block-profile factors were generated as described in section 4.4. These were then used to complete the normalisation of the low-variance data and the resultant datasets reconstructed. The axial uniformities of the images were then compared to that of the reconstructed self-normalised low-variance data. The results are plotted as a function of total acquired counts in the normalisation data in figure 4.28. It would appear that 70 million or more counts are required to generate stable values for the plane-efficiency factors. However,

even the maximum error found (~1.7%) is significantly less than the mean residual error due to scatter correction (~5-6%).

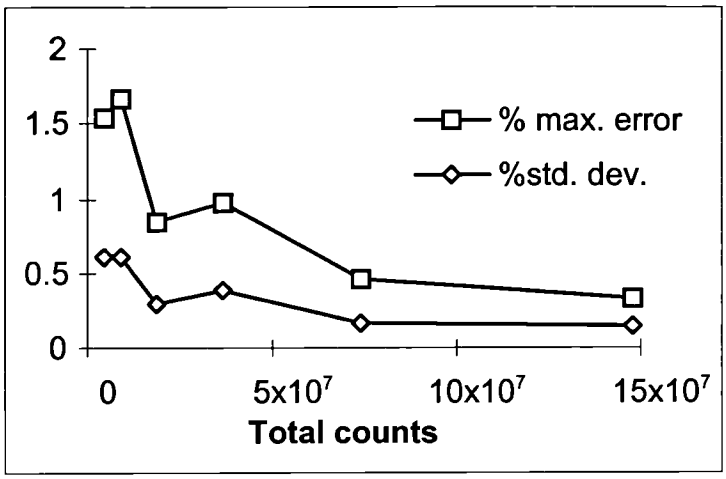

Figure 4.28. Image axial uniformity as a function of counts in the normalisation data. The graph shows percent standard deviations and maximum errors in the total counts in each image plane of the reconstructions of the low-variance scan of a 20 cm cylinder normalised using plane-efficiency and axial block-profile factors derived from shorter scans. The curves are plotted as a function of total counts in the shorter scans.

4.5.4. Detector efficiency

A histogram of detector efficiencies (ε_{ui}) is shown in figure 4.29. The FWHM of the distribution is 0.28. A summed sinogram and reconstructed image uncorrected for variations in ε_{ui} is shown in figures 4.31 and 4.32. Failure to correct for ε_{ui} results in increased noise in the image, which manifests as radial streaking.

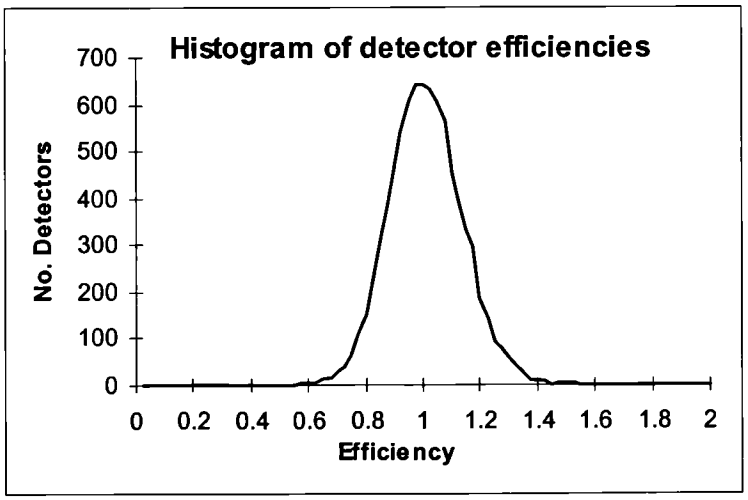

Figure 4.29. Histogram of crystal efficiencies.

4.5.5. Crystal interference

Crystal interference factors derived from a rotating line-source acquisition are shown in figure 4.30. A summed sinogram and an image reconstructed without correcting for crystal interference are shown in figures 4.31 and 4.32. A "saw-tooth" artefact, similar to that found in images reconstructed without correction for block-profile is seen.

4.5.6. Time-window alignment

Time-window alignment factors calculated from the scanning line-source data are shown in figure 4.30. The factors have a standard deviation of 2.42%, and range from to 0.872 to 1.120. Reconstructions of images with and without time-alignment correction are shown in figures 4.31 and 4.32. It can be seen that absence of the time-alignment correction results in a low-frequency "mottling" effect.

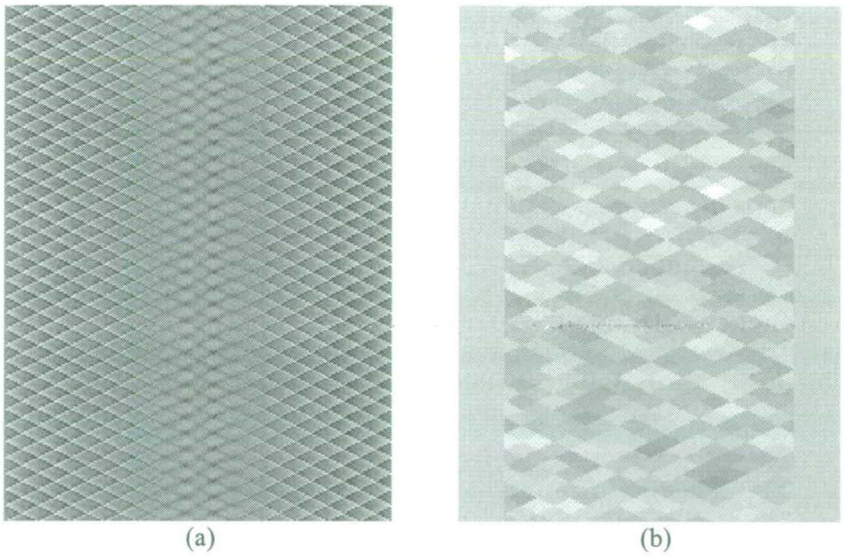

Figure 4.30. Crystal interference factors (a) and time-window alignment factors (b) calculated from a rotating line-source acquisition.

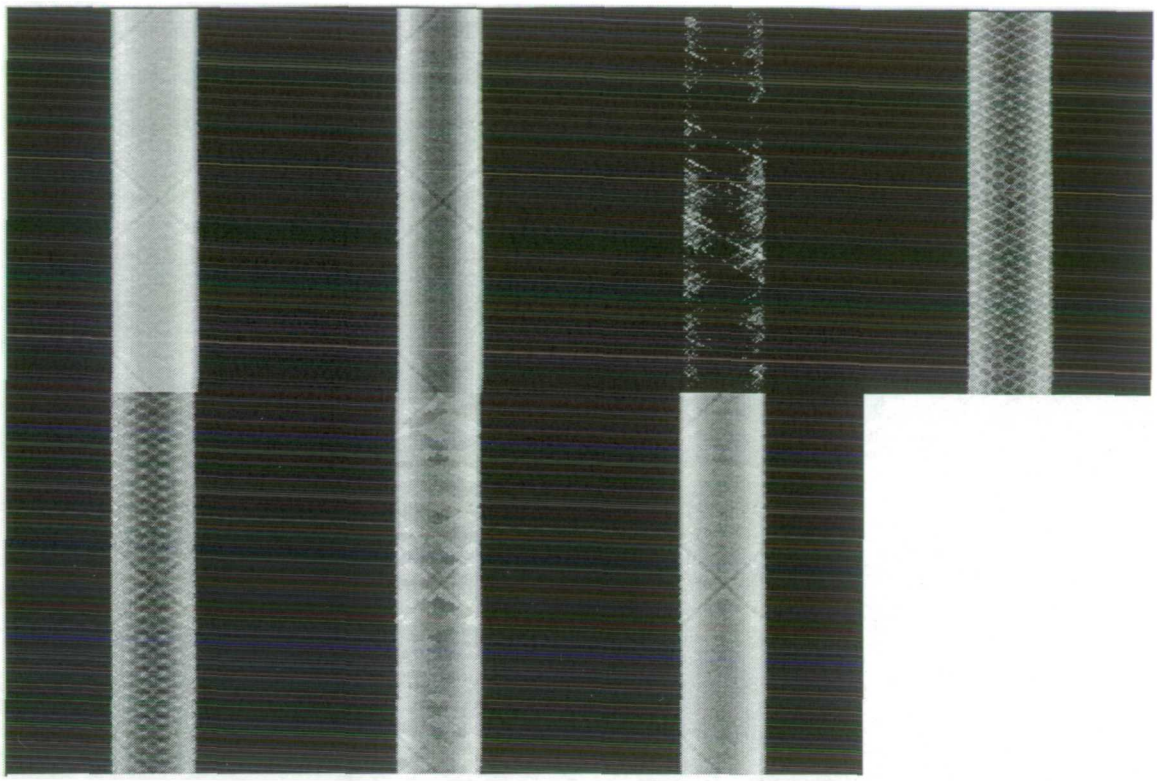

Figure 4.31. Summed sinograms from low-variance 20 cm cylinder acquisition.
The dark diagonal lines in the sinograms are attenuation artefacts from the laser positioning sources. Zero-point of grey-scale set to 75% of maximum.
From left to right:
Upper row: no scatter correction; no radial geometric correction; no crystal efficiency correction; no block-profile correction
Lower row: no crystal interference correction; no time-window alignment correction; fully normalised.

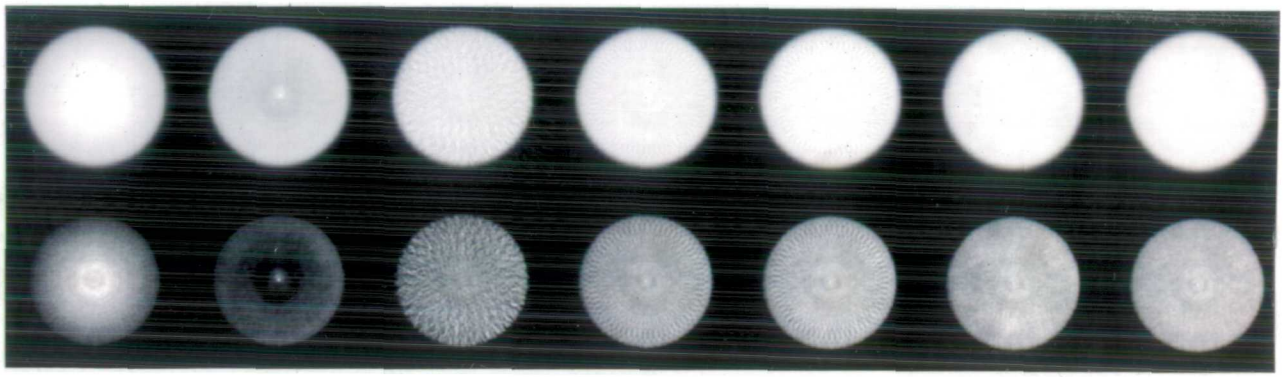

(a) (b) (c) (d) (e) (f) (g)

Figure 4.32. Summed images from low-variance 20 cm cylinder acquisition, 50 MBq in FOV.
Unless otherwise stated, all images were normalised with a composite radial profile correction.
Upper row - grey scale covering entire dynamic range
Lower row - grey scale, zero-point set to 75% of image maximum
a) no scatter correction
b) no radial geometric correction
c) no crystal efficiency correction
d) no block-profile correction
e) no crystal interference correction
f) no time alignment correction
g) fully normalised.

4.6. Significance of normalisation components in realistic imaging situations

Figure 4.33 shows selected images from reconstructions ^{18}F-FDG brain scan. The data has been normalised with corrections for various components missing. The example dataset shown contains a total of ~200 million counts (before scatter correction) and displays excellent FDG uptake. ^{18}F-FDG brain studies tend to have the most favourable statistical properties of any clinical protocol, so normalisation components which are unimportant in these circumstances are unlikely to be important in any other, with the exception of rate-dependent components. Visually, the images all look very similar. While the absence of a geometric correction (row 1) appears to have little visual effect, profiles through the images reveal changes in the pixel values consistent with those found in the reconstructed 20 cm cylinder studies. All the images show a central "spike" artefact in image plane 10.

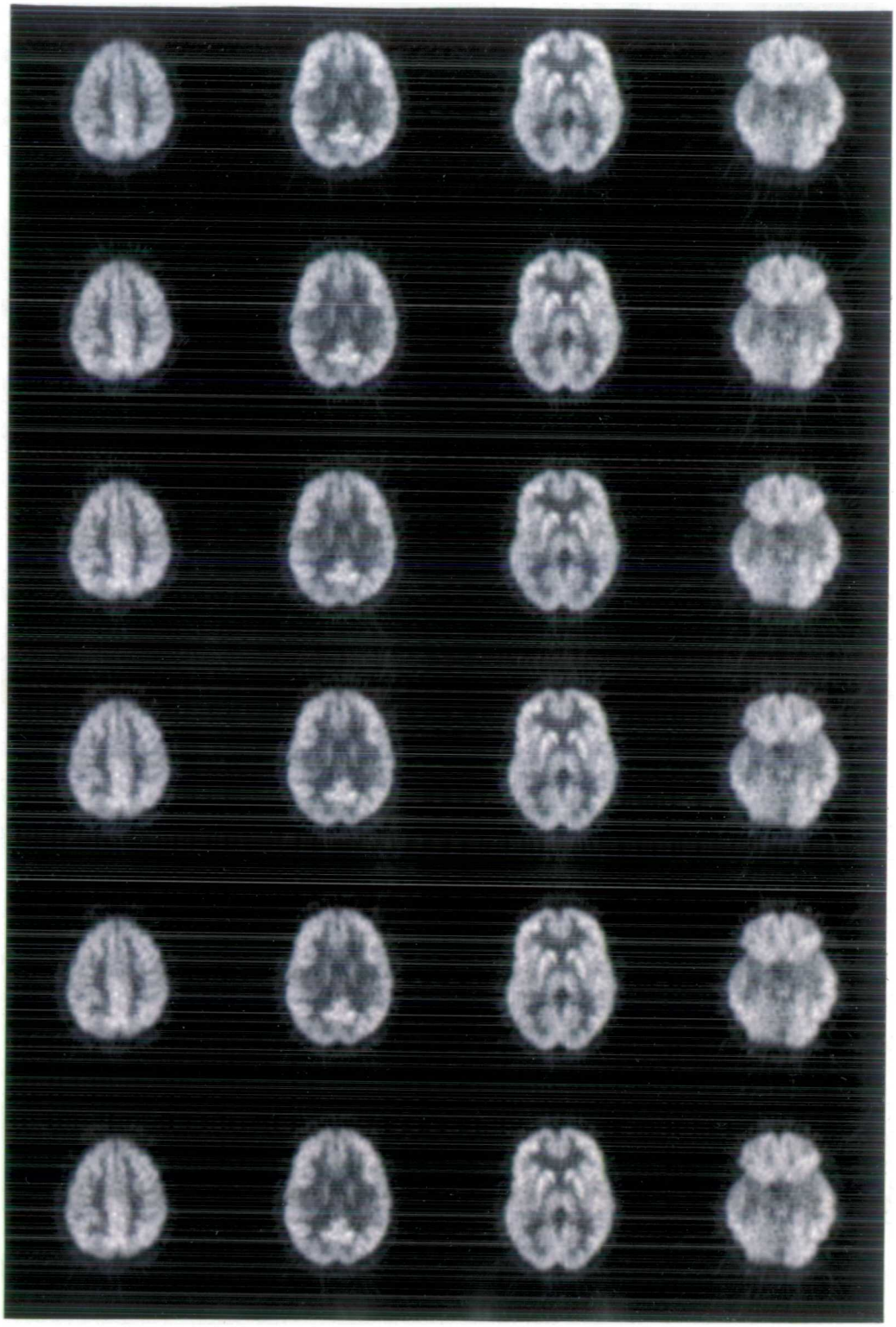

Figure 4.33. Reconstructed images derived from an ^{18}F-FDG adult human brain scan. Total of 2 x 10^8 counts acquired. From left to right: image planes 10,15,20,25.
Row 1: no radial geometric correction
Row 2: no block-profile correction
Row 3: no crystal efficiency correction
Row 4: no crystal interference correction
Row 5: no time-alignment correction
Row 6: fully normalised
Visually, the different normalisations produce images which are very similar. A central spike artefact is visible in image 10 in all reconstructions.

4.7. Discussion

The normalisation and scatter-correction process presented here has been shown to be reasonably effective for central source distributions, although the occasional presence of high-frequency "spikes" in the exact centre of the FOV remains a problem.

The two most important normalisation components are the radial geometric profile and the axial block-profile. The accuracy of the axial block-profile factors is determined principally by the accuracy of the scatter correction, which has been shown to be around 5-6% for the Gaussian fit and model-based algorithms. However, none of the methods for measuring the radial geometric correction factors presented here are entirely satisfactory. Both of the line-source measurements contain scatter, the distribution of which is not well characterised. The correction derived from the cylinder source is clearly contaminated by residual scatter, and the degree of contamination has been shown to vary in the axial direction. Implementation of fully-3D rod-windowing for rotating line-source acquisitions would help to characterise the scatter in such data, although such a scheme could not be expected to be as accurate as rod-windowing with the septa extended. Further investigation to clarify the role (if any) of count-rate on the radial geometric profile would be useful, as would an investigation of the effects of incidence angle on sensitivity for scattered events.

The separation of crystal efficiencies into rate-dependent and rate-independent components has been shown to be useful, particularly since the transaxial rate-dependent components can be obtained from the emission data. This self-normalisation process can remove artefacts introduced by a poor match between the activity concentration in the normalisation source and the patient, and can even remove artefacts due to the systematic variation in crystal efficiencies across a block without reference to any normalisation data at all. It could be argued that self-normalisation of emission data renders routine normalisation superfluous, since drift of random variations in crystal efficiencies appears to be a small effect, and the axial block-profile, being an average of many efficiencies, is unlikely to change very rapidly either. Unfortunately the data presented here does not settle this matter conclusively.

It appears that the other fixed normalisation components are relatively unimportant in realistic imaging situations. However, since the crystal interference and time-window

alignment factors can easily be obtained from the same data required for the calculation of the radial geometric factors, there is little to be gained by ignoring them.

The effects of energy level discrimination have not been investigated here. However, it is very likely that both LLD and ULD will affect normalisation, and in particular the correction factors for the block-profile component.

It should be noted that the block singles rate dead-time correction scheme presented here is based on the manufacturer's model which is supplied for 2D mode operation, and has not been thoroughly validated for 3D mode. However, it has been shown that the manufacturer's model in very similar equipment (Siemens-CTI ECAT 953B) performs extremely well in 3D mode (Bailey, 1996).

4.8. References

DL Bailey 1997 "A Comparison of Reconstructions from the UK PET Centres" Proceedings of the ECAT Technical Users Meeting, Dresden, Germany, Sept 5-9, 1997

DL Bailey 1996 Quantification in 3D Positron Emission Tomography PhD Thesis, University of Surrey, United Kingdom

ME Casey, H Gadagkar and D Newport 1995 "A component based method for normalisation in volume PET" Proceedings of the 3rd International Meeting on Fully Three-Dimensional Image Reconstruction in Radiology and Nuclear Medicine, Aix-les-Bains, France.

G Germano and EJ Hoffman 1991 "An Investigation of methods of pileup rejection for 2D Array detectors employed in high-resolution PET" *IEEE Trans. Med. Imag.* **10**(2) 223-227

G Germano and EJ Hoffman 1990 "A study of data loss and mispositioning due to pileup in 2-D detectors in PET" IEEE trans. Nucl. Sci. 37(2), 671-675

EJ Hoffman, TM Guerrero, G Germano, WM Digby and M Dahlbom 1989 "PET system calibrations and corrections for quantitative and spatially accurate images" *IEEE Trans. Nuc. Sci.* **36**(1), 1108-1112

JM Ollinger 1995 "Detector efficiency and Compton scatter in fully 3D PET" *IEEE Trans. Nucl. Sci.* **42**(4) 1168-1173

WH Press, SA Teukolsky, WT Etterling and BP Flannery 1992 Numerical Recipes in C, Second Ed., Cambridge University Press, ISBN 0 521 43108 5

CW Stearns 1995 "Scatter correction method for 3D PET using 2D fitted Gaussian functions" *J. Nucl. Med.* **36**(5) 105P

CC Watson, D Newport and ME Casey 1996 "A single-scatter simulation technique for scatter correction in 3D PET" Fully Three-Dimensional Image Reconstruction in Radiology and Nuclear Medicine, Eds P Grangeat and JL Amans, Kluwer Academic Publishers, ISBN 0 7923 4129 5

CC Watson 1997 *private communication*

5. Comparison of performance in 2D and 3D PET

5.1. Introduction

System performance in 2D and 3D PET is dependent on a range of parameters including object size and attenuation characteristics, activity in and adjacent to the FOV, and LLD. The purpose of the work presented in this chapter is to investigate the conditions under which 3D acquisition has the potential to offer improvement over 2D acquisition, and to measure the possible level of improvement, with particular reference to imaging of the body. The factors that limit 2D and 3D PET performance in various imaging situations have also been investigated.

As explained in section 1.3, it is reasonable to expect significant differences in performance between 2D and 3D mode operation. Due to the increase in the number of possible LORs and removal of the septa shadowing effect, there is an increase in sensitivity to true coincidences in 3D mode. However, the absence of septa means that there is also an increase in sensitivity to scattered coincidence events. In addition, removal of the septa increases the sensitivity to single events, increasing system dead-time and the random coincidence rate. A meaningful comparison of scanner performance in 2D and 3D mode must take all of these factors into account. The parameter used here to quantify scanner performance is the Noise Equivalent Count (NEC) rate described by Strother *et al* (1990). The NEC rate is a global measure of scanner count rate performance which effectively corrects the true coincidence count-rate for the statistical noise introduced by scatter and random coincidences.

The NEC rate at the centre of a uniform cylinder of activity is given by Strother et al (1990) as :

$$NEC = \frac{T^2}{T + S_{PHAN} + 2kR} \qquad (5.1)$$

where T is the true coincidence rate, k is the projection fraction, S_{PHAN} is the scatter coincidence rate integrated within the object boundary, and R is the random coincidence rate. The projection fraction k is defined as the number of projection elements crossing the cylinder divided by the total number of projection elements.

In this formula the assumption is made that the correction for randoms is subject to Poisson statistics, whereas the correction for scatter is not. This is because randoms correction is usually performed on-line using a delayed coincidence channel, and is therefore subject to Poisson statistics, whereas most algorithms for the estimation of scatter generate smooth distributions.

NEC rate analysis has been performed by several authors to characterise 3D PET in the brain using both phantoms and simulated data (e.g. Bailey *et al* 1991, Dahlbom *et al* 1993, Stearns *et al* 1995, Bailey *et al* 1996, Bailey *et al* 1997). In this chapter a similar analysis is performed using phantom data, and the measurements have been extended to the torso. The NEC rate has also been investigated as a function of LLD.

By comparing NEC rates, the optimum LLD values have been determined for phantoms with a mean diameter ranging from 13 cm to 41 cm, in both 2D and 3D mode. The optimum activity ranges for 3D acquisition have been determined, and 2D and 3D NEC rates have been compared to obtain an indication of the difference in performance between the two modes. The relative importance of scatter, random events and dead-time in limiting performance in 2D and 3D mode has also been examined.

Although the results obtained are particular to the ECAT 951R scanner used here, the trends observed should be more widely relevant.

5.2. Materials and Methods

5.2.1. Scanner and Phantoms

All acquisitions were performed on an ECAT 951R scanner as described in chapter 2. Measurements were made on four phantoms. The smallest was approximately equal in size to the head of an infant. The next largest was a 20 cm cylinder, an object which has been widely used for this purpose (e.g. Bailey *et al* 1991, Dahlbom *et al* 1993). Two larger phantoms were used to simulate the chest of a thin adult and the chest of an obese adult. These were constructed from an EEC emission phantom (Jordan 1990). The dimensions of the phantoms used are given in Table 5.1.

phantom name	mean diameter (cm)	axial length (cm)	projection fraction*	construction
13 cm cylinder	13.0	26.0	0.24	water filled PVC
20 cm cylinder	20.0	19.0	0.36	water filled perspex
23x30 cm chest	26.5	17.5	0.45	water filled perspex (EEC Emission phantom)
37x48 cm chest	41.0	17.5	0.69	EEC Emission phantom surrounded by tissue equivalent material†

Table 5.1. Physical properties of the phantoms.
* Projection fraction obtained by examining transmission scan of cold phantom.
† Composition: soft paraffin 46.4% by mass, acrylic granules 53.6% by mass. Linear attenuation coefficient within 1% of water over energy range 150 - 500 keV, linear absorption coefficient within 1% of water over energy range 150-500 keV.

5.2.2. Scatter Measurements

The scatter fraction across the entire FOV (F_{FOV}) is defined as follows:

$$F_{FOV} = \frac{S_{FOV}}{T + S_{FOV}} \tag{5.2}$$

where T represents the true unscattered counts and S_{FOV} represents the scattered counts over the entire FOV. F_{FOV} was evaluated for each phantom in 2D and in 3D at LLDs varying in 50 keV steps from 50 keV to 550 keV.

Scatter measurements were made at each LLD value using a germanium line source (length 11 cm, diameter < 6 mm, and activity ~ 25 MBq). In order to obtain a scatter fraction representative of the whole object, data were acquired with the line source positioned at

several different radii within each phantom using the method described by Guzzardi and Bellina (1990).

The scatter component S_r at each radial position r was obtained by integrating under the scatter tails and interpolating under the true coincidence peak in the sinogram profile. The unscattered true count rate T_r at each position r was obtained by subtracting the total scattered counts from the total counts in the summed profile. The overall scatter fraction was then calculated as follows :

$$F_{FOV} = \frac{\sum_r A_r S_r}{\sum_r A_r T_r + \sum_r A_r S_r} \tag{5.3}$$

where A_r is the area of an annulus at radius r. The values for A_r used correspond to the regions shown in figure 5.1. The rod source positions and the outer boundaries of the annuli are described in table 5.2.

The outermost annuli for the chest phantoms are non-circular. While use of non-circular annuli in this way will inevitably lead to some inaccuracies in the calculation of F_{FOV} , the estimate of the scatter fraction should be more accurate than that derived from a central line source measurement alone.

The calculation of NEC rates uses the scatter fraction within the object, F_{PHAN}. This is defined similarly to F_{FOV} , except that the scatter contribution is integrated only within the object boundary. The object boundaries were determined from septa-extended 2D-mode transmission sinograms of the cold phantoms. For the largest phantom, where the activity did not extend to the edge of the phantom, scatter was integrated to the object boundary, but the outermost annulus used in the calculation of F_{PHAN} extended only to the edge of the active region.

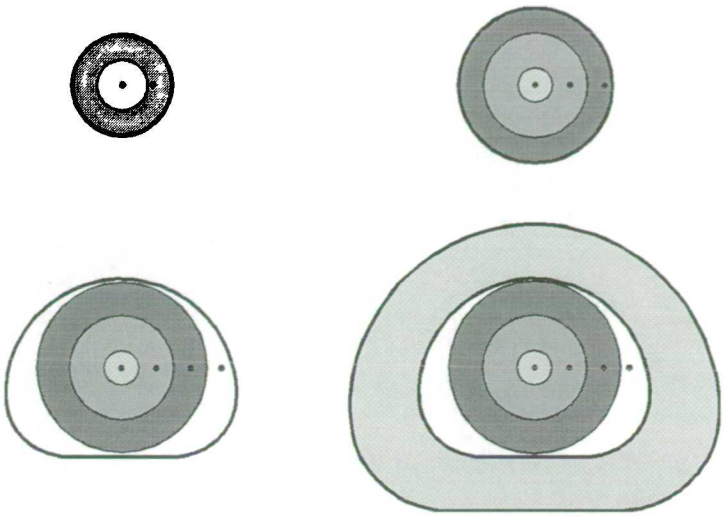

Figure 5.1. Phantoms used in the NEC rate measurements.
The rod source positions and annuli used to calculate scatter fractions are shown.
Clockwise from top left: 13cm cylinder, 20 cm cylinder, 20x30 cm chest, 27x48cm chest.
Dots indicate line-source positions. The outermost annulus of the largest phantom shows the extent of the tissue-equivalent padding material.

The transmission source spill-over effect described in chapter 2 was corrected for by acquiring a 3D emission scan with the septa and transmission source retracted at each LLD used. An appropriate correction for each measurement was then generated from this data.

Phantom	Rod 1	Rod 2	Rod 3	Rod 4	Annu. 1	Annu. 2	Annu. 3	Annu. 4
13 cm cylinder	central	4.0	-	-	3.25	6.5	-	-
20 cm cylinder	central	4.5	9.0	-	2.25	6.75	10.0	-
23x30 cm chest	central	4.5	9.0	13.0	2.25	6.75	11.0	11.25 x 15.0
37x48 cm chest	central	4.5	9.0	14.5	2.25	6.75	11.25	11.25 x 15.0

Table 5.2. Rod source positions and annulus outer boundaries for scatter measurements.
Units are cm. For non-circular outer boundaries, extremal radii are given.

5.2.3. Count-Rate Measurements.

Count rate data were obtained as function of activity in the FOV, LLD, phantom size and acquisition mode.

The 3 smaller phantoms were filled with a uniform distribution of ^{18}F in water such that there were between 170-250 MBq in the FOV for the first measurement. The largest phantom had a similar amount of ^{18}F solution placed within the volume of the EEC emission phantom. Scans of one minute duration were repeatedly acquired at LLDs varying in 50 keV steps from 150 to 500 keV over a period of 6 - 8 half-lives (12 - 16 hours). Scans were performed in 2D and in 3D mode.

The random coincidence rate R was measured by the delayed coincidence channel, and the true coincidence rate T was obtained by multiplying the net coincidence rate C_{net} (defined as prompt - random coincidences) by the overall trues fraction (1- F_{FOV}). The scatter coincidence rate within the phantom boundary S_{PHAN} was derived from C_{net} according to the following equation :

$$S_{PHAN} = C_{net} \cdot \frac{F_{PHAN}\left(1 - F_{FOV}\right)}{\left(1 - F_{PHAN}\right)} \tag{5.4}$$

For all phantoms at fixed LLDs, the ratio of net coincidence rate to activity in the FOV was obtained by linear regression for data points where the dead-time was negligible (activity in the FOV less than 2 MBq, all prompt coincidence rates between 1500 and 7000 cps). These ratios were used in conjunction with observed net coincidence rates to calculate fractional dead-times at higher activity levels.

Finally NEC rates were calculated as a function of activity in the FOV, phantom size, LLD and acquisition mode.

Since the outermost 15-18 cm of the largest phantom consisted of tissue-equivalent padding, the activity was more centralised than would have been the case with a uniformly filled phantom. Both dead-time effects and NEC rates will be affected by this. Nevertheless, the padded phantom would be expected to be a better model for an obese patient than the EEC chest phantom alone.

5.3. Results

5.3.1. Scatter Fractions

Scatter fractions for the larger phantoms show a strong dependence on LLD. This can be seen in figures 5.2a and 5.2b, which show the scatter fraction within the object boundary F_{PHAN} as a function of LLD for each phantom in 3D and 2D mode respectively. For the 37x48 cm chest phantom in 3D the scatter fraction is 60% at an LLD of 250 keV, whereas at an LLD of 450 keV the scatter fraction drops to 41%.

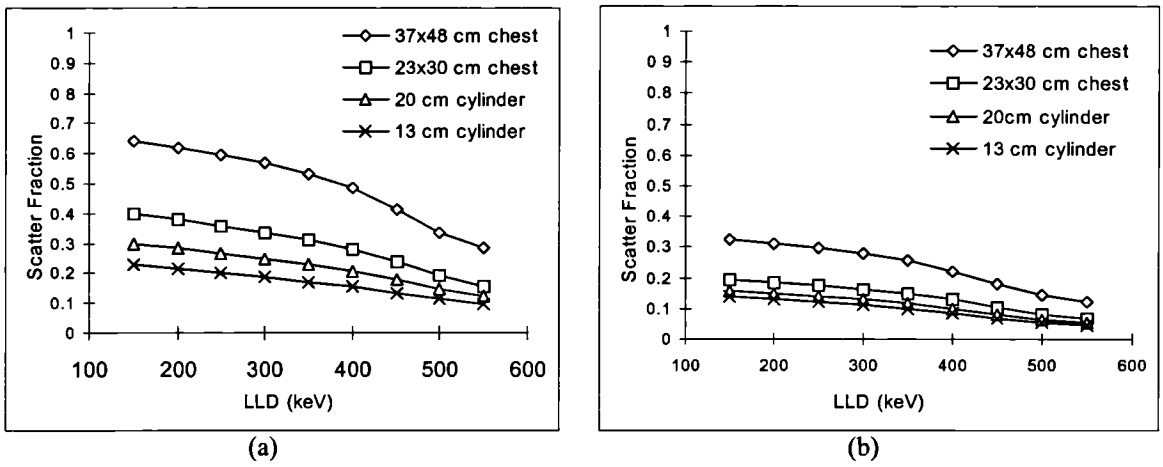

Figure 5.2. Scatter fractions.
(a) 3D scatter fraction as a function of LLD for all phantoms.
(b) 2D scatter fraction as a function of LLD for all phantoms.

5.3.2. Count Rates

The total prompt, random, scatter and true coincidence rates at any given activity in the FOV in 3D mode all increase significantly as the phantom size is reduced. These rates are plotted for the smallest and largest phantoms at an LLD of 250 keV in figure 5.3. With 50 MBq in the FOV the prompts rate is approximately five times greater for the 13 cm cylinder than it is for the 37x48 cm chest phantom, leading to a significant increase in dead-time. The effect of dead-time can be clearly seen for the 13 cm cylinder (figure 5.3a) where the trues rate saturates with about 80 MBq in the FOV. The calculated fractional dead-times for all the phantoms are plotted as a function of activity in the FOV in figure 5.5, and it can be seen that for a given activity in the FOV the dead-time becomes significantly lower as the phantom size is increased. For the largest phantom the dominant effect at high activities is not dead-time but random coincidences (figure 5.3b).

As expected the count rates in 2D mode are very much lower at the activities studied than those for the same phantoms in 3D. The 2D count rates for the smallest and largest phantoms are shown in figures 5.4a and 5.4b. With 50 MBq in the FOV the prompts are lower in 2D than in 3D by a factor of 6 for the small phantom, and by a factor of 10 for the large phantom. The random coincidence rates are also very significantly lower in 2D. For both phantoms with 50 MBq in the FOV the randoms rates lie between 3% and 5% of their 3D values.

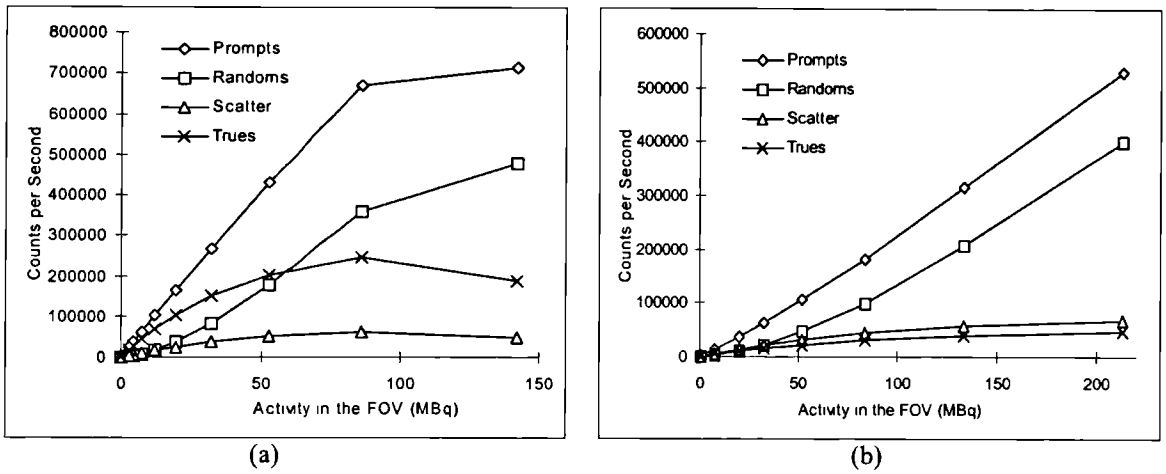

Figure 5.3. 3D mode count-rates as a function of activity in the FOV.
(a) 3D prompt, random, scatter and true coincidence rates for the 13 cm cylinder. The LLD is set to 250 keV. Scatter is integrated up to the cylinder boundary.
(b) 3D prompt, random, scatter and true coincidence rates for the 37x48 cm chest phantom. The LLD is set to 250 keV. Scatter is integrated up to the phantom boundary.

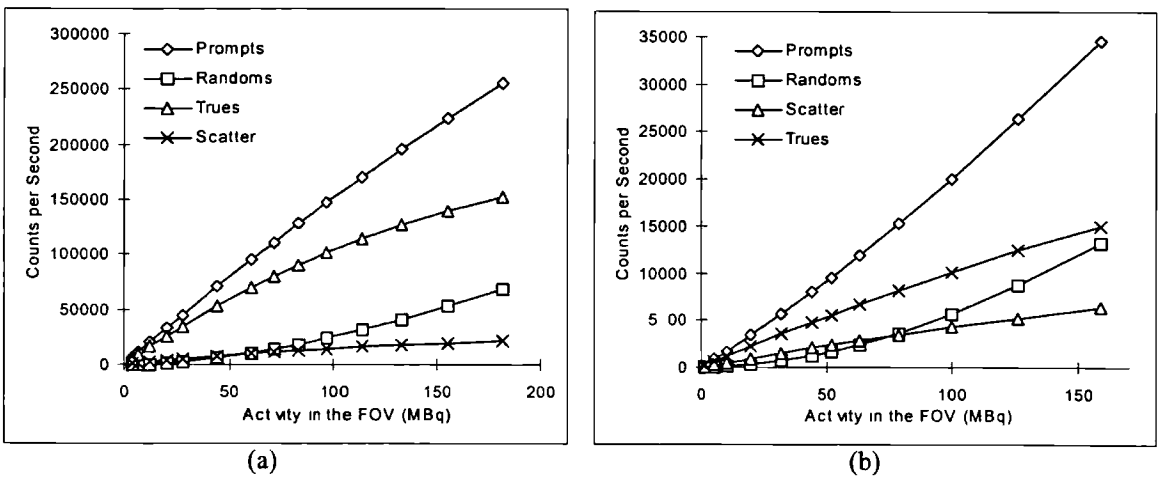

Figure 5.4. 2D mode count-rates as a function of activity in the FOV.
(a) 2D prompt, random, scatter and true coincidence rates for the 13 cm cylinder. The LLD is set to 250 keV. Scatter is integrated up to the cylinder boundary.
(b) 2D prompt, random, scatter and true coincidence rates for the 37x48 cm chest phantom. The LLD is set to 250 keV. Scatter is integrated up to the phantom boundary.

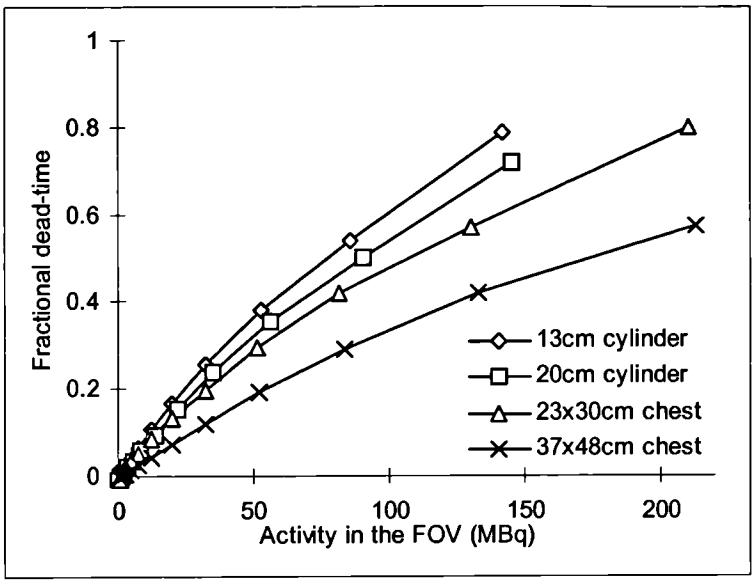

Figure 5.5. Calculated fractional dead-times in 3D mode for all phantoms as a function of activity in the FOV.
The LLD is set to 250 keV.

5.3.3. NEC Rates

The 3D mode NEC rates for the smallest and largest phantoms are plotted as a function of LLD and activity in the FOV in figures 5.6 and 5.7 respectively. For both phantoms it can be seen that there is little to be gained in terms of NEC by increasing the activity in the FOV much beyond 50 MBq. For the larger phantom, doubling the activity in the FOV from 50 to 100 MBq gives only a 20% increase in NEC at optimum LLD, and for the smaller phantom the benefit is even less. The absolute NEC rates are much lower overall for the larger phantom (note that the vertical scale is reduced by a factor of 20 in figure 5.7 compared to figure 5.6).

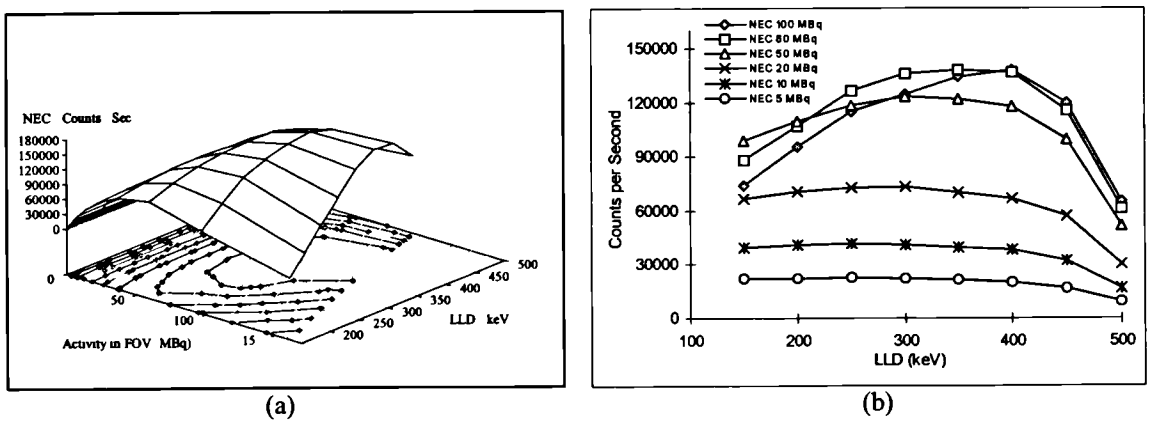

(a) (b)

Figure 5.6. 3D NEC as a function of activity in the FOV and of LLD for the 13 cm cylinder.
(a) Surface plot. Contours of equal NEC rate are plotted at intervals of 10 % of the maximum.
(b) Line plots at selected activities.

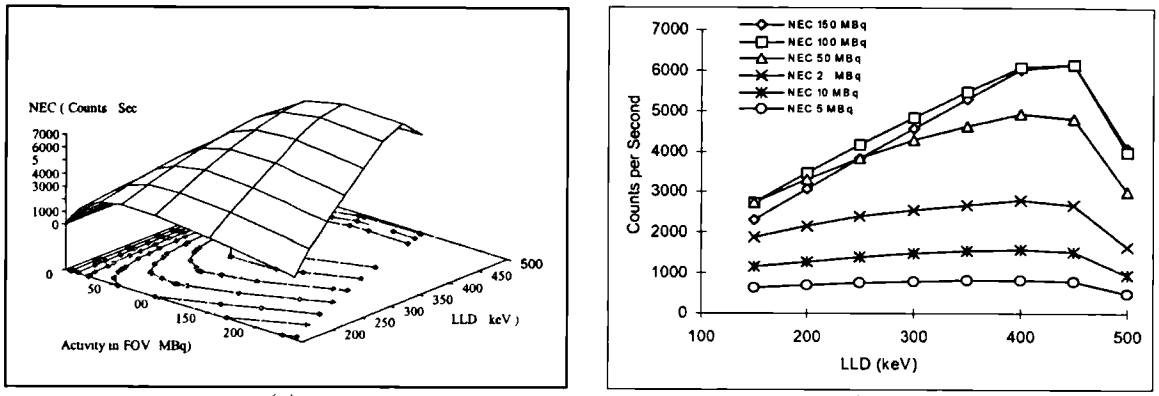

(a) (b)

Figure 5.7. 3D NEC as a function of activity in the FOV and of LLD for the 37x48 cm chest phantom.
(a) Surface plot. Contours of equal NEC rate are plotted at intervals of 10 % of the maximum.
(b) Line plots at selected activities.

For both phantoms the dependence of NEC on LLD becomes stronger as the activity in the FOV is increased. However, for the larger phantom the LLD value giving optimum NEC (the "optimum LLD") is consistently higher than for the smaller one. For the smaller phantom the optimum LLD value changes significantly as the activity in the FOV changes, rising from 250 keV with 5 MBq in the FOV, to 400 keV with 100 MBq in the FOV.

LLD values giving optimum measured 3D NEC performance for all phantoms over a range of activities are given in table 5.3. These values are limited by the fact that the LLD was sampled in 50 keV steps. This is unlikely to prove important for the smaller phantoms and for activities in the FOV of 50 MBq or less, since under these conditions NEC changes quite slowly with LLD.

Phantom	Optimum LLD 10 MBq in FOV	Optimum LLD 20 MBq in FOV	Optimum LLD 50 MBq in FOV	Optimum LLD 100 MBq in FOV
13 cm cylinder	250	300	300	400
20 cm cylinder	250	300	350	400
23x30 cm chest	300	350	400	400
37x48 cm chest	400	400	400	450

Table 5.3. Optimum 3D-mode LLDs in keV at different activities for all phantoms.

Figures 5.8 and 5.9 show 2D NEC rates as a function of activity in the FOV and LLD for the smallest and the largest phantoms. This time the two plots are of very similar shape, indicating a weaker dependence of the optimum scanning parameters on phantom size. NEC rates show a more linear response to changes in activity in the FOV up to 100 MBq than is the case in 3D. They also display less dependence on LLD than in 3D. For the smaller phantom the LLD value giving optimum NEC performance changes from 200 to 250 keV as

the activity in the FOV is increased from 5 to 100 MBq, whereas for the larger phantom the optimum LLD rises from 250 to 400 keV over the same activity range. Again there is a greater dependence of NEC on LLD for the larger phantom.

LLD values giving optimum 2D NEC performance for all phantoms over a range of activities are given in table 5.4.

Phantom	Optimum LLD 10 MBq in FOV	Optimum LLD 20 MBq in FOV	Optimum LLD 50 MBq in FOV	Optimum LLD 100 MBq in FOV
13 cm cylinder	200	200	250	250
20 cm cylinder	200	250	250	250
23x30 cm chest	250	250	250	300
37x48 cm chest	250	250	400	400

Table 5.4. Optimum 2D-mode LLDs in keV at different activities for all phantoms.

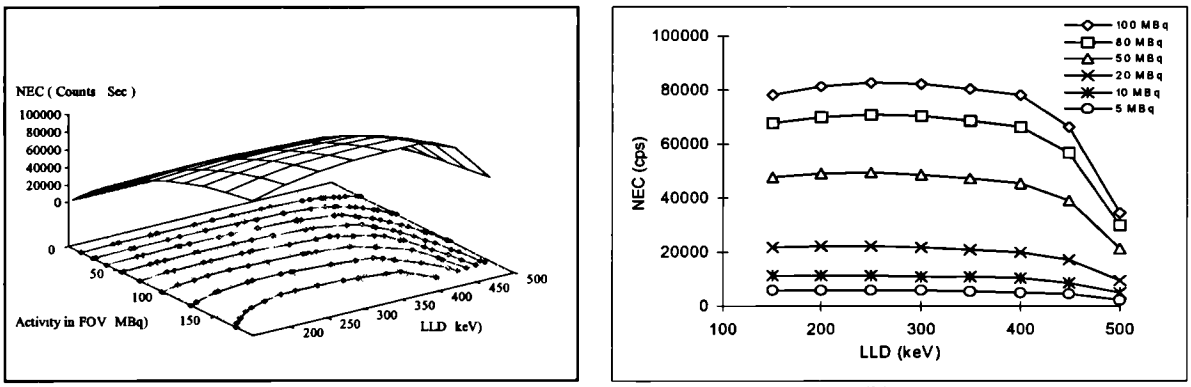

(a) (b)

Figure 5.8. 2D NEC as a function of activity in the FOV and of LLD for the 13 cm cylinder.
(a) Surface plot. Contours of equal NEC rate are plotted at intervals of 10 % of the maximum.
(b) Line plots at selected activities.

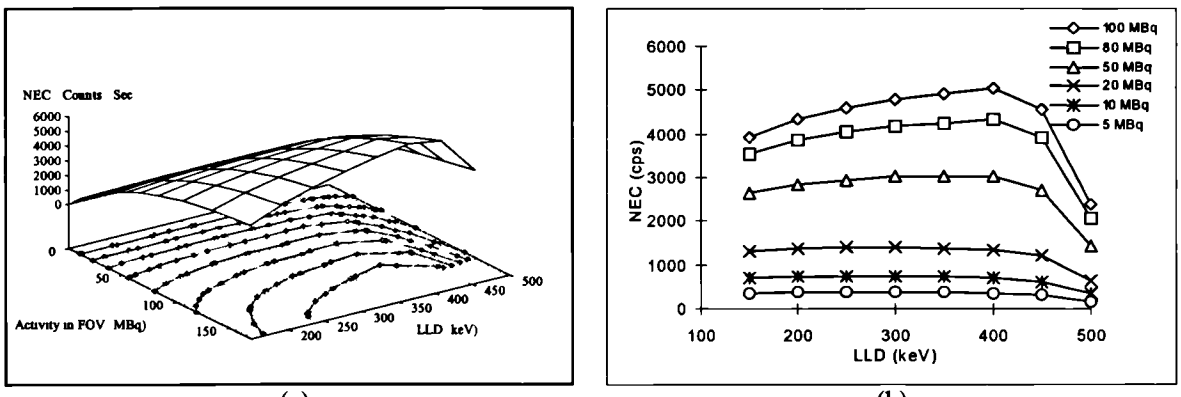

(a) (b)

Figure 5.9. 2D NEC as a function of activity in the FOV and of LLD for the 37x48 cm chest phantom.
(a) Surface plot. Contours of equal NEC rate are plotted at intervals of 10 % of the maximum.
(b) Line plots at selected activities.

Typically, clinical brain studies and whole body studies are performed with approximately 20 MBq in the FOV. In the case of a child this may be scaled with body weight. Figure 5.10 shows 3D NEC rates as function of activity in the FOV for all phantoms at LLDs selected with these protocols in mind (see table 5.5). The peak NEC rate decreases with increasing phantom size, and for the 37x48 cm chest phantom, the peak rate is less than 4.5% of that of the 13 cm cylinder. While the data sampling is quite sparse at high activities, it can be seen that the activity giving rise to peak NEC rate increases with increasing phantom size. In all cases the NEC rate starts to decrease when the activity in the FOV is raised above 120 MBq.

Phantom	3D LLD (keV)	2D LLD (keV)
13 cm cylinder	250	200
20 cm cylinder	350	300
23x30 cm chest	350	250
37x48 cm chest	400	300

Table 5.5. Optimum LLDs for typical clinical studies (20 MBq in the FOV)

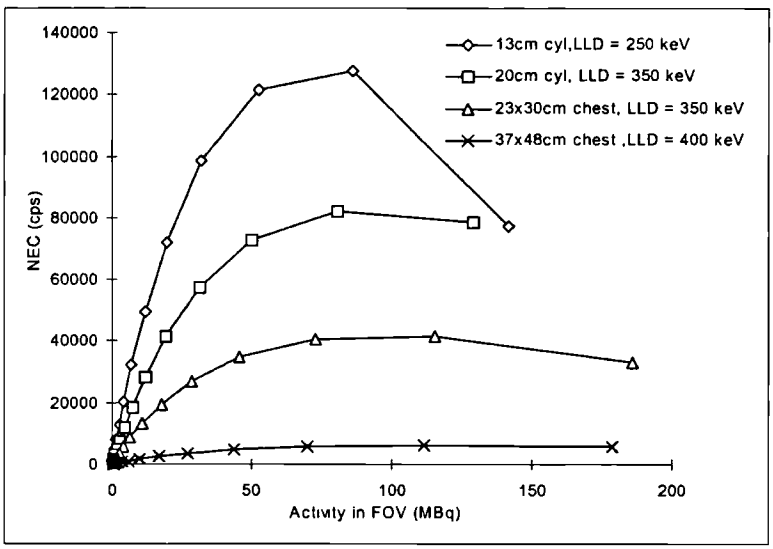

Figure 5.10. 3D NEC rates as a function of activity in the FOV for all phantoms. The curves are plotted at the LLDs given in table 5.5.

5.3.4. Comparison of 3D and 2D NEC rates

In order to establish the activities at which 3D mode shows improved NEC performance over 2D, ratios of NEC rates were calculated for each phantom. The NEC rates were evaluated at the LLD values shown in table 5.5 and the resultant curves are plotted in figure 5.11(a). The 3D to 2D mode NEC ratios decrease monotonically with increasing activity in the FOV. 3D to 2D mode NEC ratios are greater than 2 when less than ~ 35 MBq is present in the FOV for

all phantoms except the largest, where a ratio of 2 is never achieved. No significant gains in NEC can be expected in 3D mode for any phantom when the activity in the FOV is greater than 150 MBq.

To investigate the potential for dose reduction when using 3D mode, the ratios of 3D NEC rates over a range of activities to 2D NEC rates at a constant activity were calculated. For the three largest phantoms the 2D NEC rate was chosen to be that obtained with 20 MBq in the FOV, whereas for the smallest phantom it was chosen to be that obtained with 6 MBq in the FOV (a typical value for a 2D brain study of a young child). These curves are plotted in Figure 5.11(b). For the 13 cm and 20 cm cylinders, use of 3D mode together with a reduction in dose by 30% still results in a 2-fold gain in NEC compared to 2D mode. There is less scope for dose reduction for the larger phantoms.

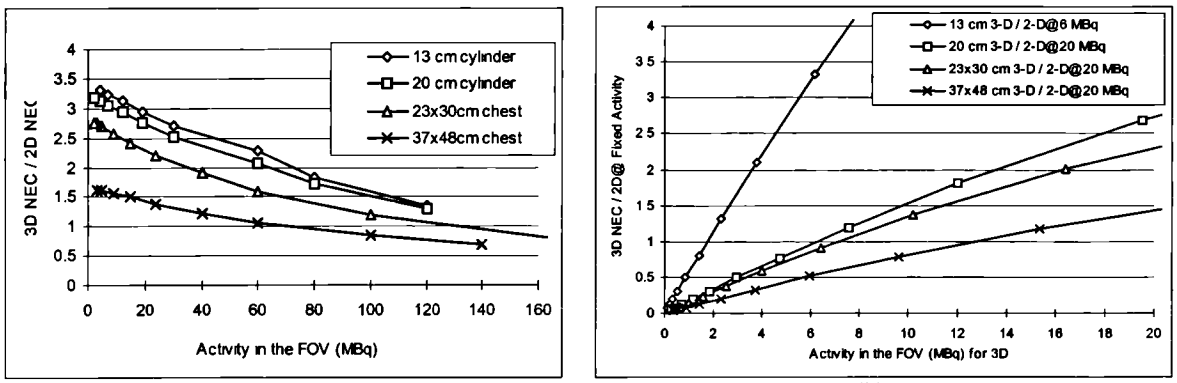

(a) (b)

Figure 5.11. 2D and 3D mode NEC ratios.
(a) Ratios of 3D NEC to 2D NEC as a function of activity in the FOV for all phantoms. LLD values are those given in table 5.5.
(b)Ratios of 3D NEC to (2D NEC at selected activity) for all phantoms as a function of activity in the FOV. LLD values are those given in table 5.5.

5.4. Discussion

5.4.1. Factors limiting NEC rates

Aside from system sensitivity, there are three main factors limiting NEC rates in PET. These are scatter, random coincidences and dead-time. In 3D mode, the data presented here indicate that random coincidences are an important factor, and that they become more so as the phantom size increases. For the largest phantom the randoms term ($2kR$) becomes greater than the scatter term (S_{PHAN}) in the NEC formula at an activity in the FOV of 27 MBq for all LLDs. For the smallest phantom this occurs at the slightly higher activity of 35 MBq. At activities in the FOV giving peak NEC rates, $2kR$ is considerably larger than S_{PHAN}. The importance of random coincidences has significant consequences for the use of tracers with short half-lives. For example, quantitative studies of myocardial blood-flow using ^{13}N-NH_3 involve the injection of large amounts of activity (~600 MBq) and the acquisition of dynamic datasets shortly after injection. It is difficult to see how this could be successfully performed in 3D mode without significant alterations to the protocol.

It also appears that whereas for the smallest phantom dead-time is the most important factor limiting the peak NEC rate, for the largest phantom randoms are more significant. This is supported by two facts. Firstly, with around 100 MBq in the FOV (the region where the NEC curves start to fall) and at an LLD of 250 keV, the percentage dead-time is approximately 70% for the 13 cm cylinder, which is almost twice that found for the 37x48 cm chest phantom. Secondly, as the activity in the FOV rises beyond 100 MBq , the true coincidence rate for the smallest phantom starts to fall, whereas that for the largest phantom continues to increase, and is still increasing as the activity in the FOV passes 150 MBq.

Random coincidences are far less important in 2D than in 3D at the activities studied. For the smallest phantom the randoms term in the NEC calculation overtakes the scatter term when the activity in the FOV rises above 110 MBq for all LLDs (compared to 35 MBq in 3D mode). For the largest phantom this occurs at the higher activity of 120 MBq. This is the reverse of the 3D case, suggesting that in 2D the increase in the randoms to prompts ratio for the largest phantom is not as important as the increase in scatter fraction.

The random coincidence rate has a significant effect on NEC not only because it increases with the square of the activity in the FOV, but also because element by element subtraction using measurements from a delayed coincidence channel itself introduces noise. Techniques for randoms correction which do not increase the noise contribution in this way could improve NEC rates, particularly for larger objects. This matter is investigated further in the following chapter.

Since the randoms coincidence rate is directly proportional to the coincidence resolving time, the use of faster scintillation crystals would be desirable. In particular LSO has a scintillation decay time which is an order of magnitude less than that of BGO. If this improvement could be realised in terms of reduction of the coincidence resolving time, further gains in NEC rates could be obtained.

5.4.2. Optimisation of NEC rates

The data indicate that significant gains in performance can be obtained by optimising acquisition parameters. For example, the 3D mode NEC rate at 50 MBq for the largest phantom can be increased by 25-30% and the scatter fraction reduced by approximately 20% by increasing the LLD from 250 to 400 keV. Optimisation of LLD becomes even more important with greater amounts of activity in the FOV.

Since the benefits of 3D are greater at low activities for all phantoms, dose fractionation (whereby the administered activity is divided into smaller sequential administrations) would improve the ratio of total NEC to total administered activity. The potential benefits of dose fractionation have been quantified for head-sized phantoms by Dahlbom *et al* (1993), and the technique has proved very successful in brain activation studies with ^{15}O-water (Cherry *et al* 1993, Silbersweig *et al* 1993), with up to 12 low activity administrations being given in succession. The method is particularly suited to the short half-life of ^{15}O (123 sec) and to the requirements of brain activation protocols. It may be possible to develop similar strategies to optimise 3D imaging with ^{13}N and ^{11}C - labelled tracers, but this poses many problems. The longer half lives mean that only a small number of repeat administrations would be possible if studies are not to be made impractically long, and careful attention would have to be paid to tracer kinetics.

A feature of the 3D technique is that the statistical quality of the data improve from the edge to the centre of the axial FOV (see sections 1.3 and 2.4). Caution should therefore be exercised where the improvements in NEC are small, as NEC rates only provide an average signal-to-noise index for the whole dataset. If a large field of view is required, it is probably unwise to assume that where the 3D to 2D NEC ratio is close to unity, the 3D method will produce a scan as useful as the 2D method. However, if the region of interest can be accurately placed in the centre of the scanner, then the NEC ratio will underestimate the potential benefits of 3D.

It is interesting to note that while at optimum LLD the scatter fraction for the largest phantom in 3D mode is approximately 50%, in 2D mode at the typical LLD of 250 keV it is still around 30%. While the 2D scatter fraction may be reduced to 22% by increasing the LLD to 400 keV, this may still have implications for calculations of Standard Uptake Values (Strauss and Conti 1991), since scatter corrections are not often performed in whole-body studies.

Both the random and true coincidence rates are a function of the resolving time of the coincidence circuitry. It seems likely therefore that further optimisation of the NEC rate could be obtained by varying this parameter. It is not a simple matter to change the coincidence resolving time on most current PET scanners but the capability could be incorporated into future designs.

5.4.3. The effect of scanner geometry on NEC rates.

Brain scanners and more recent whole-body scanners have a smaller ring diameter and a larger acceptance angle than the ECAT 951R used in this study. These differences may have a significant impact on the factors affecting NEC rates. For example the value for 3D scatter fraction obtained in this work for a 20 cm cylinder at an LLD of 250 keV is 0.27, whereas that obtained for an ECAT 831 brain scanner is 0.32 (Cherry *et al* 1991). Such geometrical factors, together with differences in detectors and electronics may alter the optimum values for the parameters examined here. Dahlbom *et al* (1993) made direct comparisons of different scanners, and showed that the LLD giving optimum 2D NEC performance for an ECAT EXACT with a 20 cm cylinder uniformly filled with activity was 350 keV while that for an ECAT EXACT HR the optimum LLD was 250 keV with a similar activity in the

FOV. The difference between 2D and 3D mode performance on tomographs with a larger axial FOV (such as the ECAT HR+) is difficult to predict without direct measurements. The larger acceptance angle and greater number of detector rings present on such scanners compared to the ECAT 951R will certainly mean greater sensitivity in 3D mode, but may also adversely affect both the randoms to prompts ratio and the scatter fraction.

This study does not explicitly address the issue of activity outside of the FOV. The phantoms used extended 40-50 mm either side of the FOV, which is within the region of sensitivity to single events (see section 2.2.1), so the data shown here do include the effects of some activity adjacent to the FOV. However, it is quite possible in realistic imaging situations to have similar amounts or even very much more activity adjacent to the FOV than there is within it. Examples include cardiac NH_3 studies where there is significant uptake in the liver, or head and neck studies with ^{18}F-FDG, where the brain overlays the edge of the FOV. In these circumstances the randoms rates and scatter fractions are likely to be greater than those found in this study. This is supported by the results of phantom studies carried out by Townsend *et al* (1995).

For the latest generation of septaless scanners such as the ECAT ART and HR++, NEC studies along the lines described here may well be misleading, as the FOV for single events is considerably larger than for the 951R and in such circumstances a phantom of length ~20 cm is a poor model of a human body. Recent work has shown that for these cameras random coincidences can be a very significant problem (Bailey *et al* 1997, Bailey *et al* 1998, Spinks *et al* 1998).

5.5. Conclusions

The data shown here indicate that for an ECAT 951R use of 3D mode acquisition results in significant increases in NEC rate compared to 2D mode for most scanning situations, including scanning of the torso, provided the scanning parameters are optimised. The greatest improvements are likely to be seen when children are scanned. However, the gains likely when scanning obese patients are modest, even with small amounts of activity in the FOV.

Scanning parameters should be optimised for individual protocols. For example an NH_3 cardiac study may consist of two parts, the first (immediately after injection) having approximately 600 MBq in the FOV, and the second (as the activity decays) having between 150 and 50 MBq in the FOV. Such a protocol would require a mixture of 2D and 3D acquisitions to make the best use of injected dose.

With large objects and large amounts of activity in the FOV the most important factors limiting 3D mode NEC are randoms and dead-time rather than scatter, and for all types of studies we would expect to see degradation of data quality compared to 2D mode if the activity in the FOV is allowed to rise above 150 MBq.

5.6. References

DL Bailey, T Jones, TJ Spinks, MC Gilardi and DW Townsend 1991 "Noise Equivalent Count Measurements in a Neuro-PET Scanner with Retractable Septa" *IEEE Trans. Med. Imag.* **10**(3):256-260

Bailey D L, Lee K S, Stocks G, Meikle S R, Dobko T 1993 "Clinical 3D PET for Improved Patient Throughput" *J Nucl Med* **34**(5):184P

DL Bailey, H Young, PM Bloomfield, SR Meikle, D Glass, MJ Myers, TJ Spinks, CC Watson, P Luk, AM Peters and Terry Jones 1997 "ECAT ART - a continuously rotating PET camera: performance characteristics, initial clinical studies, and installation considerations in a nuclear medicine department" *Eur. J. Nucl. Med* **24** (1) 6-15

DL Bailey, SR Meikle and T Jones 1997 "Effective Sensitivity in 3D PET: The Impact of Detector Dead Time on 3D System Performance" *IEEE Trans Nucl Sci.* **44**(3):1180-1185

DL Bailey, MP Miller, TJ Spinks, PM Bloomfield, L Livieratos, HE Young and T Jones 1998 "Experience with fully 3D PET and implications for future high resolution 3D tomographs" *Phys. Med. Biol.* **43**(4) *to appear*

SR Cherry, M Dahlbom and EJ Hoffman 1991 "3D PET using a Conventional Multislice Tomograph without Septa" *J Comput Assist Tomogr* **15**(4):655-668

SR Cherry , RP Woods, EJ Hoffman and JC Mazziotta 1993 "Improved Detection of Focal Cerebral Blood Flow Changes Using Three-Dimensional Positron Emission Tomography" *J Cereb Blood Flow Metab* **13**(4):630-638

M Dahlbom, SR Cherry, L Eriksson, EJ Hoffman and K Wienhard 1993 "Optimization of PET Instrumentation for Brain Activation Studies" *IEEE Trans Nucl Sci.* **40**(4):1049-1054

R Guzzardi and CR Bellina 1990 Reconstructed Scatter Fraction *Chapter 5, "Performance Evaluation of Positron Emission Tomographs", Medical and Public Health Research Programme of the European Communities*

EJ Hoffman, S-C Huang, ME Phelps, and DE Kuhl 1981 "Quantitation in Positron Emission Computed Tomography: 4. Effect of Accidental Coincidences" *J Comput Assist Tomogr* **5**(3):391-400

K Jordan 1990 EEC Emission phantom *Appendix, "Performance Evaluation of Positron Emission Tomographs", Medical and Public Health Research Programme of the European Communities*

PE Kinahan, F Jadali, D Sashin, ML Brown, MA Mintun, RL Baron and DW Townsend 1995 "A comparison of 2D and 3D abdominal PET imaging" *J Nucl Med* **36**(5):7P

DA Silbersweig , E Stern , CD Frith, C Cahill, L Schnorr, S Grootoonk, T Spinks, J Clark J, R Frackowiak, and T Jones 1993 "Detection of Thirty-Second Cognitive Activations in Single Subjects with Positron Emission Tomography: A New Low-Dose $H_2{}^{15}O$ Regional Cerebral Blood Flow Three-Dimensional Imaging Technique" *J Cereb Blood Flow Metab* **13**(4)617- 629

TJ Spinks, MP Miller, DL Bailey, PM Bloomfield, L Livieratos and T Jones 1998 "The effect of activity outside the direct field of view in a 3D-only whole-body positron tomograph" *Phys. Med. Biol.* **43**(4) *to appear.*

CW Stearns, SR Cherry and CJ Thompson 1995 "NECR Analysis of 3D Brain PET Scanner Designs" *IEEE Trans Nucl Sci.* **42**(4):1075-1079

LG Strauss and PS Conti 1991 "The Application of PET in Clinical Oncology" *J Nucl Med* **32**(4):623-648

SC Strother, ME Casey and EJ Hoffman 1990 "Measuring PET Scanner Sensitivity: Relating Count rates to Image Signal-to-Noise Ratios using Noise Equivalent Counts" *IEEE Trans Nucl Sci* **37**(2):783-788

D Townsend, P Kinahan , T Beyer , F Jadali , D Sashin and M Mintun 1995 "Performance Characteristics of PET Scanners operated in 3D mode" *Proceedings of the 1995 CEA/LETI International Meeting on Fully Three-Dimensional Image Reconstruction in Radiology and Nuclear Medicine.*

6. Variance reduction techniques for random coincidences in 3D PET

6.1. Introduction

In the previous chapter it was shown that the noise introduced by random coincidences is an important limiting factor of peak NEC performance in 3D mode. The recent trend of producing tomographs with extended FOVs and more open geometries has exacerbated this problem, as such tomographs have a significantly increased sensitivity to photons arising from outside of the coincidence FOV (Bailey *et al* 1998). These developments have re-kindled interest in methods of reducing the effect of random coincidences on acquired data.

The number of random coincidences detected may be reduced by altering the camera geometry to restrict the singles FOV (e.g. Spinks *et al* 1998) or by reducing the coincidence resolving time of the system. Alternative ways to reduce the effect of random coincidences on the data revolve around the methods used to correct for their presence.

The number of random coincidences on a particular LOR may be estimated in two different ways. Given that rate of random coincidences R_{ij} on an LOR joining two detectors i and j is

$$R_{ij} = 2\tau\, r_i\, r_j \tag{6.1}$$

where r_i and r_j are the singles rates on detectors i and j respectively and τ is the resolving time of the coincidence circuitry, the randoms rate may be calculated from the relevant singles rates. However, few of the current generation of cameras allow the collection of singles rates from individual detector elements, and the delayed coincidence channel approach is more common. The resulting estimate of the number of random coincidences in each LOR is then subtracted from the number of prompt coincidences to yield the combined number of true and scattered coincidences. Both of these approaches are described in more detail in section 1.6.3.

If R_{ij}, S_{ij} and T_{ij} are the numbers of random, scattered and true coincidences in the LOR joining detectors i and j respectively, the noise in the prompt signal N_P (assuming Poisson statistics) is given by:

$$N_P = (R_{ij} + S_{ij} + T_{ij})^{1/2} \tag{6.2}$$

If the randoms as measured by the delayed channel method are subtracted the noise becomes:

$$N_{T+S} = (N_P^2 + R_{ij})^{1/2} = (2R_{ij} + S_{ij} + T_{ij})^{1/2} \tag{6.3}$$

since the delayed channel estimate is also subject to Poisson statistics. However, if a noise-free estimate of R_{ij} could be used, the noise would be:

$$N_{T+S} = (R_{ij} + S_{ij} + T_{ij})^{1/2} \tag{6.4}$$

and the expression for NEC given in equation 5.1 changes from

$$NEC = \frac{T^2}{T + S_{obj} + 2kR}$$

to

$$NEC = \frac{T^2}{T + S_{obj} + kR} \tag{6.5}$$

where T is the true coincidence rate, S_{obj} is the scatter fraction within the object, k is the projection fraction and R is the random coincidence rate. That is, direct subtraction of the delayed coincidence measurement results in a doubling of the effective noise contribution of random coincidences to the data.

Two approaches to the problem of obtaining noise-free or noise-reduced estimates of the number of random coincidences obtained using the delayed coincidence method have been suggested in the literature. These are smoothing of the randoms data prior to subtraction (Hoffman *et al* 1981) and a variance reduction approach similar to that used in normalisation (Casey and Hoffman, 1986). The difficulty with the former approach is that there are high-frequency components in the randoms data which arise from variations in detector efficiency, and extreme care has to be taken to avoid the creation of artefacts in the reconstructed image.

The latter approach has been shown to be effective in 2D mode (Casey and Hoffman, 1986), and some workers have also implemented it in 3D mode (Ollinger 1995).

In this chapter it is shown how the algorithms discussed in chapter 3 for the calculation of detector efficiencies may be used for variance reduction of random coincidence measurements, and the performance of these algorithms in this application is compared. The effects of randoms variance reduction on NEC rates, on SNRs of reconstructed phantom data and on images reconstructed from human studies are examined, and the effects on NEC rates of reducing the fraction of random coincidences detected is briefly investigated.

6.2. Materials and Methods

All acquisitions were performed on an ECAT 951R scanner as described in chapter 2.

6.2.1. Applicability and implementation of normalisation algorithms

If the random coincidences measured in the LOR joining detectors i and j are measured over a period of time T, then from equation 6.1 we have

$$\int_0^T R_{ij}\,dt = 2\tau \int_0^T r_i r_j\,dt \tag{6.6}$$

which reduces to a set of equations of the form

$$U_{ij} = const \times u_i u_j \tag{6.7}$$

providing that the relative distribution of radioactivity within the singles FOV of the camera remains the same throughout the duration of the acquisition. In normal practice it is found that the distribution of random coincidences is fairly uniform across the FOV and depends only weakly on activity distribution, so this condition is not as limiting as it might seem.

Equation 6.7 is analogous to the equation for normalisation following correction for geometric and other systematic effects:

$$\eta_{ij} = \varepsilon_i \varepsilon_j \tag{6.8}$$

where η_{ij} is the LOR efficiency and ε_i and ε_j are the relative detector efficiencies.

Since equations 6.7 and 6.8 have the same form, all six of the algorithms discussed in chapter 3 are candidates for use in randoms variance reduction. However, there are some differences in implementation which have to be taken into account when applying these algorithms to random coincidence data:

1) Data scaling. The normalisation algorithms generate relative efficiencies for each detector or LOR. When used in the context of randoms variance reduction, the noise-reduced sinograms must be scaled to contain the same total number of counts as the original randoms sinogram.

2) Plane efficiencies. The fan-sum algorithms will create bias in the plane-efficiencies of the noise-reduced sinograms if there is significant variation in the axial distribution of random coincidences. This bias can be removed by setting the plane-efficiencies of the noise-reduced sinogram equal to those of the original randoms sinogram.

3) Treatment of zero LOR sums. All of these algorithms involve the calculation of sums of LORs. When the number of counts per LOR is extremely low, the probability that there will be zero counts in particular LOR sums becomes non-negligible. The algorithms break down in the presence of zero-valued LOR sums. To avoid this problem, the algorithms were modified such that any LOR sum with zero value was set to the value of the mean LOR sum for that dataset. The bias introduced by this process should be small provided the number of zero-valued LOR sums is small compared to the number of non-zero LOR sums.

6.2.2. The effect of randoms variance reduction and reduction in randoms fraction on NEC rates.

The effect of randoms variance reduction on NEC rates was demonstrated by plotting the ratio of NEC rates before and after randoms variance reduction as a function of activity for the three largest phantoms used in chapter 5. Since the algorithms used reduce the statistical variance in the randoms data by at least a factor of 50, randoms variance reduction was assumed to produce a noise-free estimate of the randoms distribution. The count-rate and scatter fraction data used was that presented in the previous chapter.

The use of faster scintillators such as LSO could potentially reduce the randoms rate for a given trues rate by allowing the use of a shorter coincidence resolving time. A rough estimate of the potential benefits of this at given activities in the FOV may be obtained by re-calculating NEC rates using the measured true and scattered coincidence rates but using reduced values of the randoms term in equation 3.4. NEC rates were therefore calculated for

fixed true and scatter rates as a function of the ratio of randoms rate to the measured randoms rate for a range of situations reflecting those which might be encountered in clinical practice.

6.2.3. Accuracy of the variance reduction algorithms

In order to determine the accuracy of the different algorithms when applied to randoms noise reduction, a phantom experiment was performed. A 20 cm cylindrical phantom filled with ^{18}F such that there was approximately 100 MBq in the FOV at the start of the experiment was placed in the scanner with its axis 8 cm below the centre of scanner. Data was acquired in 3D mode for one hour. The randoms rate at the start of the experiment was 295 kcps, and the randoms to trues ratio was approximately 1:1. Events from the delayed coincidence channel were stored in separate sinograms to those from the prompt coincidence channel.

Noise-reduced estimates of the randoms distribution were obtained by applying the six different variance reduction methods. Sinograms containing ratios of the resulting datasets with the original randoms dataset were obtained. The uniformity of the ratio sinograms is a measure of the accuracy of the noise reduction methods. The uniformity was measured by calculating the percentage standard deviation of all elements within the sinogram before and after an 8x8 element running-mean smooth.

6.2.4. Measurement of the effect of randoms variance reduction on image SNRs in phantom studies.

A series of phantom experiments were used to assess the effect of randoms variance reduction on image SNRs. Acquisitions were performed using a 20 cm cylinder, the EEC chest phantom, and the EEC chest phantom padded to 37x48 cm with tissue-equivalent material. Each phantom was scanned for 5 minutes, once with approximately 20 MBq in the FOV and once with approximately 100 MBq in the FOV. For all acquisitions, attenuation correction factors were obtained from a septa-extended acquisition using rotating rod-sources with rod-windowing enabled. A model-based scatter correction (Ollinger, 1996) was applied and the data normalised and dead-time corrected as described in chapter 4.

Three reconstructions were then performed for each acquisition, one after subtraction of the measured randoms data and the others after subtraction of noise-reduced estimates created using SP-C and 3D-ED. A large ROI was drawn on each image plane and the fractional

standard deviation within it calculated. A mean value of the fractional standard deviation was then calculated over all image planes for each acquisition and processing method. These mean values were then used to calculate the percentage gain in SNR obtained by application of the two different methods of variance reduction in each imaging situation.

To investigate the effect of statistical noise on the measurement of SNR gain, the large ROI used was divided into four quadrants and the SNR gains recalculated and compared.

6.2.5. The effect of randoms variance reduction in human studies.

Finally three scans of human subjects were performed and reconstructed with and without randoms variance reduction. Resultant images were visually compared. The regions scanned were of the head and neck, the heart and the pelvis. The tracer used was ^{18}F-FDG. Again for all acquisitions, attenuation correction factors were obtained from a septa-extended acquisition using rotating rod-sources with rod-windowing enabled, Ollinger's model-based scatter correction was applied and the data normalised and dead-time corrected as described in chapter 4.

6.3. Results

6.3.1. The effect of randoms variance reduction on noise-equivalent count-rates.

Ratios of NEC curves with and without randoms variance reduction for the three phantoms are shown in figure 6.1. It can be seen that the greatest improvements may be obtained for large objects. With 20 MBq in the FOV (a situation similar to those encountered in FDG whole-body imaging), randoms variance reduction gives an improvement in NEC of roughly 10-15%. There is more to be gained at higher activities, which may be encountered in dynamic studies with short-lived isotopes. There is also a significant increase in the effect of randoms variance reduction at very low activities (< 2 MBq in the FOV). This is due to random coincidences arising from the retracted transmission rod-sources.

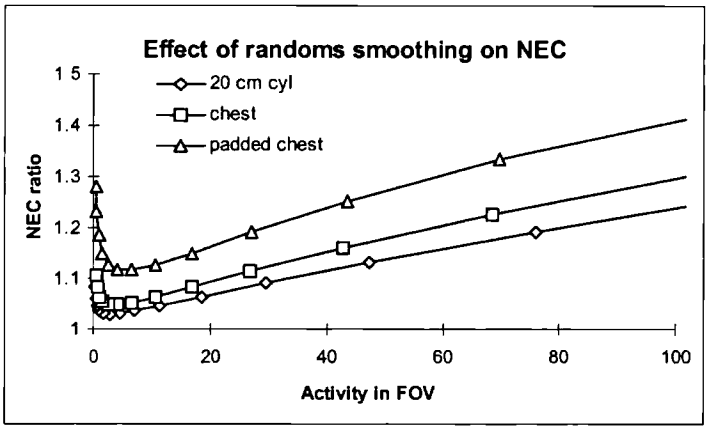

Figure 6.1. Improvement in NEC due to randoms variance reduction as a function of activity in the FOV.
LLD = 400 keV.

NEC for fixed true and scatter rates as a function of the ratio of randoms rate to the measured randoms rate are shown in figure 6.2. It has been assumed that a randoms variance reduction technique has already been applied. Halving the randoms rate may be compared to halving the coincidence resolving time, although these curves should be interpreted with care, as they do not represent a full simulation of the situation. For the 20 cm cylinder with 20 MBq in the FOV it can be seen that randoms smoothing and randoms reduction has little effect on NEC. For the torso phantoms with 20 MBq in the FOV, a combination of randoms variance reduction and a reduction in the randoms rate of 80% (corresponding to a similar reduction in the coincidence resolving time) gives rise to an improvement in NEC of between roughly

15% and 30%, depending on the size of the object. Greater benefits may be obtained with more activity in the FOV.

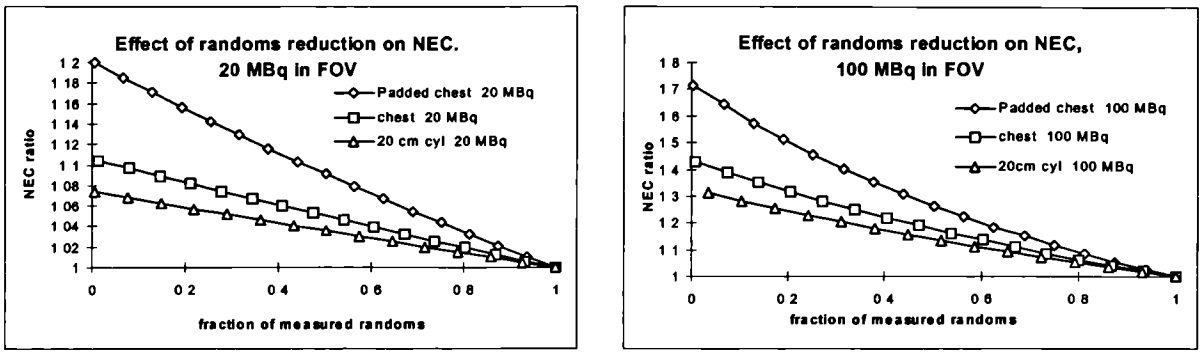

(a) (b)

Figure 6.2. Effect of randoms reduction on NEC.
(a) 20 MBq in the FOV
(b) 100 MBq in the FOV
Note the change in the vertical scale for the 100 MBq data.

6.3.2. Comparison of accuracy of randoms variance reduction methods.

The uniformity of the ratio datasets for the different phantoms and algorithms are shown in table 6.1. The non-uniformity seen when the exact algorithms are used is extremely close to that predicted if the dataset were only subject to Poisson statistics (12.3%), whereas the non-uniformity seen when the fan-sum algorithm is used is somewhat higher. After smoothing the residual non-uniformity seen in the data processed using the fan-sum method is significantly larger than that seen when the exact algorithms are used, indicating the presence of low-frequency bias.

Figure 6.3 shows the randoms sinogram, summed over all axial planes. The discontinuities due to normalisation effects can clearly be seen. Figure 6.4 shows sinograms generated by calculating the ratio of the randoms sinogram and the noise-reduced version generated by 3D-ED, SP-C and 3D-FS. The sinograms have again been summed over all axial planes. A perfect noise reduction scheme would result in a ratio sinogram containing random noise and no structure. While all three algorithms are reasonably effective in dealing with the discontinuities due to normalisation effects, it can be seen that significant bias is introduced by the fan-sum method.

Algorithm	%std dev. of ratio dataset	%std dev. of ratio after smoothing
3D-FS	14.3	7.1
SP-FS	14.4	7.3
3D-ED	12.6	1.9
SP-ED	12.7	2.2
3D-C	12.6	1.9
SP-C	12.4	1.6

Table 6.1. Uniformity of ratio of variance reduced to raw randoms sinograms using different algorithms.
The mean number of counts per LOR was 66.

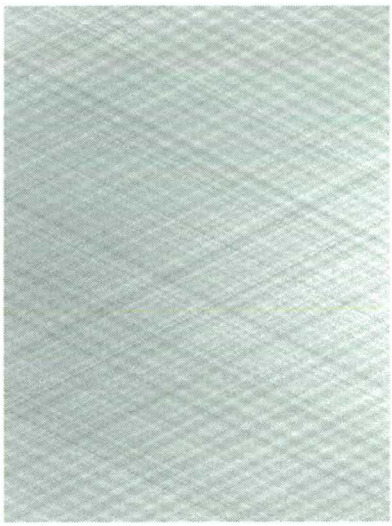

Figure 6.3. Raw randoms sinogram summed over all axial planes.
The zero-point of the colour-scale has been set to the minimum data value.

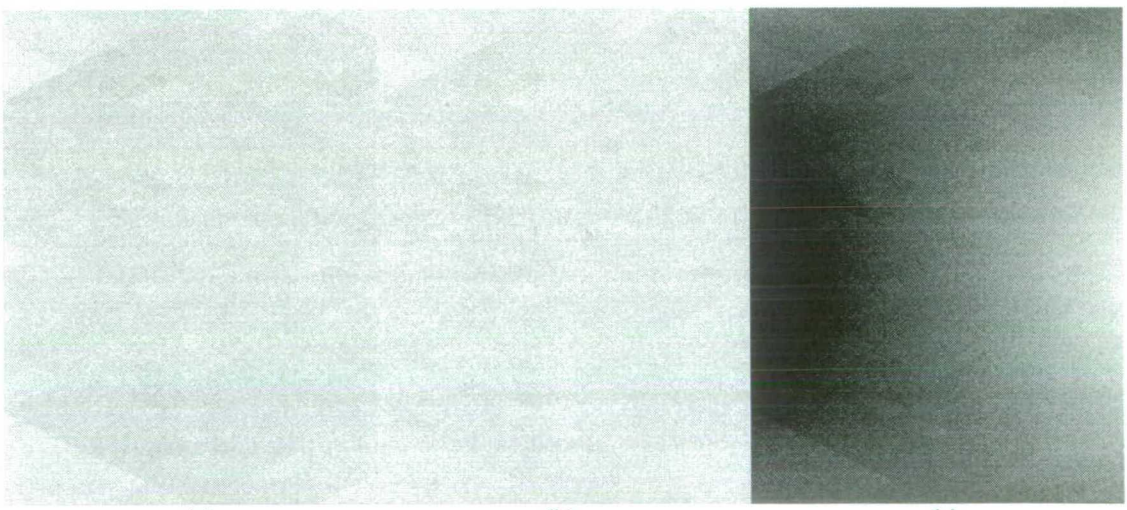

(a) (b) (c)

Figure 6.4. Effect of randoms variance reduction on sinogram uniformity.
Ratios of raw and noise-reduced randoms sinograms generated using (a) 3D-ED, (b) SP-C and (c) 3D-FS. The sinograms have been summed over all axial planes and the zero-point of the colour-scale has been set to 75% of the maximum data value. Bias introduced by 3D-FS can clearly be seen.

6.3.3. Measurement of the effect of randoms variance reduction on image SNRs in phantom studies.

Ratios of mean SNRs were calculated for images reconstructed with and without randoms variance reduction using SP-C and 3D-ED for the six situations considered are shown in table 6.2. Unsurprisingly, the benefit obtained by randoms variance reduction is greater when there is more activity in the FOV. There appears to be no correlation between phantom size and SNR improvement, but this may be related to inaccuracies in the estimates of the amount of activity in the FOV at the start of the acquisitions. No significant difference in performance is seen between SP-C and 3D-ED.

The maximum variation in calculated SNR gain found when the ROI used was divided into 4 quadrants was 10% or less for every case except for the two chest phantoms with 20 MBq in the FOV, where the variation was considerably higher. For the smaller chest phantom with 20 MBq in the FOV, the gains varied from 4.1% to 6.3%. For the padded chest phantom with 20 MBq in the FOV the gains varied from 3.7% to 9.6%. This suggests that reasonable confidence may be placed in the figures for the calculated gains in SNR in all cases except for the two larger phantoms at low activities.

Phantom	Approx. activity in FOV (MBq)	Prompt coincidence rate (kcps)	Randoms fraction (%)	Gain in image SNR, SP-C (%)	Gain in image SNR, 3D-ED (%)
20 cm cylinder	20	138	23	5.3	5.3
EEC chest	20	62	19	5.4	5.4
Padded EEC chest	20	25	27	6.6	6.5
20 cm cylinder	100	640	56	13.7	14.0
EEC chest	100	288	46	12.4	12.5
Padded EEC chest	100	138	52	13.3	13.3

Table 6.2. SNR gain due to randoms variance reduction (phantom studies).
Ratio of SNRs with and without randoms variance reduction for reconstructed images of the different phantoms at levels of activity in the FOV, together with prompt coincidence rates and randoms fractions. Acquisition times were 5 minutes and the randoms fraction is calculated across the entire FOV.

6.3.4. The effect of randoms variance reduction in human studies.

Selected images from the three human studies are shown in figures 6.5 to 6.7. While comparison of SNR values using ROIs yields gains consistent with those measured in the phantom studies, there are few visually discernible differences between the images.

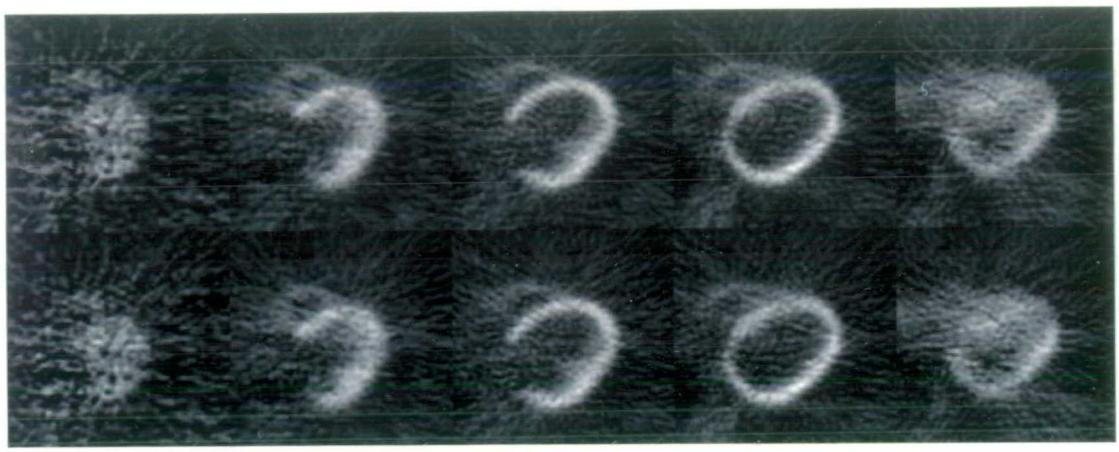

Figure 6.5. Visual effect of randoms variance reduction on an ^{18}F- FDG cardiac study.
The randoms-to-prompts ratio was 27%. No smoothing has been applied to the images and the linear grey-scale covers the entire dynamic range. Top: randoms variance reduction used. Bottom: no randoms variance reduction. From left to right: image planes 1,6,11,16,21.

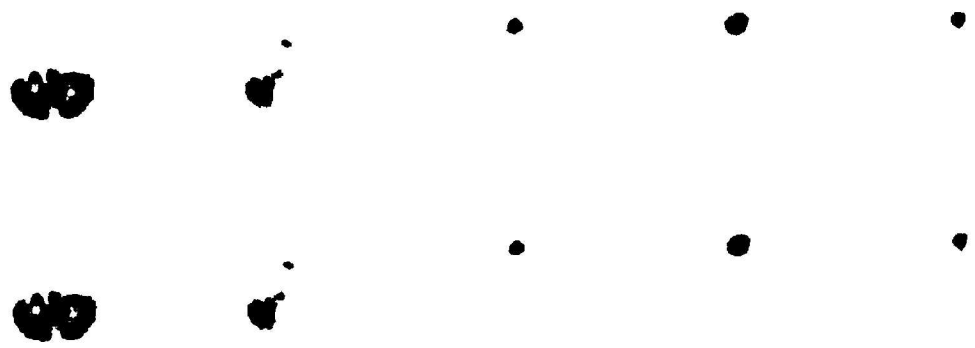

Figure 6.6. Visual effect of randoms variance reduction on an ^{18}F- FDG head and neck study.
The randoms-to-prompts ratio was 21%. No smoothing has been applied to the images and the maximum of inverse linear grey-scale is set to 50%. Top: randoms variance reduction used. Bottom: no randoms variance reduction. From left to right: image planes 11,16,21,26,31.

Figure 6.7. Visual effect of randoms variance reduction on an ^{18}F- FDG pelvic study.
The randoms-to-prompts ratio was 14.5%. No smoothing has been applied to the images and the maximum of inverse linear grey-scale is set to 50%. Top: randoms variance reduction used. Bottom: no randoms variance reduction. From left to right: image planes 1,6,11,16,21.

6.4. Discussion and conclusions

It has been shown here that the fan-sum method is not appropriate for randoms variance reduction as it introduces bias. However, exact methods can be used successfully.

NEC analysis suggest that for the ECAT 951R scanner operating in 3D mode, only modest gains in image SNR may be obtained from randoms variance reduction in typical imaging situations using ^{18}F-FDG. This is confirmed by direct measurements of image SNRs, and it is difficult to visually distinguish images reconstructed with and without using the technique (although randoms variance reduction has not been assessed in human studies with large amounts of activity in the FOV). Further benefits are likely to be obtained if the overall randoms rate can be reduced by use of faster detector systems, but on scanners with geometries similar to the 951R these are only likely to be important when imaging large objects containing a large amounts of activity.

It has been shown here that for randoms variance reduction there is very little difference in performance between 3D-ED and SP-C. However, it should be noted that if the randoms dataset is very sparse, SP-C will be more susceptible to zero-valued LOR sums that 3D-ED.

Randoms variance reduction (and the use of faster detection systems) may prove to be more useful on scanners with a longer axial FOV such as the ECAT ART (Bailey *et al* 1997) or the ECAT HR++ (Jones *et al* 1996). These scanners routinely employ mashing techniques to reduce dataset sizes (section 1.3.1), making implementation of fully-3D variance reduction techniques difficult. However, provided the randoms dataset is not too sparse, the single-plane Casey algorithm could be used on these cameras without sacrificing SNR gain or introducing significant bias.

6.5. References

ME Casey and EJ Hoffman 1986 "Quantitation in Positron Emission Computed Tomography: 7. A technique to reduce noise in accidental coincidence measurements and coincidence efficiency calibration" *J. Comput. Assist. Tomogr.* **10**,845-850

DL Bailey, H Young, PM Bloomfield, SR Meikle, D Glass, MJ Myers, TJ Spinks, CC Watson, P Luk, AM Peters and Terry Jones 1997 "ECAT ART - a continuously rotating PET camera: performance characteristics, initial clinical studies, and installation considerations in a nuclear medicine department" *Eur. J. Nucl. Med* **24** (1) 6-15

DL Bailey, MP Miller, TJ Spinks, PM Bloomfield, L Livieratos, HE Young and T Jones 1998 "Experience with Fully 3D PET and Implications for Future High Resolution 3D Tomographs" *Phys. Med. Biol.* **43**(4), *to appear.*

E J Hoffman, S-C Huang, ME Phelps and DE Kuhl 1981 "Quantitation in Positron Emission Computed Tomography: 4. Effect of Accidental Coincidences." *J Comput Assist Tomogr* **5**(3):391-400

EJ Hoffman, TM Guerrero, G Germano, WM Digby and M Dahlbom 1989 "PET system calibrations and corrections for quantitative and spatially accurate images" *IEEE Trans. Nuc. Sci.* **36**(1), 1108-1112

T Jones, DL Bailey, PM Bloomfield, TJ Spinks, W Jones, K Vaigneur, J Reed, J Young, D Newport, C Moyers, ME Casey, and R Nutt 1996 "Performance characteristics and novel design aspects of the most sensitive PET camera for high temporal and spatial resolution" *J. Nucl. Med.* **37** 85P

JM Ollinger 1996 "Model-based scatter correction for fully 3D PET" *Phys. Med. Biol.* **41** 153-176

CW Stearns 1995 "Scatter correction method for 3D PET using 2D fitted Gaussian functions" *J. Nucl. Med.* **36**(5) 105P

7. Human studies in 2D and 3D mode

7.1. Introduction

While studies of uniform phantoms can yield useful information on likely changes in performance between 2D and 3D mode imaging, they are not a substitute for *in vivo* comparison. In particular, it is difficult to accurately mimic realistic activity distributions both in and outside of the FOV in phantom studies. In this chapter some example *in vivo* human studies are presented. A series of 2D and 3D datasets have been acquired following protocols designed to allow a reasonably fair visual comparison of reconstructed images in a range of imaging situations. The purpose of this comparison is not to quantify the differences in performance between 2D and 3D mode, but to give an indication of the likely benefits in terms of image quality which can be obtained in practice, and to show any obvious artefactual differences between 2D and 3D images when the latter are normalised and scatter-corrected using state-of-the art techniques.

7.2. Methods

In order to expose the detectors to a roughly equal integrated photon flux and to minimise the effects of tracer redistribution, each study consisted of 2 scans in one mode separated by double-length scan in the second mode. The scans were then appropriately dead-time corrected and summed. Dead-time correction was applied on a bucket-by-bucket basis using the singles-based dead-time model supplied by the manufacturer. A measured attenuation correction was performed on all studies (using a post-injection transmission scan). The 3D data was scatter corrected using the model-based technique of Ollinger (1996) and normalised (including self-normalisation for transaxial block-profile) as described in chapter 4. In 3D mode random coincidences were acquired in a separate sinogram and a variance reduction technique (3D-ED) applied prior to subtraction from the prompt data. In 2D mode no scatter correction was applied. All acquisitions were reconstructed using a ramp filter with a cut-off at the Nyquist frequency (with a generalised Colsher filter for 3D reconstruction), and where necessary spatial smoothing was applied equally to the 2D and 3D images. The small changes in transaxial resolution with axial position in 3D mode described in section 2.4 were ignored in this comparison. All studies were performed on adult patients. Singles rates,

the total number of prompt coincidences and the percentage dead-time were recorded for each acquisition, together with the fraction of random coincidences measured.

The following studies were performed:

Brain, ^{11}C-flumazenil	Brain, ^{18}F- FDG	Head-and-neck, ^{18}F- FDG
Axillae, ^{18}F- FDG	Heart, ^{18}F- FDG	Pelvis, ^{18}F- FDG
Pelvis, ^{18}F- F-		

Flumazenil is a benzodiazepine receptor antagonist, useful in localisation of epileptic foci, FDG is a tracer for glucose metabolism and F^- is a tracer for bone formation.

7.3. Results

Selected images from the human studies together with injection times and count-rate data are shown below. In general, the 3D mode images have visibly better signal-to-noise properties than the 2D mode images, particularly in the central planes. The effect of large amounts of activity adjacent to the FOV may be seen by comparing the count rates observed for the ^{18}F-FDG head-neck and brain studies. In the head and neck study the ratio of singles to prompt coincidences is virtually doubled compared to the brain study, resulting in a larger randoms fraction even though the overall singles rate is reduced by 35%. Nevertheless, the 3D mode image is still improved compared to the 2D image, although the improvement is not as marked as for the brain study. Scatter fractions calculated using Ollinger's model-based scatter correction method have values of around 18-20% for the brains and head-neck studies. However, similar values are also obtained for the pelvic studies, indicating that the correction scheme is likely to be significantly underestimating the scatter in these situations. There are no obvious artefactual differences between the 2D and 3D mode images except in the ^{18}F-F- pelvis study (see section 7.4 below).

7.3.1. Adult brain, ^{11}C-flumazenil

In this study the basal ganglia appear to be slightly more intense in the 2D image than in the 3D image. This effect becomes more apparent if a heavier spatial smoothing is applied to the two image volumes, and is still seen if a Gaussian fit scatter correction is applied rather than a model-based estimate. This may possibly be due to tracer redistribution between the scans. The 3D mode images show improved visual appearance compared to the 2D images, particularly in the central planes.

Injected activity at t = 0	Emission scans	mean singles rate (kcps)	mean prompt rate (kcps)	Randoms fraction (%)	dead-time (%)
339 MBq	2D - 7 mins @ t = + 19 min	693	24.1	3.2	1.3
	3D - 7 mins @ t = + 31 min	1100	51.1	7.2	2.5
	3D - 8 mins @ t = + 50 min	720	20.3	6.9	1.6
	2D - 8 mins @ t = + 67 min	150	2.1	0.8	0.4

Table 7.1. Protocol details and count-rates for adult ^{11}C-flumazenil brain study.

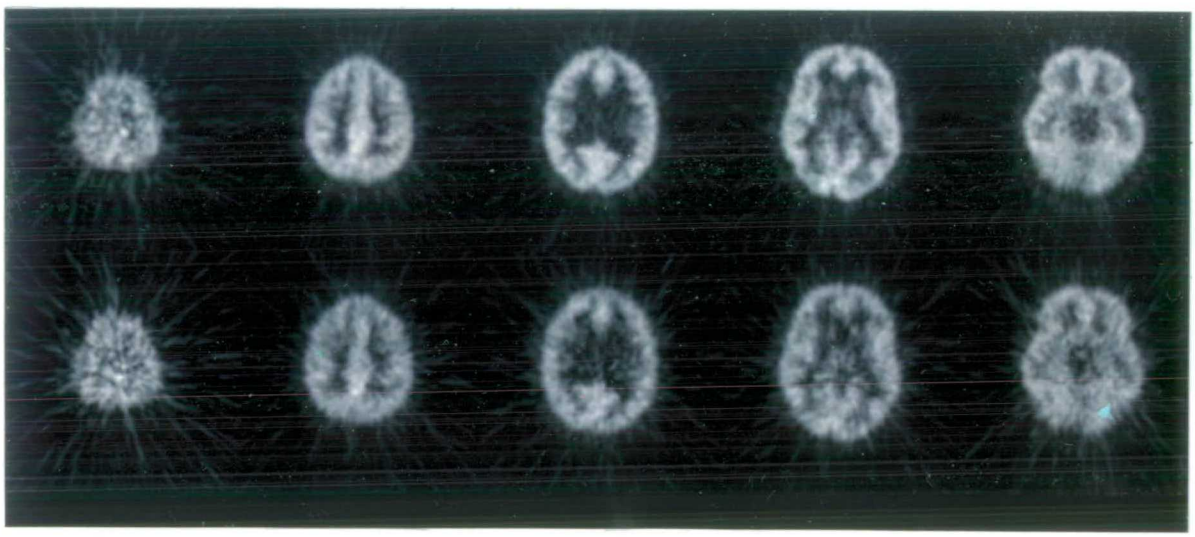

Figure 7.1. Selected image planes from adult ^{11}C-flumazenil brain study.
Top: 3D mode. Bottom: 2D mode. From left to right: image planes 1,6,11,16,21. A 3-D Gaussian smoothing kernel of FWHM 3.5 mm has been applied to both image volumes.

7.3.2. Adult brain, ^{18}F- FDG

This study exhibits the greatest improvement of 3D mode over 2D mode. A Gaussian spatial smoothing kernel of FWHM of just 2.5 mm has been applied to both image volumes, but the SNR in the 3D image is sufficiently great that even the unsmoothed images are of acceptable quality. In an ^{18}F- FDG brain study there is very little activity adjacent to the FOV and this is a likely explanation for the excellent statistical quality of the 3D image.

Injected activity at t = 0	Emission scans	mean singles rate (kcps)	mean prompt rate (kcps)	Randoms fraction (%)	dead-time (%)
233 MBq	3D- 15 mins @ t = + 50 min	4140	194.5	18.3	8.5
	2D- 15 mins @ t = + 68 min	1200	28.5	4.4	2.2
	2D- 15 mins @ t = + 85 min	1110	26.2	4.1	2.0
	3D- 15 mins @ t = +102min	3360	150.3	15.6	6.7

Table 7.2. Protocol details and count-rates for adult ^{18}F- FDG brain study.

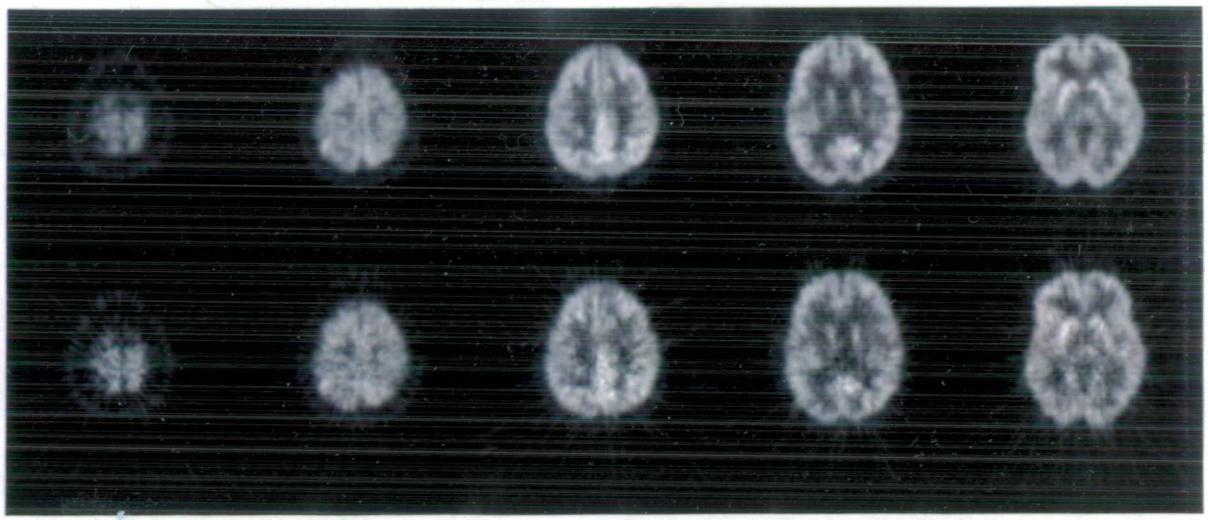

Figure 7.2. Selected image planes from adult ^{18}F- FDG brain study.
Top: 3D mode. Bottom: 2D mode. From left to right: image planes 1,6,11,16,21. A 3-D Gaussian smoothing kernel of FWHM 2.5 mm has been applied to both image volumes.

7.3.3. Adult head and neck, ^{18}F- FDG

There is visible improvement in image quality in the 3D data compared to the 2D data in all planes except plane 31, where the quality appears very similar. The improvement is most noticeable in plane 16. Unfortunately the pathological region of interest lies at the edge of the FOV. One of the disadvantages of 3D mode imaging is that at the edge of the FOV gains in image quality are modest, and the images are not quantitative, as neither the reconstruction technique nor the scatter correction technique is particularly accurate (see sections 2.5 and 4.2).

Injected activity at t = 0	Emission scans	mean singles rate (kcps)	mean prompt rate (kcps)	Randoms fraction (%)	dead-time (%)
275 MBq	2D - 7 mins @ t = + 71 min	1110	18.3	5.7	2.1
	3D - 7 mins @ t = + 84 min	2700	72.1	21.7	6.1
	3D - 8 mins @ t = + 97 min	2540	66.5	20.9	5.7
	2D - 8 mins @ t = +114 min	890	14.0	4.9	1.7

Table 7.3. Protocol details and count-rates for adult ^{18}F- FDG head and neck study.

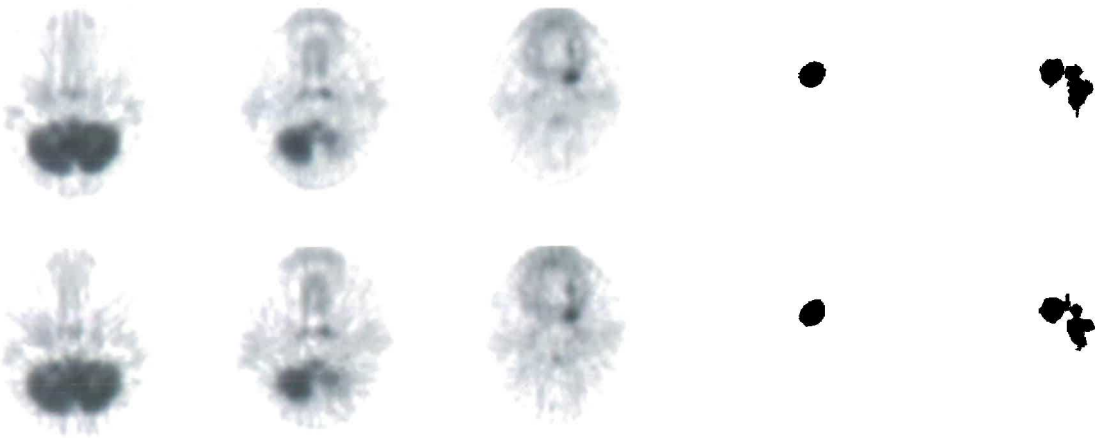

Figure 7.3. Selected image planes from adult ^{18}F- FDG head and neck study.
Top: 3D mode. Bottom: 2D mode. From left to right: image planes 11,16,21,26,31. A 3-D Gaussian smoothing kernel of FWHM 5.0 mm has been applied to both image volumes.

7.3.4. Adult axillae, ^{18}F- FDG.

Patient weight: 61 kg Patient height: 159 cm

Visual assessment indicates that the 3D study has improved SNR, and on sagittal cuts through the image volume (not shown), anatomical features such as the spine are better visualised. However, it is not clear whether or not the increase in contrast between the mediastinum and the lungs seen in the 3D image is artefactual.

Injected activity at t = 0	Emission scans	mean singles rate (kcps)	mean prompt rate (kcps)	Randoms fraction (%)	dead-time (%)
339	2D: 7.5 mins @ t = + min	1040	16.1	5.7	2.0
	3D: 15 mins @ t = + min	2620	71.2	20.3	6.0
	2D: 7.5 mins @ t = + min	790	12.0	4.5	1.5

Table 7.4. Protocol details and count-rates for adult ^{18}F- FDG axillae study.

Figure 7.4. Selected image planes from adult ^{18}F- FDG axillae study.
Top: 3D mode. Bottom: 2D mode. From left to right: image planes 11,16,21,26,31. A 3-D Gaussian smoothing kernel of FWHM 5.0 mm has been applied to both image volumes and the maximum of the inverse grey-scale has been set to 70% of the data maximum

7.3.5. Adult heart, ^{18}F- FDG.

Patient weight: 78 kg Patient height: 166 cm

There is a clear improvement in image SNR in all images planes including the end plane, and the right ventricle of the heart is better visualised in the 3D images. As with the ^{18}F- FDG brain study, this study again demonstrates that 3D mode imaging performs particularly well when the bulk of the activity is concentrated within the FOV, rather than adjacent to it.

Injected activity at t = 0	Emission scans	mean singles rate (kcps)	mean prompt rate (kcps)	Randoms fraction (%)	dead-time (%)
244	2D - 10 mins @ t = + 36 min	1450	18.8	9.7	2.8
	3D - 20 mins @ t = + 51 min	3270	84.8	27.0	7.7
	2D - 10 mins @ t = + 81 min	1040	12.9	7.3	2.0

Table 7.5. Protocol details and count-rates for adult ^{18}F- FDG heart study.

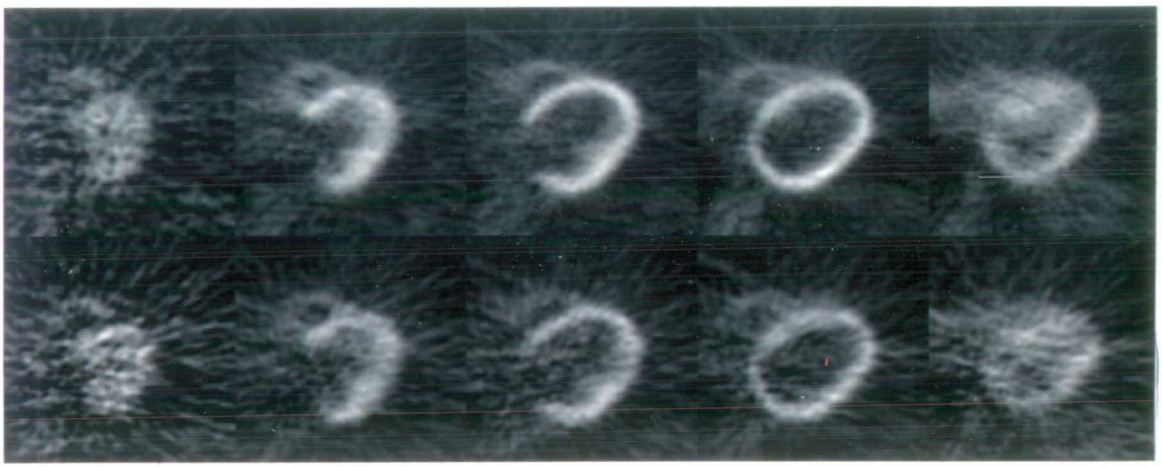

Figure 7.5. Selected image planes from adult ^{18}F- FDG heart study.
Top: 3D mode. Bottom: 2D mode. From left to right: image planes 1,6,11,16,21. A 3-D Gaussian smoothing kernel of FWHM 3.5 mm has been applied to both image volumes.

7.3.6. Adult pelvis, ^{18}F- FDG.

Patient weight: 61 kg Patient height: 175 cm

The singles to prompts ratio is high in 3D mode compared to the other studies (~52 compared to ~21 for the ^{18}F- FDG brain study), and a relatively high randoms fraction is seen. This is due in part to the larger object size and in part to the fact that the bladder, which contains a significant amount of activity, overlays the upper edge of the FOV. The SNR of the 3D image is clearly better than the 2D image. It should be noted however, that the patient is quite slim. As stated above, the scatter fraction calculated using a model-based method is about 20%, which is significantly less than the 30% or so predicted by phantom studies (see chapter 5). This suggests that the scatter correction algorithm is significantly underestimating the scatter within the object, and the distribution of this residual scatter is unknown. It should also be noted that no scatter correction has been applied to the 2D image, where the scatter fraction is likely to be of order 20%.

Injected activity at t = 0	Emission scans	mean singles rate (kcps)	mean prompt rate (kcps)	Randoms fraction (%)	dead-time (%)
257 MBq	2D - 8 mins @ t = +120 min	430	5.0	3.3	0.8
	3D - 15 mins @ t = +132 min	1260	24.0	14.5	2.9
	2D - 7 mins @ t = +157 min	370	3.5	2.9	0.7

Table 7.6. Protocol details and count-rates for adult ^{18}F- FDG pelvis study.

Figure 7.6. Selected image planes from adult ^{18}F- FDG pelvis study.
Top: 3D mode. Bottom: 2D mode. From left to right: image planes 1,6,11,16,21. A 3-D Gaussian smoothing kernel of FWHM 5.0 mm has been applied to both image volumes.

7.3.7. Adult pelvis, ^{18}F- F$^-$.

Patient weight:64 kg Patient height:166 cm

There is a clear improvement in image SNR in all images planes including the end plane, and fine details of the bony structures are visible in the 3D scan which cannot be distinguished from noise in the 2D scan. There is less visible activity within the patient's body in the 3D scan. In the 3D scan a convex hot "rim" feature can be seen joining the iliac crests. A similar feature is also seen in the 2D scan.

Injected activity at t = 0	Emission scans	mean singles rate (kcps)	mean prompt rate (kcps)	Randoms fraction (%)	dead-time (%)
171	2D - 15 mins @ t = + 93 min	420	4.4	3.6	0.8
	3D - 30 mins @ t = +112 min	1210	19.0	16.3	2.7
	2D - 15 mins @ t = +151 min	330	2.7	3.5	0.6

Table 7.7. Protocol details and count-rates for adult ^{18}F- F$^-$ pelvis study.

Figure 7.7. Selected image planes from adult ^{18}F- F$^-$ pelvis study.
Top: 3D mode. Bottom: 2D mode. From left to right: image planes 11,16,21,26,31. A 3-D Gaussian smoothing kernel of FWHM 3.5 mm has been applied to both image volumes.

7.4. Discussion

Medical image assessment is a notoriously difficult problem. For quantitative assessment of image quality in terms of diagnostic utility, receiver-operator characteristic (ROC) studies (REF) should be performed. Such studies are time-consuming and require large datasets for reliability. However, when attempting to compare two images of the same object, the nature of the difference between the two images is important. If it is assumed that both 2D and 3D PET images can be made quantitative, and if the spatial resolution of the images is similar and does not depend on the activity distribution, then the primary difference between the two images will be related to changes in SNR due to improved statistical accuracy in one or other of the datasets. In such cases, if one of the images demonstrates visibly better SNR, it can be said to be the "better" image, in that it can reasonably be expected to have improved diagnostic utility. The difficulty here is that PET images are not always quantitative, principally because of scatter. However, visual inspection of images should still yield information regarding potential improvements in image quality and fruitful areas for further work. For example, if a class of images does not demonstrate visibly improved SNR when the data is acquired in 3D mode rather then 2D mode, it would be hard to justify significant further effort towards quantitative 3D for that class.

For brain studies, 3D mode acquisition delivers images which are far superior in terms of visually assessed SNR to those obtainable from 2D mode acquisition. Other workers have demonstrated that 3D brain studies with appropriate scatter correction generate images which are at least as accurate in quantitative terms as 2D brain scans (e.g. Bailey, 1996). It is therefore clear that 3D mode imaging is appropriate for most static brain studies. However, it should be noted that the accuracy of the scatter correction technique used has not been tested with statistically sparse datasets, and this could adversely impact the accuracy of early frames of dynamic studies carried out in 3D.

Every study of the thorax and abdomen presented here has demonstrated visual improvements in SNR throughout most image planes. However the quantitative accuracy of the 3D images in the thorax and abdomen is not known and is quite difficult to measure. It is common practice to ignore scatter in 2D mode, particularly when imaging the body. However, it has been shown in chapter 5 that the scatter fraction in the body in 2D mode is of the order of 20%. As a result, the 2D images cannot be used as a "gold standard" against

which the 3D images can be measured. This is illustrated in figure 7.7 below, where heavily smoothed images from the ^{18}F-F^- pelvis scans are shown. This is a demanding test of quantitative accuracy because F^- is a bone-seeking agent with very little uptake in soft tissue. In the 3D images there are two oval ring features, one in the region of the peritoneum and one further out, at the body boundary. Both of these could well be artefactual. There are also large regions containing negative pixel values. However, the 2D images (not scatter corrected) also show a range of anomalous features, including similar oval rings and significant background within soft tissue. Possible explanations include interactions between scatter, attenuation and respiratory motion.

Figure 7.8. Heavily smoothed selected image planes from adult ^{18}F- F- pelvis study.
Top: 3D mode. Bottom: 2D mode. From left to right: image planes 11,16,21,26,31. A 3-D Gaussian smoothing kernel of FWHM 7.5 mm has been applied to both image volumes, and the inverse grey-scale maximum has been set to 35% of the image maximum.

It is unfortunate that no data comparing 2D and 3D images for short-lived isotopes or for very large subjects could be presented, as it is in such studies that the effectiveness of the 3D technique (in terms of SNR improvement) is more questionable.

7.5. Conclusions

Significantly improved images of the brain may be obtained using 3D mode rather than 2D mode.

3D mode also shows considerable promise in several situations when imaging the body, but more work is needed to characterise and correct for scatter. These results concur with those of other workers using similar equipment (e.g. Kinahan *et al* 1995). Of the types of study presented here, the most promising appear to be those scans where the uptake is strong and highly structured, such as cardiac scans using ^{18}F-FDG and bone scans using ^{18}F-F-. In these cases the improved SNR obtained in 3D mode allows improved realisable spatial resolution, and the effects of residual scatter are perhaps less important.

7.6. References

PE Kinahan, F Jadali, D Sashin, ML Brown, MA Mintun, RL Baron and DW Townsend 1995 "A comparison of 2D and 3D abdominal PET imaging" *J Nucl Med* **36**(5):7P

CE Metz 1986 "ROC methodology in Radiologic Imaging", Invest. Radiol. **21**(9) 720-733

JM Ollinger 1996 "Model-based scatter correction for fully 3D PET" *Phys. Med. Biol.* **41** 153-176

8. Summary, conclusions and future work.

8.1. Summary

In chapter 1 the basic principles of PET were outlined, and some of the practical issues involved in obtaining quantitative (particularly when operating in 3D mode) were discussed. These included attenuation correction, scatter correction, dead-time correction and normalisation. The problem of optimisation of acquisition parameters was also introduced.

In chapter 2, the basic features and performance parameters of the ECAT 951R camera and reconstruction algorithms used in this work were described. Of particular importance was the measurement of sensitivity to single events arising from outside of the FOV of the camera, and it was shown that for the ECAT 951R the most sensitive region lies within 15 cm of the edge of the FOV.

In chapter 3, a review of some existing algorithms for calculation of variance-reduced estimates of detector efficiency normalisation coefficients was presented, together with new algorithms derived from these. The new and existing algorithms were compared in terms of systematic accuracy and variance reduction power for 3D mode normalisation. Those algorithms which made use of all possible lines of response were shown to have the greatest variance-reducing effect - however, the algorithm of Casey and Hoffman (1986) extended for use in 3D mode was shown to be the most systematically accurate. Some other interesting observations were also made regarding the importance of random variations in detector efficiency in normalisation, and it was shown that in fact such variations have quite a small effect on reconstructed image uniformity.

In chapter 4, issues in component-based normalisation in 3D PET were discussed, and a model containing new components presented. The idea, first introduced by Casey *et al* (1995), of combining corrections for dead-time effects with normalisation was developed further, and a simple and effective method for correcting for systematic variations in detector efficiency with crystal position within the block detector and simultaneously for removing artefacts caused by event mispositioning due to pulse pile-up was presented. This method uses emission data itself to obtain the appropriate correction factors and does not require a multi-parameter normalisation dataset or any temporal information on dead-times during

acquisition. The characteristics of other normalisation components for the ECAT 951R scanner were also obtained and presented. It was found that the most important remaining difficulty with normalisation in 3D mode lies in obtaining accurate radial geometric profile factors, and none of the methods presented for doing this proved entirely satisfactory. Inaccuracies in measurements of the radial geometric correction factors can lead to central hot-spots in scans of uniform cylinder phantoms. An *ad-hoc* correction for this effect was developed using uniform phantom data, but not validated for significantly different activity distributions. A problem of lesser importance was found to be the existence of a high-frequency low-intensity concentric ring artefact centred on the centre of the camera FOV. Similar artefacts have been reported by other workers (e.g. Ollinger 1997, Oakes *et al* 1998) and no adequate explanation for this phenomenon has yet been proposed.

In chapter 5, the issue of optimising acquisition parameters in 2D and 3D PET was addressed. Scanner performance was quantified using noise-equivalent count (NEC) rates (Strother *et al* 1990). It was shown that the lower energy level discriminator (LLD) has an important effect on NEC rate, and that the dependence of NEC on LLD becomes stronger as the object size and the activity in the camera field-of-view (FOV) increases, particularly in 3D mode. It was also shown that on the ECAT 951R, increasing the amount of activity in the FOV much beyond 50 MBq gives only a small increase in NEC when operating in 3D mode, and that for some protocols where large amounts of short-lived radiotracers are used, a combination of 2D and 3D mode operation is likely to give the best results. The limiting factors on scanner performance were also investigated, and it was found that in 3D mode random coincidences become much more important in this regard as the object size and the activity in the camera FOV increases.

In chapter 6, it was shown how the problems of variance reduction for normalisation of detector efficiencies and for estimates of random coincidences obtained from delayed coincidence channel measurements are mathematically similar (Casey and Hoffman 1986). The performance of three representative algorithms developed in chapter 3 were assessed in the context of randoms variance reduction, and it was found that the approximate algorithms introduce systematic low-frequency bias into the randoms estimates. No significant difference in performance in terms of reducing reconstructed image variance was found between those algorithms which used all possible lines of response (3D type) and those

which did not (SP type). The similarity in performance of the 3D type and SP type algorithms is particularly significant for cameras (such as the ECAT ART or HR++) which employ summation of adjacent LORs in routine acquisition, as implementing 3D type variance reduction algorithms is very difficult in such circumstances. For the ECAT 951R it was found that variance reduction of random coincidence estimates delivers only a modest improvement in image variance for a wide range of normal imaging situations.

In chapter 7 some comparative human studies in 2D and 3D mode were presented. The images obtained were compared visually for gains in signal to noise. Visual improvements were seen in all cases, particularly in brain, cardiac and bone studies. However, scatter fractions as computed by Ollinger's model-based scatter correction were inconsistent with those found in phantom studies for images of the body, and in one case significant artefacts were seen in the image. These effects are almost certainly due to inaccurate scatter correction and this remains an important barrier to quantitative 3D imaging outside of the brain.

8.2. Key conclusions

- The most important normalisation components in 3D PET are the radial geometric profile and the axial block-profile, rather than the individual detector efficiencies. Currently there is no accurate way of measuring the radial geometric profile.
- Radial saw-tooth artefacts arising from differences in dead-time effects between the normalisation and emission scans can be removed by self-normalisation of emission data. This process is simple and effective.
- 3D mode should give improved SNR compared to 2D mode provided the objects being imaged do not contain too much activity (< 150 MBq in the FOV) and are not too large.
- Noise introduced by random coincidences is an important limiting factor for peak NEC rate in 3D mode.
- Randoms variance reduction improves image SNR in 3D without introducing bias provided exact methods are used. However in practice the level of improvement obtained on a camera with a small axial FOV such as the ECAT 951R is modest.

8.3. Future work

At the end of chapter 1, the following questions were posed:

1. How may 3D PET data be accurately corrected for scattered coincidences?
2. How may attenuation correction factors be obtained in the absence of septa?
3. How may 3D PET data be accurately normalised?
4. How may 3D PET data be accurately corrected for pulse pile-up effects?
5. What are the optimum acquisition parameters for 3D PET?
6. Under what circumstances does the increase in sensitivity to true coincidences obtained in 3D mode outweigh the effect of increased sensitivity to scatter and random coincidences?

In this work, progress has been made in answering questions 3-6, but many questions remain to be addressed.

Outstanding issues in normalisation principally revolve around methods of obtaining accurate values for radial geometric correction factors. Further questions revolve around the proper treatment of scatter in normalisation and in particular, how geometrical considerations affect scatter normalisation coefficients. Variation of efficiency along a given line of response is also an effect which so far has received little attention.

In terms of correction for pulse pile-up effects, the scheme presented here for the variation in block-profile with count rate removes visible artefacts without addressing the underlying cause of those artefacts, which is incorrect treatment of multiple coincidences where two low-energy events occur in the same block detector. These events should ideally be rejected rather than treated as trues as they have been here. It is possible that pulse pile-up effects may also interact with other normalisation components such as the crystal interference effect and the radial geometric profile.

Although the issue of scatter correction has only been superficially examined in this work, it is clearly a key area of weakness in the 3D technique when used outside of the brain. While model-based methods show considerable promise, they still do not adequately address the issue of scatter arising from activity outside of the FOV, and the degree of error which may be expected is not well quantified. It may be that a combination of measured and calculated

scatter estimation techniques will be needed to address this problem. In any case, it would be highly desirable to know the characteristics of residual scatter after application of model-based techniques in different circumstances, and how such residual scatter interacts with attenuation correction, before using 3D PET in clinical imaging of the body.

When performing dynamic scans, the source distribution both within and outside of the FOV is changing and the data in each frame is usually extremely sparse. It is not clear what the best approach to scatter correction is in such circumstances. This is an outstanding problem which could seriously limit the usefulness of the 3D technique, even for brain scanning. A possible approach when using calculated scatter correction algorithms might involve temporal smoothing of the data prior to application, but this would have to be validated for individual protocols. Some scatter correction methods are likely to prove more robust with regard to sparse datasets than others, and it would be useful to characterise the behaviour of a range of scatter correction algorithms with high variance data.

One of the interesting results from the clinical studies is that for a wide range of situations, random coincidences are not a significant problem. Also, residual scatter does not appear to produce many noticeable artefacts (although no claims for the quantitative accuracy of the whole-body images can be made from the data presented). This can probably be attributed to the narrow acceptance angle and small singles FOV of the ECAT 951R design. It would be interesting to simulate the effect of varying camera geometry on performance in 3D mode. It his been suggested that future PET tomographs will have small ring diameters, large axial FOVs and no septa, as such design features can increase spatial resolution and sensitivity without significantly increasing cost. However, it may be that such developments would be counter-productive, as the increased susceptibility to scatter and random coincidences might outweigh the advantages, particularly in whole-body scanning.

The work presented in this thesis shows that at this stage caution should be exercised before acquiring septaless cameras - it may well be that such cameras cannot perform all the tasks a camera with retractable septa can without a great deal of work. However, 3D mode acquisition shows promise in a wide range of situations where it is not currently in common clinical use, and further work, particularly on scatter correction, should prove worthwhile.

8.4. References

ME Casey, H Gadagkar and D Newport 1995 "A component based method for normalisation in volume PET" Proceedings of the 3rd International Meeting on Fully Three-Dimensional Image Reconstruction in Radiology and Nuclear Medicine, Aix-les-Bains, France.

ME Casey and EJ Hoffman 1986 "Quantitation in Positron Emission Computed Tomography: 7. A technique to reduce noise in accidental coincidence measurements and coincidence efficiency calibration" *J. Comput. Assist. Tomogr.* **10**,845-850

JM Ollinger 1997 *private communication*

TR Oakes, V Sossi and TJ Ruth 1998 "Normalization for 3D PET with a low-scatter planar source and measured geometric factors" *Phys. Med. Biol.* **43**(4) *to appear.*

SC Strother, ME Casey and EJ Hoffman 1990 "Measuring PET Scanner Sensitivity: Relating Count rates to Image Signal-to-Noise Ratios using Noise Equivalent Counts" *IEEE Trans Nucl Sci* **37**(2):783-788